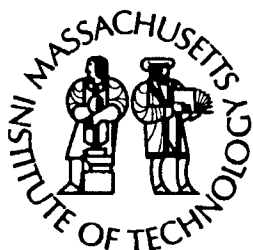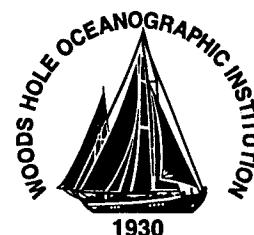# Massachusetts Institute of Technology
Woods Hole Oceanographic Institution

Joint Program
in Oceanography/
Applied Ocean Science
and Engineering

1930

DOCTORAL DISSERTATION

*Quantifying Channelized Submarine Depositional
Systems From Bed to Basin Scale*

by

William J. Lyons, III

September 2004

20050627 088

MIT/WHOI

2004-15

Quantifying Channelized Submarine Depositional Systems From Bed to Basin Scale

by

William J. Lyons, III

Massachusetts Institute of Technology
Cambridge, Massachusetts 02139

and

Woods Hole Oceanographic Institution
Woods Hole, Massachusetts 02543

September 2004

DOCTORAL DISSERTATION
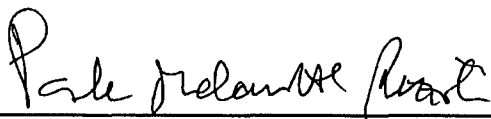
Approved for Distribution:

Susan E. Humphris

Susan E. Humphris, Chair
Department of Geology and Geophysics

Paola Malanotte-Rizzoli

Paola Malanotte-Rizzoli
MIT Director of Joint Program

John W. Farrington

John W. Farrington
WHOI Dean of Graduate Studies

Quantifying Channelized Submarine Depositional Systems from Bed to Basin Scale

By

William J. Lyons, III

B.A., Connecticut College, 1988
M.S., University of Wyoming, 1998

Submitted in partial fulfillment of the requirements for the degree of

Doctor of Philosophy

at the

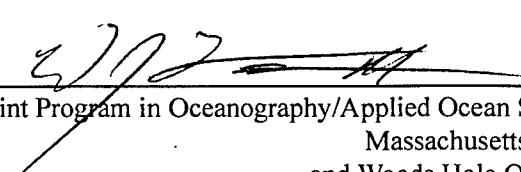MASSACHUSETTS INSTITUTE OF TECHNOLOGY

and the

WOODS HOLE OCEANOGRAPHIC INSTITUTION

September 2004
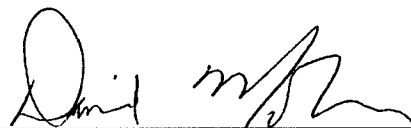
© 2004 William J. Lyons, III
All rights reserved.

The author hereby grants MIT and WHOI permission to reproduce paper and electronic copies of this thesis in whole or in part and to distribute them publicly.

Signature of Author

Joint Program in Oceanography/Applied Ocean Science and Engineering
Massachusetts Institute of Technology
and Woods Hole Oceanographic Institution
September 2004

Certified by

David Mohrig
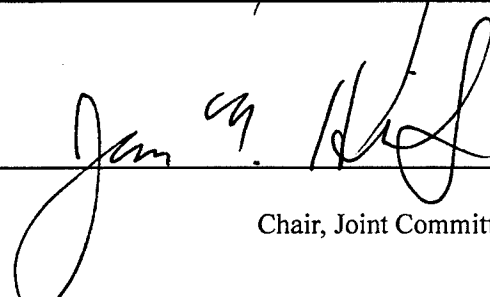Thesis Supervisor

Accepted by

J. Gregory Hirth
Chair, Joint Committee for Marine Geology and Geophysics
Woods Hole Oceanographic Institution

Quantifying Channelized Submarine Depositional Systems

from Bed to Basin Scale

by

William J. Lyons, III

Submitted to the Joint Program in Oceanography, Massachusetts Institute of
Technology and Woods Hole Oceanographic Institution,
on June 23, 2004, in partial fulfillment of the
requirements for the degree of

Doctor of Philosophy

Abstract

The challenges of directly observing active turbidity currents necessitates the consideration of preserved deposits for deciphering the behavior of these systems. In this thesis, I take advantage 3-D subsurface seismic data and outcrop exposures to study turbidites at scales ranging from bed to basin. At the basin scale, I develop a method to estimate the time-frame over which sedimentation and subsidence come into equilibrium. Using seismic data from the Fisk Basin, Gulf of Mexico, I find that, during periods of broadly distributed, sheet-like deposition, equilibrium time is on the order of 4.6×10^5 years. In contrast, during periods of confined channel development, that time drops to 2.0×10^5 years. Identifying these equilibrium times is critical because, at times below equilibrium, autogenic and allogenic stratigraphic signals cannot be distinguished. At the scale of turbidite beds, detailed grainsize analyses of sediment samples from the Capistrano Formation, San Clemente, California reveal the potential for misinterpretation that arises when deposits are studied without consideration for the dynamics of sedimentation. Previously interpreted as the result of anomalous sandy turbidites, using simple bed shear calculation and Froude scaling, I show that these coarse sediments are consistent with classical muddy, low-density turbidity currents. Finally, at the scale of amalgamated turbidite beds, I use outcrop mapping and aerial photography of the Zerissenne Turbidite System, Namibia to provide a measure of lateral and vertical continuity of a deepwater turbidite system. Previous studies have been hampered by limited exposure while the extensive continuous exposure of the Zerissenne show that correlation lengths of these systems can exceed 1.5 km.

Thesis Supervisor: David Mohrig
Title: Assistant Professor of Geology

Thesis Supervisor: John Grotzinger
Title: Roger P. Shrock Professor of Geology

Acknowledgments

This thesis is submitted under my name but its completion would never have been possible without the support and guidance of many. The risk in writing acknowledgments is that someone will be omitted. I apologize to any whose name does not appear here explicitly but please know that my thanks include you.

My career in Geology began when Paul Heller at the University of Wyoming agreed to accept a Masters student in sedimentology whose background was in International Relations and Russian studies. Without Paul, I would not be writing this today.

My tenure at MIT was made possible by John Grotzinger who agreed to admit and support me knowing that my interests did not necessarily mesh with his. Yet John always allowed me the flexibility to chose my own path and was incredibly supportive in the process.

Diverging from the path of your advisor has obvious risks and David Mohrig acted as the cavalry arriving at the best possible time. I can not thank David enough for his patience, dedication and friendship in guiding me through the substance of this thesis.

The list of friends who have provided support, in one form or another, during this process is virtually endless. At MIT, Amy Draut always provided a critical sounding board and a smile at those times when pursing a PhD was less than fun. The many miles that I logged running the Charles River with Payal Parekh were a wonderful diversion. Kyle Straub was an understanding officemate, and a good friend, when a trip to the Muddy was in order. On the 'outside', Mary Ann Guillette and the rest of the Holy Cross crowd including Dan and Paula, Christine and Jim, Mitch, Bob, John and Johnny Mac provided the distractions and companionship that were critical for my sanity.

Thanks to Doug McCalmont for being a great friend.

Roberta Bennett-Calorio deserves special mention. It is not possible to put in words how important she is to the 8th floor and to my tenure here in specific. All I can say is thanks.

Without Kellie Farrell, and her extended family, none of this would have happened. Not only did Sis and Bernie Sr. provide a place to live for a boy and his dog, but they raised one of the most tolerant, understanding and loving woman I have ever known. Thanks.

Thanks to Kellie for being one of the most tolerant, understanding and loving women I have ever known. And thanks for putting up with me!

Thanks also to my family. Even though you thought I was nuts, you never said so to my face and supported me the entire way. And Mom and Jerry, I thank you for your understanding of the demands on my time.

Thanks to Kasha, my first Golden Retriever and the worlds best pup, for 14 1/2 years of unconditional love. There is nothing quite so therapeutic as coming home to a happy dog.

Finally, I have to acknowledge my dad, William J. Lyons Jr., MIT '48. He instilled in me an appreciation for learning that drove me on through this process and I know will stay with me forever. My dad has been my strength through the many twists and turns of my education. Not once did I ever doubt that he would stand behind me and support me in any decision. Knowing he was there is the single most important thing that made this possible. Thanks dad.

Scientific Support

ChevronTexaco provided much of the funding for this degree.

Shell International Exploration and Production provided the seismic data from the Fisk Basin. Carlos Pirmez was instrumental in obtaining that data and was also a great friend and source of knowledge.

Roger Swart, and others at NAMCOR, provided invaluable logistical support for field studies in Namibia. Roger and Jane were also great friends and made working in Africa incredibly enjoyable.

Contents

7

9

List of Figures

15

19

24

27

28

31

32

35

36

List of Tables

Chapter 1

Introduction

The purpose of this work is to expand our knowledge and understanding of sediment transport and deposition in the deepwater with a specific focus on the mechanics of turbidity current systems. Seascapes reflect and record the interplay between sedimentary systems and basin development but our ability to decipher the history of that interplay is hampered by our limited understanding of the dynamics of deepwater sediment transport. Gaps in our knowledge exist at a range of scales — from the dynamics of individual beds and flows, to the behavior of depositional systems over distances of hundreds of kilometers and millions of years. In this work, I address problems across this range — at the scale of beds and flows, at the scale of packages of beds and turbidite lobes, and at the scale of cumulative basin fill.

One of the defining models in sedimentology is that of a graded profile as described by Mackin in 1948. A system is 'graded' if erosional and depositional dynamics respond to boundary and input conditions so as to maintain a steady-state equilibrium topography. This model has since been applied, directly or indirectly, to such diverse environments as channel erosion in the Himalayas (*e.g.* Whipple (2001)) and sedimentary fill in deep marine basins (*e.g.* Prather et al. (1998)).

The concept of basin equilibrium is a powerful one. It provides a framework within which to interpret stratigraphic features and provides a mechanism by which we can tie depositional events to either short time-scale dynamics inherent in the system or to long time-scale external forcing. Key then to such an interpretation

is a fundamental knowledge of what distinguishes short and long time scales. That question is addressed here. In Chapters 2 and 3 of this dissertation, I examine the concept of equilibrium between sedimentation and subsidence in a basin, quantify the scales at which this balance holds, and explore the dependence of that scale on the transport system distributing sediment throughout a basin.

In Chapter 2, I develop a method for determining the characteristic timescales for deepwater deposits and apply that method to broadly-distributed, unconfined sediments from Late Pliocene deposits in Fisk Basin, Gulf of Mexico. My method is an adaptation to natural systems of an experimental approach described by Sheets et al. (2002). Through detailed stratigraphic mapping and biostratigraphic dating of the Fisk Basin sediments, I constrain patterns of sediment deposition at scales ranging from a few tens of thousand years to several million years. Likewise, I determine the shape and rate of basin subsidence for the interval over which the sediment was deposited. The fit of sedimentation to subsidence for each depositional package can be characterized and shown to improve as the time interval of sedimentation increases; the rate of that change provides a measure of the equilibrium time and length scales of the system. Armed with this quantification of the sedimentation/subsidence response rate, it is then possible to differentiate the signal of external forcing from that of small-scale system instability.

In Chapter 3, I turn my attention to an interval of channelized sediment transport — a period with a very different stratigraphic architecture than the sheet-like deposition in Chapter 2 — and assess the characteristic time for this system. Fisk Basin provides a unique opportunity in that it contains sediments delivered under varying transport conditions but with similar boundary and input conditions. Immediately overlying the sheets that serve as the focus of Chapter 2 is an interval dominated by channel/levee complexes. Unlike the poorly confined sheets in the stratigraphy below, these channelized systems build significant local topography and are characterized by high local deposition rates and areally restricted sediment distribution. I apply the method developed in Chapter 2 to this channelized period. The unconfined sheets of Chapter 2 and the channel/levee complexes of Chapter 3 are end-member deepwater

systems and the contrast in characteristic times illustrates how system response times change with sediment transport dynamics.

I change scales dramatically in Chapter 5 of this thesis and turn my attention to individual turbidite beds and associated flows. One of the more common, yet enigmatic, turbidite deposits in the deepwater are coarse-grained massive beds. These sediments lack the high percentage of silts and muds often associated with turbidity currents and are also devoid of common sedimentological features such as cross-bedding and lamination. There has been considerable speculation on the characteristics of the flows responsible for deposition of these beds (*e.g.* Lowe (1982); Shanmugan (1996), Parker et al., in prep) however a powerful source of data has been neglected — that of detailed grainsize analysis. In this chapter, I use grainsize analyses of sediments from the Capistrano Formation at San Clemente, CA. I obtained a unique dataset of closely spaced vertical and lateral sediment samples and show it is possible to constrain the flow depths, vertically averaged flow velocities, and a measure of the vertical sediment distribution, or vertical mixing, in the flows through detailed grainsize analyses of these samples. The results of my analyses indicate that coarse-grained structureless beds, though unique in coarseness and grainsize composition, can be reasonably explained by classic, mud-rich turbidity currents.

Finally, in Chapter 6, I address deepwater stratigraphy at the scale of amalgamated beds with thicknesses on the order of meters to tens of meters and widths on the order of ten kilometers. We know from outcrop that stratigraphy can vary widely on this mesoscale but in the deepwater, where the vast majority of our data is in the form of reflection seismic surveys or widely spaced well penetrations, these details are rarely captured. A fundamental question that arises in unconfined deepwater systems is that of the lateral and vertical continuity of deposits. Outcrops rarely provide adequate exposure to fully capture the variability of broadly distributed turbidite systems. The Zerrissene Turbidites of west-central Namibia are an exception. The Zerrissene outcrops are the best exposed examples of laterally continuous deepwater deposits in the world. Through the use of aerial photographic mosaics and fieldwork, it was possible to constrain the unprecedented lateral continuity of the Zerrissene

43

Turbidite system. This study provides a data set that increases our insight into the broad distribution of sediment possible from unconfined deepwater flows.

This thesis is written as four independent papers, each of which can stand on its own. The common thread that runs throughout is an attempt to broaden our understanding of the behavior of deepwater depositional systems. In each case, I have tried to take a simple approach to a fundamental problem in order to broaden our understanding of deepwater sediment dynamics at a range of scales.

Chapter 2

Equilibrium time scale for an intra-slope basin: Assessing the balance between sedimentation and subsidence and its implications for interpreting deepwater stratigraphy

2.1 Introduction - Sheet deposition and equilibrium time

A key element for interpreting the topography of any landscape, be it terrestrial or marine, is an understanding of the system equilibrium time. That is, we must know the time interval associated with reestablishment of steady state topography following system perturbation by an external forcing. This characteristic time is a measure of the response rate of the system to change. In recent years, a great deal of work has gone into understanding the controls on the equilibrium time in terrestrial systems,

particularly mountain belts subjected to changes in climatic and/or tectonic forcing (Whipple, 2001). The physics of these terrestrial systems is well enough understood that both the duration of adjustment and the relative effects of different forcings have been explored quantitatively within a theoretical framework (*e.g.* Whipple (2001)). This is not the case for the submarine environment. Processes controlling transport in submarine systems are not as fully studied and have not yet been synthesized into a framework that can be used to predict system-scale response times. Fortunately, submarine systems possess attributes not commonly found in terrestrial systems that make the marine realm particularly amenable to the direct measurement of this system property: marine basins commonly preserve a significant fraction of the volume of sediment associated with the evolving seascape surface and the stratigraphy commonly possesses the time control necessary to quantify intervals of system adjustment. I have taken advantage of such data, specifically a 3-D reflection seismic survey and an excellent microfossil record, to determine the equilibrium time-scale for a submarine system traversing a small basin on the continental slope in the Gulf of Mexico. Here I have focused on data defining the Late Pliocene section preserved in Fisk Basin (informally referred to as Auger Basin by Booth et al. (2000); Winker and Booth (2000); Booth et al. (2003)). This volume of strata, about 1.5 km thick, 20 km wide, and 30 km long, documents the competition between sedimentation via the transport system and basin subsidence via salt withdrawal over 1.2×10^6 years. I use this stratigraphic data to measure convergence between the patterns of sedimentation and subsidence with increasing time. This convergence defines the establishment of an equilibrium condition where adjustments in the sediment-transporting system balance basin subsidence to produce steady state topography.

Processes controlling the production, erosion, transport, and deposition of sediment within a landscape are broadly diffusional, acting through time to reduce topographic relief (*e.g.* Dietrich et al. (2003)). Steady state or equilibrium topography therefore requires a regenerative source/sink term in the form of rock uplift or subsidence in order to be maintained. Recent laboratory studies generating both erosional (Hasbargen and Paola, 2000) and depositional (Sheets et al., 2002) topography have

clearly shown that this steady state must be statistically defined. Patterns of erosion or sedimentation must be averaged over time to filter out natural variability associated with the transport systems. Balance between the pattern of uplift and erosion or the pattern of subsidence and sedimentation only holds when averaged over some appropriately long time-scale. Potentially significant departures from this balance, arising from feedbacks internal to the transport system, can occur over shorter time scales. The transition from short to long scales is characterized by the equilibrium time of the basin. Having some knowledge of what is short versus long time is fundamental to reconstructing the mechanisms controlling temporal changes recorded within sedimentary strata filling basins (Paola et al., 1992). Identifying an equilibrium time is necessary for separating records of change associated with external or allogenic forcing, from change due to internally generated or autogenic processes of the system. The equilibrium scale defines a unit stratigraphic interval inside of which both autogenic variability associated with the transport system and allogenic variability in environmental conditions must be considered when interpreting the cause of vertical trends in stratigraphic properties such as mean grain size, mean bed thickness, and stacking patterns of preserved channel-filling deposits. Variability in autogenic processes average out at the level of the unit stratigraphic interval, so any systematic change occurring over greater deposit thicknesses can be unambiguously related to longer-term, externally imposed variations in environmental conditions.

Changes through time in the patterns of sediment erosion and deposition on the continental slope are commonly viewed as adjustments by the sediment-transporting system necessary to re-establish or maintain an approximately steady-state topography. Most frameworks for interpreting deep-water stratigraphy and submarine-landform evolution employ a steady state or graded profile metric against which departures from this idealized profile form are both measured and interpreted (*e.g.* Prather et al. (1998)). It is generally assumed that modifications recorded in the seascape and associated subsurface stratigraphy document changes in allogenic forcing (*e.g.* sealevel, climate or sediment flux). Essentially, depositional and erosional seascape features are interpreted to reflect adjustments to the elements controlling

the initial and/or boundary conditions for the sediment-transporting system and, as imaging of these features improves in resolution, there has been a resultant increase in interpretation scale.

It is likely many geologists would agree that adjustments associated with only meters of topographic change and/or intervals of time up to tens of years in duration could be entirely the result of natural variability within the transport system, even under conditions of approximately constant external forcing. It is less obvious how best to interpret the causes of change associated with vertical intervals of 10's to 100's of meters and time intervals of thousands to hundreds of thousand years. What component of such a response should be assigned to autogenic variability versus allogenic change? The answer to this question is fundamental to the accurate interpretation of submarine landscape evolution because this mesoscale response spans the time range for all Milankovich orbital cycles and their associated allogenic signals of climate and sea-level change. Here I attempt to directly measure the signal of autogenic variability at the mesoscale so that it might be separated from signals associated with allogenic forcing.

Using a volume of seismic data made available by the Auger Asset Team of Shell Exploration and Production Company (SEPCo), I have mapped and subdivided the Late Pliocene deposits of Fisk Basin into eight successive stratigraphic intervals. Four of these eight intervals have been dated directly using recovered assemblages of microfossils from multiple wellbores in the basin. The basin-wide mapping of regional surfaces tied to age control defines the basin history associated with construction of a 1.5×10^3 m stratigraphic section spanning 1.2×10^6 yr. I use this chrono-stratigraphic framework first to determine the long-term pattern for subsidence in the basin during the Late Pliocene and then to compare this subsidence pattern against measured patterns of sediment accumulation over increasing intervals of time. I make these comparisons using a modified version of the method developed by Sheets et al. (2002) for quantifying differences between sedimentation and subsidence patterns through time. Maps of interval thickness are compared to maps of space created via basin subsidence. To make such comparisons, the value from one map is divided by the value

from the other map at every point and the statistics for the resulting distribution of sedimentation/subsidence ratios are calculated. If sedimentation perfectly balanced subsidence throughout the basin, the mean of the ratios would always equal 1 and the standard deviation would always equal 0. Mean values for the Late Pliocene system are indeed close to 1 and do not systematically vary as a function of increasing time or interval thickness. Standard deviation values, on the other hand, systematically decrease with increasing time or interval thickness. For example, the average value for the standard deviation associated with 1×10^5 years of sedimentation is 2×10^{-2}, while the average value for standard deviation associated with 1×10^6 years of sedimentation is 2×10^{-4}. I use this ten-fold decrease in standard deviation to determine the 'equilibrium' time for the submarine system filling Fisk Basin. Following the proposal of Sheets et al. (2002) this characteristic time is indicated by the e-folding value associated with the exponential decay in standard deviation measured as a function of time. I find this interval of time to be 4.6×10^5 years, corresponding to an interval thickness of about 600 m and vertical trends in the basin-filling stratigraphy must be interpreted in light of these characteristic values.

2.2 Fisk Basin

The Fisk Basin is located on the upper continental slope of the Gulf of Mexico about 350 km southwest of New Orleans, LA, at an average water depth of about 900 m (Figure 2-1). A number of papers describing the stratigraphy and depositional history of this basin have been recently published (Booth et al., 2000; Winker and Booth, 2000; Booth et al., 2003) and this work builds on the stratigraphic framework presented therein. These papers and others refer to the location as Auger Basin, an informal name derived from the presence of the Auger hydrocarbon exploration field. I will refer to the basin by its official name, Fisk Basin (http://pubs.usgs.gov/of00-019/data/misc/gomnames.dbf; Bouma and Bryant (1994)). In its Late Pliocene configuration, the Fisk Basin was about 12 km wide by 20 km long and positioned about 120 km down slope from the contemporaneous shelf edge (Winker and Booth, 2000;

Booth et al., 2003). Representative seismic lines defining basin configuration and stratigraphy are shown in Figures 2-2 and 2-3. Three hydrocarbon-producing fields flank the eastern side of the basin and our work takes advantage of much of the data collected from wellbores in the Auger, Oregano, and Macaroni fields (Figure 2-1). Well data include the paleontological analyses providing age control for the system, lithologic samples used to connect seismic attributes to rock types, and check-shot data establishing the relationship between seismic two-way-travel time and true vertical depth below the sea floor. Each of these data are discussed below.

The Gulf of Mexico, in current modern form, originated during rifting between the North American and South American and African plates in the Late Triassic (Salvador, 1991). Rifting continued through the Jurassic. In the late Middle Jurassic, periodic encroachments of the sea on the rifting basin resulted in the formation of extensive salt deposits. The main drifting episode in the Gulf, which separated the Yucatan block from the North American Plate, occurred in the early Late Jurassic. This drifting took place after deposition of the salt and emplaced true oceanic crust in the basin. Since the Late Jurassic, the Gulf of Mexico has been tectonically stable with subsidence driven by crustal cooling and sediment loading.

The Cenozoic structural evolution of the northern Gulf of Mexico is dominated by deformation and migration of the Jurassic Louann Salt (Diegel et al., 1983). Differential sediment loading of this relatively mobile layer has produced a variety of structures including low-relief anticlines and pillows, high-relief plugs and walls, and extensive salt sheets (Nelson, 1991). Sediment loading in the region offshore of Texas and Louisiana has been from the north and the salt has subsequently migrated southward producing a set of shore-parallel tectono-stratigraphic provinces (Diegel et al., 1983). The most distal of these is the tabular salt/mini-basin province that extends southward from about the position of the modern shelf-slope break and is bordered in deeper water by the Sigsbee Escarpment (Nelson, 1991; Diegel et al., 1983). The Fisk Basin is located in the northern part of this province and is bordered to the east, west and south by allochthonous, high-relief salt bodies. The alternate name of the basin (Auger Basin) is derived from the salt plug forming the Auger Dome in the

north of the basin (Figure 2-1).

The oldest hydrocarbon-bearing sand in Fisk Basin is no older than 3.95 Ma and, since much of the exploration in the Gulf is economically driven, the earlier development of the basin is poorly constrained. However, since 3.95 Ma, sediment into the basin has come primarily from the north and west while subsidence has been focused in the south (Booth et al., 2000; Winker and Booth, 2000; Dean et al., 2002; Booth et al., 2003).

2.2.1   Fisk Basin age control

A relatively high-resolution chronology is required to extract the necessary temporal trends from Fisk Basin stratigraphy. Fortunately there is an extensive biostratigraphic framework and related age control for the Gulf of Mexico resulting from the long history of hydrocarbon exploration (Breard et al., 1993, 1996; Styzen, 1996; Breard et al., 1997; Lawless et al., 1951; Rosen et al., 1999; Breard et al., 2002). This biostratigraphic framework was subsequently tied to the Fisk Basin stratigraphy based upon core data acquired from the hydrocarbon fields (*e.g.* Booth et al. (2000); Dean et al. (2002); Figure 2-1). All dated samples were collected from relatively fine-grained stratigraphic packages that are enriched in their volume concentration of microfossils. This reduction in grain size and enrichment in microfossils are interpreted to signal periods of relatively low delivery rates for detrital sediment to the site and these sedimentary packages are referred to as condensed sections. Shell geoscientists have dated seven condensed sections using population trends observed in calcareous nannofossils, shelfal foraminifera, and benthic and planktonic bathyal foraminifera (Dean et al. (2002); Table 2.1). Age control for the Pliocene section of Fisk Basin is derived from five of those condensed sections that can be mapped basin-wide in the 3-D seismic data. These condensed sections are CS7, CS9, CS12, CS13 and CS14 and have associated ages of 3.47 Ma, 3.09 Ma, 2.55 Ma, 2.30 Ma and 1.95 Ma, respectively (Table 2.1).

2.2.2 Fisk Basin seismic data

My mapping of the Late Pliocene section was carried out in a 3-D reflection seismic data volume provided by SEPCo. Stratigraphic horizons were mapped in two-way travel time (TWT) and then converted to true depth before carrying out the analyses described below. This time-depth conversion required acoustic velocity data also provided by SEPCo. I constructed the conversion algorithm from borehole-derived check-shot data directly measuring the acoustic velocity for the rock as a function of depth below the sea floor. This check-shot data was collected from an Auger Field wellbore and a polynomial fit to the time-depth pairs are presented in Figure 2-4. The polynomial fit to these data is:

$$D = 83.52 m/s^2 (TWT_{ss} - TWT_{sf})^2 + 835.8 m/s \; (TWT_{ss} - TWT_{sf}) \qquad (2.1)$$

where D is vertical distance beneath the seafloor in meters, TWT_{ss} is the two-way travel time at the subsurface horizon of interest and TWT_{sf} is two-way travel time at the seafloor. Both TWT_{ss} and TWT_{sf} are measured in seconds. Equation 2.1 is applied locally to convert grids of points defining horizons in time to grids of points defining the same horizons in depth below the seafloor. Seismic mapping and Equation 2.1 can be combined with the age-control data presented in Table 2.1 to generate a function describing the thickness of accumulated sediment through geologic time (Figure 2-5).

2.2.3 Late Pliocene stratigraphy of the Fisk Basin

The stratigraphy of Fisk Basin has been the subject of several recent studies (Booth et al., 2000; Winker and Booth, 2000; Booth et al., 2003) and that framework is adopted here with minor modifications. This stratigraphy is based on the identification of a succession of condensed sections both in the seismic-data volume and in multiple wellbores. Here I am particularly interested in seven of these condensed sections: CS7, CS8, CS9, CS10, CS11, CS12, and CS13 (Booth et al., 2000; Winker

and Booth, 2000; Dean et al., 2002; Booth et al., 2003). This interval brackets a large fraction of the Late Pliocene section of the basin. Well logs from the Auger and Macaroni fields (Figure 2-1) interpreted by Booth and colleagues (see Figure 7 of Booth et al. (2000); or Figure 9 of Booth et al. (2003)) show that reasonable estimates for the mean and median thickness of these seven condensed sections are 25 m and 24 m, respectively. As I have already described, these relatively fine-grained, microfossil-enriched intervals are interpreted to represent times of basin-wide reduction in sediment accumulation rates and the deposits are interpreted to drape over the pre-existing basin-floor topography, which is always composed of coarser-grained detritus. The interfaces between condensed sections and coarser-grained deposits can be mapped seismically because of the large contrast in impedance between the lower porosity condensed sections and the higher porosity, coarser deposits. I have mapped the zero-crossings on seismic traces throughout the basin corresponding to the seven interfaces separating condensed sections below from coarser-grained deposits above. These seven basin-wide horizons are treated here as approximate timelines, separating older strata below from younger strata above.

While the condensed sections in the basin fill are essential for establishing the time-stratigraphic framework for Fisk Basin, these sections make up only a small fraction, approximately 10% by volume, of the Late Pliocene interval under study here. The remaining section, shown in detailed seismic lines in Figures 2-6 and 2-7, is made up of sandier deposits. Details of the depositional and erosional geometries associated with these condensed section deposits are difficult to extract from the seismic data alone because the thickness, depth, or relief associated with these structures is small relative to the dominant wavelength of the seismic pulse. The stratigraphy associated with sedimentary interval between CS7 and CS13 is not as sheet-like as a quick glance at Figures 2-6 and 2-7 might suggest — maps of seismic-loop attributes (*e.g.* amplitude and coherency) reveal that at least some of the sheet-like deposits are constructed out of amalgamated channel fills. Examples of the sediment-filled channel forms can be found in Figure 4 of Booth et al. (2003). Booth and his colleagues have imaged channel forms, up to a few hundreds of meters wide, within the sandy sheet-like

deposits that persist laterally for a number of kilometers in the interval between CS7 and CS8 and between CS11 and CS12. These images are consistent with the stratigraphic patterns inferred from well logs collected from multiple, closely space wellbores in all three oil fields (Figure 2-1). For example, Booth et al. (2000, 2003) interpret much of the variability in bed thickness and sand fraction between these wells as being the signature of numerous single channel fills amalgamating laterally to form relatively sand-rich intervals with overall sheet-like geometries.

A 45 m section of core from Fisk Basin is presented as Figure 2-8. This core samples the interval between CS11 and CS12 at the Oregano Field (Figure 2-1) and documents a rapid vertical transition from background deposition of mud at its base to channel-filling sands at its top. The middle section of the core is composed of 2 m of thinly bedded mudstones and intervening ripple-stratified sandstones — an assemblage characteristic of sediment deposition in channel margin and/or proximal overbank locations. Sedimentary structures, textures and facies preserved in core recovered from the Late Pliocene section of Fisk Basin are consistent with the larger scale architecture for the basin filling stratigraphy defined by well log and seismic data. Evidence for channelization is found at every scale of inquiry. The degree of focused erosion associated with this channelization is small relative to what is observed in the overlying Quaternary section (see Figures 2-6 and 2-7). Even so, a few erosional surfaces of sub-basin extent can be mapped within the Late Pliocene section. I have mapped two of these surfaces and include them in my stratigraphic framework for subdividing the basin fill. One of these surfaces is located between CS9 and CS10 and the other between CS12 and CS13 and are referred to here as horizons E9.5 and E12.5, respectively. The only channel form with measurable thickness in the Late Pliocene section is near its top between CS12 and E12.5.

2.2.4 Fisk Basin configuration from Late Pliocene to the present

The present-day bathymetry of the Gulf of Mexico off-shore of Texas and Louisiana is composed of numerous topographic depressions — under-filled basins of which Fisk Basin is one (Figure 2-1). It is tempting to adopt the present-day morphology and geology of Fisk Basin as a template for interpreting the Late Pliocene configuration of the system. While sedimentary fill of the earlier basin does lie directly beneath the present-day form, temporal changes throughout the last 3.47 Ma limit the applicability of near seafloor analyses to interpretation of the older system. These changes include: 1) a steady, long-term increase in sediment accumulation rate throughout the Quaternary; 2) a shift in the basin-wide pattern of sediment accumulation; and 3) a shift in architecture of the stratigraphic elements composing the basin fill. Implications for each of these points are discussed below.

The location of Fisk Basin relative to the edge of the continental shelf has changed through time. Mapping of the shelf-edge position using seismic data reveals a progressive southward migration of the shelf-slope break of about 50 km from the Early Pliocene to the present (see Figure 5 of Winker and Booth (2000); Figure 1 of Booth et al. (2003)). This basin-ward shift reduced the slope length connecting the basin to the shelf edge by about 40% over that time. Assuming most of the sediment deposited in Fisk Basin is terrestrial in origin, this reduction in separation between the basin and the shelf edge is consistent with, and provides an explanation for, the increasing rate of sediment accumulation within the basin over the last 3.47 Ma (Figure 2-5).

A trendline describing sediment accumulation as a function of time provides a remarkably accurate fit to the data for the last 3.47 Ma (Figure 2-5). Only two points depart significantly from the long-term trendline and one of those points, that associated with CS14, I discuss here. The CS14 horizon represents an interval of strata located less than 200 m above the Late Pliocene section focused on in this chapter (Figures 2-2, 2-3, 2-6 and 2-7). The age of CS14 (Table 2.1) defines a rate of sediment accumulation for the section between CS13 and CS14 that is

only two-thirds the accumulation rate associated with the section between CS7 and CS13. Seismic mapping within the CS13-CS14 interval reveals a plausible explanation for this reduction — the occurrence of large submarine channels that traverse the entire basin width. At least two erosionally-based channel forms having seismically resolvable thickness can be seen in Figure 2-6, both positioned < 100 ms above CS13. I hypothesize that these deeper, flow-confining channels conveyed a greater fraction of incoming sediment through Fisk Basin and further down the slope, thereby reducing the basin-averaged sediment accumulation rate for this limited interval of time. (See Chapter 3 for a detailed analysis of this channelized interval.)

Channels comparable in thickness and areal extent to those described between CS13 and CS14 occur throughout the Quaternary stratigraphy of Fisk Basin. This introduction of strongly erosional channel forms into Fisk Basin stratigraphy is approximately coincident with a re-organization of depositional patterns within the basin that, because of the long time intervals involved, I interpret as signaling a change in the pattern of basin-floor subsidence. Figure 2-9 shows a map of relative deposit thicknesses for the section between CS7 and CS13 and the section between CS14 and the seafloor. The depocenter clearly shifts from the SW corner of the basin during the Late Pliocene (CS7 to CS13) to the SE corner of the basin (CS14 to the sea floor) and the overall shape of the basin-filling deposit changes as well. My mapping indicates that this adjustment occurs relatively quickly, primarily within the section bounded by CS13 and CS15, and that the gross sedimentation pattern was approximately constant thereafter. Fisk Basin subsidence, like all mini-basins in the central Gulf of Mexico, has been driven primarily by preferential evacuation of the thick Louann Salt (late Middle Jurassic) from beneath the basin floor (Figure 2-1; Nelson (1991); Diegel et al. (1983)). The change in basin floor subsidence pattern is followed shortly thereafter by an increase in basin-margin relief. Evidence for development of this local relief along the basin margin is documented by the first occurrence of seismically definable, mass-transport complexes in the basin immediately above H14.5. An example of one such mass slump complex, interpreted from its chaotic seismic character, is marked on all four cross-sections in Figures 2-2, 2-3, 2-6 and 2-7. These

56

complexes, composed of submarine slides, slumps and/or debris flows, are sourced from the margins of the basin itself. Steepening of the basin margin relief is most likely associated with an increased vertical migration of remobilized Louann Salt at these locations and the age of these mass transport complexes provide an indication of the time of this vertical salt migration.

The Late Pliocene section between CS7 and CS13 is dominated by shallow submarine channels that, via multiple lateral shifts in their positions, coalesce to form larger stratigraphic elements that appear approximately sheet-like at the resolution of the seismic data. This style of stratification is quite different from the erosionally-defined channels and mass-transport complexes commonly found in the overlying Quaternary section of the basin fill. The change in basin-filling stratigraphy from sheets to mass transport deposits is most likely a result of a change in the pattern of Louann Salt motion in and around the basin itself, which increased local basin relief, in turn promoting channel incision and the release of slides, slumps and/or debris flows. Hence, I believe that local basin topography was subdued in the Late Pliocene relative to the modern-day bathymetry.

2.3   Equilibrium time and the graded profile

On short time scales, an active channel or depositional lobe occupies only a fraction of a basin and at this timescale (that of individual yearly floods or the migration of meander bends) deposition is confined to the immediate area in, and adjacent to, the active depositional system (Figure 2-10). Patterns of sedimentation are then set by the dynamics of sediment transport. If we 'zoom out', temporally to the geologic scale and spatially to the basin scale, these local features are lost in favor of larger-scale dynamics. Integrating the behavior of a river system or a delta over thousands to millions of years, depositional architecture is no longer dominated by individual channels or lobes. At these long time scales, deposition is dominated by the subsidence patterns of the basin (Figure 2-10). The equilibrium scale for a basin is the time at which stratigraphy goes from being transport/deposition dominated to

being subsidence dominated and, while the distinction may be clear in the extreme, the point at which this transition occurs is not.

Mackin (1948) described a graded stream as one in which "...over a period of years, slope is delicately adjusted to provide, with available discharge and prevailing channel characteristics, just the velocity required for the transportation of the load supplied by the drainage basin". In other words, the transport system is adjusted so that the sediment load moving through any particular reach is equal to the load entering it. This adjustment leads to the development of a steady-state topography when applied to a drainage basin. The connection between a graded system and steady-state topography is described by the erosion equation (Fredsöe and Deigaard, 1994), an expression for the conservation of sediment mass in a flow moving over an erodible bed:

$$\frac{\partial \eta}{\partial t} = -\frac{1}{\epsilon_{bed}}(\nabla \cdot q_s + \frac{\partial V_s}{\partial t}) \tag{2.2}$$

where η is elevation of the uppermost layer of non-moving grains, t is time, ϵ_{bed} is concentration of sediment in the bed (1-porosity), q_s is sediment flux or sediment discharge per unit width, and V_s is volume of sediment in motion per bed area. Equation 2.2 states that the rate of change in bed elevation via sedimentation or erosion is equal to the divergence or spatial change in the sediment flux plus the rate of change in suspended sediment concentration (approximately V_s). Over time intervals of many days and longer, values for $\partial V_s/\partial t$ are much smaller than associated values for $\nabla \cdot q_s$ and the former term is often dropped from the balance to yield

$$\frac{\partial \eta}{\partial t} = -\frac{1}{\epsilon_{bed}}(\frac{\partial q_s}{\partial x} + \frac{\partial q_s}{\partial y}) \tag{2.3}$$

where x is the down-flow direction, y is the cross-flow direction, and $(\partial q_s/\partial x + \partial q_s/\partial y) = \nabla \cdot q_s$. Mackin (1948) defined a graded system as one adjusted so that $\nabla \cdot q_s = 0$ and Equation 2.3 shows that this requires $\partial \eta/\partial t = 0$ everywhere — the definition for an equilibrium profile and necessary condition for steady state topography.

58

Equation 2.3 describes the connection between spatial change in the sediment flux and temporal change in the bed elevation along a transport system. This connection is diagrammatically illustrated for the case of two small basins on the continental slope in Figure 2-11 (left). In this figure, spatial variation in the sediment transport field results in sediment deposition and erosion, adjusting local bed elevations and modifying the shape of its long profile. Further adjustments could eventually lead to the development of an approximately graded system with steady state values of elevation at every point along the long profile. In this example, the modifications to the long profile only occur via the addition and removal of mass from the surface by the transporting flows. The surface itself is treated as rigid — an assumption that typically is appropriate at short or engineering time scales ($\leq$ hundreds of years). This treatment breaks down at longer or geologic time scales where rates of surface uplift or subsidence can accumulate to significantly deform the profile. Working at these longer scales a source/sink term must be added to Equation 2.3 so that:

$$\frac{\partial \eta}{\partial t} = \sigma(x, y, t) - \frac{1}{\epsilon_{bed}}(\frac{\partial q_s}{\partial x} + \frac{\partial q_s}{\partial y}) \tag{2.4}$$

where σ is the source/sink term associated with deformation of the earth surface. In Fisk Basin, σ is a subsidence rate, measured in mm/yr, that varies as a function of x, y and t.

We can now consider the condition required to establish and maintain a graded or equilibrium topography in a system including subsidence and/or uplift. Equation 2.4 describes the components affecting topographic change and steady state topography requires $\partial \eta / \partial t = 0$. The necessary condition to develop an equilibrium profile then becomes:

$$\sigma(x, y, t) = \frac{1}{\epsilon_{bed}}(\frac{\partial q_s}{\partial x} + \frac{\partial q_s}{\partial y}). \tag{2.5}$$

For sedimentary basins, Equation 2.5 describes the balance between subsidence rate and sedimentation rate necessary to preserve a steady-state profile. A diagrammatic example of this balance is shown in Figure 2-11 (right). The divergence in

the sediment flux is not equal to zero, as would be required for steady state under conditions described by Equations 2.2 and 2.3, but equals a spatially variable rate that perfectly balances the rate of subsidence. As already described, these two rates (Equation 2.4) will not balance at all time scales because of natural variability in the transport system. For example, self-channelization of sediment-transporting flows completely controls the pattern of deposition over relatively short intervals of time (Sheets et al., 2002). However, over longer time intervals, differences will average out and patterns of sedimentation and subsidence will come into agreement. The time scale associated with establishment of this agreement and development of an equilibrium condition for the Late Pliocene Fisk Basin is determined in the following sections.

2.3.1 Measuring equilibrium time in a basin

Sheets et al. (2002) proposed a method for quantifying the equilibrium time scale for a depositional system. To test it, they used an experimental facility in which they controlled subsidence shape and rate, continuously introduced sediment to the basin, and, at discreet intervals, measured the topography that developed as a result (Figure 2-12). Their goal was to quantify the fit between the subsidence pattern and the resulting topography in such a way as to determine the time scale at which subsidence and deposition balanced.

As a measure of comparison between subsidence and deposition, Sheets et al. (2002) chose to use the standard deviation in the ratio between known space created by subsidence (accommodation) and thickness of aggrading deposits beneath measured topography (accumulation). Specifically, they divided their map of deposit thickness point-wise by the known subsidence pattern for a given time interval during the experiment. They then calculated the standard deviation associated with sets of ratios and used this metric as a measure of the fit between the two maps. This exercise was conducted repeatedly during the course of an experiment using progressive topographic maps to determine deposit thickness and progressive measurements of space created by the basin to determine subsidence (Figure 2-12). Sheets and his col-

leagues found that the standard deviation of the ratio data decayed exponentially as the experiment progressed and the depositional system progressively occupied more and more of the subsiding basin. To characterize the convergence between sedimentation and subsidence, they plotted standard deviation as a function of time and fit that data with an exponential function (Figure 2-13). They chose the e-folding time — the time required for the standard deviation to decay by a factor of $1/e$ — as a representative scale of system behavior. Below, I adopt this approach and extend it to the natural example of Fisk Basin with modification.

2.4 Method of determining basin equilibrium time

2.4.1 Stratigraphic mapping

All condensed section horizons for this study were mapped seismically at the transitions between the condensed sections below and the sandier deposits above. Specifically, I employ nine mapped surfaces (CS7, CS8, CS9, E9.5, CS10, CS11, CS12, E12.5 and CS13) within the Late Pliocene stratigraphy with the oldest being CS7 and the youngest CS13. The surfaces E9.5 and E12.5 are not regionally extensive condensed sections but rather are widely mappable erosional surfaces that provide sub-condensed section resolution. Erosional surfaces E9.5 and E12.5 were mapped at the erosional boundary, where present, and at the conformable boundary between sheets in the areas where underlying stratigraphy was not removed. For reasons described above, I consider each condensed section and associated mapped horizon to represent an approximate time line. Subtracting one horizon from another therefore generates an isochron representing vertical depositional thickness for a discreet time interval. For example, it is possible to constrain the depositional pattern in TWT over the 0.38 Ma period between CS7 (3.47 Ma) and CS9 (3.09 Ma) by calculating the difference in TWT between these two surfaces. I constructed isochrones using every possible combination of mapped horizons (Table 2.2). Of course, Late Pliocene depositional packages have been deformed due to post-depositional tectonism but,

because we are interested only in stratigraphic thickness, this structural deformation does not affect my results.

2.4.2 Calculating depositional thickness

In order to work in depositional thickness (*e.g.* meters) rather than time (*TWT*), isochrones must be converted to isopachs. Every point in *TWT* defining a surface must be converted from time to true vertical depth using Equation 2.1 and these converted surfaces are then subtracted from one another to generate thickness maps. The isochrones described above reflect vertical thicknesses in time and, strictly speaking, my method of differencing these surfaces produces 'isochors' (maps of vertical thickness). The term 'isopach' refers to thickness perpendicular to one of the bounding surfaces. Slopes on bounding surfaces in this study are small hence isopach and isochor thicknesses differ little and I use the more conventional term 'isopach' to refer to depositional packages measured in meters. Once isopachs are generated, a final correction is required to approximate true depositional thickness. This correction accounts for a reduction in porosity due to post-depositional compaction and hence a reduction in deposit thickness with burial. To restore isopachs to near-seafloor values, a decompaction factor was applied assuming a near-seafloor porosity of 40% (Sclater and Christie, 1980) and a final porosity at depth of 30% taken from core samples as provided by SEPCo. This simple porosity adjustment increases all thicknesses mapped at depth by 17% for near-seafloor conditions. Within about 3 km of the seafloor, compaction, and hence porosity, varies strongly with depth of burial. Below 3 km, porosity versus depth functions approach a constant value (Steckler and Watts, 1980; Bond et al., 1983; Angevine et al., 1990). Angevine et al. (1990) describe changes in porosity as a function of depth with a simple exponential:

$$\phi = \phi_0 e^{-cz} \qquad (2.6)$$

where ϕ is buried porosity, ϕ_0 is initial/depositional porosity, c is a lithologically dependent compaction constant, and z is depth of burial below the seafloor. All

stratigraphic packages included in this study are located at 3.5 km depth or below (*e.g.* H14.5 in Figure 2-2). The horizon with the greatest vertical relief is CS7 (Figure 2-2). The northern end of this horizon is 4.25 km below the seafloor while the deepest portion at the southern end is at about 4.75 km. From Equation 2.6, sediments at this horizon would experience differential compaction (ϕ at $z = 4.25$ km versus ϕ at $z = 4.75$ km) amounting to less than 15% porosity difference therefore the constant porosity correction described above is sufficient.

2.4.3 Determining age for mapped horizons

While the three hydrocarbon fields in the Fisk Basin provide excellent temporal control for the stratigraphy (Table 2.1), this control is limited to four horizons in the Late Pliocene and is at a coarser level than required for my analysis. I further subdivide the time history, assigning ages to each of the mapped horizons, using a functional relationship between time and depositional thickness.

For the period of specific interest to this study (CS7 to CS13), a simple linear fit does an excellent job describing sedimentation as $z = 1.3$ km/Ma $\times t$ ($R^2 = 0.999$) where z is depositional thickness in km and t is time measured in millions of years (Figure 2-5). Based upon the slope of the linear function, the average sedimentation rate for the Late Pliocene was 1.3 mm/yr. Therefor, using average sedimentation rate, all isopachs can be assigned ages based upon isopach thickness. Time intervals associated with all Late Pliocene isopachs are found in Table 2.2.

2.4.4 Determining basin subsidence

The advantage of an experimental study like that of Sheets et al. (2002) is that subsidence history is prescribed. In a natural system, subsidence rate and pattern are not as easily constrained. Often, basin depositional patterns are used as proxies for subsidence. I contend, however, that depositional patterns do not accurately reflect sedimentation unless those patterns are considered above a certain scale and that critical scale is unknown. Hence, it was necessary to develop a strategy for

63

determining the representative basin subsidence shape.

I determine subsidence pattern by adding successive isopachs and comparing their patterns to that associated with the entire Late Pliocene section between CS7 and CS13. If a given subsidence pattern is approximately constant for an extended interval of time, then any cumulative set of isopachs within that period, regardless of basal horizon, should converge on that long-interval shape. For example, a series of isopachs of increasing thickness beginning with CS7 should approach the overall basin subsidence shape as thickness increases. Likewise, this same convergence should be seen if I choose CS8 or any other mapped horizon as a basal horizon. Figure 2-14 compares the overall pattern from CS7 to CS13 to interval patterns defined by CS7 to CS10, CS8 to CS11 and E9.5 to CS13, respectively. Stratigraphic increments converge on the same southwest-focused bull's eye shape defined by the CS7 to CS13 isopach. I take the reproducibility of this pattern, regardless of basal horizon, as evidence for an invariant subsidence pattern throughout the Late Pliocene and take the map of normalized deposit thickness for CS7 to CS13 (Figure 2-9) as the map of basin subsidence against which all other depositional patterns are compared.

2.4.5   Scaling basin subsidence

In this study, I compare the pattern of basin subsidence against each interval thickness mapped within the Late Pliocene section of the Fisk Basin. To accomplish this, the normalized map of subsidence must be appropriately scaled so that it can be compared to the map of aggradational thickness. The properly scaled dimensional subsidence map for a particular time interval is generated through the following operation:

$$S_{Dim} = S_{Norm} R_I T_I \qquad (2.7)$$

where S_{Dim} is a matrix describing the dimensional isopach as a function of geologic position, S_{Norm} is the normalized subsidence matrix, R_I is a scalar deposition rate, and T_I is a scalar value representing the time encompassed during deposition of the isopach, S_{Dim}.

64

I need simply to choose an appropriate rate, R, and time scale, T, in Equation 2.7. A logical choice of rate is the long-term average value for maximum subsidence rate calculated simply by dividing the maximum value of the dimensional subsidence isopach (CS7 to CS13) by the time difference between the two bounding condensed sections. I use the maximum total subsidence so that I recover the known subsidence pattern completely for the interval from CS7 to CS13. The average subsidence rate, R, is 1.8 mm/yr. A reasonable time, T, with which to scale normalized subsidence is simply the length of time incorporated between the bounding condensed sections a and b, that is, the time required to deposit a particular isopach of interest.

To apply the approach of Sheets and his colleagues to an isopach bounded by condensed sections a and b, I calculate a matrix of ratios, U:

$$\mathsf{U}_{i,j,a-b} = \frac{\mathsf{I}_{i,j,a-b}}{\mathsf{S}_{Dim,i,j,a-b}} \tag{2.8}$$

where $\mathsf{U}_{i,j}$ is a matrix of the ratios of the i,j elements of isopach I_{a-b} and the i,j elements of $\mathsf{S}_{Dim,a-b}$ in Equation 2.7. The matrix $\mathsf{S}_{Dim,a-b}$ is the appropriately scaled version of normalized subsidence defined as:

$$\mathsf{S}_{Dim,a-b} = \mathsf{S}_{Norm} R T_{a-b} \tag{2.9}$$

The operation defined in Equation 2.8 has been performed for each time interval and relevant statistics for each $\mathsf{U}_{i,j}$ are presented in Table 2.2.

2.5   Results of equilibrium analyses in sheet deposits

The final step of my analysis is to characterize the ratio matrix, U, in Equation 2.8 in such a way as to constrain the fit between isopach and subsidence and to calculate a characteristic scale that describes how U evolves with time. For each isopach/subsidence ratio matrix, I characterize U through the standard deviation of the distribution of ratios and then plot each standard deviation as a function of

the scaling time, T_{a-b}. Where Sheets and his colleagues varied sediment flux and sedimentation rate, in this study, I have purposely limited my analyses to a period of relatively constant depositional style and hence I group all data and fit with a single curve (Figure 2-15).

While the standard deviation data describes the convergence between isopach and subsidence as isopach time intervals increase, it is also illustrative to plot the actual distribution behavior of sedimentation/subsidence (accumulation/accommodation) ratio values. Histograms representing the distributions of ratio data for the CS7 and CS10-based series are presented in Figures 2-16 and 2-17. In both cases, these plots show that the ratio distributions collapse on a ratio of '1' as increasingly thicker isopachs are compared to scaled subsidence. This reflects the fact that the thickening depositional packages increasingly fit the scaled subsidence. It is also interesting to note that, while both series cluster about a ratio of '1', the histogram peaks fall below '1' in the CS7 series and above '1' in the CS10 series. This slight variation in the locations of the peaks can be interpreted geologically: a peak situated below '1' suggests an under-filled basin (sedimentation lags behind subsidence) while a peak located above '1' may well correspond to a case where the basin is over-filled and sedimentation is outpacing subsidence.

The standard deviation data for each condensed section combination reported in Table 2.2 and plotted in Figure 2-15 is best described by the function:

$$\sigma = 0.1771 e^{-2.1551t} \qquad (2.10)$$

where σ is the standard deviation and t is the scaling time, T_{a-b}, described in detail in Section 2.4.5 above (the time over which the isopach was deposited). The number of data points in this analyses is 34. Error between the functional relationship and the data can be characterized by an $R^2 = 0.846$. The characteristic e-folding time scale calculated from the exponential function in Equation 2.10 is 4.6×10^5 years. Error on these time values, as determined by a Root Mean Square analyses between known time on the dated horizons and calculated time from Equation 2.10, is $\pm 5.6 \times 10^3$

66

years.

The characteristic times reported above are a general description of the entire data set. It is also useful to consider the range of values that could be extracted from our analyses by characterizing individual standard deviation 'progressions'; that is, by characterizing the standard deviation decay of a series of isopachs with a common basal condensed section. In Figure 2-18, I present the results of curve fits to four sets of isopachs beginning with CS7, CS8, CS9 and CS10. These individual progressions provide examples of the range of behaviors that might be expected from individual isopach progressions. The results for each progression are:

based on CS7: $\sigma = 0.1626e^{-2.4262t}$ $R^2 = 0.967$ e-folding : 4.1×10^5 yrs.

based on CS8: $\sigma = 0.1249e^{-1.4544t}$ $R^2 = 0.986$ e-folding : 6.9×10^5 yrs.

based on CS9: $\sigma = 0.1279e^{-1.7671t}$ $R^2 = 0.880$ e-folding : 5.7×10^5 yrs.

based on CS10: $\sigma = 0.2279e^{-2.7695t}$ $R^2 = 0.994$ e-folding : 3.6×10^5 yrs.

These analyses produce a mean e-folding of 5.1×10^5 years and a standard deviation from that mean of 29%. In all four cases, data population is four.

2.5.1   Data outliers

Two data points, both with exceptionally large standard deviations, may be included or excluded from the analyses with little change in the results. These outliers are the left-most data points in Figure 2-15 corresponding to standard deviations of 0.2641 and 0.2567. These large standard deviation values are associated with two isopachs: one bounded by CS9 and E9.5 and the other bounded by CS12 and E12.5. The standard deviation values for these packages relative to subsidence are large for different reasons. The isopach from CS9 to E9.5 is exceptionally thin (55 m/0.04 Ma; Table 2.2) and falls well below the equilibrium scale. Because this package is so thin, small variations in mapping the bounding surfaces dominate the isopach and these variations then cause a large standard deviation when compared with the appropriately scaled subsidence. Many of these variations are likely mapping artifacts and not associated with the real depositional stratigraphy but these artifacts are large

relative to the exceptionally thin CS9-E9.5 package so the standard deviation is not useful for our analyses.

The second isopach that we might chose to ignore also has an exceptionally high standard deviation but for a distinctly different reason. As described previously, above CS13, there is a clear change in depositional architecture away from the broadly distributed sheets that dominate the earlier stratigraphy between CS7 and CS13. Above CS13, there is a transition to channel/levee complexes with distinctly erosional channel bases and aggradational levee structures. These channels lead to substantial sediment bypass through the basin and a clear change in system conditions. On closer inspection, we find that the interval from CS12 to E12.5 also contains a channel in the northern portion of the basin and this channel results in a thickening of the CS12 to E12.5 isopach. It is this channel, located at the basin margin where depositional thicknesses and subsidence in the basin are typically small, that results in large variations in sedimentation/subsidence ratios for that region and affects the standard deviation. While the departure in the CS12 to E12.5 isopach is geologically driven, it is the result of a distinct change in transport and depositional behavior and hence does not belong in my analyses of the characteristic scales for sheet-like deposits. The influence of this channel on the isopachs is short-lived, affecting only the CS12 to E12.5 package, and so other cumulative isopachs that include the CS12 to E12.5 isopach as a component are unaffected.

2.5.2 Short-interval isopachs

The age of the analyses above incorporate time intervals of slightly more than 40,000 years to over 1 million years. Of the total population of 34 total data points, 14 incorporate time intervals greater than the *e*-folding time and these far-field points could disproportionately dominate the exponential fit used to calculate equilibrium scales. Therefore, I also calculated *e*-folding times based upon standard deviation data from isopachs of about 500,000 years or less (Figure 2-19). This subset data was selected because the full population was weighted towards the long-range data (*i.e.* isopachs which represented many times the characteristic scales) at the cost of losing

sensitivity to the shorter time scale information. Much of the change in standard deviation in the sheet data occurred within the first few data points and it is these points that, arguably, should be used to constrain the exponential function that forms the basis of my analyses. Omitting the two outliers, the short interval data result in an e-folding time of 4.3×10^5 years ($n = 19$; $\sigma = 0.1706e^{-2.3454t}$; $R^2 = 0.616$). Including the outliers, that time drops to 3.3×10^5 years ($n = 21$; $\sigma = 0.2173e^{-3.0253t}$; $R^2 = 0.707$).

2.6 Discussion of equilibrium analyses in sheet deposits

2.6.1 Significance of the temporal scale

The response of depositional systems to allocyclic forcing is not a simple linear one. Paola et al. (1992) show the behavior of a depositional system depends greatly upon both the nature of the forcing as well as the temporal scale or periodicity, P, of the input condition relative to the equilibrium time of the basin, T_{eq}. Slow variations in input conditions ($P/T_{eq} \gg 1$) result in stratigraphy that is a reasonably accurate record of the allocyclic history. However, when the forcing time scale is equal to or shorter than basin equilibrium ($P/T_{eq} \leq 1$), the allocyclic signature seen in the rock record can be dramatically modified from that of the forcing event; the phase of the forcing event can be shifted, the shape of the event can be distorted, or the event may be absent from the stratigraphy altogether (Paola et al., 1992).

Simply considering the nonlinear response of basins to allocyclic forcing makes it clear that ascribing allogenic significance to stratigraphy at scales near or below the equilibrium scale of the basin is suspect. However, there is an additional limitation to the Paola model that lends further complication to stratigraphic analyses. The model is two-dimensional and contains no autocyclic depositional behavior. Once in equilibrium, depositional patterns in the Paola model are homogeneous unless perturbed by a sufficient change in input or boundary conditions (Paola et al., 1992). In a natural,

three-dimensional system, autocyclic behavior is present and results in stratigraphic variations (*e.g.* delta lobe switching) that are not necessarily tied to, or indicative of, external forcing. Hence, the equilibrium state of a natural depositional system does not necessarily result in homogeneous stratigraphy. Once these autocyclic variations are included in the system, the requirement that we interpret stratigraphy at scales greater than equilibrium becomes even more critical. Below T_{eq}, stratigraphy is a combination of distorted and modified allocyclic forcing and random autocyclic behavior. Confidently assigning allogenic significance to sub-equilibrium scale features is simply not possible.

My analysis of characteristic time-scales for the entire dataset (Figure 2-15) from the Late Pliocene Fisk Basin produces a characteristic equilibrium time of 4.6×10^5 years. Hence, it takes somewhere on the order of a half million years for the autocyclic behavior of the system to fully compensate for an allocyclic perturbation. We know that sea level changes in the Gulf of Mexico during the Pliocene occurred with periodicities ranging from 10,000 years to 100,000 years (Haq et al., 1987; Styzen, 1996). Such fluctuations, while not necessarily affecting Fisk Basin directly, are thought to change sediment delivery to the continental slope and, by extension, affect deposition in the deepwater. This reasoning has been used as the basis for interpreting individual condensed sections in Fisk Basin as corresponding to allocyclic sealevel events (Prather et al., 1998; Booth et al., 2000; Dean et al., 2000; Winker and Booth, 2000; Dean et al., 2002). The critical point is that, judging by the equilibrium time of the basin, the system cannot possibly respond fully to these known but relatively short-period perturbations and hence is in a constant state of adjustment and response. At an allocyclic forcing scale of 100,000 years, Equation 2.5 is not satisfied and the equilibrium or graded model simply can not hold.

2.6.2 Spatial scaling

The stratigraphy of Fisk Basin has been interpreted at relatively fine vertical scales and these interpretations have been used to drive stratigraphic models (*e.g.* Booth et al. (2000); Winker and Booth (2000); Mitchell and Dean (2000); Win). Based upon

the sedimentation rate determined from the data in Figure 2-5, the equilibrium time scale can be converted to an equilibrium depositional thickness, H_{eq}, which defines a unit thickness of sediment that must be deposited for sedimentation and subsidence to reach equilibrium. Condensed section bounded packages in the Late Pliocene of Fisk Basin have an average mean thickness of 259 m (Table 2.2). Small channels in the data set are on the order of a few tens of meters in thickness (Figure 2-6 and 2-7). The largest channel complexes in the Late Pliocene occur between CS13 and CS14 (above our period of interest from CS7 to CS13) but, for reference, sediment accumulation of these features is 100 m at the thickest (Figure 2-6 and 2-7) and individual channels within these complexes are less than 50 m in height. Sheet-like deposits in the basin are also about 50 m thick (Figure 2-6 and 2-7). With an equilibrium length scale of 600 m, the likelihood that the assumption of equilibrium is reflected in sheets and channels with thicknesses of several 10's to at most 100 meters is called into question. By the same reasoning that calls into question our ability to accurately interpret 100,000 year forcings, we must also be wary of allogenic interpretations of stratigraphic features with thicknesses less than H_{eq}. At the scale of condensed section-bounded packages, channels and channel/levee complexes, it is simply impossible to differentiate autocyclic behavior from allocyclic forcing and hence it is unreasonable to ascribe extrinsic meaning to these sub-equilibrium features and trends.

2.6.3 Implications of basin equilibrium time

1. *High-frequency couplets* — The stratigraphy of Fisk Basin contains regular packages of sheet-like and channelized sands (Figures 2-2 , 2-7, 2-6 and 2-7; Booth et al. (2000); Winker and Booth (2000); Mitchell and Dean (2000); Win). These 'couplets' occur at the sub-condensed section scale and below the equilibrium scale of Fisk Basin and it is difficult to attribute these recurring patterns to anything other than autocyclic behavior. While the affects of variations in input and boundary conditions (*e.g.* eustatic changes resulting in variations in sediment input or the episodic breaching of salt sills confining sedimentation in

71

the basin) can not be ruled out as the cause of this stratigraphic pattern, it is equally possible that what we see here is nothing more then autocyclic signal of local variability in deposition or, at best, a convolution of auto- and allogenic responses (Paola et al., 1992).

2. *Large-scale stratigraphic trends* — Equilibrium scales on the order of 500,000 years and 600 meters suggest that only long-term trends can be confidently interpreted from Fisk Basin stratigraphy. These length and time scales define the height of a 'box car' filter that must be applied to stratigraphic interpretations and this filter encompasses the multi-condensed section scale. There are, however, interpretable, long time-scale trends in the basin. For example, between CS1 (3.95 Ma) and CS15 (1.7 Ma), Fisk Basin does exhibit a trend from onlap dominated, ponded and healing phase deposits to chaotic-dominated, bypass-type facies and back (Winker and Booth, 2000). Spanning about 2.3 Ma, this trend can be interpreted with confidence. Likewise, there is a general progression in the Fisk stratigraphy from sheets to channel/levee complexes and then to mass transport complexes and this change occurs over several million years. Assigning allogenic significance to this stratigraphic progression is also reasonable.

3. *Marine diffusion coefficient* — Paola et al. (1992) show that $T_{eq} = L^2\nu$ where L is the length scale of the basin and ν is the diffusion coefficient of the basin. In these terrestrial examples, diffusivities range over two orders of magnitude from $\nu = 2 \times 10^{-4} \text{km}^2\text{yr}^{-1}$ for the Plio-Pleistocene St. David Formation of Arizona (Lindsay et al., 1990; Heller and Paola, 1992) to $\nu = 2 \times 10^{-2} \text{km}^2\text{yr}^{-1}$ for the Miocene Andes Bermejo Basin (Jordan et al., 1988; Flemings and Jordan, 1989; Reynolds et al., 1990). Using a representative length for Fisk Basin of 20 km (the width of the basin), $\nu = 1.6 \times 10^{-2} \text{km}^2\text{yr}^{-1}$, falling between the two terrestrial examples. Effective diffusivity in this deepwater example does not appear to be radically different from those of the terrestrial environments.

4. *Applicability to other basins* — The results presented in this chapter are specific

to the period of sheet sand deposition in the Late Pliocene Fisk Basin. While the method is general, there is no reason that the equilibrium value for one basin should apply to any other. However, assuming that diffusion coefficients do not vary widely in the upper slope basins of the Gulf of Mexico, the $T_{eq} = L^2 \nu$ relationship shows that equilibrium times should go as the size of the basin — the smaller the basin, the shorter the equilibrium time scale and vice versa. Therefore, as a general rule, the appropriate scale of stratigraphic interpretation of allocyclic signal also goes as L. Hence smaller basins may more appropriately lend themselves to more detailed stratigraphic analyses. Of course, this assumes that sediment supply and subsidence rates do not vary dramatically between basins.

2.7 Conclusions on equilibrium analyses in sheet deposits

Stratigraphic models based upon the assumption of basin equilibrium and graded slope profile hold only at time and length scales greater than the scale at which subsidence and sedimentation reach equilibrium in the basin. Below this scale, stratigraphy is a complex combination of the autocyclic behavior of the depositional system and a distorted signal of the allocyclic history of the basin. Therefore, in order to appropriately apply stratigraphic models, we must first constrain the equilibrium scale of the system and then be sure to apply equilibrium-based models only at scales greater than equilibrium.

Basin equilibrium has been constrained for a natural system in the Gulf of Mexico using an approach adapted from experimental analyses. By comparing cumulative stratigraphic isopachs to a basin-wide subsidence profile, we can assess how well the isopachs fit subsidence. As thicker and thicker cumulative isopachs are considered, the standard deviation in the point-wise ratio between the depositional isopach and the subsidence profile decays exponentially. Characteristic scales can be extracted

from this exponential decay profile in the form of an *e*-folding time and it is this characteristic scale that defines basin equilibrium.

For the Late Pliocene Fisk Basin in the Gulf of Mexico, we find a characteristic time scale of 4.6×10^5 ($\pm 5 \times 10^3$) years and an equilibrium thickness of 600 (± 7) m. This equilibrium time is much greater than the periodicities of known allocyclic forcings such as sea level variations in the Plio/Pleistocene and the equilibrium length is greater than the thickness of condensed section-bounded stratigraphic isopachs. Paola et al. (1992) have shown that, when allocyclic forcings occur at scales equal to or less than the equilibrium scale of the basin system, the stratigraphic result is a complex combination of filtered and phase shifted responses mixed with autocyclic depositional behavior. Hence, at scales less than about 500,000 years and 600 m, it is questionable whether detailed stratigraphy of Fisk Basin can be interpreted to represent specific forcing events or equilibrium-based behavior. Interpretations at larger scales may be valid however. The overall shift from sheet-like deposition to channel/levee complexes and then on to mass transport complex deposits occur over a period of 3.5 Ma. This trend is well above the equilibrium time and may be reasonably interpreted to represent changes in basin subsidence patterns and salt migration during basin development.

74

2.8 Tables

Table 2.1: Gulf of Mexico biostratigraphic markers.

Biostratigraphic markers used for condensed section dating in Fisk Basin and for sedimentation rate function in Figure 2-5. The right-most column, labeled 'Interval Time', reports the difference in ages between successive condensed sections (*e.g.* the time interval between CS13 and CS14 is 0.35 Ma). From Breard et al. (2002); Dean et al. (2002).

Condensed Section	Biostratigraphic Marker	Fossil Type	Event Type	Age (Ma)	Interval Time (Ma)
CS20	Pseudoemiliania lacunosa	calcareous nannofossil	increase	1.02	0.05
CS19	Trimosina B	shelfal foraminifera	present	1.15	0.80
CS14	Discoaster brouweri	calcareous nannofossil	extinction	1.95	0.35
CS13	Globorotalia miocenica	shelfal foraminifera	present	2.30	0.25
CS12	Ceratobulimina pacifica	bathyal foraminifera	extinction	2.55	0.54
CS9	Globoquadrina altispira	shelfal foraminifera	present	3.09	0.38
CS7	Sphenolithus neoabies	calcareous nannofossil	extinction	3.47	

Table 2.2: Isopach characteristics — CS7 to CS13.

Statistics for isopachs used in this study. Table includes isopach name listing basal and top bounding condensed sections, mean isopach thickness, the interval of time associated with each isopach, and the standard deviation of the accumulation/accommodation ratio for each isopach when compared to basin subsidence (Figure 2-9). Standard deviation decays exponentially with increased mean thickness and time interval. This data is presented graphically in Figure 2-15.

Isopach	Mean Thickness, m	Time Interval, Ma	Standard Deviation
CS7 to CS8	221	0.17	0.1140
CS7 to CS9	486	0.38	0.0584
CS7 to E9.5	541	0.42	0.0519
CS7 to CS10	779	0.60	0.0398
CS7 to CS11	942	0.73	0.0356
CS7 to CS12	1221	0.94	0.0245
CS7 to E12.5	1343	1.04	0.0173
CS8 to CS9	266	0.21	0.0938
CS8 to E9.5	320	0.25	0.1298
CS8 to CS10	558	0.43	0.0644
CS8 to CS11	721	0.56	0.0568
CS8 to CS12	1000	0.77	0.0434
CS8 to E12.5	1122	0.87	0.0318
CS8 to CS13	1269	0.98	0.0000
CS9 to E9.5	55	0.04	0.2641
CS9 to CS10	292	0.23	0.0562
CS9 to CS11	456	0.35	0.0679
CS9 to CS12	734	0.57	0.0631
CS9 to E12.5	856	0.66	0.0508
CS9 to CS13	1003	0.78	0.0303
E9.5 to CS10	238	0.18	0.1003
E9.5 to CS11	401	0.31	0.0650
E9.5 to CS12	680	0.53	0.0530
E9.5 to E12.5	802	0.62	0.0572
E9.5 to CS13	948	0.73	0.0412
CS10 to CS11	163	0.13	0.1566
CS10 to CS12	442	0.34	0.0930
CS10 to E12.5	564	0.44	0.0819
CS10 to CS13	711	0.55	0.0485
CS11 to CS12	279	0.22	0.1001
CS11 to E12.5	401	0.31	0.1064
CS11 to CS13	547	0.42	0.0623
CS12 to E12.5	122	0.09	0.2567
CS12 to CS13	269	0.21	0.1095
E12.5 to CS13	147	0.11	0.1558

2.9   Figures
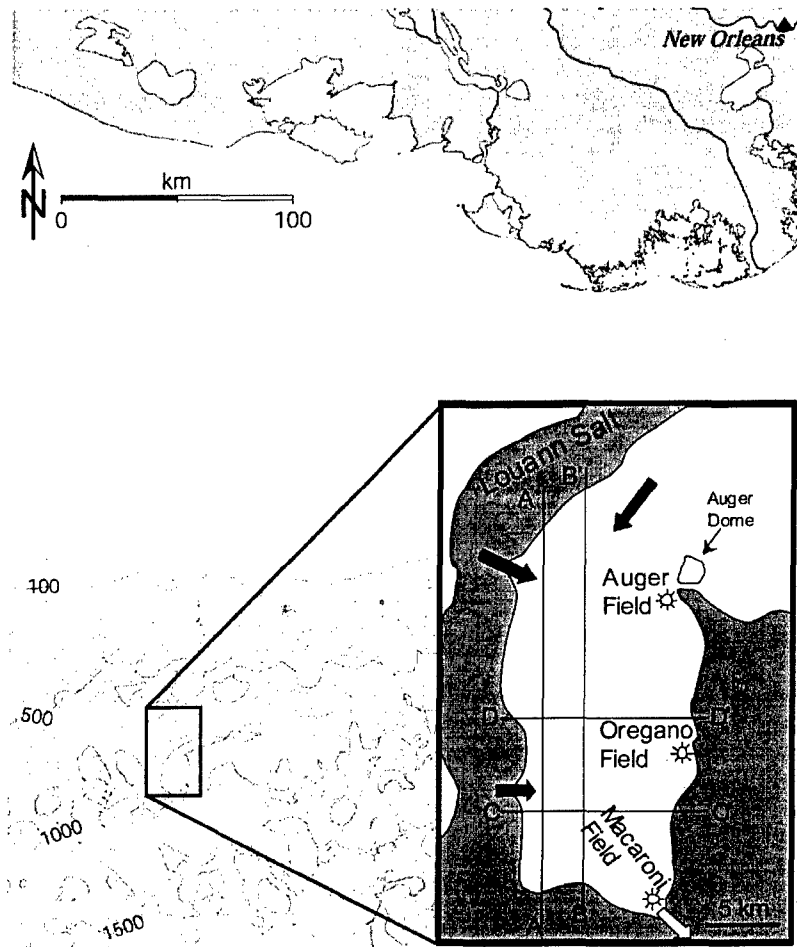
Figure 2-1: Fisk Basin location. Fisk Basin is situated about 350km southwest of New Orleans, LA in the Gulf of Mexico. The basin is the result of withdrawal and diaperism of the Louann Salt which can now be seen surrounding the basin. Sediment input to the basin is form the west, northwest, and north (black arrows) and there is an exit point in the southeast (white arrow). There are three active hydrocarbon fields in the basin – Auger, Oregano and Macaroni – which provide lithologic, temporal and acoustic velocity constraints on Fisk Basin stratigraphy. This basin is known informally as the Auger Basin, taking this name from the Auger Field which, in turn, is named after the Auger Dome salt diapere.
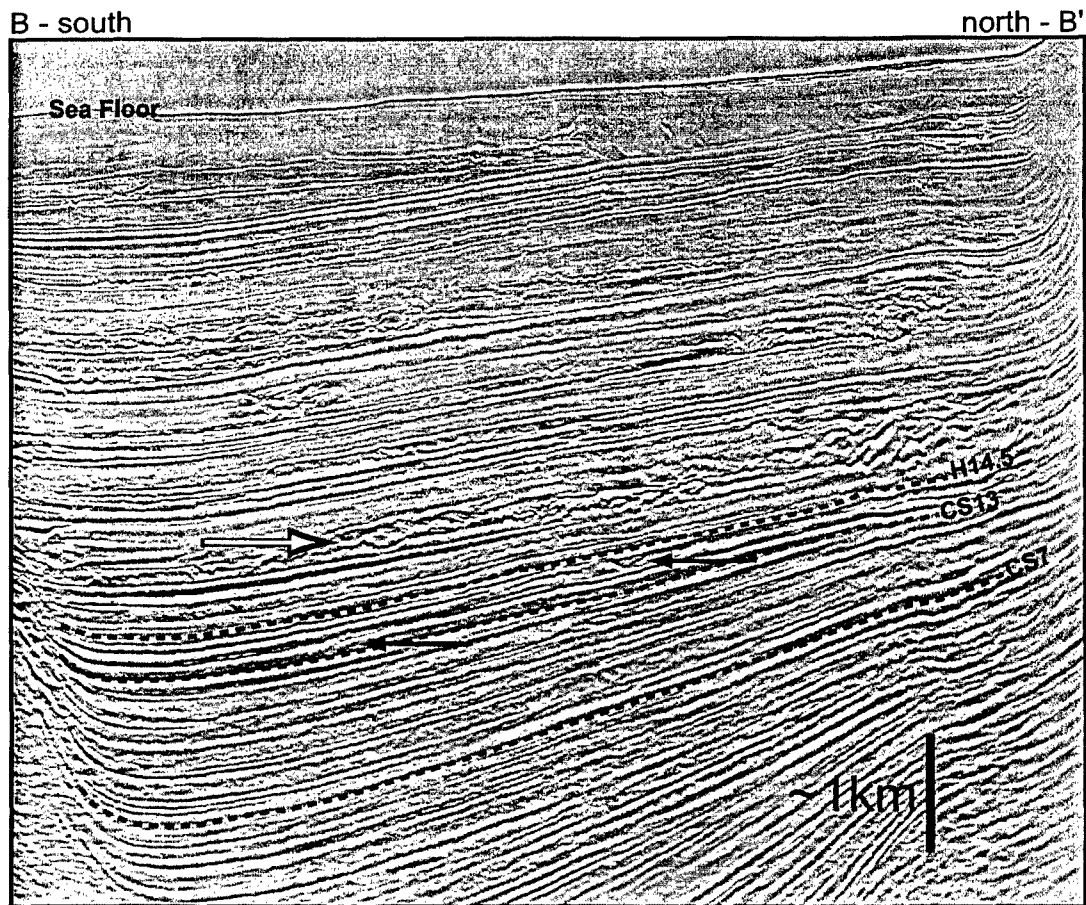
Figure 2-2: Seismic line B-B' (Figure 2-1) showing large portion of Fisk Basin stratigraphy from seafloor to below area of interest in this study. Three condensed sections are mapped using dashed lines: CS7 (3.47Ma), CS13 (2.30Ma) and H14.5 (1.89Ma). This paper focuses on the sheet-like deposits between CS7 and CS13. Above CS13 and below H14.5, at least two channel/levee complexes traverse the basin (black arrows) indicating a change in sediment transport from small-scale channels to well-confined flows. This change in transport characteristics also corresponds approximately with a change in subsidence behavior in the basin (Figure 2-9). Above H14.5, the stratigraphy changes again to include large mass transport complexes (*e.g.* white arrow). These sediments are sourced from the basin margin and signal the initiation of significant topography around the periphery of the basin coincident with vertical migration of salt. The vertical axis of this data is two-way-travel time. Velocity increases with depth so vertical scale is an approximate vertical average for the section. Line is 30km from B to B'.
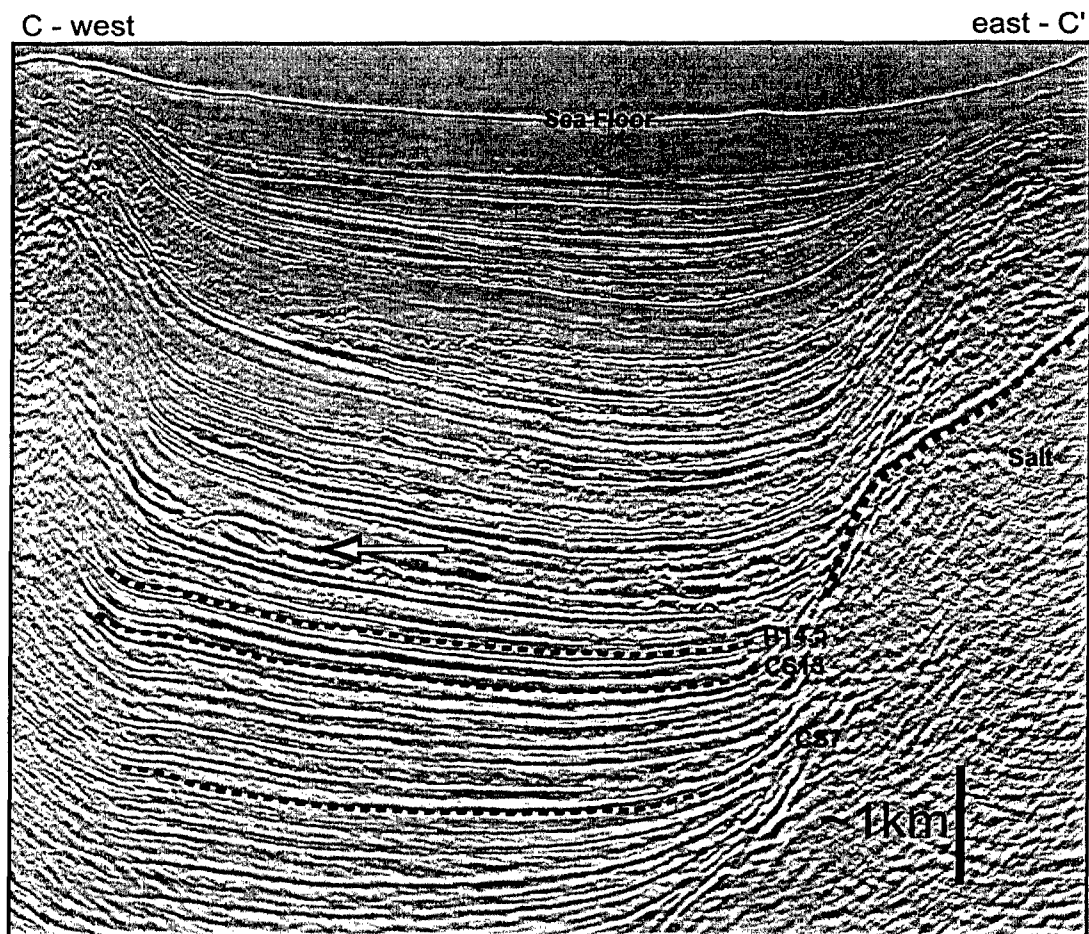
Figure 2-3: Seismic line C-C' (Figure 2-1) showing large portion of Fisk Basin stratigraphy from seafloor to below area of interest in this study. Three condensed sections are mapped using dashed lines: CS7 (3.47 Ma), CS13 (2.30 Ma) and H14.5 (1.89 Ma). The heavy dotted line maps the top of the migrating salt which forms the east side of the basin. This paper focuses on the sheet-like deposits between CS7 and CS13. Between CS13 and H14.5, at least two channel/levee complexes traverse the basin (Figure 2-2) however this line is oriented parallel to the direction of sediment transport and the channe/levee complexes are not apparent. Above H14.5, the stratigraphy changes again to include large mass transport complexes (*e.g.* white arrow). These sediments are sourced from the basin margin and signal the initiation of significant topography around the periphery of the basin coincident with vertical migration of salt. The vertical axis of this data is two-way-travel time. Velocity increases with depth so vertical scale is an approximate average for the section. Line is 20 km across.
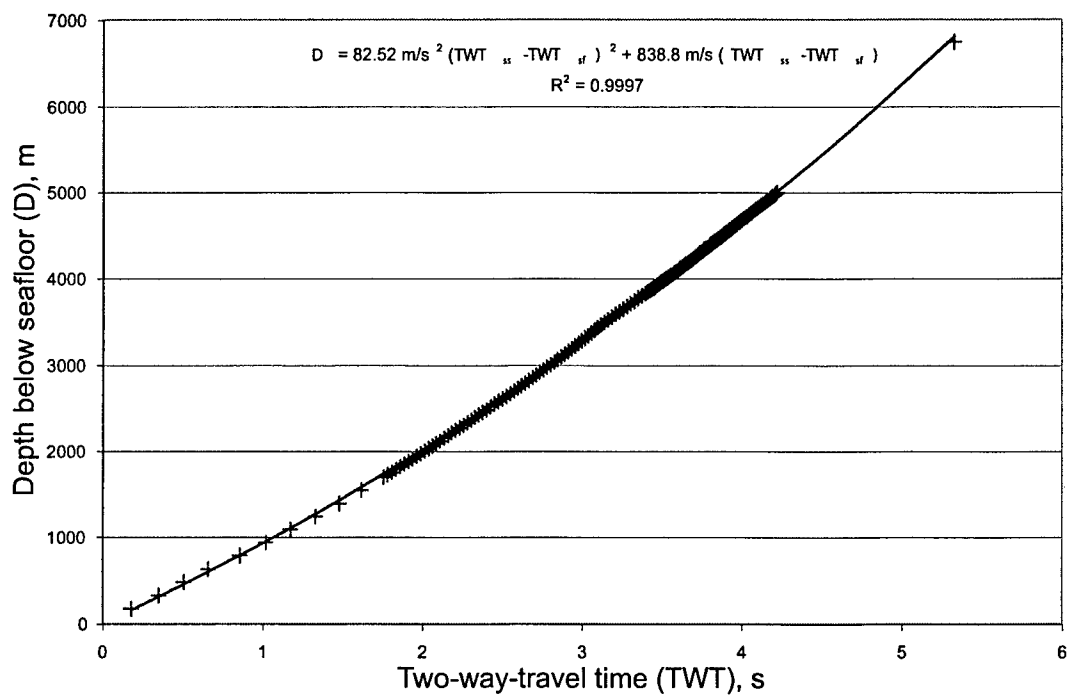
Figure 2-4: Time-Depth relationship used to convert seismic data in TWT to true vertical depth (provided but the Auger Asset Team of Shell Expoloration and Petroleum Co.). This relationship is derived from checkshot data from the Auger Field (Figure 2-1) and was applied basin-wide.
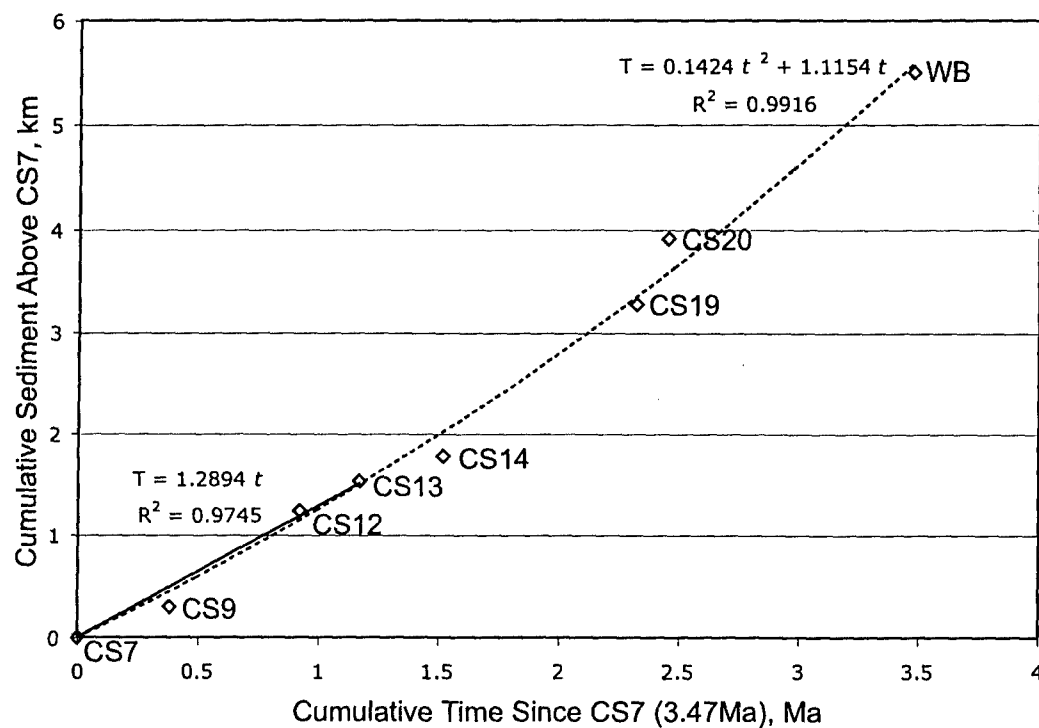
Figure 2-5: Deposition rate in the Fisk Basin. Cumulative mean isopach thickness as a function of elapsed time beginning at CS7 and proceeding to the present (WB – water bottom). Overall, sedimentation increases exponentially through time. Sedimentation during the period of interest in this paper (CS7 to CS13) can be approximated linearly by $T = 1.34t$ ($R^2 = 0.975$) in units of km and Ma. See Table 2.1 for condensed section age data.
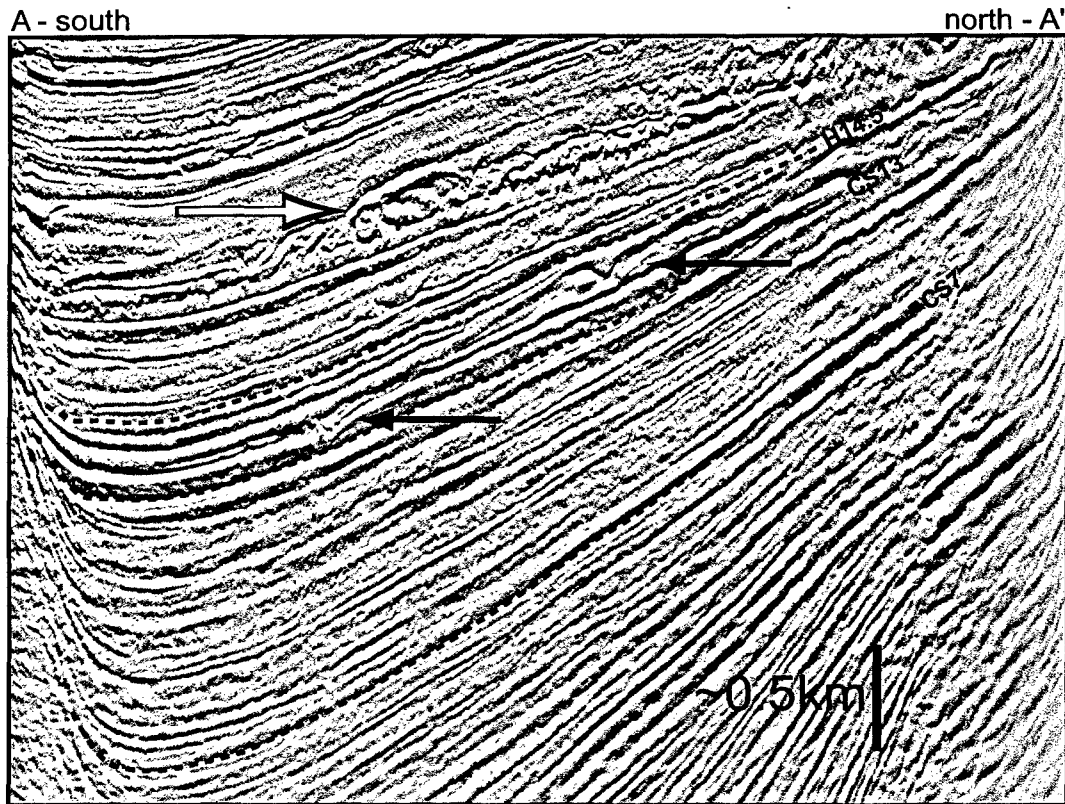
Figure 2-6: Seismic line A-A' from Figure 2-1. Condensed sections CS7, CS13 and H14.5 are mapped, from bottom to top, with dashed lines. The sheet-like stratigraphy between CS7 and CS13 is the focus of this work. Between CS13 and H14.5, two channel/levee complexes are present (black arrows). Above H14.5, the stratigraphy changes once again, this time to include mass transport complexes (*e.g.* white arrow). These sediments are sourced from the basin margin and signal the initiation of significant topography around the periphery of the basin coincident with vertical migration of salt. The vertical axis of this data is two-way-travel time. Velocity increases with depth so vertical scale is an approximate average for the section. Line is 30 km across.
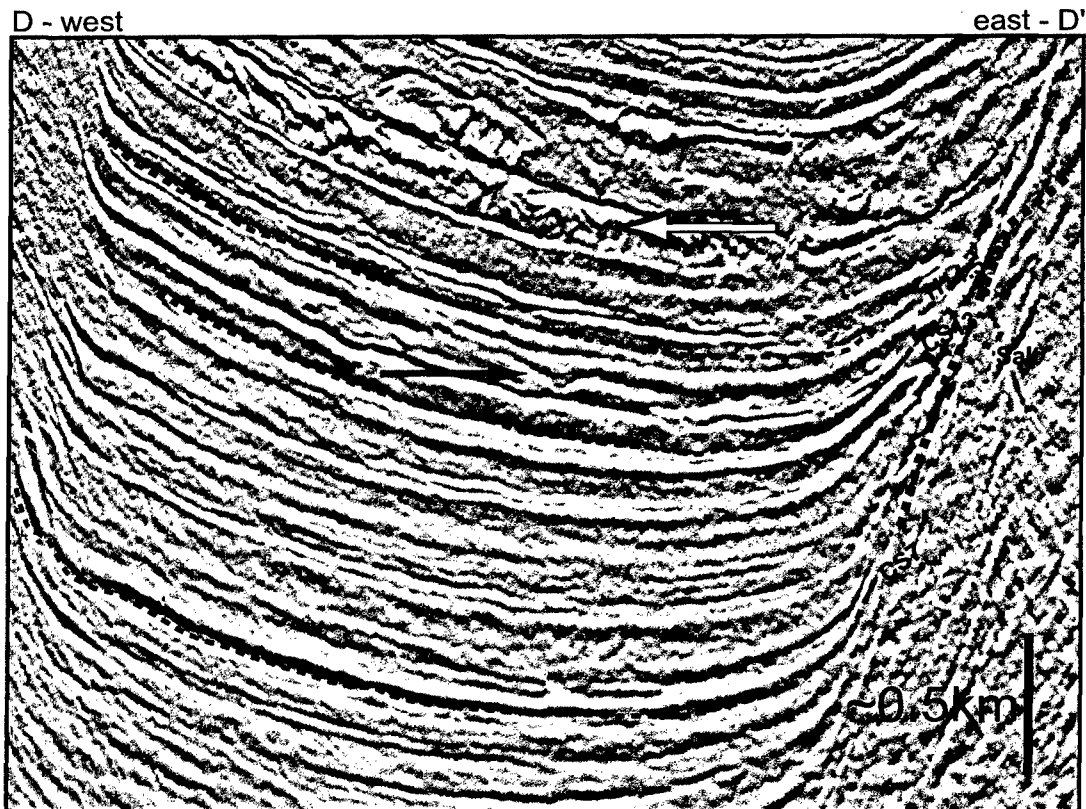
Figure 2-7: Seismic line D-D' from Figure 2-1. Condensed sections CS7, CS13 and H14.5 are mapped, from bottom to top, with dashed lines. The approximate boundary between basin-filling stratigraphy and the migrating salt that forms the east side of the basin is indicated with a heavy dotted line. The sheet-like stratigraphy between CS7 and CS13 is the focus of this work. Between CS13 and H14.5, two channel/levee complexes are present (one channel/levee complex is indicated with a black arrow; these features are poorly imaged in this line oriented parallel to the direction of sediment transport). Above H14.5, the stratigraphy changes once again, this time to include mass transport complexes. These sediments are sourced from the basin margin and signal the initiation of significant topography around the periphery of the basin coincident with vertical migration of salt. The vertical axis of this data is two-way-travel time. Velocity increases with depth so vertical scale is an approximate average for the section. Line is 20 km across.

84
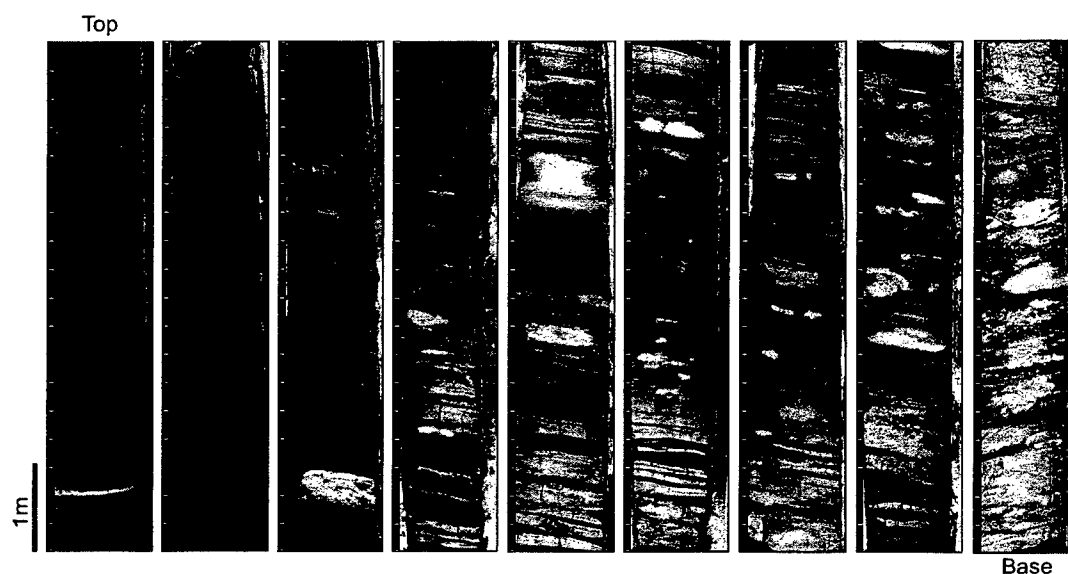
Figure 2-8: Core from Oregano Field (Figure 2-1) showing typical facies of sheet-like stratigraphy between CS7 and CS13 (Figures 2-2, 2-3, 2-6 and 2-7). Base and top of section are marked and a scale is provided at left ('tic' marks on core are in feet). This core reveals a progression in facies at the sub-seismic scale. Sediments begin as muddy, distal deposits at the bas of the core. The muds slowely give way to interbedded mud and sand layers with climbing ripples and cross-bedding. This facies is common to proximal, channel margin or levee deposits. Evantually, the core is dominated by structureless, homogenous sands found within submarine channel fills. This facies distribution highlights the fact that, while at the scale of a seismic loop, deposits are broadly and continuously distributed, the sediment was actually transported into the basin via channelized turbidity currents.

85
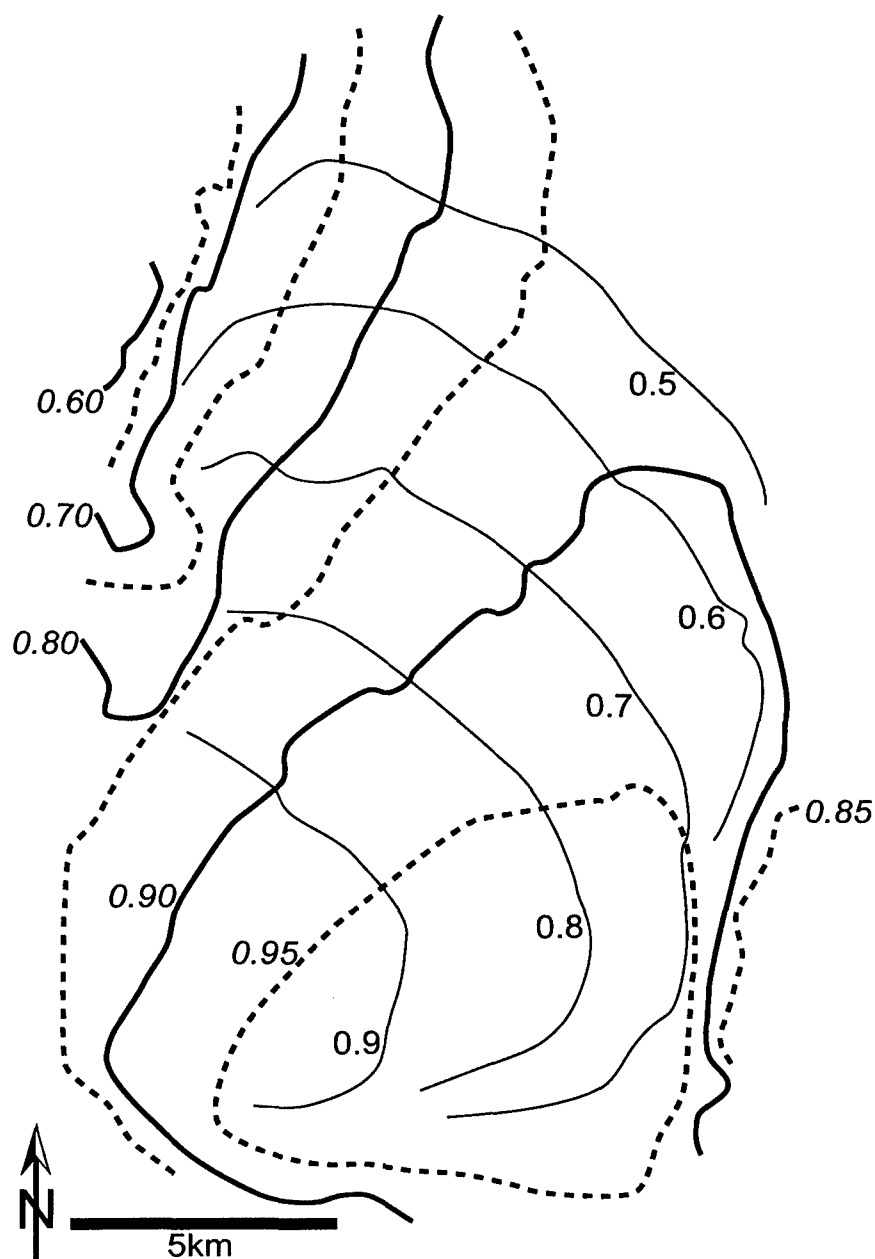
Figure 2-9: Comparative sediment thickness for CS7 to CS13 interval (fine lines; Contour Interval, CI = 0.1) and H14.5 to water bottom (thick solid and dashed lines; CI = 0.50). These intervals are normalized by their respective maximum thicknesses and contours represent fractional values. There is a clear shift in maximum accumulation from the southwest corner of the basin during the earlier interval to the southeast corner from H14.5 to the present day bathymetry. This shift corresponds temporally with the transition from sheet-like deposits to the appearance of deeper, flow-confining channels (Figures 2-2, 2-3, 2-6 and 2-7).

Basin
History:

t_1 t_2 t_3

Accumulation
and
Accommodation:
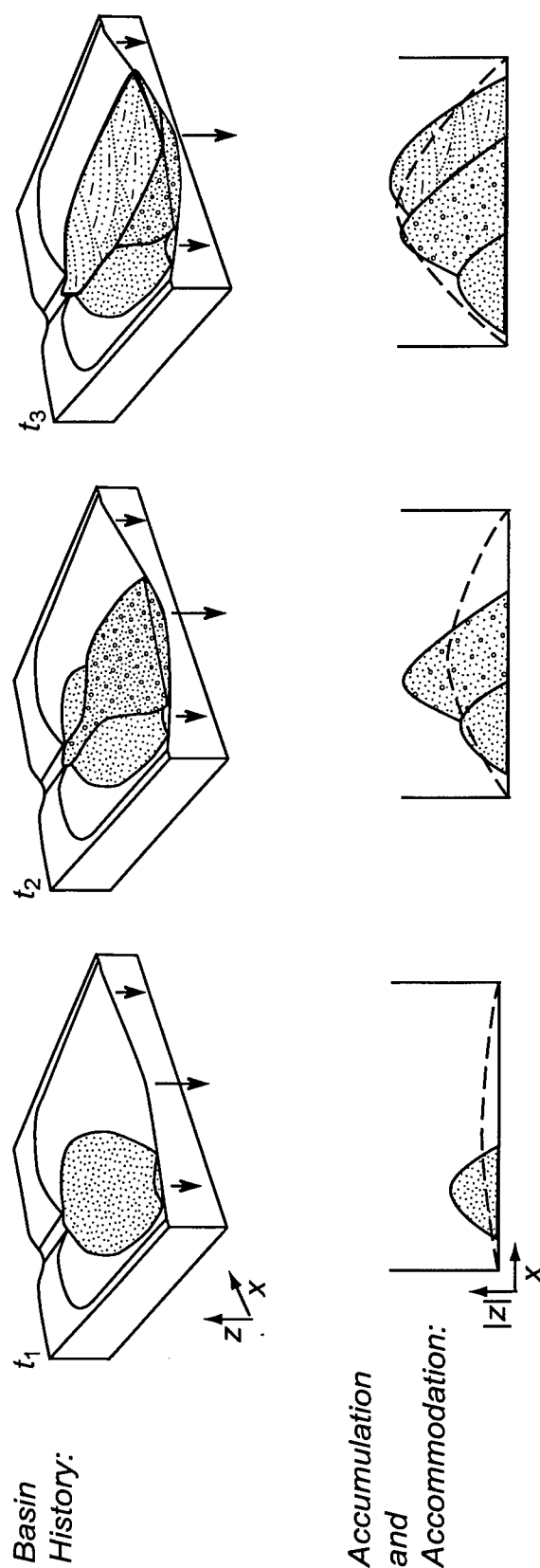
Figure 2-10: The progression of a basin towards equilibrium. The balance between sedimentation and subsidence in a basin improves over time. In the block diagrams illustrating basin history, subsidence (indicated by arrows) is temporally constant but spatially variable. Sedimentation, represented by patterned lobes (the patterns do not infer lithology), is both temporally and spatially variable. The balance between sedimentation (accumulation) and subsidence (accommodation) for an arbitrary cross-section at the three time steps is represented graphically below each block (accumulation is again represented by patterned shapes while accommodation is indicated by a dashed line). At the earliest time, t_1, accomodation is small and accumulation is local resulting in a poor fit between the two. However, as the basin develops, subsidence increases and the sedimentary system has an opportunity to occupy a larger fraction of the total area. The result then, at later times t_2 and t_3, is that the fit between accumulation and accommodation improves. Taking the ratio of accumulation over accommodation point-wise across the basin for each time step would produce ratio distributions with decreasing standard deviations over time (see Figures 2-16 and 2-17 for practical examples of this behavior). It is this improved fit, represented by an exponential decay in standard deviation over time, that allows us to identify a characteristic response time for the basin.

87
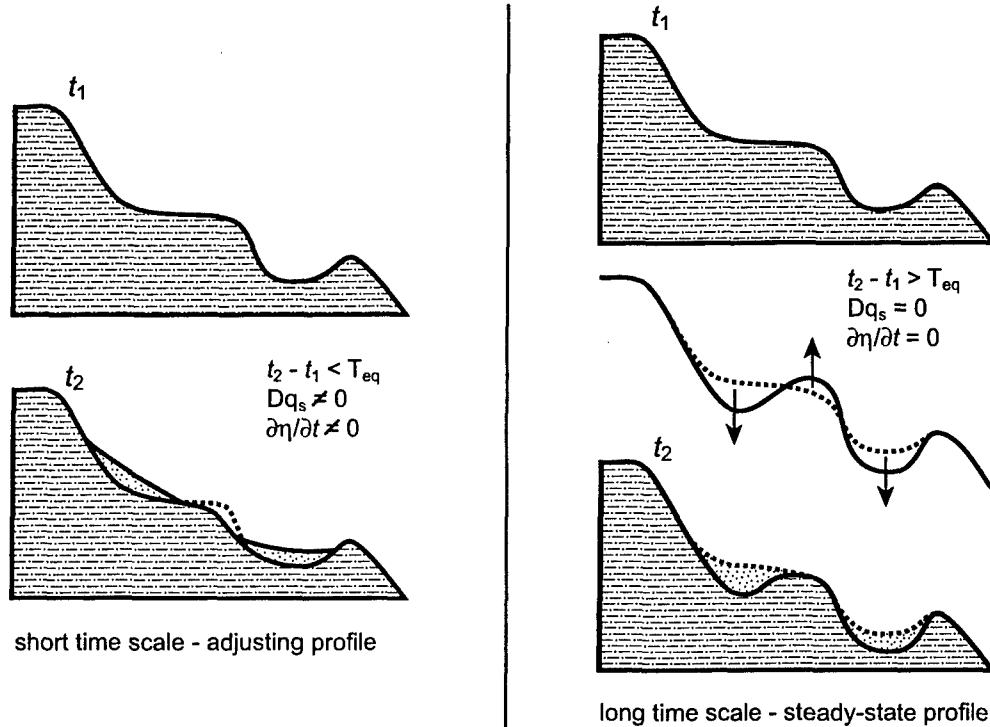
Figure 2-11: Short time scale (left) and long time scale (right) topography. At short time scales, where the time interval is much less than the equilibrium time, subsidence and uplift are inconsequential and topography changes diffusively (Equation 2.2). The spatial sediment flux, Dq_s, is non-zero and the bed position, η, changes over time. At long time scales (right), where the time interval is greater than the equilibrium time of the system, uplift and subsidence (black arrows) act as source or sink terms in Equation 2.4 and topography is maintained through sediment flux from areas of uplift to areas of subsidence. At this long time scale, stratigraphy deposited in areas of uplift reflect the history of basin subsidence.
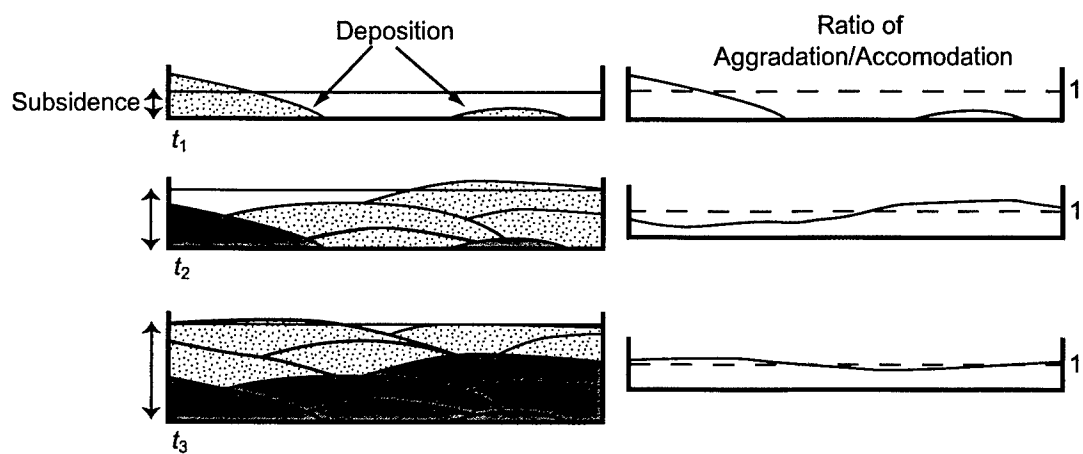
Figure 2-12: Schematic from Sheets et al. (2002) illustrating the development of an alluvial section (left) and a representation of the ratio of aggradation to subsidence (right). As the depositional system sweeps across the basin depositing sediment, local ratio values approach '1'. In addition, the distribution of the ratios narrows as characterized by a decrease in the standard deviation of the distribution.
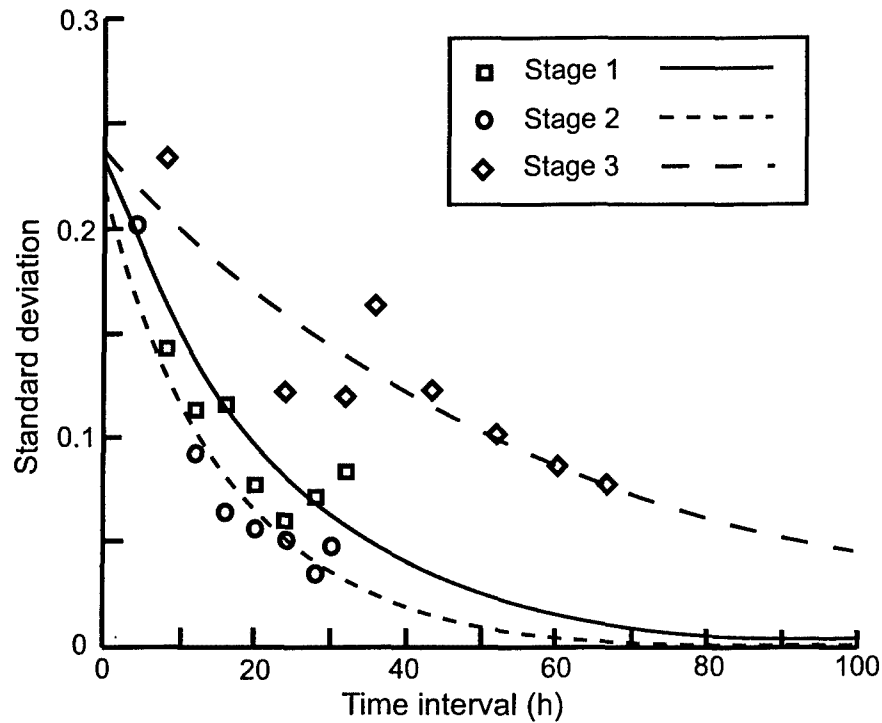
Figure 2-13: Plot from Sheets et al. (2002) showing the decay of standard devitation describing ratios of aggradation over accomodation. Three stages of the experiment are presented. In Stages 1 and 2, depositional conditions were esentially the same. In Stage 1, a cross-stream variation in subsidence rate was imposed in contrast to Stage 2 in which subsidence consisted of a simple down-stream tilting, rigid-beam form. In Stage 3, rigid beam subsidence was imposed and all rates, including accomodation rate and water and sediment flux, were reduced by 25% relative to Stage 2. In all cases, standard deviation of the aggradation/accommodation ratio decays exponentially. Fitting functions to the data from each stage makes it possible to estimate characteristic times for the varied conditions.

90

CS7 to CS10 CS8 to CS11 E9.5 to CS13
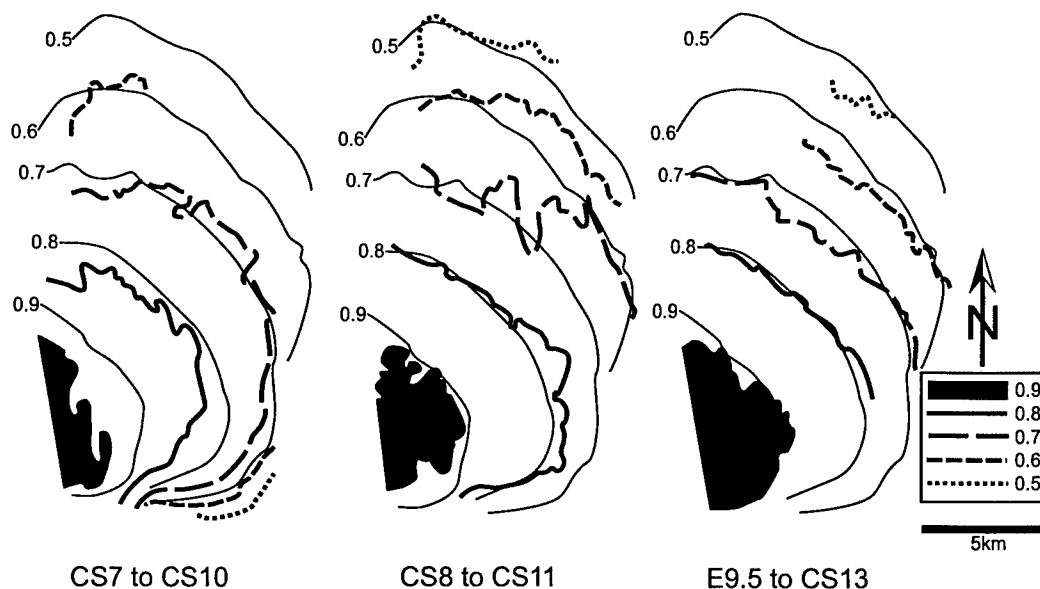
Figure 2-14: Normalized cumulative isopachs illustrating the common sedimentation pattern found regardless of basal horizon. Depositional isopachs are represented in heavy lines with a contour interval of 0.1. The light lines represent the normalized isopach between CS7 and CS13. Three cases are presented: an isopach bounded by CS7 and CS10 (left), an isopach bounded by CS8 and CS11 (center), and an isopach bounded by E9.5 and CS13. In all cases, the depositional isopachs indicate maximum thickness in the southwest part of the basin and map closely the normalized isopach between CS7 and CS13. Because all isopachs converge on this form, we take this as the reference subsidence shape in the basin during the period of interest.
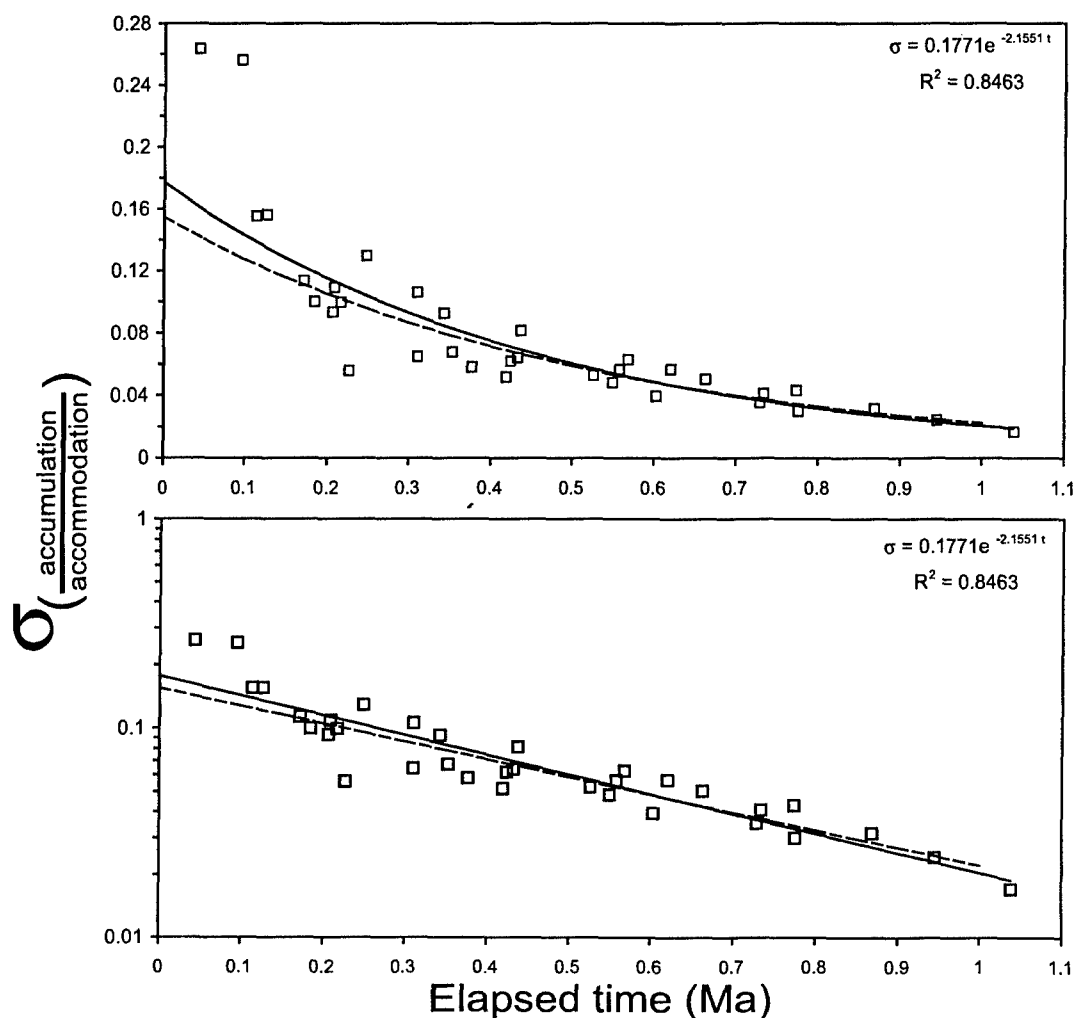
Figure 2-15: Standard deviation of accumulation/accommodation as a function of elapsed isopach time (Table 2.2). Both plots present the same data; lower plot is in semi-log space. With increased total elapsed time, standard deviation decays exponentially indicating improved fit between accumulated sediment and accommodation due to subsidence. Solid line in both indicates functional fit to entire data set while dashed line is functional fit to data omitting two outliers (left-most data points in each plot). The functional relationship between s and time can be used to determine a characteristic e-folding time representing the response time of the sedimentation/subsidence system.

92
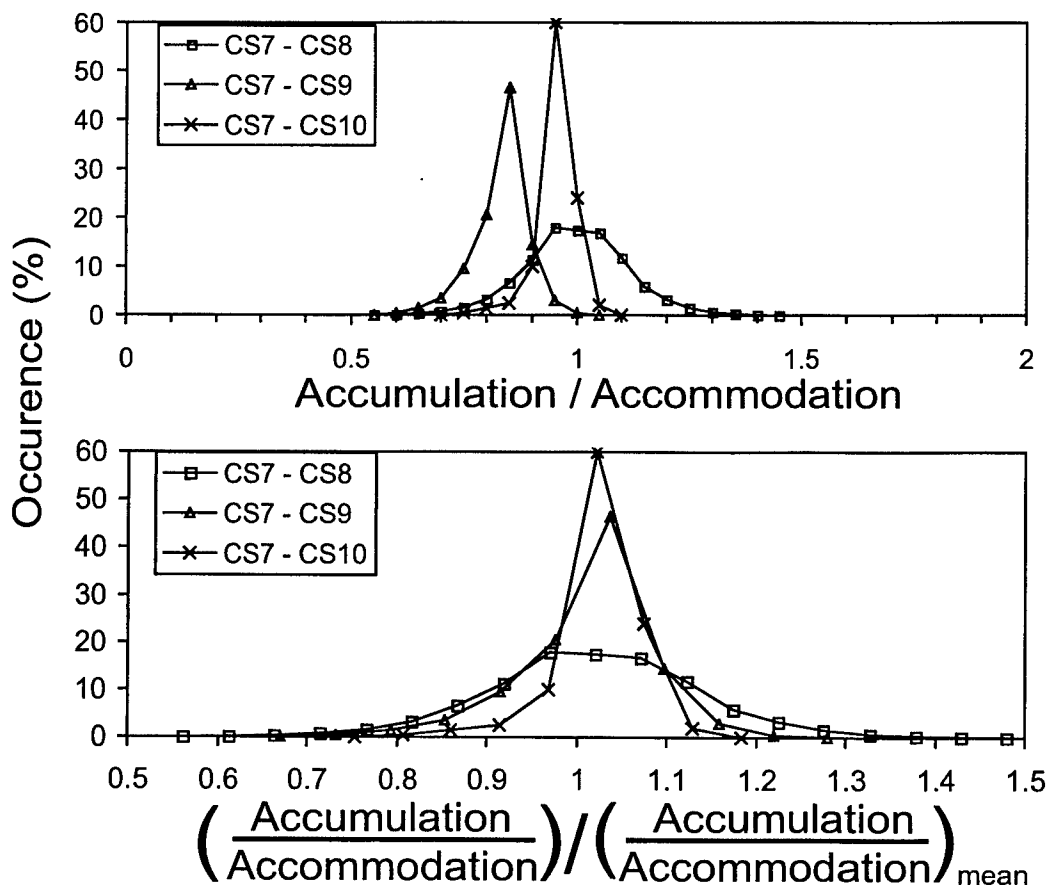
Figure 2-16: Histograms of accumulation/accommodation ratios for three isopachs illustrating the reduction in standard deviation of the ratio distributions with thickness or time. All isopachs are based at CS7. The upper plot incorporates true ratio values while the lower normalizes the distribution for each isopach by the mean ratio of that isopach. The upper plot highlights the fact that, while the distributions narrow with thickness, they are centered at a value slightly less than '1' indicating an underfilled basin. The lower plot, with all distributions shifted to approximately center on '1', highlights the collapse of the distributions with increased isopach thickness. Note that a normalized distribution does not necessarily center exactly on a ratio of '1' because the mean of that distribution does not necessarily equal one of the discreet ratio datapoints on the distribution curve.
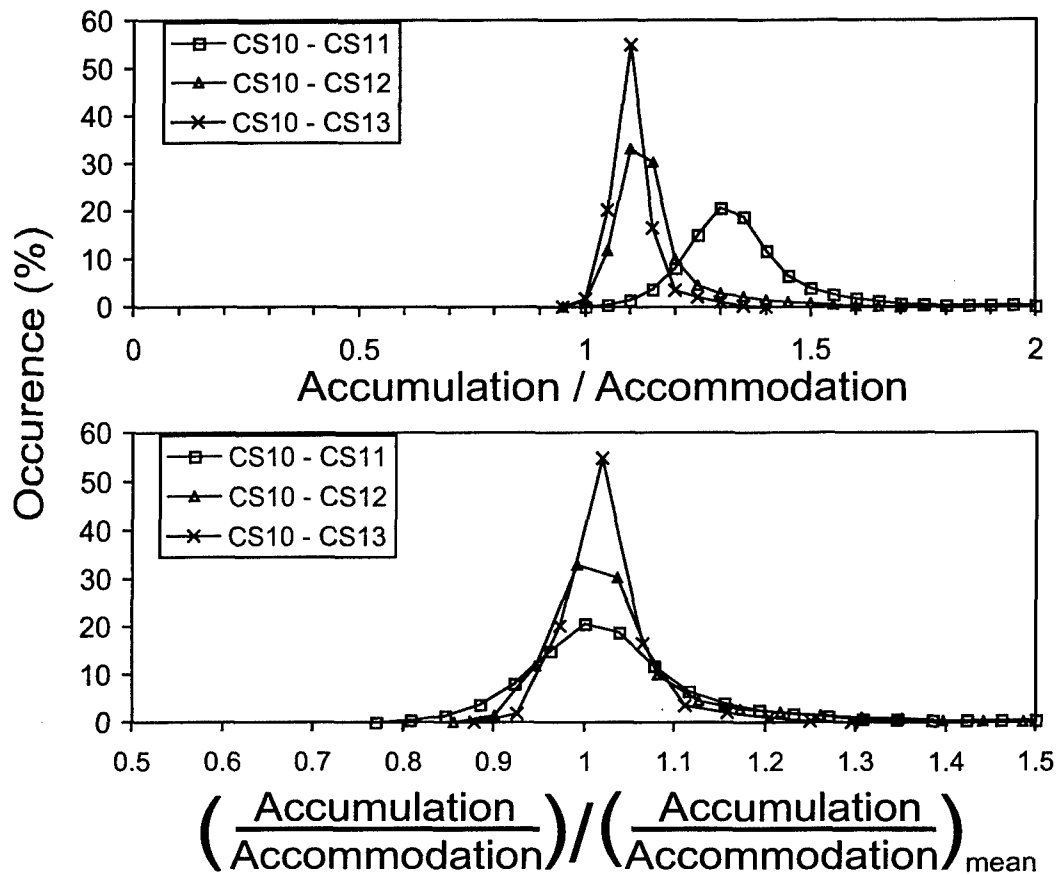
Figure 2-17: Histograms of accumulation/accommodation ratios for three isopachs illustrating the reduction in standard deviation of the ratio distributions with thickness or time. All isopachs are based at CS10. The upper plot incorporates true ratio values while the lower normalizes the distribution for each isopach by the mean ratio of that isopach. The upper plot highlights the fact that, while the distributions narrow with thickness, they are centered at a value greater than '1' indicating that the basin is over-filled. The lower plot, with all distributions shifted to center on '1', highlights the collapse of the distributions with increased isopach thickness. Note that a normalized distribution does not necessarily center exactly on a ratio of '1' because the mean of that distribution does not necessarily equal one of the discreet ratio datapoints on the distribution curve.
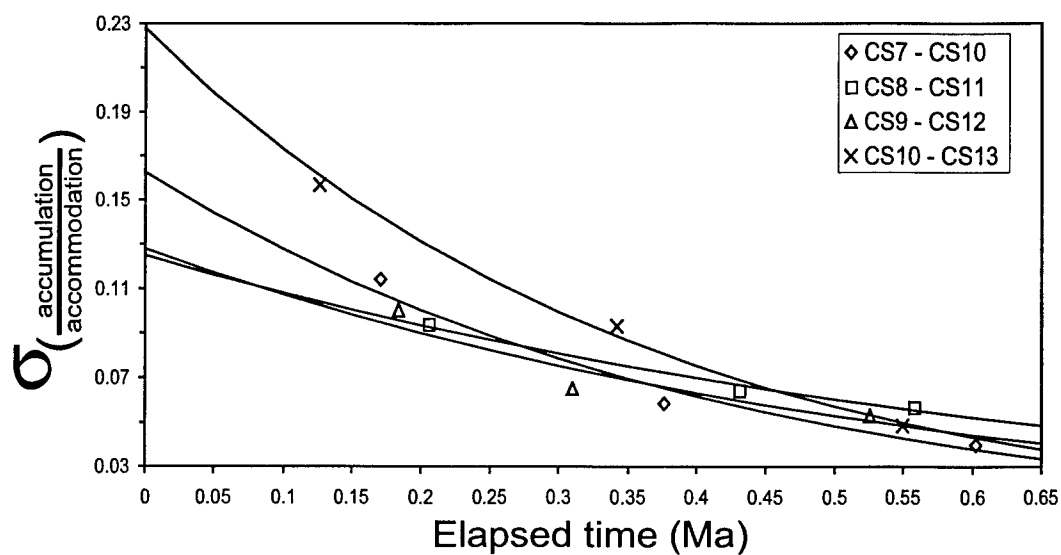
Figure 2-18: Standard deviation decay of four isopach series based at CS7, CS8, CS9 and CS10 illustrating the range of standard deviation behaviors. Data is limited to the first four cumulative isopachs for each series. The series based on CS7 is best fit by the function $\sigma = 0.1626e^{-2.4262t}$ for an e-folding time of 4.1×10^5 Ma. The coefficient, exponent and e-folding time for CS8 are 0.1249, -1.4544 and 6.9×10^5 Ma, for CS9 are 0.1279, -1.7671 and 5.7×10^5 Ma and for CS10 are 0.2279, -2.7695 and 3.6×10^5 Ma. See Table 2.2 for data.
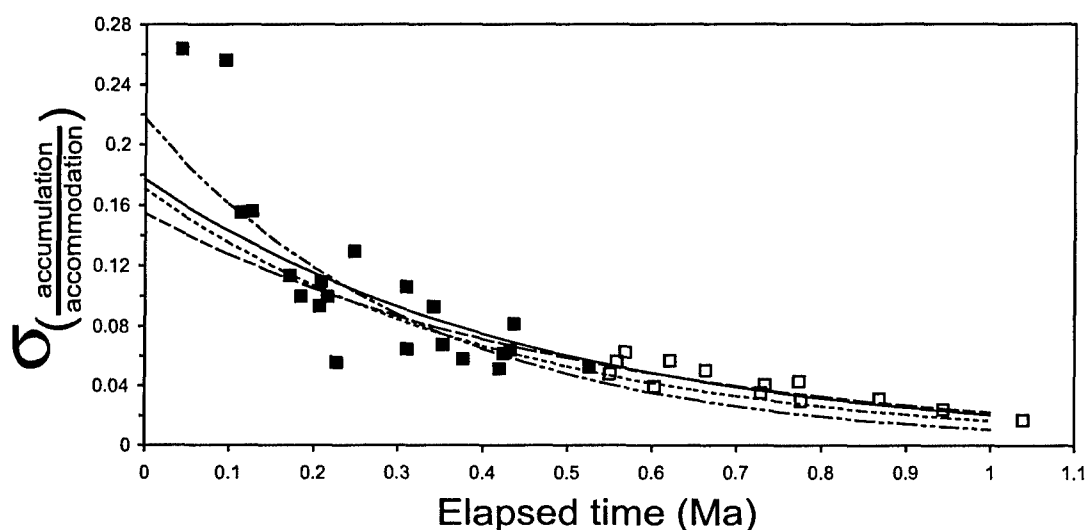
Figure 2-19: Short-interval data from sheet-like stratigraphy between CS7 and CS13. Because much of the variation in standard deviation is contained in the shorter interval isopachs, we calculate e-folding times for isopachs encompassing time intervals of 500,000 years or less (dark squares). This eliminates any possible loss of sensitivity to the short-interval data due to the large number of long time interval data points. The solid and dashed lines above represent best-fits to both short and long interval data with the solid line representing a fit to all data and the dashed line omitting the two outliers in the upper left of the plot. The dashed/dotted line represents a fit to all short-interval data including the outliers while the dotted line represents a fit to the short-interval data minus the outliers. See Section 2.5 for the equations describing these short-interval lines. Short-interval data with outliers is characterized by an e-folding time of 3.3×10^5 years while the data omitting the outliers results in an e-folding time of 4.3×10^5 years. For the reasons described in Section 2.5.1, omitting the outliers provides the most reasonable e-folding results.

Chapter 3

The contrast between equilibrium time scales for channel/levee complexes and sheet-like deposits: Fisk Basin, Gulf of Mexico

3.1 Introduction — Channel/levee complexes and equilibrium time

Landscapes and seascapes reflect and record the interplay between sedimentary systems and basin development. To interpret the record of this interplay from topography or stratigraphy, we must have a measure of the system equilibrium time. At long time scales, sedimentation and subsidence are in balance, the system is considered to be in equilibrium, and landforms or deposits reflect the history of allogenic forcing. This is only true, however, at those long time scales above which stratigraphy and topography reflect a steady-state condition (Mackin, 1948). At short time scales, the system is in a constant state of adjustment as it responds to local slopes, changes in boundary conditions, and stochastic autogenic forcing. There is, therefore, a critical scale that distinguishes autogenic stratigraphic architecture, or transient topographic

features, from the equilibrium state in which stratigraphy responds to, and reflects only, changes in significant global boundary or input conditions. The physics of terrestrial transport systems is well enough understood that both the relative effects of and response rates to different forcings have been explored quantitatively (*e.g.* Whipple (2001)) but our insight into equilibrium scales in subaerial environments is well ahead of that for the submarine. The submarine environment poses unique observational and modeling challenges with the result that we currently lack the framework to predict system-scale response times. Fortunately, while the submarine environment presents unique challenges, it also possesses unique attributes that facilitate the measurement of rates of system response. Where subaerial systems are dominantly or ultimately erosional, marine systems commonly preserve a significant fraction of the volume of sediment associated with the evolving seascape. In addition, those preserved sediments often contain the time control necessary to characterize intervals of system adjustment. In Chapter 2 I demonstrated that stratigraphic and temporal constraints can be used to determine the characteristic response time for a deepwater basin. Here, I extend this work from the previously studied sheet-like deepwater stratigraphy to stratigraphy dominated by distinctly different transport dynamics and explore how equilibrium scales compare between contrasting depositional systems within the same basin. I turn my attention to the Late Pliocene stratigraphy of the Gulf of Mexico Fisk Basin dominated by channel/levee complexes which exhibit significant depositional topography and restricted regional sediment distribution. These channels immediately overlie the sheet-like deposits studied previously (Chapter 2) and serve as an excellent comparison in behavior between different depositional systems with similar boundary conditions. Fisk Basin is about 20 km wide and 30 km long and the stratigraphic interval studied here is about 350 m thick and encompasses 4.8×10^5 years. Temporal constraints from microfossils and stratigraphic interpretations from reflection seismic data allow me to measure the convergence between patterns of sedimentation and subsidence over time and use the rate of that convergence to establish the equilibrium time of the sedimentation/subsidence system.

Changes in patterns of erosion and deposition are commonly interpreted to rep-

resent adjustments of the sediment-transporting system necessary to re-establish or maintain an approximately steady-state equilibrium profile. Most erosional or depositional models employ this steady-state or graded profile metric against which departures from this idealized profile are measured and interpreted (Mackin, 1948). In the submarine environment, we assume that these adjustments are the result of perturbations in boundary or input conditions such as changes in sealevel or variations in subsidence/uplift rate or pattern. As imaging of subsurface stratigraphy improves, so too has the resolution of our interpretation scale with the result that smaller features are assigned such allogenic significance. Practically, we know that adjustments associated with only meters of topographic change and/or intervals of tens of years can be the result entirely of natural variability within the transport system, even under constant boundary and input conditions. However, it is less clear how to interpret changes on the order of 10's to 100's of meters and at time scales of thousands to hundreds of thousands of years. This is a critical stratigraphic scale because it spans the range of Milankovich cycles driving allogenic climate and sealevel change. If the autogenic variability of a basin system operates at a scale equal to or greater than this mesoscale, then we must question our ability to extract the signal of mesoscale forcing events from stratigraphy. To confidently reconstruct the factors controlling temporal changes recorded in sedimentary strata, we must have some knowledge of the characteristic time that distinguishes short time periods from long. This characteristic is the equilibrium time and provides a reference necessary for separating records of change associated with external forcing from change due to internally generated processes in the system. The equilibrium scale defines a unit stratigraphic interval inside of which both autogenic variability associated with the transport system and allogenic variability in environmental conditions must be considered when interpreting temporal stratigraphic trends in properties such as grain size, bed thickness and stacking patterns of channel-filling deposits. Above the equilibrium scale, autogenic variability is averaged out such that any systematic change in stratigraphy can be unambiguously related to longer-term, externally imposed variations in environmental conditions.

In Chapter 2, I established a method for determining the equilibrium time in a nat-

ural basin and applied that method to sheet-like Late Pliocene deposits in Fisk Basin, Gulf of Mexico. In this chapter, I extend that analyses to channelized stratigraphy immediately overlying the subject of my earlier work. Not only does the nature of the transport system change over this interval but the rate of sedimentation decreases to 0.9 mm/yr, down from 1.3 mm/yr during the period of sheet-like deposition. I have mapped six stratigraphic surfaces in the basin using a seismic volume provided by the Auger Asset Team of Shell Exploration and Production Company (SEPCo). Four of the surfaces are regional or sub-regional horizons while the reamaining two define the final topographic expressions of two channel/levee complexes. Topographic relief on these features can be 100 m or more. The oldest surface in the section is directly dated at 2.30 Ma using microfossil assemblages and I project the age of the youngest surface to be 1.82 Ma. The total section is about 350 m thick. I use stratigraphic and temporal data to determine the long-term pattern of basin subsidence and then compare the channel/levee complexes and compensating sediment accumulation to this pattern. I make these comparisons using a modified version of the method developed by Sheets et al. (2002) for quantifying differences between sedimentation and subsidence patterns through time. To compare sedimentation and subsidence, I divide each horizon-defined isopach by an appropriately scaled subsidence map. I divide one map by the other at every point and use the statistics of the resulting ratio distributions to characterize the fit between sedimentation and subsidence. As the time interval or thickness interval of the sedimentation isopachs increses, the distribution of ratios collapses as indicated by a steadily decreasing standard deviation. Standard deviation decays exponentially and, following Sheets et al. (2002), I use a functional fit to this decay to extract a characteristic e-folding time for the sedimentation/subsidence system over the period of interest. In the channel/levee system considered here, I find the characteristic time to be 2.0×10^5 years. This value is roughly half the 4.6×10^5 years estimated from comparable isopachs during the period of sheet-like deposition which indicates that this interval of localized sedimentation, with sediment bypass and reduced basin-wide deposition rates, responds to external forcing twice as quickly as the broadly distributed, high-deposition rate stratigraphy immediately below.

100

3.2 Fisk Basin

The Fisk Basin is located on the upper continental slope of the Gulf of Mexico about 350 km southwest of New Orleans, LA, at an average water depth of about 900 m (Figure 2-1). A number of papers describing the stratigraphy and depositional history of this basin have been recently published (Booth et al., 2000; Winker and Booth, 2000; Booth et al., 2003) and my work builds on the stratigraphic framework presented therein. These papers refer to the location as Auger Basin, an informal name derived from the presence of the Auger hydrocarbon exploration field. I will refer to the basin by its official name, Fisk Basin (http://pubs.usgs.gov/of00-019/data/misc/gomnames.dbf; Bouma and Bryant (1994). The basin, in its Late Pliocene configuration, was about 12 km wide by 20 km long and positioned about 120 km down slope from the contemporaneous shelf edge (Winker and Booth, 2000; Booth et al., 2003). Representative seismic lines defining basin configuration and stratigraphy are shown in Figures 2-2, 2-3, 3-2 and 3-3. Three hydrocarbon-producing fields flank the eastern side of the basin and my work takes advantage of much of the data collected from wellbores in the Auger, Oregano, and Macaroni fields (Figure 2-1). Well data from cores include the paleontological analyses providing age control for the system, lithologic samples used to connect seismic attributes to rock types, and check-shot data establishing the relationship between seismic two-way-travel time and true vertical depth below the sea floor. Each of these data are discussed below.

The Gulf of Mexico, in current modern form, originated during rifting between the North American and South American and African plates in the Late Triassic (Salvador, 1991). Rifting continued through the Jurassic. In the late Middle Jurassic, periodic encroachments of the sea on the rifting basin resulted in the formation of extensive salt deposits (REF). The main drifting episode in the Gulf, which separated the Yucatan block from the North American Plate, took place in the early Late Jurassic. This drifting occurred after the deposition of the salt and emplaced true oceanic crust in the basin. Since the Late Jurassic, the Gulf of Mexico has been tectonically stable with subsidence driven by crustal cooling and sediment loading.

The Cenozoic structural evolution of the northern Gulf of Mexico is dominated by deformation and migration of the Jurassic Louann Salt (Diegel et al., 1983). Differential sediment loading of this relatively mobile layer has produced a variety of structures including low-relief anticlines and pillows, high-relief plugs and walls, and extensive salt sheets (Nelson, 1991). Sediment loading in the region offshore of Texas and Louisiana has been from the north and the salt has subsequently migrated southward producing a set of shore-parallel tectono-stratigraphic provinces (Diegel et al., 1983). The most distal of these is the tabular salt/mini-basin province that extends southward from about the position of the modern shelf-slope break and is bordered in deeper water by the Sigsbee Escarpment (Nelson, 1991; Diegel et al., 1983). The Fisk Basin is located in the northern part of this province and is bordered to the east, west and south by allochthonous, high-relief salt bodies. The alternate name of the basin (Auger Basin) is derived from the salt plug forming the Auger Dome in the north of the basin (Figure 2-1).

The oldest hydrocarbon-bearing sand in Fisk Basin is no older than 3.95 Ma and, since much of the exploration in the Gulf is economically driven, the earlier development of the basin is poorly constrained. However, since 3.95 Ma, sediment has been provided to the basin from various sources to the north and west while subsidence has been primarily focused in the south (Booth et al., 2000; Winker and Booth, 2000; Dean et al., 2002; Booth et al., 2003). Stratigraphic analyses suggest that subsidence was relatively constant and there are no indications of punctuated uplift.

3.2.1 Age control

A relatively high-resolution chronology is required in order to extract necessary temporal trends from Fisk Basin stratigraphy. The extensive hydrocarbon exploration history in the Gulf of Mexico has resulted in excellent age control for the basin-filling strata (Breard et al., 1993, 1996; Styzen, 1996; Breard et al., 1997; Lawless et al., 1951; Rosen et al., 1999; Breard et al., 2002). This biostratigraphic framework has been applied to the Late Pliocene in Fisk Basin by Booth et al. (2000) and Dean

et al. (2002), among others, using samples collected from multiple wells in all of the three fields shown in Figure 2-1. These workers collected samples for dating from relatively fine-grained stratigraphic packages that are enriched in their volume concentration of microfossils. This reduction in grain size and enrichment in microfossils are interpreted as signals of relatively low delivery rates for detrital sediment to the site and these sedimentary packages are referred to as 'condensed sections'. Shell geoscientists have dated seven condensed sections using population trends observed in calcareous nannofossils, shelfal foraminifera, and benthic and planktonic bathyal foraminifera (Dean et al. (2002); Table 2.1). Age control for the Pliocene section of Fisk Basin is derived from five condensed sections that can be mapped basin-wide using 3-D seismic data. These condensed sections are CS7, CS9, CS12, CS13 and CS14 and have associated ages of 3.47 Ma, 3.09 Ma, 2.55 Ma, 2.30 Ma and 1.95 Ma, respectively (Table 2.1). The next dated horizon, CS19, occurs in the Quaternary with an age of 1.15 Ma.

3.2.2 Seismic data

My mapping of the Late Pliocene section was carried out in a 3-D seismic reflection data volume of seismic data provided by SEPCo. Stratigraphic horizons were first mapped in two-way travel time (TWT) and then converted to true depth before carrying out the analyses described below. This time-depth conversion required acoustic velocity data also provided by SEPCo. The conversion algorithm is constructed from wellbore-derived check-shot data directly measuring travel times as a function of depth below sea floor. The check-shot data was collected from an Auger Field well and a polynomial fit to the time-depth pairs is presented in Figure 2-4. The polynomial fit to these data is described in Equation 2.1 in Section 2.2.2. Equation 2.1 is applied locally to convert matrices of points defining horizons in time to matrices of points defining the same horizons in depths below the seafloor. Seismic mapping and Equation 2.1 can be combined with the age-control data presented in Table 2.1 to generate a function describing the thickness of accumulated sediment through geologic time (Figure 3-1).

3.2.3 Late Pliocene stratigraphy

The stratigraphy of Fisk Basin has been the subject of several recent studies (Booth et al., 2000; Winker and Booth, 2000; Booth et al., 2003) and that framework is adopted here with minor modifications. This stratigraphy is based on the identification of a succession of condensed sections both in the seismic-data volume and in multiple wellbores. Here I am interested in the stratigraphy between CS13 and a younger horizon I will refer to as H14.5 as shown in Figures 3-2 and 3-3 (Booth et al., 2000; Winker and Booth, 2000; Dean et al., 2002; Booth et al., 2003). The interval between these two horizons span the end of the Late Pliocene section of the basin. Specifically, I consider condensed sections CS13 and CS14, two prominent channel/levee complexes between CS13 and CS14 designated as Channel 1 and Channel 2 (with Channel 1 being the oldest) and two additional sub-regional horizons, H14.25 and H14.5, above CS14 (Figures 3-2 and 3-3). As described above, relatively fine-grained, microfossil-enriched condensed section intervals such as CS13 and CS14 are interpreted to represent times of basin-wide reduction in sediment accumulation rates and the deposits are interpreted to drape over the pre-existing basin-floor topography. These two basin-wide horizons, as well as the sub-regional horizons H14.25 and H14.5, are treated here as approximate timelines, separating older strata below from younger strata above.

The prominent channel/levee complexes imaged between CS13 and CS14 are not the only channelized sediments in the Late Pliocene Fisk Basin. Channelization is found to occur in Fisk Basin at many scales. The underlying sediments between CS7 and CS13 are sheet-like at the seismic scale but maps of seismic-loop attributes (*e.g.* amplitude and coherency) reveal that at least some of the sheet-like deposits are constructed of amalgamated channel fills (Figure 4 of Booth et al. (2003)). Core from stratigraphy between CS7 and CS14 also contains facies consistent with channelized deposits (see Chapter 2 and Figure 2-8). In fact, mean condensed section thickness in the stratigraphy between CS7 and CS13 is on the order of 25 m and these condensed section deposits comprise only 10% of the total section. Therefore, as much as 90%

104

of the sheet-like section may be composed of coalesced channelized deposits. In the absence of core, the lithology and sub-seismic scale stratigraphy between CS13 and H14.5 is more difficult to constrain. However, there is a clear shift from small-scale, poorly confined channel systems between CS7 and CS13 to the focused, confined flow of the prominent channel/levee complexes between CS13 and H14.5 (Figure 2-2 and 2-3). There is a second shift in depositional architecture above H14.5 at which point the stratigraphy becomes dominated by channels and slump deposits (Figure 2).

3.2.4 Basin configuration from Late Pliocene to the present

The present day bathymetry of the Gulf of Mexico off shore of Texas and Louisiana is composed of numerous topographic depressions under-filled basins of which Fisk Basin is one (Figure 2-1). It is tempting to adopt the present-day morphology and geology of Fisk Basin as a template for interpreting the Late Pliocene configuration of the system but the modern seafloor expression of the Fisk Basin did not necessarily exist in the Late Pliocene. While sedimentary fill of the earlier basin does lie directly beneath the present-day form, temporal changes throughout the last 3.47 Ma limit the applicability of near seafloor analyses to interpretation of the older system. Biostratigraphic data shows a steady increase in sedimentation rate from 3.47 Ma to the present (Figure 3-1). Mapping of the shelf-edge position from seismic data reveals a progressive southward migration of the shelf-slope break of about 50km from the Early Pliocene to present (see Figure 5 of Winker and Booth (2000); Figure 1 of Booth et al. (2003)). This basin-ward shift reduced the slope length connecting the basin to the shelf edge by about 40% over that time. Assuming that most of the sediment deposited in Fisk Basin is terrestrial in origin, this reduction in distance between the basin and the shelf edge is consistent with, and provides an explanation for, the increasing rate of sediment accumulation within the basin.

A polynomial trendline describing sediment accumulation as a function of time fits the data for the last 3.47 Ma quite well with the exception of two points (Figure 3-1). One of those points, CS14, falls within the interval of interest in this paper. The CS14 horizon shows a dramatic decrease in sedimentation rate relative to the period from

CS7 to CS13. The age of CS14 (Table 2.1) defines a rate of sediment accumulation for the section between CS13 and CS14 that is two-thirds the accumulation rate associated with the section between CS7 and CS13. Seismic mapping of the channel/levee complexes within the CS13-CS14 interval may explain this change in sediment deposition in the basin. These two erosionally-based channel forms shown in Figures 3-2, 3-3 and 3-4 traverse the basin and I hypothesize that these deeper, flow-confining channels conveyed a greater fraction of incoming sediment through Fisk Basin and further down the slope, thereby reducing the basin-averaged sediment accumulation rate for this limited interval of time.

Channels comparable in thickness and areal extent to those described between CS13 and CS14 occur throughout the Quaternary stratigraphy of Fisk Basin. This introduction of strongly erosionally based channel forms into Fisk Basin stratigraphy is approximately coincident with a re-organization of depositional patterns within the basin that, because of the long time intervals involved, I interpret as signaling a change in the pattern of basin-floor subsidence. Figure 2-9 shows a map of relative deposit thickness for the section between CS7 and CS13, as well as the section between CS14 and the seafloor. The depocenter clearly shifts from the SW corner of the basin during the Late Pliocene (CS7 to CS13) to the SE corner of the basin (CS14 to the seafloor) and the overall shape of the basin-filling deposit changes as well. My mapping indicates that this adjustment occurs relatively quickly — primarily within the section bounded by CS13 and CS15 — and that the gross sedimentation pattern was approximately constant thereafter. Fisk Basin subsidence, like all mini-basins in the central Gulf of Mexico, has been driven primarily by preferential evacuation of the thick Louann Salt (late Middle Jurassic) from beneath the basin floor (Figure 2-1; Nelson (1991); Diegel et al. (1983)). The change in basin floor subsidence pattern is followed shortly thereafter by a change in basin-margin relief. Evidence for development of this local relief along the basin margin is documented by the first occurrence of seismically definable, mass-transport complexes in the basin immediately above H14.5. An example of one such mass slump complex, interpreted from its chaotic seismic character, is marked on the cross-sections in Figures 2-2, 2-3, 3-2

and 3-3 . Mapping of many such complexes, composed of submarine slides, slumps and/or debris flows, reveals that they are sourced from the margins of the basin itself. A transition from lateral to vertical migration of the Louann Salt would result in a steepening of the basin margin and the generation of slumps and slides. Not only might the age of these mass transport complexes provide an indication of the time of salt grounding and vertical migration, the absence of such chaotic deposits in the earlier stratigraphy suggests that vertical relief on the basin margin was relatively subdued prior to the occurrence of H14.5.

3.3 Equilibrium time and the graded profile

On short time-scales, an active channel or delta lobe occupies only a fraction of a basin and at such a time-scale (that of individual yearly floods or the migration of meander bends) deposition is confined to the immediate area in, and adjacent to, the active depositional system. Patterns of sedimentation are then set by the dynamics of sediment transport. If we 'zoom out', temporally to the geologic scale and spatially to the basin scale, these local features are lost in favor of larger-scale dynamics. Integrating the behavior of a river system or a delta over thousands to millions of years, depositional architecture is no longer dominated by individual channels or lobes. At these long time-scales, deposition is dominated by the subsidence patterns of the basin. The equilibrium scale for a basin is the time at which stratigraphy goes from being transport/deposition dominated to being subsidence dominated and, while the distinction may be clear in the extreme, the point at which this transition occurs is not.

Mackin (1948) described a graded stream as one in equilibrium where "...over a period of years, slope is delicately adjusted to provide, with available discharge and prevailing channel characteristics, just the velocity required for the transportation of the load supplied by the drainage basin". In other words, the transport system is adjusted so that the sediment load moving through any particular reach is equal to the load entering it. At long time scales, this graded condition leads to the development

of a steady state long profile for the transport system, and by extension, steady state topography when applied to a drainage basin as a whole.

The functional difference between short time-scale and long time-scale basin behavior is described in Section 2.3 above. Essentially, at short time-scales, the change in position of the bed over time, $\partial \eta / \partial t$, is described by the Erosion Equation (Fredsöe and Deigaard, 1994):

$$\frac{\partial \eta}{\partial t} = -\frac{1}{\epsilon_{bed}} \left(\frac{\partial q_s}{\partial x} + \frac{\partial q_s}{\partial y} \right) \tag{3.1}$$

where ϵ_{bed} is the sediment concentration in the bed, q_s is sediment flux, x is the downflow direction, y is the cross-flow direction, and $(\partial q_s / \partial x + \partial q_s / \partial y) = \nabla \cdot q_s$. At long time-scales, this form of the Erosion Equation must be augmented with the addition of a source/sink term that describes uplift or subsidence of the substrate. When in equilibrium (*i.e.* $\partial \eta / \partial t = 0$), Equation 3.1 becomes:

$$\sigma(x, y, t) = \frac{1}{\epsilon_{bed}} \left(\frac{\partial q_s}{\partial x} + \frac{\partial q_s}{\partial y}. \right) \tag{3.2}$$

Equation 3.2 describes the balance between subsidence rate and sedimentation rate necessary to preserve a steady-state profile and the equilibrium time of the sedimentation/subsidence system identifies the threshold at which basin behavior is best described by either Equation 3.1 or Equation 2.5.

3.3.1 Measuring equilibrium time

Sheets et al. (2002) proposed a method for quantifying the equilibrium time scale for a depositional system. To test it, they used an experimental facility in which they controlled subsidence shape and rate, continuously introduced sediment to the basin, and, at discreet intervals, measured the topography that developed as a result (Figure 2-12). Their goal was to quantify the fit between the subsidence pattern and the resulting topography in such a way as to determine the time scale at which subsidence and deposition balanced.

As a measure of comparison between subsidence and deposition, Sheets et al.

108

(2002) chose to use the standard deviation in the ratio between known space created by subsidence (accommodation) and thickness of aggrading deposits beneath measured topography (accumulation). Specifically, they divided their map of deposit thickness point-wise by the known subsidence pattern for a given time interval during the experiment. They then calculated the standard deviation associated with sets of ratios and used this metric as a measure of the fit between the two maps. This exercise was conducted repeatedly during the course of an experiment using progressive topographic maps to determine deposit thickness and progressive measurements of space created by the basin to determine subsidence (Figure 2-13). As a result, Sheets and his colleagues found that the standard deviation of the ratio data decayed exponentially as the experiment progressed and the depositional system occupied more and more of the subsiding basin. To characterize the convergence between sedimentation and subsidence, they plotted standard deviation as a function of time and fit that data with an exponential function. They chose the e-folding time — the time required for the standard deviation to decay by a factor of $1/e$ — as a representative scale of system behavior. I modified this approach in Chapter 2 for application to natural basins and apply it here to channelized deposits.

3.4 Method

3.4.1 Stratigraphic mapping

The horizons for this study were mapped seismically at the transitions between the condensed sections below and the sandier deposits above. I mapped two condensed sections, CS13 and CS14 and two sub-regional surfaces, H14.25 and H14.5, to provide higher-resolution maps than achieved from condensed section maps alone (Figures 3-2 and 3-2). These two additional horizons interpreted above CS14 also represent fine-grained drapes over existing topography but their regional significance has not been established. The interfaces between condensed sections and coarser-grained deposits can be mapped seismically because of the large contrast in impedance between the

lower porosity condensed sections and the higher porosity, coarser deposits above and below. I also mapped two channel/levee complexes between CS13 and CS14 designated as Channel 1 for the older and Channel 2 for the younger (Figures 3-2 and 3-2). For these channel/levee complexes, I mapped at the upper extent of the topographic expression. The latter channel, Channel 2, clearly onlaps the older Channel 1 along the entire width of the basin (Figure 3-4). Since the deposits from the two channel systems do not interfinger, I conclude that Channel 1 was active and subsequently abandoned prior to Channel 2 being established. Hence I treat the maps of channel topography as coeval surfaces as well. Since all mapped surfaces can be treated as timelines, subtracting one from another produces an isochron representing depositional thickness for a discreet time interval. I constructed isochrons using every possible combination of mapped surfaces for a total of 15 packages (Table 3.1). These depositional packages have been deformed via post-depositional tectonism but, because I am interested only in stratigraphic thickness, this structural deformation does not affect my results.

3.4.2 Calculating depositional thickness

In order to work in depositional thickness (*e.g.* meters) rather than time (*TWT*), isochrones must be converted to isopachs. Every point in *TWT* defining a surface must be converted from time to true vertical depth using Equation 2.1. These converted surfaces are then subtracted from one another to generate thickness maps. This process is described in detail in Section 2.4.2.

3.4.3 Determining ages for basin-wide horizons and locally depositing channel/levee systems

While the three fields in the Fisk Basin provide excellent temporal control in the late Pliocene (Table 2.1), for the stratigraphy of interest in this paper, temporal control is limited to two Late Pliocene condensed sections (CS13 dated at 2.30 Ma and CS14 dated at 1.95 Ma) and the next dated horizon does not occur until the Quaternary

110

(CS19 dated at 1.15 MA). This resolution is at a coarser level than required for my analysis and I must assign ages to the two undated sub-regional horizons (H14.25 and H14.5) using a functional relationship between time and depositional thickness. Generally, sedimentation rate increases over time in the basin with the exception of CS14 that lies significantly below the polynomial trend. As described previously, I believe that this reduction in sedimentation rate is reasonably explained by the transport of sediment across and out of the basin by the channel/levee systems (Figure 3-4). In my previous analyses of the sheet-like deposits in Chapter 2, I found that a simple linear fit did an excellent job describing sedimentation as a function of time for the period from CS7 to CS13 and so used a basin averaged rate of 1.3 km/Ma to assign ages to undated horizons. I take a similar approach here, relying on a linear sedimentation rate, and base my time-thickness function on the established dates for CS12 (2.55 Ma), CS13 (2.30 Ma) and CS14 (1.95 Ma) (Table 2.1). The linear fit to this data results in a sedimentation function $z = 0.9 km/Ma \times t$ ($R^2 = 0.941$) where z is depositional thickness in km and t is time measured in millions of years (Figure 3-1). Based upon the slope of this function, the average sedimentation rate for this channelized period of the latest Pliocene was 0.9 mm/yr. I use this function to assign ages of 1.89 Ma to CS14.25 and 1.82 Ma to CS14.5 based upon mean isopach thickness.

My method of assigning ages to regional condensed sections breaks down when applied to the areally restricted channel/levee packages. A problem arises because my dating method makes an assumption of basin-wide deposition that allows me to relate mean isopach thickness directly to time. The channel/levee complexes between CS13 and CS14 occupy less than half the total area of the basin (Figures 3-2, 3-3 and 3-4). Channel/levee complexes are local features with the potential for high local deposition rates and hence basin-averaged approximations are not appropriate. Using mean thickness in combination with basin averaged sedimentation rate will over-predict the time associated with deposition of a channel/levee complex. Figure 3-5 illustrates the problem of dating local features with basin-averaged sedimentation rates. The stratigraphy in both the CS13-CS14 interval (Figures 3-2 and 3-3) and in my example

(Figure 3-5) consists of the following: two bounding condensed sections, two areally limited channel/levee complexes with thicknesses comparable to that between the condensed sections, and a final package of reciprocal sedimentation that fills the topographic form left by the abandoned channel systems. The ispopach thickness between the two bounding condensed sections is l meters which, based upon a basin-averaged sedimentation rate, would correspond to some time interval, t, separating the horizons. However, the three packages internal to the isopach (two channels and a period of reciprocal sedimentation) have mean thicknesses on the order of $l/2$ and dating these with basin-averaged sedimentation rates results in three packages roughly of age $t/2$ for a cumulative age of $3t/2$ — the sum of the parts exceeds the whole. The solution then is to date the channel/levee packages and final infilling sedimentation simply by apportioning the time t between bounding isopachs based upon some weighting factor and I chose the relative volume of each isopach for that weighting factor. The isopach bounded below by CS13 and above by the top of the first channel-levee complex, comprises 11% of the total volume between CS13 and CS14. The volume between a composite lower bounding surface created by combining CS13 and the first channel-levee complex and an upper bounding surface marking the final topography of the second channel-levee complex is 33% of the total volume. The volume of sediment that drapes over the final channel forms and fills to CS14 accounts for the remaining 56% of the sediment volume between CS13 and CS14. As a result, the weighting factors for the three isopachs are 0.11, 0.33 and 0.56, respectively. The elapsed time between CS13 and CS14 determined from biostratigraphy is 0.35 Ma so the weighted time for the deposition of Channel 1 is 0.039 Ma, for Channel 2 is 0.116 Ma, and for the final infilling sediments is 0.196 Ma.

3.4.4 Determining Basin Subsidence

In an experimental study like that of Sheets et al. (2002), subsidence history is prescribed but, in a natural system, actual subsidence rate and pattern are not as easily constrained. Often in basin studies, depositional patterns are used as proxies for subsidence. However, I contend here and in Chapter 2 that depositional patterns do not

accurately reflect sedimentation unless those patterns are considered above a certain scale and that critical scale is unknown. Hence, in Chapter 2, I developed a strategy for determining the representative basin subsidence shape.

I determined the subsidence pattern during the period between CS7 and CS13 by adding successive isopachs and recognizing that, regardless of basal condensed section, cumulative isopachs converged on a stable form (Figure 2-14). The fact that all isopachs converge to a consistent pattern was convincing evidence that basin subsidence during that period is defined by that pattern. I therefore took that stable form as the representative basin subsidence pattern from CS7 to CS13 and used it as a reference shape for comparison (Figure 2-9). Comparable behavior can be found from H14.5 to the seafloor — cumulative isopachs converge on a stable form as we incorporate more and more stratigraphy into the isopach and that form is independent of basal horizon. The subsidence pattern above H14.5 persists and matches quite closely the modern seafloor bathymetry (Figures 2-1 and 2-9). While the pre-CS13 and post-H14.5 intervals achieved fixed subsidence shapes, those shapes are not the same — before CS13, subsidence was focused in the southwest corner and subsequently shifted to the southeast corner (Figure 2-9).

The interval of interest in this chapter between CS13 and H14.5 does not incorporate sufficient stratigraphic thickness to converge on a stable form and therefore cannot be used to determine a reference subsidence pattern. It is logical then to use the subsidence shape either preceding or post-dating deposition between CS13 and H14.5. To determine which shape was more appropriate, I compared the total isopach from CS13 to CS14.5 to both subsidence forms by calculating the point-wise ratio of isopach divided by subsidence. I found that the standard deviation of the ratio distribution was smaller when using the subsidence pattern from H14.5 to the seafloor ($\sigma = 0.0401$) than when using the pattern from CS7 to CS13 ($\sigma = 0.0569$) describing a better fit to the more recent pattern. Therefore I use the depositional pattern from CS14.5 to the seafloor, normalized by maximum isopach thickness, as a reference subsidence shape for analyses of the channelized stratigraphy between CS13 and H14.5.

3.4.5 Scaling basin subsidence

In this study, I compare the pattern of basin subsidence from H14.5 to the seafloor against each interval thickness mapped from CS13 to H14.5 (Table 3.1). To accomplish this, the normalized map of subsidence must be appropriately scaled so that it can be compared to the map of aggradation represented by each isopach.

The process of generating scaled susbidence isopachs for comparison to depositional isopachs is described in Section 2.4.5. To summarize, a dimensionless subsidence pattern, S_{Norm}, is generated by normalizing the total isopach from CS7 to CS13 by maximum isopach thickness. For comparison to depositional isopachs, that normalized subsidence is then scaled, producing a dimensional subsidence isopach such that:

$$S_{Dim,a-b} = S_{Norm}RT_{a-b} \qquad (3.3)$$

where a and b indicates the bounding stratigraphic horizons, R is a calculated subsidence rate (1.8 mm/yr) and T is the time interval for the depositional isopach of interest. The fit between a given isopach, I_{a-b} is determined by calculating a pointwise ratio matrix, U:

$$U_{i,j,a-b} = \frac{I_{i,j,a-b}}{S_{Dim,i,j,a-b}} \qquad (3.4)$$

where $U_{i,j,a-b}$ is a matrix of the ratios of the i,j elements of isopach I_{a-b} and the i,j elements of $S_{Dim,a-b}$ and fit is quantified with the standard deviation of U_{a-b}.

3.5 Results

The ratio matrix, U_{a-b} (Equation 3.4), constrains the fit between isopach and subsidence and I use the standard deviation of that matrix as a representative statistic and to calculate a characteristic scale that describes how U evolves with time. For each isopach/subsidence ratio matrix, I plot standard deviation as a function of the scaling time, T_{a-b}, and fit an exponential to that data. Where Sheets and his colleagues

114

varied sediment flux and sedimentation rate, in this study, I assume that, over the 480,000 year period between CS13 and H14.5, constant depositional and subsidence conditions existed. Hence, I can combine the results of the fit matrix, U, group all of my data to maximize the sample population, and fit with a single curve to describe sedimentation/subsidence behavior.

The standard deviation data for each condensed section combination is reported in Table 3.1 and plotted in Figure 3-6. This data is best described by the function:

$$\sigma = 0.3701e^{-5.1008t} \tag{3.5}$$

where: σ is the standard deviation and t is the scaling time, $T_{a.b}$, described in detail in Section 2.4.5 above (the time over which the isopach was deposited). The number of data points is 15. Error between the functional relationship and the data can be characterized by an $R^2 = 0.830$. The characteristic e-folding time scale calculated from the exponential function is 2.0×10^5 years.

3.5.1 Sheets vs channels

The e-folding time of 2.0×10^5 years for this period of channel/levee deposition is less than half the 4.6×10^5 years found for the sheet-like deposits situated immediately below the CS13-CS14.5 section (Chapter 2). However, to compare the two results, I must show that the data used to derive an e-folding time for the sheets in my earlier chapter is comparable to the data used to calculate an e-folding time for the channels in this chapter. Specifically, I must show that the source data (*i.e.* isopach time intervals) for both studies have been derived from similar data distributions. If I were to characterize two systems using data with very different source distributions, it would be difficult to say whether or not differences in characteristic times between the two transport systems were statistically significant or simply an artifact of the disparate source data. To compare channel/levee and sheet complexes I must choose isopach data from each environment that describe comparable distributions and establish the similarity of that data.

In Chapter 2, I determined e-folding times for the sheet-like stratigraphy using the entire range of isopachs available between CS7 and CS13 (Figure 2-15). This resulted in 34 data points with the shortest time interval between bounding horizons being 42,000 years and the longest being 1.03 million years. I also performed e-folding analysis for a subset of the isopach data between CS7 and CS13 (Figure 2-19); I determined e-folding times for sheets based upon short interval data in which I limited the analyses to those isopachs spanning about 500,000 years or less. This subset data was selected because the full isopach population was weighted towards the long-range data ($i.e.$ isopachs which represented many times the characteristic scale) at the potential cost of losing sensitivity to the shorter time scale information when fitting an exponential function to the data. The short interval data (omitting the two outliers as described in Section 2.5.1) result in an e-folding time of 4.3×10^5 years (n = 19; $R^2 = 0.616$). The total time between CS13 and H14.5 is 480,000 years and so I compare my channel/levee results to the short interval data set from the sheets rather than to the full population.

3.5.2 Kolmogorov-Smirnov and data set similarity

The Kolmogorov-Smirnoff (K-S) Test is a statistical assessment of the goodness-of-fit between two empirical distributions or between an empirical distribution and an ideal distribution. See Benjamin and Cornell (1970); Davis (1986) for further descriptions of the K-S test. I employ K-S here to make two determinations: 1) that the distribution of my source data sets (isopach time intervals) from both sheets and channels are similar enough to support a comparison of results and 2) that the distributions of standard deviation data from the two environments are different and hence contrasting e-folding times are significant.

Kolmogorov-Smirnov measures whether or not two data sets are derived from similar distribution functions. This test is based upon the cumulative probability distribution (CPD) of one empirical data set and returns a statistic, P, which characterizes the goodness-of-fit between the empirical CPD and either a theoretical distribution ($e.g.$ normal distribution) or a CPD derived from a second set of empirical data. Here

116

I compare two empirical data sets: isopach time values between CS13 and H14.5 and short-interval ($\leq$500,000 years) time values from CS7 to CS13 (Figure 3-6). The advantage of K-S is that the test is non-parametric and distribution free, that is, it assumes nothing about the distributions of data used and is based solely upon the empirical distribution function.

The K-S test is based upon the maximum value of the absolute difference between the two distributions of interest. When comparing two empirical distributions, D is defined by:

$$D = \max_{-\infty < x < \infty} |S_{N_1}(x) - S_{N_2}(x)| \tag{3.6}$$

where x is the value of the data for comparison (e.g. isopach time or standard deviation or ratio matrices), S_{N_1} is the cumulative probability distribution for one data set (e.g. sheet data between CS7 and CS13) and S_{N_2} is the cumulative probability distribution for the second data set (e.g. channel/levee complexes between CS13 and CS14.5). The statistical probability, P, then is calculated as:

$$P = Q_{KS} \left\{ \left(\sqrt{N_e} + 0.12 + \frac{0.11}{\sqrt{N_e}} \right) \right\} \tag{3.7}$$

where:

$$Q_{KS} = 2 \sum_{j=1}^{\infty} (-1)^{j-1} e^{-2j^2 \lambda^2} \tag{3.8}$$

and N_e is the effective number of data points defined as:

$$N_e = \frac{N_1 N_2}{N_1 + N_2} \tag{3.9}$$

for the comparison of two empirical data sets. In this analyses, N_1 is 15 derived from the channel/levee data discussed in this chapter and N_2 is 19 comprising the short-interval sheet deposit isopachs in Chapter 2. The null hypothesis of the K-S test is that the two data sets are derived from the same CPD. A small P value indicates that the null hypothesis of data set similarity can be rejected.

A K-S analysis of the temporal source data for sheets and channels returns a probability, P, of 0.788 (Figure 3-7, left). This is considered to be 'large' even if we accept a confidence interval as strict as 0.01 (Benjamin and Cornell, 1970). The null hypothesis of similarity is accepted and I can confirm that isopach distributions from the two environments are comparable. Temporal data are statistically similar and it is unlikely then that a difference in characteristic times is related to biases induced by the source data. Conversely, the standard deviation data that results from the sedimentation/subsidence ratio calculations are statistically different. The K-S analysis of the standard deviation CPD returns a P of 0.017 which is small at a 0.05 confidence interval (Figure 3-7, right). The null hypothesis is rejected. Hence, attempts to explain the factor of two difference between e-folding times for sheets and for channel/levee complexes are justified.

3.6   Discussion

The Fisk Basin provides a unique opportunity to compare response times between two end-member depositional systems: one dominated by broadly distributed sheet-like deposits and one dominated by erosional and constructional channel/levee complexes. Not only do these two depositional systems occur in the same basin, they are immediately juxtaposed in time (Figures 2-2 and 2-3). Based upon the method developed in Chapter 2, I can constrain the characteristic scales of both sheet-like and channel/levee deposits subjected to similar basin and input conditions. I find that these two end-member depositional systems have measurable differences in the time-scales over which sheets and channels distribute sediment across the basin. I attribute this difference in characteristic times to the mechanics of sediment transport and deposition and we find that equilibrium scales for sheets and channels do not conform to existing deepwater depositional models.

Sheet-like deposits are generally believed to be sensitive to subsidence rates and basal slope. These low-relief, broadly distributed packages are thought to bypass regions of high slope and focus deposition in areas of maximum subsidence. Under

this model, the thickness of a sheet deposits is directly proportional to local subsidence. The supposed sensitivity of the unconfined system to local conditions means that deposits are expected to rapidly achieve a graded profile and to quickly reflect equilibrium between sedimentation and subsidence. In contrast to sheet systems, channel/levee complexes are dominated by confined flow with periods and regions of significant erosion and high local deposition rates. Further, channel/levee systems occupy only a portion of the basin at a time and convey a significant fraction of sediment directly through the basin and down slope (Figure 3-4). All of these factors suggest that channel/levee systems should respond quite slowly to boundary and input conditions. Relative to sheet-like deposits, channel/levee deposits should take a long period of time to achieve a basin-wide balance between subsidence and sedimentation. My results do not support this conclusion.

In Chapter 2, I showed that the sheet-like deposits in Fisk Basin are relatively insensitive to subsidence. These deposits are not ponded at the scale of individual condensed section-bounded packages but rather are distributed basin-wide with sub-equal thicknesses at both the basin flanks (areas with low deposition rates and the potential for high slopes) and in the basin center (where the converse is true). While in conflict with conceptual basin-fill models, there is evidence to suggest that sheet-like deposits in deep water settings need not focus deposition in the region of maximum subsidence and my results support this. Imran et al. (1998) showed that turbidity currents channelize within a relatively restricted range of particle Reynolds numbers and basal slope. At slopes above those associated with the channelized condition, the system enters what Imran refers to as a 'sheet-like' regime where sedimentation is broadly distributed on that slope in both the cross-stream and down-stream directions. I cannot reconstruct basal slopes at the time of sheet deposition in Fisk Basin but I can say that deposition during the interval from CS7 to CS13 was broadly distributed in contrast to the southwest-focused subsidence pattern. It is not until we integrate isopachs over several condensed sections that the basin shape begins to emerge. This mantelling of the basin with sub-equal thicknesses of sediment is not an efficient method of compensating for subsidence or for attaining a graded profile.

119

The result of the broad distribution pattern of sheets during the Late Pliocene in Fisk Basin is that this unconfined transport system takes a surprisingly long period of time, almost half a million years, to average out autogenic behavior and to approach equilibrium with subsidence. Below an isopach thickness of about 600m, the unconfined depositional system does not truly reflect the pattern of basin subsidence and should not be thought of as graded.

The short response time of the channel/levee complexes relative to the sheets — 200,000 years versus 430,000 years — likely reflects a difference in the transport efficiency between the two systems. The unconfined sheet systems collapse rapidly and sediment is deposited shortly after introduction to the basin. This lack of efficiency in the unconfined regime makes it difficult to transport sediment long distances from the point of input to the basin without first depositing sediments proximally. Thus, the basin is filled via progradation of sediment packages from proximal to more distal parts of the basin. This progradation takes time and may account for the disparity in characteristic times. In contrast, channels are quite good at focusing transport energy and moving sediment long distances. The channels in the interval between CS13 and H14.5 encompass 40,000 and 120,000 years indicating rapid occupation, sedimentation, and subsequent avulsion to a new position within the basin. By focusing sedimentation and driving channel migration, channel/levee complexes cover the basin more quickly and therefore can reach equilibrium more rapidly. This is not to suggest however that individual channel/levee complexes, or avulsions from one to the next, represent external forcing. Channel abandonment is the result of local conditions (channel super-elevation or slope; Mohrig et al. (2000)) and part of the autogenic behavior of the system. We must still integrate then over multiple channel iterations before we can confidently interpret allogenic signals.

3.7 Conclusion

The Fisk Basin provides an opportunity to directly compare the characteristic response times of different sediment transport systems under similar boundary and

initial conditions. The conceptual model of a graded depositional system, one that results in steady-state profile, is critical to models of landscape (*e.g.* Whipple (2001)) and seascape (*e.g.* Prather et al. (1998)) evolution. However, this presumed equilibrium between sedimentation and subsidence only holds above some characteristic time scale at which autogenic behavior is averaged out of the stratigraphy. Until Chapter 2, that critical scale had never been identified in a deepwater environment. Here, employing the methodology developed above (Chapter 2), I have shown that such characteristic times are heavily dependent upon the mode of sediment transport and deposition in the basin.

In contrast to the sheet-like deposits of the previous chapter, I focus here on the stratigraphy dominated by channel/levee complexes immediately overlying those sheets. These channelized systems are limited in depositional width, represent a period of reduced basin-averaged sedimentation rate, and build significant topography. I find that the characteristic *e*-folding time for the Late Pliocene channel/levee stratigraphy in Fisk Basin is 2.0×10^5 years which, using a basin averaged sedimentation rate, translates to a unit equilibrium thickness of 180 m. Compared with the *e*-folding time of 4.6×10^5 years (600 m) found in the sheet deposits (Chapter 2), the channel/levee systems respond more than twice as quickly to allogenic forcing than do the sheet-like deposits.

My results are in contrast to common models of deepwater deposition. It is generally thought that sheet-like deposits are very sensitive to basal slope and subsidence rates such that sheet thickness directly reflects basin behavior. If this model were correct, sheet deposits would achieve balance between sedimentation and subsidence relatively quickly. However, the results in Chapter 2 shows that sheets are relatively insensitive to basin behavior. In the Late Pliocene of Fisk Basin, sheet deposition was sub-equal across the basin and subsidence patterns did not emerge until isopachs incorporated multiple condensed section-bounded packages. The fact that sheets actually respond much more slowly than channels is likely a direct result of the transport efficiency of the channel/levee system. Channel/levee systems focus deposition resulting in significant topography and hence force migration of the system across

the basin at relatively high rates. This high mobility of channel/levee complexes is evident in the fact that the two channels mapped for this study represent deposition over the course of 40,000 and 120,000 years, respectively. Hence each channel/levee complex does not represent external forcing — individual complexes still represent short time-scale autocyclic behavior — but the rapid shifting of the systems does allow channel/levee deposition to more-quickly respond to allogenic perturbations.

3.8 Tables

Table 3.1: Isopach characteristics — CS13 to H14.5.

Statistics for isopachs used in this study. Table includes isopach name listing basal and top bounding condensed sections, the interval of time associated with the isopach, and the standard deviation of the sedimentation/subsidence ratio for each isopach when compared to basin subsidence. Standard deviation decays exponentially with increased mean thickness and time interval. This data is presented graphically in Figure 3-6.

Isopach	Time Interval	Standard Deviation
CS13 to Channel/Levee 1	0.04	0.5604
CS13 to Channel/Levee 2	0.15	0.2617
CS13 to CS14	0.35	0.0712
CS13 to H14.25	0.41	0.0682
CS13 to H14.5	0.48	0.0523
Channel/Levee 1 to Channel/Levee 2	0.12	0.4704
Channel/Levee 1 to CS14	0.31	0.1301
Channel/Levee 1 to H14.25	0.37	0.1276
Channel/Levee 1 to H14.5	0.44	0.0839
Channel/Levee 2 to CS14	0.20	0.1455
Channel/Levee 2 to H14.25	0.26	0.1477
Channel/Levee 2 to H14.5	0.32	0.1244
CS14 to H14.25	0.06	0.2454
CS14 to H14.5	0.13	0.1497
H14.25 to H14.5	0.07	0.2326

3.9 Figures
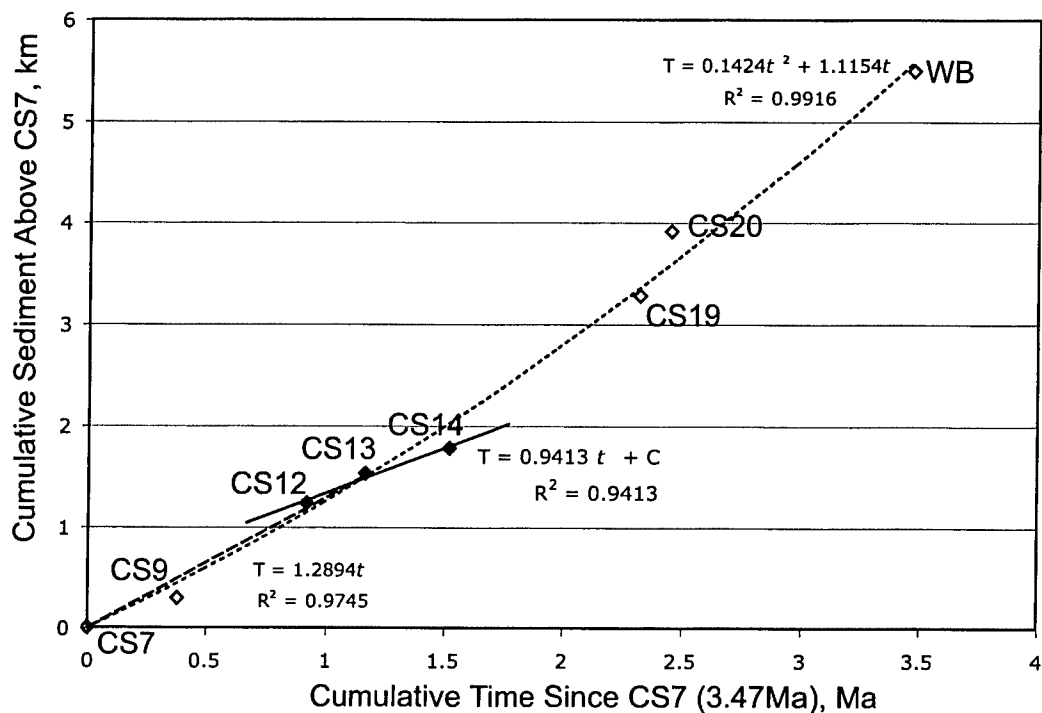
Figure 3-1: Deposition rate in the Fisk Basin. Cumulative mean isopach thickness as a function of elapsed time beginning at CS7 and proceeding to the present (WB – water bottom). Overall, sedimentation increases exponentially through time. Sedimentation from CS7 to CS13 can be approximated linearly (dashed line) by $T = 1.3t$ ($R^2 = 0.975$). Likewise, the sedimentation rate for the period between CS13 and H14.5 (solid line) can be approximated using CS12, CS13 and CS14. Sedimentation is represented by $T = 0.9t + C$ ($R^2 = 0.9413$) where C is some constant. See Table 2.1 for condensed section age data.
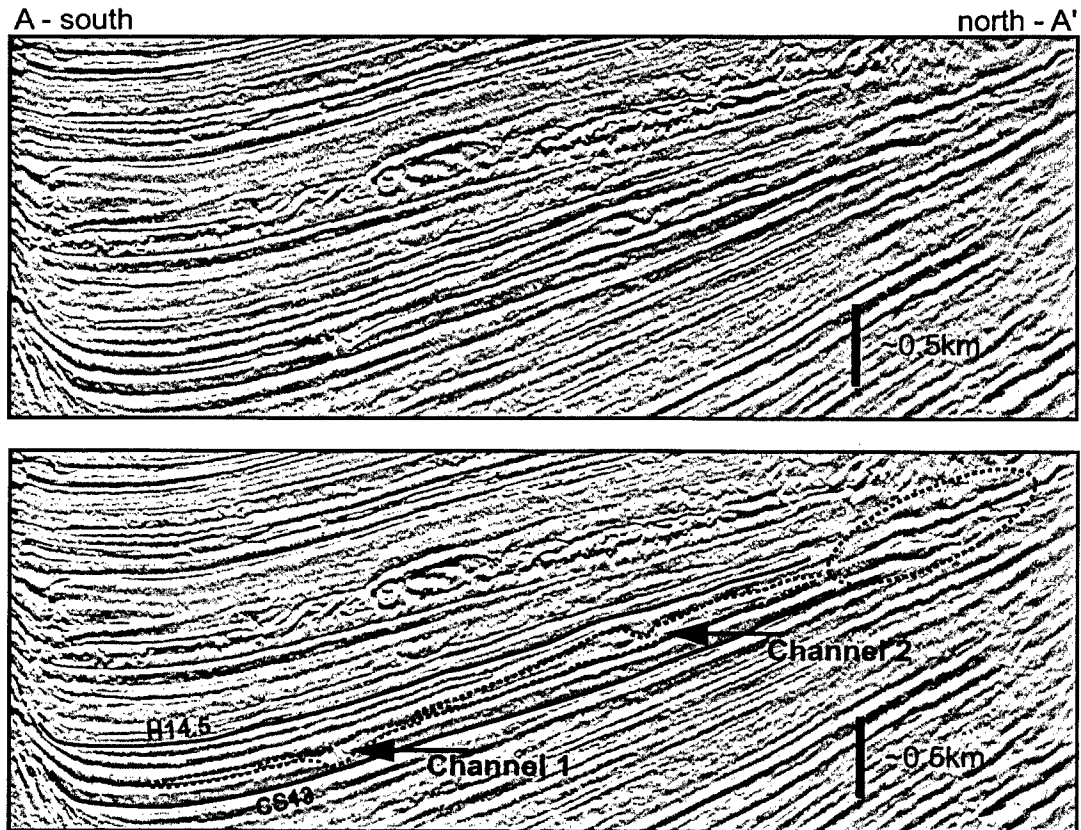
Figure 3-2: Uninterpreted and interpreted seismic sections (A-A', Figure 2-1) of channel/levee complexes proximal to source at west side of basin. The two channel/levee complexes are mapped with dashed lines and a potential third system is highlighted with a dashed oval. Condensed sections CS13 and H14.5 are indicated with solid lines for reference. The second channel/levee complex clearly shingles onto the first indicating that the first system was abandoned prior to activity in the second. This seismic data is in two-way-travel time. Acoustic velocity varies as a function of depth so the vertical scale is an approximate average for the section. Line is 30 km across.
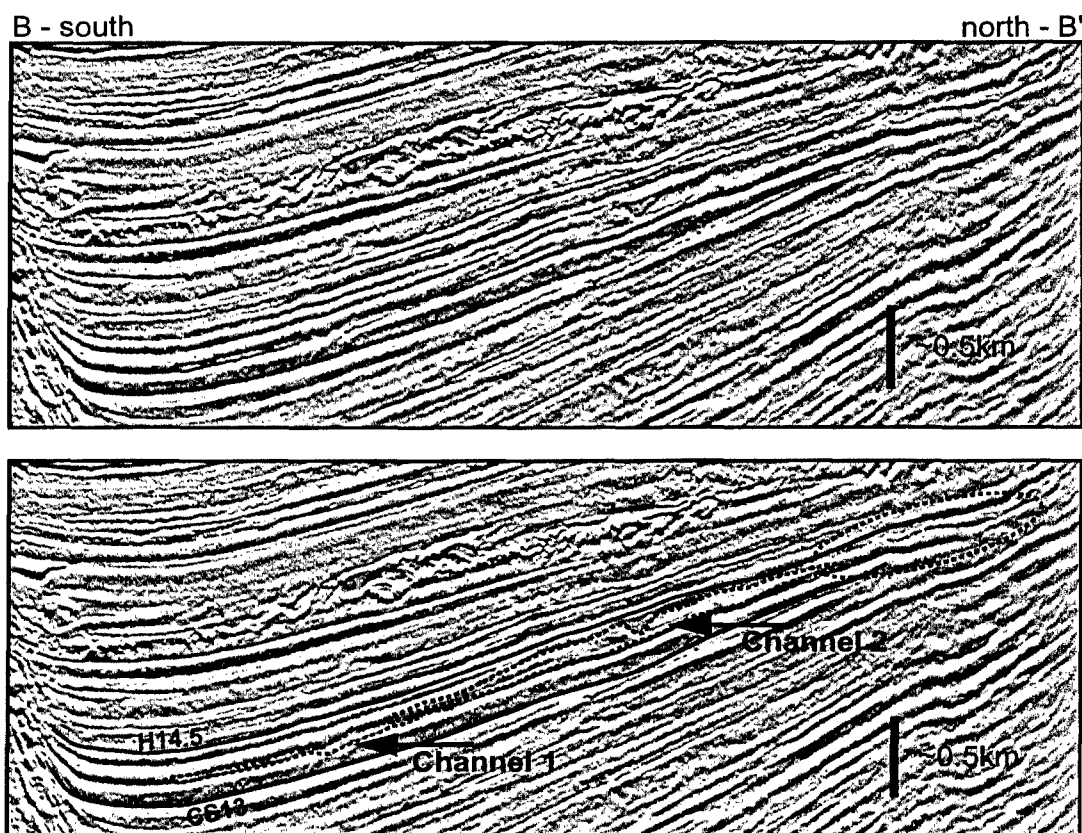
Figure 3-3: Uninterpreted and interpreted seismic section (B-B', Figure 2-1) of channel/levee complexes relatively distal to source at west side of basin. The two channel/levee complexes are mapped with dashed lines and a potential third system is highlighted with a dashed oval. Condensed sections CS13 and H14.5 are indicated with solid lines for reference. Note that, relative to Figure 3-2, the older channel (left) does not appear to erode as deeply into inderlying strata. This seismic data is in two-way-travel time. Acoustic velocity varies as a function of depth so the vertical scale is an approximate average for the section. Line is 30 km across.
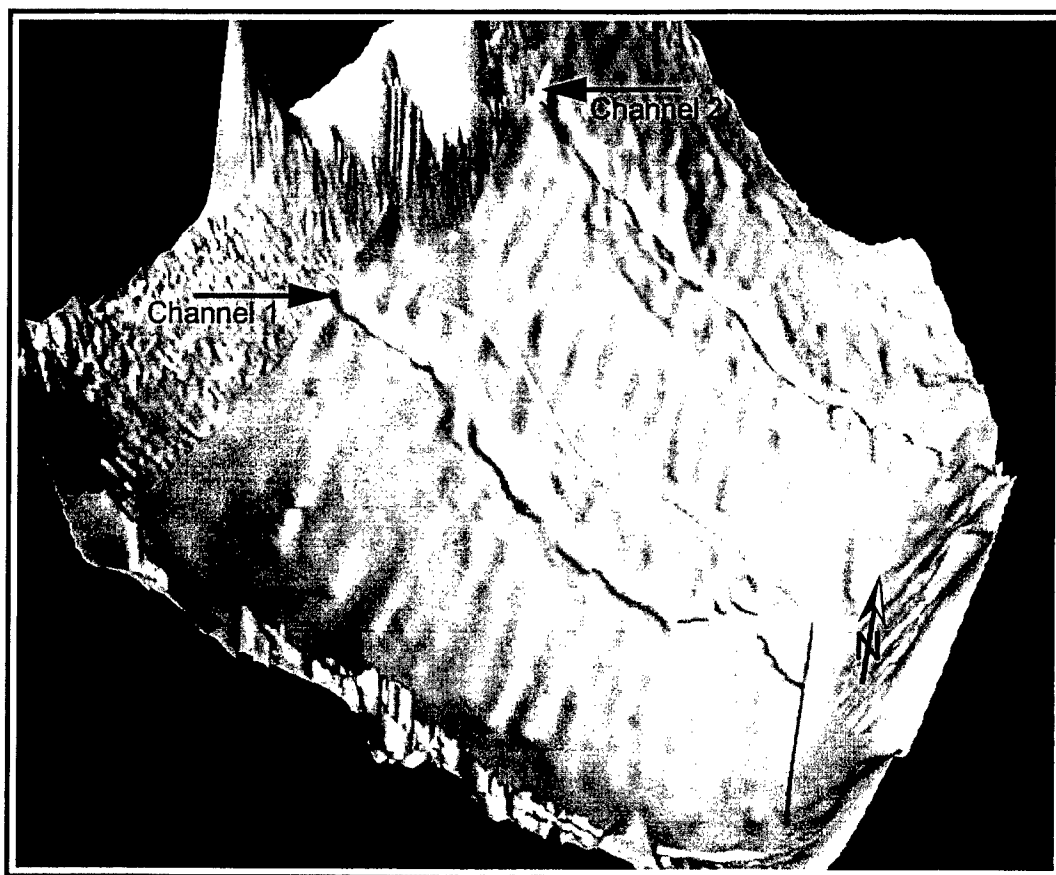
Figure 3-4: Shaded relief of channel/levee topography. This surface is presented as mapped in two-way-travel time and vertically exagerated. Surface is 30 km long from north to south and 20 km wide. Topography reflects post-depositional folding during subsequent basin development. The input points for Channels 1 and 2 are indicated with arrows. Channels traverse the basin from left to right, conveying sediment through Fisk Basin to basins further down dip.
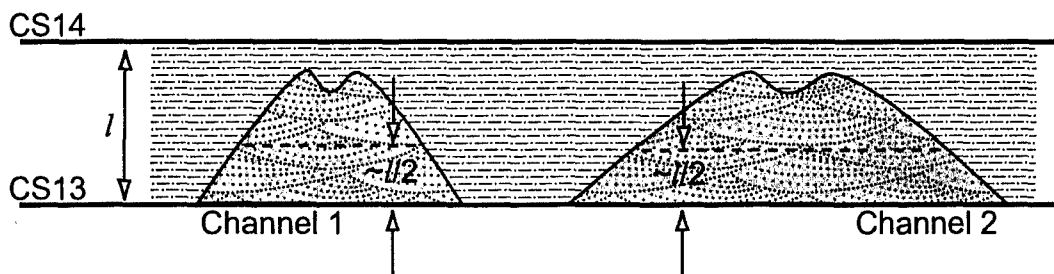
Figure 3-5: Schematic cross-section through channel/levee stratigraphy bounded by CS13 and CS14. The two channel/levee complexes (Channel 1, left, and Channel 2, right; see Figures 2-2, 2-3, 3-2, 3-3 and 3-4) are indicated in gray and the final in-filling sediment is represented by dashed/dotted fill. Because channels are regionally limited in depositional area, using mean thickness and basin-averaged sedimentation rates results in improper age dating. The entire package between CS13 and CS14 encompasses some time t. A basin averaged sedimentation rate of t/l would assign ages of $t/2$ to both channels as well as to the subsequent fill resulting in a total cumulative time of $3t/2$ which is clearly incorrect. As an alternative, I chose to date channels and fill by distributing the total time, t, between the three discreet depositional packages based upon a weighting factor. In this two-dimensional cartoon, that weighting would be based upon the area, A, of each package where $A_{Ch1} < A_{Ch2} < A_{fill}$ such that $t_{Ch1} < t_{Ch2} < t_{fill}$ and $A_{Ch1} + A_{Ch2} + A_{fill} = t$. In the three-dimensional case of Fisk Basin, I use the volume of sediment packages as the weighting factor.

128
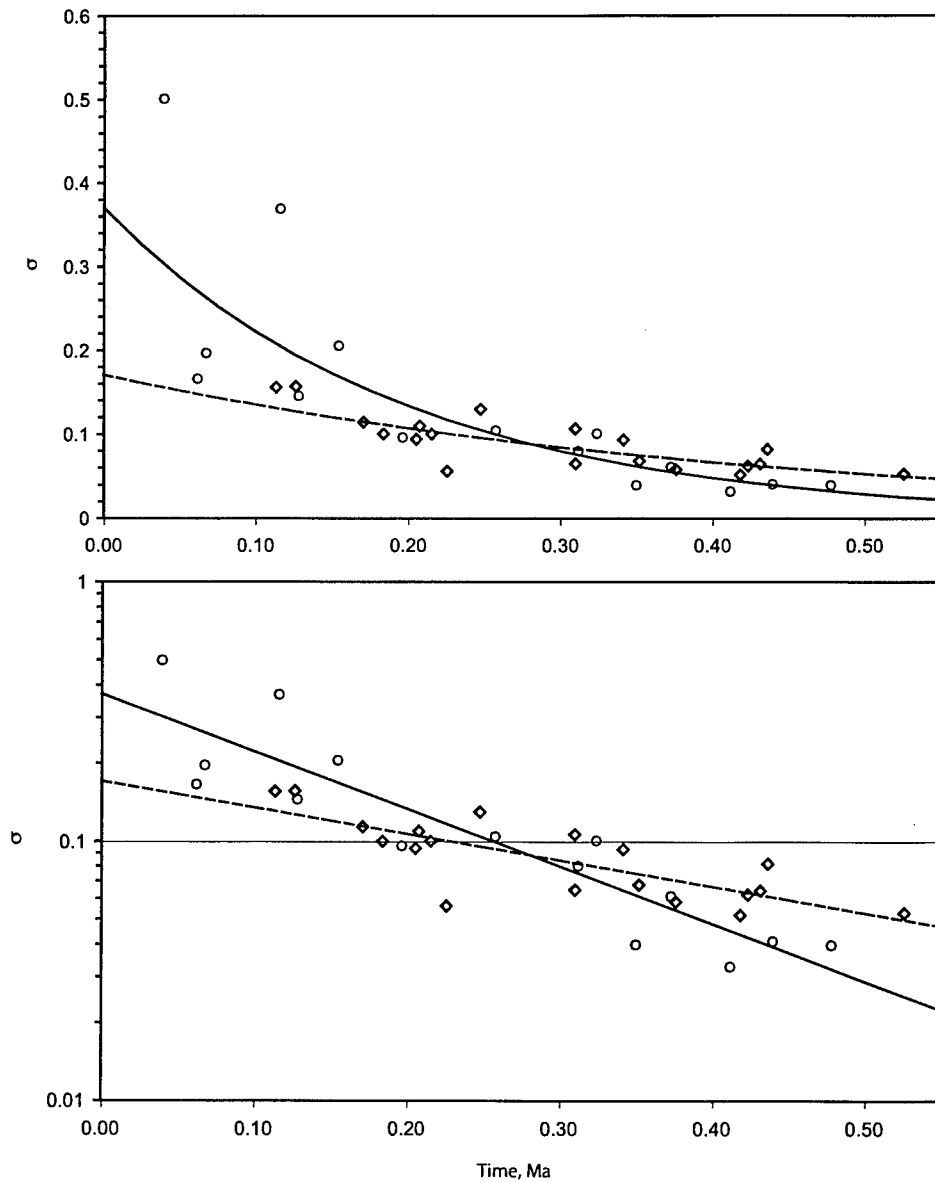
Figure 3-6: Standard deviation of sedimentation/subsidence as a function of elapsed isopach time (Tables 2.2 and 3.1). Circles represent the results from this study and diamonds are the results of sheet data from Chapter 2. Solid line is a fit to the channel/levee data and the dashed line is a fit to the sheet data. Both plots present the same data; lower plot is in semi-log space. With increased elapsed time, standard deviation decays exponentially and fits to that data can be used to constrain the characteristic e-folding time for the sedimentation/subsidence system. Channel/levee data decays more rapidly than sheet data indicating a shorter response time for the channel/levee complexes relative to the sheets. The fit to the channel/levee data is best described by the function $\sigma = 0.37013e^{-5.1008t}$ with a resulting e-folding time of 200,000 years.
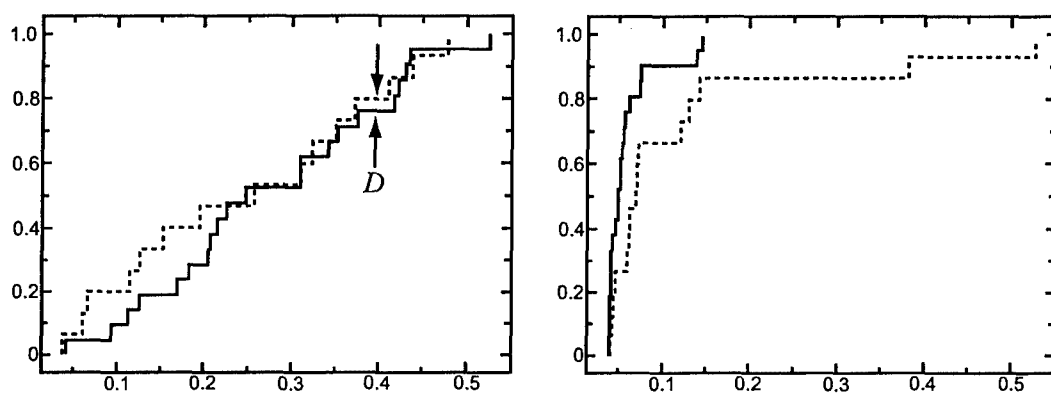
Figure 3-7: Cumulative probability distributions for temporal source data (left) and standard deviation data (right) based upon difference, D, between cumulative distributions (see Section 3.5.2). In both plots, the sheet data is indicated with a solid line and the channel/levee data by a dashed line. A Kolmogorov-Smirnov test for the goodness-of-fit returns a probability, P, of 0.788 for the temporal data and 0.017 for the standard deviation. At a confidence interval of 0.05, these P values are considered to be large for the temporal data and small for the standard deviation data (Benjamin and Cornell, 1970). Therefore, the null hypothesis of distribution similarity is accepted for the time data and rejected for the standard deviation data. We can then assume that the source data for the two environments is similar enough to eliminate sampling bias and that differences in standard deviation data are inherent to the system and not an artifact of our source data. Further, the standard deviation distributions are significantly different and contrasts in e-folding times are therefore significant.

130

Chapter 4

Addendum to methods of Chapters 2 and 3: Comparing normalized isopachs to normalized subsidence

4.1 Introduction

In Chapters 2 and 3, I compare dimensional isopachs (*i.e.* isopachs with thicknesses measured in meters) to scaled basin subsidence patterns (section 2.4.5). Five of the bounding horizons used to generate depositional isopachs are dated (Table 2.1) however the remaining six horizons in Chapter 2 and four horizons in Chapter 3 are undated. Based upon constant, interval-averaged deposition rates (Figures 2-5 and 3-1), I assign temporal intervals of deposition to each isopach, including those bounded by undated horizons. These estimated times enter into my analyses in the form of a scaling term used to dimensionalize my reference basin subsidence pattern (Section 2.4.5; Equation 2.9). Hence, the fit of the sedimentation isopach to the subsidence pattern is sensitive to the calculated isopach time.

My method of dating stratigraphic features assumes that sedimentation rate in the Fisk Basin is constant but this can not be proven. Additionally, subsidence is scaled by a second constant term (subsidence rate, R, in Equation 2.9) that also assumes

constant behavior in the form a steady basin subsidence. It would be ideal then to modify the method described in Chapters 2 and 3 in such a manner as to avoid, or at least limit, dependence upon assumptions of constant depositional and subsidence behavior.

4.2   Isopach normalization by median thickness

In assessing equilibrium times, I am essentially interested in how the *shape* of a depositional package matches the *shape* of basin subsidence. Such shapes can be generated by non-dimensionalizing both isopachs and subsidence pattern and would be independent of time. The key then is to identify an appropriate normalizing term to perform this non-dimensionalizatoin. Normalizing by maximum isopach thickness and maximum subsidence distance is incorrect; such a process results in normalized packages with upper-bound values of '1' and therefore would fail to capture a case where deposition outpaces subsidence (Figure 2-10). However, scaling isopachs by median thickness and subsidence by median subsidence distance both captures the shapes of sedimentation and subsidence and allows for the basin to be over-filled. Comparing normalized isopach shapes to a single normalized subsidence shape eliminates the potential for error introduced when subsidence is scaled by an estimated time interval.

Estimated times can not be avoided completely. It is still necessary to plot standard deviations as a function of time of isopach deposition (Figures 2-15, 2-18, 2-19 and 3-6). However, at this point in the analyses, the failure of the assumption of constant sedimentation rate would only result in an increase in the horizontal scatter of the data and a decrease in the quality of the exponential fit — that failure would not significantly change the *e*-folding results.

132

4.3 Results

To test the approach of median-scaling, I begin by limiting my analyses to five isopachs between CS7 and CS13 bounded by dated horizons. Each isopach is normalized by the respective median thickness. Median-scaled isopachs are then all compared to a standard subsidence shape generated by normalizing the total dimensional isopach between CS7 and CS13 by the median thickness of that total isopach. The resulting data is presented in Table 4.1 and plotted in Figure 4-1. This data is unassailable; no assumptions are made about rates or ages because all surfaces are dated directly through microfossil assemblages (Table 2.1). An exponential fit to this data is described by the function $\sigma = 0.1546e^{-2.1187t}$ ($R^2 = 0.921$) and results in an e-folding time of 4.7×10^5 years.

The results presented in Figure 4-1 are encouraging and suggest that median-scaling is an appropriate method for capturing and comparing isopach and subsidence shapes. In Figure 4-2, I extend this analyses beyond those isopachs bounded by dated horizons and include an additional 16 isopachs bounded by at least one undated horizon. The exponential fit to this expanded data set is described by $\sigma = 0.1468e^{-1.9924t}$ ($R^2 = 0.861$) and results in an e-folding time of 5.0×10^5 years. The fact that this time-independent method agrees well with the time-dependent method of Chapters 2 and 3 might be taken as evidence that the original assumptions of constant sedimentation rate and steady basin subsidence are reasonable.

4.4 Conclusion

The approach to calculating e-folding times in Chapters 2 and 3 assume constant sedimentation rate in the basin and steady basin subsidence. Scaling isopachs and subsidence with median values, and operating on these representative shapes, avoids issues that might arise if assumptions of constant sedimentation rate and steady basin subsidence fail. Calculations of e-folding times using five median-scaled isopachs bounded by dated horizons illustrate the validity of this approach and produce an e-

folding time of 4.7×10^5 years. Extending this method to 21 isopachs between CS7 and CS13, 16 of which are bounded by un-dated horizons, results in an e-folding time of 5.0×10^5 years which is comparable to the 4.6×10^5 years calculated in Chapter 2. The agreement between the normalized approach described here and the scaled approach used in Chapters 2 and 3 suggests that median-scaling is a reasonable approach to estimating e-folding times.

4.5 Tables

Table 4.1: Median-scaled isopach characteristics.

Standard deviations for isopachs normalized by median thickness compared to subsidence normalized by median depth (CS7 to CS13 divided by median value). **Bold** isopachs are those bounded by dated horizons (Table 2.1) and are plotted in Figure 4-1. The complete data set is plotted in Figure 4-2.

Isopach	Median-scaled Standard Deviation
CS7 to CS8	0.1164
CS7 to CS9	0.0575
CS7 to E9.5	0.0519
CS7 to CS10	0.0397
CS7 to CS11	0.0358
CS7 to CS12	0.0246
CS7 to E12.5	0.0174
CS8 to CS9	0.1007
CS8 to E9.5	0.1352
CS8 to CS10	0.0638
CS8 to CS11	0.0529
CS8 to CS12	0.0403
CS8 to E12.5	0.0301
CS8 to CS13	0.0210
CS9 to E9.5	0.1859
CS9 to CS10	0.0486
CS9 to CS11	0.0506
CS9 to CS12	0.0503
CS9 to E12.5	0.0409
CS9 to CS13	0.0244
CS12 to CS13	0.1161

4.6 Figures
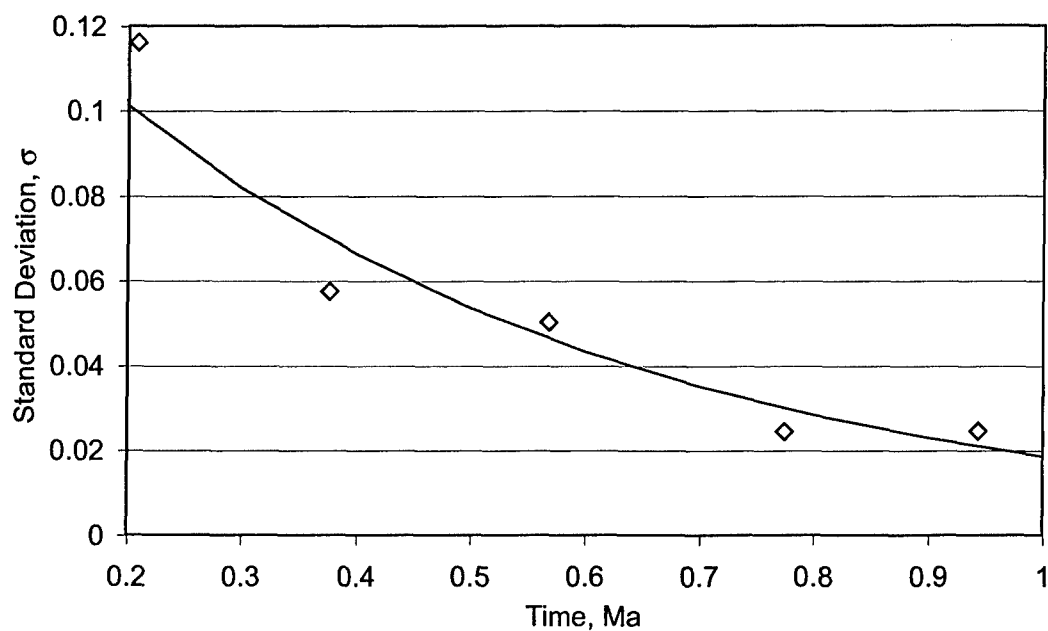
Figure 4-1: Standard deviations for median-scaled isopachs bounded by dated horizons (Table 2.1). The exponential fit to this data is described by $\sigma = 0.1546e^{-2.1187t}$ ($R^2 = 0.921$) and results in an e-folding time of 4.7×10^5 years. See Table 4.1 for data.
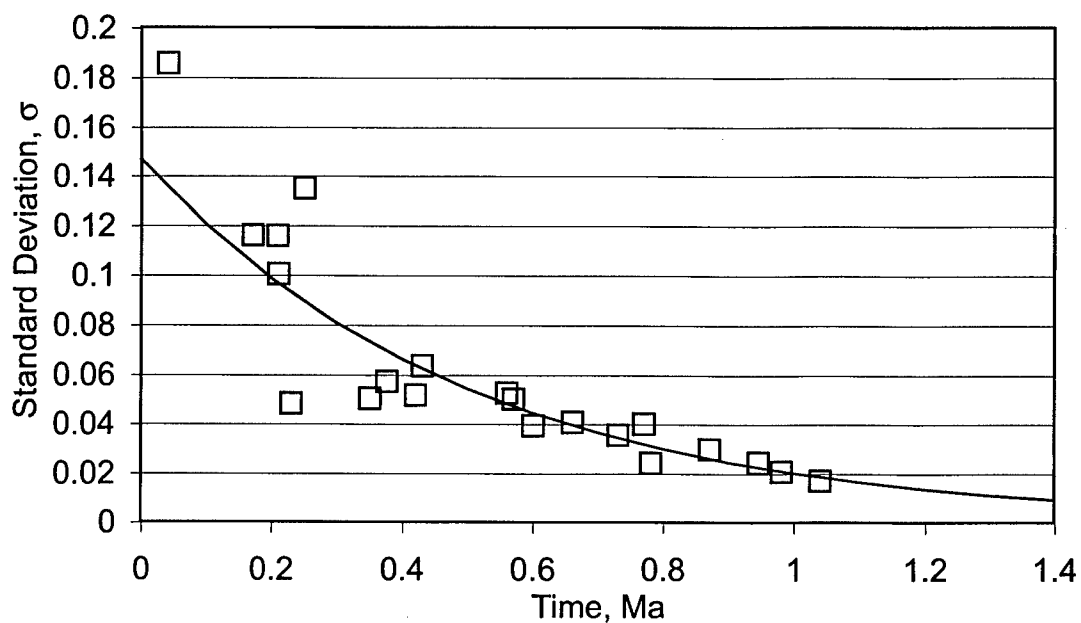
Figure 4-2: Standard deviations for median-scaled isopachs (Table 2.1). This plot includes both isopachs bounded by dated horizons (Figure 4-1) and those bounded by at least one undated horizon. The exponential fit to this data is described by $\sigma = 0.1468e^{-1.9924t}$ ($R^2 = 0.861$) and results in an e-folding time of 5.0×10^5 years. See Table 4.1 for data.

Chapter 5

Grainsize distributions and trends in channelized turbidites from the Miocene Capistrano Formation, San Clemente, CA

5.1 Introduction

Turbidity currents and debris flows are associated with major erosional and deposi-
tional features on the seafloor and dominate construction of the seascape. One of the
more common, but enigmatic, deposits associated with these submarine sediment-
gravity flows are coarse-grained, structureless (CGS) beds. Containing clasts as large
as gravel and devoid of obvious bedding or internal sedimentary structures, these
deposits provide a minimum amount of information with which to reconstruct the
dynamics associated with their transport and deposition. Unfortunately, natural
turbidity current events are difficult to directly measure, so these deposits must be
used to extract quantitative estimates of flow structure and evolution (Allen, 1973;
Pickering et al., 1989). In the case of CGS beds, it might appear initially that too
little information regarding characteristics of the sediment gravity-flows is preserved

139

in outcrop and that any inversion to reconstruct depositional conditions will be prohibitively under-constrained. This simply is not true for many cases and here I show how data collected from outcrop can be used to develop spatial and temporal snapshots of flow characteristics at the site of deposition. For CGS beds, the key to such a reconstruction is detailed analysis of vertical and lateral trends in grain size within individual beds, as well as an analysis of those trends in the context of bed geometry and relative to pre-existing topography.

Coarse-grained structureless beds, also referred to as coarse-grained massive beds (*e.g.* Walker (1975); Middleton (1993)), are poorly sorted deposits made up of particles ranging in diameter from a few tens of microns up to about one centimeter. These largest clasts are typically found distributed throughout the bed rather then being concentrated along discrete horizons and, generally, are not imbricated. By definition, CGS beds contain none of the primary sedimentary structures found in deepwater sediments such as lamination and cross-bedding and are akin to the Ta turbidite subdivision of Bouma (1962), the S3 lithofacies of Lowe (1982) and the F5 lithofacies of Mutti and Davoli (1992). The beds may contain secondary, post-depositional features such as fluid escape or de-watering structures. Grading or particle-sorting trends may not be apparent at the level of cursory, field-based observation, but such trends are commonly revealed upon detailed grain size analysis such as the work presented here.

The focus of this study is a succession of CGS beds found in the Miocene Capistrano Formation near San Clemente, CA (Figure 5-1). These deposits possess all of the characteristic attributes of CGS beds and are situated within an ancient submarine canyon system now exposed in sea cliffs (Walker, 1975; Campion et al., 2000). The Capistrano Formation is particularly well-suited for this study for three reasons. First, bounding surfaces, including bed bases and tops and larger-scale surfaces such as erosional channel scours, are well-defined (Figure 5-2). This makes it possible to accurately position samples within the bed and channel contexts that are important to my analyses. Second, the San Clemente cliffs are only weakly lithified and can be sampled by hand which greatly simplifies sample acquisition and analyses. Since drills and coring can be avoided, there are no issues of grain fracturing during sampling that

140

would compromise the results of grainsize analyses. Likewise, disaggregation of samples for measurement in the lab requires little more then light manipulation of each sample by hand. Third, the absence of substantial cementation or post-depositional diagenesis eliminates the need for detailed petrophysical analyses to distinguish depositional grain size from a modified grain size due to cementation over-growth or clay production.

To date, no one has systematically linked the characteristics of CGS beds to flow characteristics such as velocity, depth, and sediment concentration. As a result, there remains much speculation about the transport and depositional conditions that lead to CGS bed formation. There are at least three types of flows that have been proposed in association with CGS beds in deepwater environments: classic, low-density turbidity currents (Parker et al., in prep.), high-density turbidity currents (Kuenen, 1950, 1951; Lowe, 1982) and sandy debris flows (Shanmugan, 1996; Marr et al., 2001). Classic turbidity currents typically consist of less than 10% suspended sediment by volume, a significant fraction of which is commonly expected to be mud. The absence of mud in CGS deposits has prompted the promotion of the alternative explanations. Lowe (1982) proposed the existence of sandy turbidity currents with concentrations as high as 30%. At such high concentrations, it was suggested, turbulence would be damped which would, in turn, inhibit the bed remobilization necessary for the development of grading and depositional structures. Shanmugan (1996) argued that turbulence intensity in turbidity currents would always be insufficient to suspend the larger clasts found in CGS beds and appealed to sandy debris flows as the transport and depositional mechanism. Marr et al. (2001) has shown experimentally that sand-rich debris flows can indeed be sustained with low clay concentrations on the order of 0.5–5% by weight. However, these laboratory-generated flows produce deposits with a characteristic geometry not seen in beds of the Capistrano Fm. Because the mixtures of sediment and water composing these flows possess an effective yield strength, their deposits at both the experimental and field-scale (Jennette et al., 2000) are characterized by abrupt, convex-up terminations. This geometry is nowhere present in the San Clemente outcrops. With a debris-flow origin ruled out, data from the Capis-

141

trano Fm. provide an opportunity to better constrain characteristics of the turbidity currents responsible for CGS transport and deposition. My goal here is not to test each potential transport mechanism but to simply view the San Clemente deposits in light of traditional, low-density turbidity current dynamics and to assess the viability of that mechanism for CGS deposition.

My data is composed of closely spaced, digitally mapped stratigraphic horizons and sediment sample locations that enable me first to relate geometries of individual beds to the larger-scale channel forms and then to define vertical and lateral changes in grain size and sorting within the individual beds. Working with this data I show how: 1) bed geometry can be used to constrain vertical and temporal flow characteristics; 2) coarse-tail grading can be used to set bounds on current velocities and depths — information that has been particularly elusive for deepwater environments; and 3) estimates for the finest-grained component within depositing currents can be derived through analysis of sorting trends in CGS beds. I calculate that the depositing flows at the San Clemente site were moving with vertically averaged velocities of several meters per second and were on the order of a few tens of meters in thickness. These currents are capable of carrying up to very fine pebbles as suspended load. The reconstructed flow depths are one to two orders of magnitude larger than the relief on individual beds and several times greater than the local depth of confining, erosional channel forms. In other words, the stratigraphy does not seem to preserve an accurate measure for the thickness of the depositing currents. My analysis of processes associated with generation of coarse-tail grading demonstrates that the finest 25% of particles making up these beds were fully suspended at the deposition site and are present only because they were trapped within a developing framework of coarse particles. Finer particle sizes present in the depositing flows are therefore significantly underrepresented in the composition of these beds.

142

5.2 Capistrano Formation, San Clemente, CA

Field data for this study was collected from the Late Miocene (late Mohnian) Capistrano Formation at San Clemente State Beach, CA. Walker (1975) provides a comprehensive description of the stratrigraphy of the outcrops used in this study. The Capistrano Fm. is exposed in a 550 m long, 30 m high cliff that trends northwest-southeast along the coastline (Figure 5-1). Exposure of the formation is limited to about the lowermost 15 meters of these sea cliffs, which are capped with Pleistocene sandstones and gravels. The stratigraphy is composed primarily of a complex of nested, erosionally based channels, cut into mudstones of the Monterey Formation (Weser, 1971; Walker, 1975; Campion et al., 2000). Sediment filling the channel forms is siliciclastic in composition.

Weser (1971) interpreted the San Clemente outcrops in light of the deep-water fan model of Normark (1970). He proposed that these sediments were deposited at the upper or proximal portion of a fan in an embayment located south of the Los Angeles Basin. In this model, sediment was derived from a source to the northwest of the current outcrop. Walker (1975) also fit the exposures at San Clemente into the submarine fan model of Normark (Normark, 1970, 1974) arguing that the San Clemente channel system consisted of a series of laterally migrating nested channels deposited in the more distal, braided supra-fan. Walker (1975) based this determination on his interpretation of channel migration in the absence of constructional levees and on the nature of the channel fill — Walker and Mutti (1971) and Mut describe the braided-suprafan as the locus of deposition of pebbly and massive sandstones common at San Clemente. In contrast to Weser (1971) however, Walker (1975) re-interpreted paleocurrent directions to be out of the outcrop and to the northwest and southwest. While Walker limited his work to the southern-most exposures at San Clemente (see Figure 2 of Camacho et al. (2002)), Hess (1979) chose to include additional outcrop to the north-northwest and, while concurring with the interpretation of Walker (1975) of laterally migrating channels, believed those channels to have been in the more proximal inner subrafan (Normark, 1970, 1974). Clark and Pickering (1996a,b) and

143

Campion et al. (2000) concur with Walkers migrating channel model. Camacho et al. (2002), however, differ in their interpretation. They put forth the possibility that the turbidite system at San Clemente represents a single channel of at least 1 km wide cut into a low-gradient slope. In this interpretation, the erosional forms at the meter-scale interpreted in the majority of studies to be channels are taken by Camacho et al. (2002) to be local, temporary scours. The question of scale for deepwater channels is an important one. Camacho et al. (2002) raise the critical question of scale in channelized deepwater systems,

Amalgamation associated with the erosional character of the channel bases resulted in an incomplete preservation of individual channel forms. Even so, a reasonably clear picture of the characteristic channel dimensions can be determined from the stratigraphy preserved in outcrop. Lateral sections measured by Campion et al. (2000) show that all channel widths are greater than 100 m and less than 400 m. Vertical relief measured on preserved margins of individual channels is generally greater than 5 m and less than 15 m (Walker, 1975; Campion et al., 2000), but a small number of surfaces defining local channel depth exceed 15 m and the vertical extent of the rock exposure. The ratio of width to depth for individual channels in the San Clemente system therefore ranges between values of 10 and 40.

5.2.1 Bed Types

Individual beds filling channels at San Clemente can be classified as one of three types: draping, tangential or sub-horizontal (Figure 5-3). Bed type is determined by the angular relationship between the upper bed surface and the channel margin. Draping beds cover existing topography and their tops run approximately parallel to preexisting topography. The result is a sediment layer of approximately constant thickness deposited both within and outside of the channel form. Tangential and sub-horizontal beds are deposited entirely within the confinement of preexisting channels. The upper surface of a tangential bed has a concave-up shape, mimicking the topographic form of the channel edge against which it pinches out. This upper surface terminates against the edge of a channel defining small angle relative to the slope of

the margin itself. As a result, a tangential bed is generally thickest at the deepest part of the channel and thins progressively onto the channel edge. The upper surface of a sub-horizontal bed is relatively planar and nearly horizontal. The rate of thinning of sub-horizontal beds is completely determined by the slope defining the channel edge itself. A sub-horizontal bed represents the partial filling of the channel form, defining a new, relatively flat, channel base.

5.3 Methodology

In total, I collected over 400 sediment samples from fifteen beds at six different locations along the San Clemente outcrop. Data for 54 of these samples from four beds are presented here. All beds were densely sampled in vertical and lateral transects in order to capture small-scale variations in grain size (*e.g.* Figure 5-2). Each vertical transect consists of a series of samples taken one directly above the other between the bed base and bed top. Typical spacing between successive samples in a vertical transect was a decimeter or less. Each lateral transect is composed of samples collected along a line running sub-parallel to the bed base or bed top. Spacing between adjacent sample-points on a lateral transect is of the meter-scale. Sediment samples were collected from the outcrop using a hand-coring device made from a short piece of thin-walled pipe with a cap on one end. This device ensured that all particles removed from bed were captured in each sample. The location of each sample point was surveyed in using a Leica total station. This data makes it is possible to determine relative positions between all samples. In addition to sample sites, I surveyed the bases and tops of beds and other critical horizons (such as large-scale channel scours) so that grain size data could be viewed in the broader context of channel cut-and-fill (Figure 5-2).

5.3.1 Spatial framework

Figure 2 illustrates the basic layout of our sampling scheme as well as the framework terminology used throughout this chapter. Two vertical length scales are reported

145

for all samples here: Dz and dz (Table 5.1; Figure 5-2). The variable Dz describes the vertical distance separating each individual sample from the base of the bed directly beneath it. The variable dz represents the vertical distance separating any given sample from a chosen datum, the lower-most sediment sample collected from the bed. Tangential and draping beds conform to preexisting channel topography so lateral transects climb in space and have relief associated with them (Figure 5-2). Net vertical displacement, dz, between the lowermost and uppermost samples in every lateral transect exceeds one meter.

This chapter reports the grain size distribution for every individual sample. These individual measurements are connected to define vertical and lateral trends in the composition of a turbidite. A majority of the analyses below are referred to as 'sample pairs' — sets of samples from the same vertical or lateral transect. The lower-most sample in any transect (*i.e.* that sample with the smallest value for dz) is taken as the reference distribution and all other samples in that transect are compared to it. For example, in Figure 5-2, Sample A is the reference sample for Vertical Transect 1 and the sample pair is A-B. In the Upper Lateral Transect, again in Figure 5-2, Sample B has the smallest dz value and is therefore the reference for the sample pair B-D.

5.3.2 Bed Architecture and Spatial Flow Information

The key to extracting spatial flow information from outcrop is to focus our attention on those beds that have been deposited simultaneously at different vertical positions. In Figure 5-4 we present a contrived but illustrative cross-section of sediment deposited on preexisting topography. Flow can be in or out of the page. If we make the assumption that the turbidity current was much thicker than the depth of the container such that flow dynamics are not substantially affected by basal topography then we can argue that the three deposition sites, A, B and C, 'sample' different positions ($\sim z_0$, $\sim z_1$ and $\sim z_2$) within the flow. Since $C = f(z)$, sites A, B and C reflect different near-bed concentrations, C_A, C_B and C_C. In this way, it can be argued that a single bed reflects a snapshot of vertical flow conditions, assuming that

146

we can comfortably correlate A, B and C. Figure 5-5 illustrates how a single bed can reveal both temporal flow information from vertical sample transects and spatial flow information from lateral transects.

For the conditions at each of these sites to be combined into a single snapshot of flow structure, each sample must have been deposited at the same time. The temporal relationship between samples in Figure 5-4 can be established though a simple geometric argument. The base of the bed represents the earliest stage of deposition while the top of the bed represents the latest time of deposition. If the scale of the flow is larger than the basal topography, then it is reasonable to assume that deposition is laterally distributed and that there were no significant local variations in deposition rate (e.g. the flow was not depositing at A while bypassing B). This is not to say that deposition rates were the same at A, B and C. In fact, this model predicts that rates should be different at different elevations — deposition is a function of near-bed concentration. With increased elevation above the flow base, sediment concentration decreases therefore the effective near-bed concentration decreases and deposition rate decreases. The result is a reduction in bed thickness with elevation.

If the basal and upper surfaces of the bed bracket the same time interval at all points along the bed and there are no dramatic lateral variations in flow behavior, then a series points taken a fixed fraction of the distance between bed base and bed top lie on a time line. In Figure 5-4, A, B and C are positioned at the local vertical mid-point of the bed and therefore all correspond to some time, t_1. Any comparable lateral transect then should provide a similar temporal picture and multiple transects can be viewed to give an indication of temporal flow evolution. Note that, as the flow wanes, there is no reason for deposition rate to remain temporally constant so, while t_1 is positioned at the spatial midpoint of the bed, it is not necessarily at the temporal midpoint between the start and end of deposition.

Draping and tangential beds exhibit exactly the architecture necessary to satisfy the above model. In draping beds, timelines are sub-parallel to upper and lower bed bounding surfaces and therefore sample higher in the flow on the channel margins than at the channel center (Figure 5-6). Similarly, timelines in tangential beds ap-

proach the depositional surface tangentially and must also sample higher in the flow towards the point of bed pinchout (Figure 5-6). In contrast to draping and tangential beds, the simplest depositional pattern to explain sub-horizontal beds is one in which the depositional surface remains sub-horizontal over time (Figure 5-6). Therefore timelines in sub-horizontal beds are sub-horizontal and do not provide information about the vertical structure of the flow.

In any sedimentary system, the distinction between effective depositional thickness and true flow thickness is an important one and failure to consider it may lead to misinterpretation of the deposits and related flows. True flow thickness is just that, the vertical dimension from the base of the flow to the upper-most suspended sediment (Figures 5-4 and 5-6). While this is simple to define, it is not quite so simple to measure because the boundary between the flow and the ambient fluid is a complex one in which mixing of ambient fluid and the stripping off of sediment occurs constantly. However, the simplified construct of a discreet boundary is adequate for our use here.

The effective depositional thickness of a turbidity current is revealed in the relief of the turbidite deposit. Figure 5-6 illustrates the relationship between the three bed geometries seen at San Clemente and effective depositional thickness. In the case of a draping bed (Figure 5-6, left), the depositional portion of the flow must be at least as thick as the relief on the channel form. If this were not true, then it would not be possible for the flow to deposit sub-equally across the channel topography. For comparison, consider the tangential and sub-horizontal geometries (Figure 5-6, center and right). In these two cases, deposition occurs only within the channel — the depositional portion of the flow is no thicker than the erosional container. In tangential beds, the position of the bed pinchout defines the effective depositional thickness of the flow. In the sub-horizontal example, effective depositional thickness is very limited as indicated by the fact that he bed does not mantle topography at all.

The effective depositional thickness is important because it reveals one factor which can cause turbidites to be skewed indicators of turbidity current flow compo-

sition. If the sediment supply to the bed is restricted to only that material carried very near the base of the flow, then there is an entire range of sediment and grainsizes that are either under-represented or unrepresented in the deposit. Failure to consider effective thickness of turbidity currents could lead one to believe that fine-grained sediments were absent from the flows that deposited the CGS beds at San Clemente. The lack of fines may simply reflect the fact that the effective depositional thickness of the flow was only a fraction of the true flow depth and therefore the fine sediments involved in the flow and carried above the effective depositional thickness were not deposited.

Sub-Horizontal beds

If the effective thickness of a flow is very small relative to channelized container (*i.e.* limited to a few centimeters or less in thickness), then a sub-horizontal bed will result (Figure 5-6, right). Sediment is deposited from the base of the flow only and so does not mantle preexisting topography. This bed geometry should not be interpreted to represent a vertically limited flow; the bed reveals only that sediment is derived dominantly from the base of the turbidity current. It is likely that a considerable fraction of the flow consisted of sediments finer than those deposited and that this fraction was carried meters above the bed. In such depositional model, sub-horizontal beds do not have depositional relief, that is, sediment is not deposited simultaneously at different elevations — timelines in sub-horizontal beds are sub-horizontal. Therefore these beds do not reflect vertical structure of the flow and are not used in this study.

Draping beds

The draping geometry indicates that the effective thickness of the flow was large relative to the channel topography and that deposition was virtually independent of that topography (Figures 5-6, left and 5-7). In the case of draping beds, there is no indication that cross-stream depositional thicknesses vary as a function of position relative to the channel form. Effective flow thickness is at least comparable to, and

149

likely much greater than, channel relief. Timelines in draping beds are parallel to the basal and upper bed surfaces and sample at varied locations within the flow.

Tangential beds

Perhaps the most informative bed geometry at San Clemente is the tangential bed. First, vertical transects describe the temporal development of the flow and temporal fining trends lead to flow velocity and depth analyses as described above. In addition, assuming that basal and upper bed surfaces are coeval, deposition rate varies as a function of elevation as the bed laps up onto the channel margin. Such variable rates are consistent with the fact that, as we approach the channel margin and increase in elevation, we are approaching the upper limit of the effective flow thickness. The elevation-related decrease in sediment concentration is reflected in deposition rates. The vertical position of the pinchout point of the bed defines the top of the effective flow and samples taken along lateral, coeval transects sample the entire effective depositional thickness of the flow (Figure 5-6, center). Lateral transects should reflect not only the decreasing concentration profile and sedimentation rate but also reflect the extent of vertical fining within the flow.

5.3.3   Grain size analysis

The Capistrano Formation is poorly sorted and sediment ranges in size from silt to gravel. As a result of this range, no single instrument can provide an accurate quantitative measure for the entire size spectrum. Therefore, two methods were employed to obtain complete size distributions — one for the fine fraction and one for the coarse fraction. Each sample was split into its coarse and fine fractions using a wire-mesh sieve with 106 μm screen. The size distribution of the fine sediment fraction (< 106 μm) was assessed using a Horiba LA-300 laser particle size analyzer (LPSA) and the coarse fraction was measured with a Retsch Technology CAMSIZER (a digital, image-processing particle-size analyzer). The LPSA uses light scattering patterns from a diode laser to accurately measure grain sizes from 1 to 200 μm in diameter and the

CAMSIZER uses digital photographic images to accurately measure grain sizes ranging from 50 to 30,000 μm in diameter. The 106 μm cut-off was sufficiently far from the performance limitations of either instrument that I was able to avoid generating spurious results. I affirmed this by reprocessing sediment samples multiple times and confirming that the resulting grain size distribution were stable. The LPSA and CAMSIZER generate slightly different values for the same particle standard. However, this difference is small and systematic, so it was straightforward to generate the necessary calibration function. Once data were corrected using this function, the size distributions for the fine and coarse fractions were merged to construct a single size distribution for all particles in a sample.

5.4   Grain size data

We present data here from four representative beds (Figures 5-7, 5-8 and 5-9). All of these beds are deposited in erosionally based channels; one is classified as a draping bed while the other three are tangential beds (Figures 5-3 and 5-6). Table 5.1 summarizes information for the 54 samples analyzed from these four beds. This table includes: the bed type (draping or tangential); an alpha-numeric sample identifier; a qualitative description of the relative position of the sample within the bed (base, middle or top); a vertical measure of each sample position relative to the lower-most sample for each bed (dz; Figure 5-2); a vertical measure of the position of each sample relative to the local bed base (Dz); characteristic grain sizes for each sample distribution (D_5, D_{50} and D_{95}); and a sorting parameter $S_0 = \sqrt{D_{75}/D_{25}}$ (Trask, 1931).

Spatial trends in grain size associated with vertical and lateral transects can be seen by plotting the cumulative grain size distributions for all related samples in a single figure (Figures 5-10 through 5-14). While illustrative, it is difficult to pull quantitative measures of trends from these figures. Here I further quantify such trends by measuring relative change in the size of the grains defining D_5, D_{50} and D_{95} for the local particle distribution. To do this I define a 'grading ratio' (GR) for each representative size. The grading ratio, GR, is defined as:

151

$$GR = \frac{D_{n_{ref}}}{D_n} \qquad (5.1)$$

where n represents the characteristic grain size D_5, D_{50} and D_{95}, $D_{n_{ref}}$ is the reference sample for the transect and D_n refers the local sample of interest. Fining relative to the reference sample is indicated by a grading ratio greater than one and coarsening by a ratio of less than one. Grading ratio values for points on each vertical and lateral transect are presented in Table 5.2 and plotted in Figures 5-15 through 5-18.

5.4.1   Draping Bed 'Bed 100'

My example of a draping bed is located at the base of Channel 5 of Walker (1975) and is shown in Figure 5-7. Data is presented in Tables 5.1 and 5.2A and grading ratios are plotted in Figure 5-15. Because the draping bed was relatively thin I limited my sampling to a single lateral transect. Every sediment sample was collected midway between the base and top of the bed, over a horizontal distance of 10 m. Elevation difference between the lowest sample (A102) and the uppermost (A108) is 1.88 m. Sample A102 is the reference sample.

With the exception of sample pair A102-A107, this draping bed fines with increased elevation and fines at all D_n values (Figure 5-15). Sample A104, at 0.22 m above the reference sample, shows virtually no change in grainsize. However, when considering A104, A105 and A106, there is a steady decrease in grainsize as a function of increasing elevation (dz in Table 5.1). Sample A107 shows anomalous coarsening at all grainsizes. This may be due to sample contamination, the presence of an unrecognized sandy parting in the bed, or processing error from insufficient disaggragation of the sample. It is of interest to note, however, that the final sample (A108) does not follow the trend defined by the first three samples (Figure 5-15). Assuming for the moment that sample A107 is not spurious, A107 and A108 show a fining trend with a slope comparable to that seen in the first three sample pairs. A reasonable explanation for A107 and A108 may be the fact that the draping Bed 100 is actually an amalgamation of two beds. Samples A102 through A106 may be taken from a

152

lower bed while A107 and A108 lie in an overlying bed.

Bed 100 drapes topography and behaves as we might predict from what we know of the vertical structure of sediment distribution within a turbidity current — samples A102, A104, A105 and A106 are distributed vertically over 1.2 m and fine systematically at all relative grainsize fractions. This suggests that the turbulent intensity in the flow was not sufficient to suspend all sediment fractions well but rather that the flow was stratified to some extent.

5.4.2 Tangential Bed 'Bed 203'

Data for the tangential Bed 203 (Figure 5-8; in fill of Channel 4 of Walker (1975) immediately NW of path to campground) is presented in Tables 5.1, 5.2B and C and the grading ratios are plotted in Figure 5-16. Samples are distributed across an outcrop width of 7 meters and span a vertical distance of 1.22 m (Table 5.1). The tangential beds studied here are coarser than the draping bed presented above. The D_{95} values for Bed 203 samples regularly exceed 1000 μm.

Four vertical transects in this bed are composed of three sediment samples (Figure 5-8). When grading ratios are plotted for these four transects (Figure 5-16, upper left), a trend emerges. The first sample pair in this bed is a 'base sample/middle sample' comparison from the first vertical transect and the second pair is a 'base sample/top sample' comparison. The third pair is base/middle and the fourth pair base/top for the second transect. The fifth and sixth sample pairs are base/middle and base/top for the third vertical transect. Considering the grading ratios for these samples (*e.g.* $D_{50_{ref}}/D_{50}$; Figure 5-16, upper left), the values oscillate between coarsening and fining in a systematic manner: all base/middle pairs coarsen while all base/top pairs fine. Though less obvious, this trend continues to the seventh and eighth pairs derived from the fourth vertical transect. Bounding surfaces between beds can be difficult to identify in coarse-grained deposits that contain relatively little upward fining and no sedimentary structures. I believe that the 'saw tooth' behavior of the grading ratios reflects the presence of a bed bounding surface between the basal and middle samples of these four vertical transects (see dotted line in Figure 5-8). This conclusion is

153

also supported by the sorting parameter for the samples (Table 5.1). The values of S_0 are always greatest (least sorted) for the middle samples which is consistent with expected grainsize ranges in turbidite beds. Because of the potential that the vertical transects crossed a bed boundary, I present the data from Bed 203 using the middle samples as reference for the top samples (Table 5.2C; Figure 5-16, upper right). The results from the middle and upper sample comparisons are more consistent with a single continuous bed.

All vertical transects in Bed 203 fine upward (Figure 5-16, upper left). Also, fining is dominantly in the coarse end of the distribution. With the exception of the first pair, the D_5 ratio for each sample pair deviates little from a value of '1' while the ratios for the D_{95} fraction average 1.65 reflecting significant fining. The grading ratios decrease as we move laterally across the bed (compare, for example, sample pair '1' to sample pair 4 in Figure 15, upper left). The lateral transects in this bed do not show a consistent grading trend. There is 0.35 m of relief between Sample B and Sample K in the middle transect (Figure 5-16, middle right).

5.4.3 Tangential Bed 'Bed 303'

Data for the tangential Bed 303 (Figure 5-9; in Channel 3 of Walker (1975)) is presented in Tables 5.1 and 5.2D and the grading ratios are plotted in Figure 5-17. This bed is coarse with D_{95} values rarely below 1000 μm and even exceeding 1200 μm (Table 5.1). Samples are distributed across 9.5 m of outcrop. The bed is about 0.5 m thick and there is 1.46 m of relief.

Based upon grading ratios, all vertical transects of Bed 303 fine upwards (Figure 5-17, upper left) and this fining is dominantly accommodated in the D_{50} and D_{95} fractions — grading ratios for the D_{50} and D_{95} fractions are always greater than those of the D_5 fraction. Lateral transects show small changes in grainsize. Four of the eight sample pairs in the basal lateral transect show limited fining (Figure 5-17, lower left) and this grainsize trend is accommodated in the D_{50} and D_{95} fractions. The top lateral transect also shows fining in six out of eight sample pairs but here the fining is dominantly reflected in the D_{50} value (Figure 5-17, upper right). Particularly

154

in the basal lateral transect, fining that does occur is in the more distal samples with greater dz values (Table 5.1; Figure 5-9). There are only two sample pairs in the middle transect and these show virtually no change in grainsize (Figure 5-17, lower right).

Bed 303 consistently fines in the vertical transects and (Figure 5-17), in seven out of 12 cases, that fining is dominated by changes in the D_{95} fraction. Like Bed 203, Bed 303 does not show consistent grading across any of the lateral transects (Figure 5-17).

5.4.4   Tangential Bed 'Bed 304'

Bed 304 (Figure 5-9; in Channel 3 of Walker (1975)) data is presented in Tables 5.1 and 5.2E while grading ratios can be found in Figure 5-18. This is the coarsest of the beds presented here with all basal samples exceeding 1000 μm at D_{95} with a maximum of over 2.5 mm in one sample (Table 5.1). In this bed, the upper samples of the vertical transects also regularly exceed 1000 μm comprising the coarsest top lateral transect of the study. Samples from this bed are spread across 9 m of outcrop. Vertical relief on the bed is 1.28 m. Vertical spacing between samples is about 20 cm.

All vertical transects in Bed 304 fine and that fining is dominantly accommodated in the D_{95} fraction (Figure 5-18, upper left). The D_{95} grading ratios for all vertical transects are larger than grading ratios for either D_{50} or D_5. Lateral transects fine also (Figure 5-18, lower left and upper right). In both basal and top lateral transects, the first two sample pairs (A-C and A-E in the lower transect and B-D and B-F in the upper; dz = 0.00, 0.32, -0.04 and 0.30, respectively) are quite similar in grainsize but, beginning with the third sample pair in both lateral transects (dz = 0.46 and 0.68), there is a steady fining trend that increases with distance across the outcrop and with relative vertical position, dz (Table 5.1). Bed 304 shows fining in both the vertical and lateral transects and, in all of the sample pairs that fine, the trend is accommodated by the D_{95} sediment fraction.

155

5.5 Particle grading within sedimentary deposits

Grading refers most often to trends of fining-upwards or coarsening-upwards within a bed of sediment. This simplest characterization relies on a representative grainsize (*e.g.* mean or D_{50}) of the total distribution but this characteristic value provides only general information about the distribution. Missing is the critical description of exactly how the distributions at different positions in the bed differ or how they accommodate the fining or coarsening trend reflected in the representative grainsize. It is through detailed analyses of variations in cumulative distributions that we gain the information critical to constraining flow characteristics.

In describing how fining-upward and coarsening-upward grading is accommodated by changes in cumulative distributions, I attempt to identify the fraction or fractions of the distributions where variations in grainsize are focused. This information is captured in the grading ratios reported in Table reftable:grs and shown in Figures 5-15 through 5-18. For example, if I detect a fining-upward trend between samples, is the trend driven by the absence of a significant coarse component in the later sample (Figure 5-19)? Or is the decrease in representative grainsize caused by a decrease in availability across the entire grainsize distribution range in the later sample? These are clearly very different behaviors but either could result in a decrease in the mean grainsize between two samples. Middleton (1967) identified exactly these distribution variations in turbidites and suggested that different methods of fining reflect unique changes in flow dynamics.

5.5.1 Coarse-tail grading

In the first example of grading above, the fining trend results from the loss of a discreet coarse fraction of the total sediment load carried early in the flow (Figure 5-19, left). Middleton (1967) referred to this behavior as 'coarse-tail' grading and defined it as grading limited to the coarsest 5% of the distribution. Coarse-tail fining, as in our example above, indicates that a given coarse fraction of the sediment load is being preferentially removed from the total sediment load in the flow. When viewed

in terms of a temporal trend, this mode of grading can be used to identify a range of grainsizes that is effectively scrubbed from the flow over some interval of time

5.5.2 Distribution grading

In the second grading case above, fining is effected through the entire range of grainsizes in the system (Figure 5-19, right). Middleton (1967) referred to this as 'distribution grading'. In contrast to coarse-tail fining, distribution fining does not indicate a preferred range of deposited grainsizes but shows rather that the entire range of sediments are being removed from the flow sub-equally.

5.6   Estimating properties of depositing currents

Outcrop data might appear limited in dynamic information, but flow conditions such as average velocity and total flow depth can be reasonably well constrained through analyses of sediment grading trends. I constrain transport conditions here by establishing a relationship between a critical deposited grainsize in the bed and flow velocity and depth. I determine that critical grainsize by comparing grainsize distributions between samples and identifying a range of sediments that appear to be at the suspension-transport threshold. Flow reconstructions applied to San Clemente sediments are based upon approaches established originally for fluvial systems. These open-channel methods have subsequently been used to recreate conditions of channelized turbidity currents (*e.g.* REFS).

5.6.1   Shear stress and flow velocity

Turbidity current velocity can be estimated based upon a bedload/suspended load criterion for particles present in the flow or the resulting deposit (Bagnold, 1990). The entrainment of sediment into suspension can be related to interaction between a particle and the near-bed turbulent flow structure. Turbulence, in turn, can be related to flow velocity (*e.g.* Sumer and Oguz (1978); Komar (1985); Yung et al.

(1988); Garcia and Parker (1991); Garcia et al. (1996); Nino et al. (2003); Pirmez and Imran (2003)). In such models, a threshold flow velocity must be exceeded to keep a given grainsize in suspension. A failure to maintain this critical velocity results in deposition and the grainsize characteristics of the deposits reflect that critical threshold. Hence, grainsize characteristics of turbidite beds can be used to estimate gravity current velocities.

The bed shear stress, τ_b, for open channel flow can be written as (Einstein, 1950; Nelson and Smith, 1989):

$$\tau_b = \tau_{sf} + \tau_d + \tau_{ch} \tag{5.2}$$

where the boundary shear stress, τ_b, is composed of a skin friction term, τ_{sf}, describing stress at the grain scale, a form drag term, τ_d, representing drag due to bedforms such as ripples and dunes, and a term, τ_{ch}, that encompasses large-scale topographic elements in the channel such as bar forms. In the case of turbidity currents, the free surface cannot be ignored and a fourth term should also be included to account for the exchange of momentum between the current and the ambient fluid at the upper boundary. Of the shear stress components on the right side of Equation 5.2, only the skin friction term, τ_{sf}, has a direct impact on sediment transport. It is this term that describes the stress applied to grains on the bed. Further, it is the balance between this skin friction and grain characteristics, specifically settling velocity, that determines whether or not a given grainsize will be in motion and whether it will travel as suspended load or bed load within the sediment gravity flow (e.g. Bagnold (1990); Nelson and Smith (1989); Mohrig and Smith (1996); Nino et al. (2003)).

Skin friction shear stress can be written also in terms of a skin friction shear velocity, $u_{*_{sf}}$, related to τ_{sf} through the flow density (e.g. Komar (1985)):

$$\tau_{sf} = (\rho + \delta\rho) \, u_{*_{sf}}^2 \tag{5.3}$$

where ρ is the density of the ambient fluid and $\delta\rho$ is the excess density of the turbidity current. In turn, $u_{*_{sf}}$ can be related to layer-averaged flow velocity, $\langle u \rangle$, through a

coefficient of friction, C_D (Tur):

$$u_{*_{sf}}^2 = C_D \langle u \rangle^2 \qquad (5.4)$$

which is essentially a simplified momentum balance relating shear stresses to flow velocity.

It has been shown both numerically and experimentally that there is a critical value for the ratio of settling velocity, w_s, to skin friction shear velocity, $u_{*_{sf}}$, that defines the sediment suspension threshold (Bagnold, 1990; Allen, 1968; Chakrabarti and Lowe, 1981; Hand and Bartberger, 1988; Mohrig and Smith, 1996; Nino et al., 2003). Bagnold (1990) determined the suspension criteria to be $w_s/u_{*_{sf}} \leq 1$. The most recent experimental work of Nino et al. (2003) established a threshold ratio for suspension of 2.5. While Bagnold (1990) calculated critical $w_s/u_{*_{sf}}$ based upon the presence of a measurable fraction of a particular grainsize in the flow, Nino et al. (2003) defined suspension based upon very detailed observations of sediment transport and hence arrived at a relatively large suspension threshold value. Studies from natural rivers (Mohrig and Smith, 1996; Topping et al., 1999; Kleinhans) also support the existence of a $w_s/u_{*_{sf}}$ threshold and reflect behavior comparable to experimental results. Work on the North Loup River (Mohrig and Smith, 1996) showed $w_s/u_{*_{sf}}$ for suspension to range from 0.79 to 1.80 with a mean of 1.30. The work of Topping et al. (1999) on the Colorado River resulted in a suspension threshold of 0.60 while Kleinhans found a mean of 0.76 in the Waal River. The values of Topping et al. (1999); Kleinhans reflect the challenge of sampling sediment in the lowest portion of the flow in deep rivers — the coarsest grains of the suspended load travel close to the bed and failure to sample those grains will result in a reduced value of $w_s/u_{*_{sf}}$.

Settling velocity, w_s, can be calculated for a given grainsize as described by Dietrich (1982). Knowing then that the $w_s/u_{*_{sf}}$ must be less than or equal to 1 for all suspended sediment, the settling velocity of the largest suspended grainsize reveals the shear velocity of the flow. If follows also from Equation 5.4 that the layer-averaged flow velocity can be determined by

$$\langle u \rangle = \frac{u_{*sf}}{\sqrt{C_D}} \qquad (5.5)$$

All that remains is to constrain the drag coefficient, C_D. Parker et al. (1987) showed C_D to range between 0.002 in natural settings and 0.05 for experimental flumes. The drag coefficient goes as flow depth and bed roughness (*e.g.* Kuelegan (1950):

$$C_D \propto \ln \left(\frac{h}{z_0} \right)^{-1} \qquad (5.6)$$

where h is a representative current thickness and z_0 is bed roughness. Higher values of C_D on laboratory examples are consistent with the relatively shallow flows and hence small values for the ratio of representative current thickness to bed roughness. The deeper flow depth in natural currents result in a larger value for h/z_0 and a smaller C_D.

5.6.2 Flow depth

The key to estimating turbidity current flow depth is the bulk densimetric Froude Number, Fr:

$$Fr = \left(\frac{\langle u \rangle^2}{Rg \langle C \rangle H} \right)^{1/2} \qquad (5.7)$$

where R is the specific density of the sediment ($R = (\rho - \rho_w)/\rho_s$; ρ_s is the sediment density and ρ_w is the ambient fluid density), $\langle C \rangle$ is the layer-averaged volumetric sediment concentration, and H is the mean flow depth of the current. The Froude number reflects the balance between inertial forces ($\langle u \rangle$) and gravity forces ($Rg \langle C \rangle H$) acting on the flow. To solve for H, we must then constrain both the Froude number and the layer-averaged sediment concentration. Pirmez and Imran (2003) calculated Froude numbers for flows at different points in the Amazon Channel and found that Fr exceeds 1 only in areas where the flow is constrained by the deeply entrenched Amazon Canyon. Downstream of the canyon, where channels are constrained only by natural levees built through lateral flow expansion, Fr was determined to range

between 0.9 and 0.2 with a median of about 0.5 (Pirmez and Imran, 2003). Laboratory experiments on channelized currents have shown that Fr values of 0.5 or lower are a necessary condition to constrain turbidity currents as they traverse sinuous channels with multiple bends (Mohrig, pers. comm.). At Fr higher than 0.5, a significant portion of the current exits the channel at each bend.

5.6.3 Deposition and erosion

Sediment transport in turbidity currents is dominantly in the form of suspended load (Middleton, 1967). If turbulent mixing in a flow is sufficient to overcome the terminal settling velocity for a given particle size, that size will be remain in suspension (Fredsöe and Deigaard, 1994). This is not to suppose that suspended grainsizes are never deposited on the bed — there is a regular exchange of sediment between the bed and the flow — however whether or not there occurs a net flux to the bed, and hence aggradation, depends upon this balance between settling and mixing. Bed deposition or erosion is the result of the settling/mixing balance integrated across all grainsizes carried in the flow and can be written as:

$$\frac{\partial \eta}{\partial t} = \sum_{i=a}^{b} \frac{1}{\varepsilon_{bed,i}} \left[w_{s,i} \left(\varepsilon_{susp,i} - E_i \right) \right] \tag{5.8}$$

where η is the vertical position of the bed, t is time, ε_{bed} is the concentration of sediment within the bed, ε_{susp} is the concentration of suspended sediment within the flow, and E describes the entrainment of sediment from the bed. This relationship is summed for all grainsizes, i, between diameters a and b. Deposition goes as the concentration of sediment in the flow, ε_{susp}, which serves as a proxy for sediment delivery to the bed. Entrainment, E, is a local condition set by the local turbulence structure of the flow of which $u_{*_{sf}}$ is also a measure. While E is a local condition, the concentration condition, ε_{susp}, is inherited from upstream of the point of observation and reflects upstream flow conditions. Spatial or temporal changes in the flow then lead to an imbalance between inherited suspended sediment load and local shear stress with deposition or erosion as a result (Garcia and Parker, 1993).

5.6.4 Shear velocities from deposits

Just as Equation 5.8 is grainsize specific, the ratio $w_s/u_{*_{sf}}$ is a function of the grainsize-dependent settling velocity. As a result, for a local flow condition characterized by $u_{*_{sf}}$, a range of grainsize-specific values are possible for $w_s/u_{*_{sf}}$. If there is a fraction of suspended load sediment in the flow for which the $w_s/u_{*_{sf}}$ ratio is greater than 1, that fraction will be deposited to the bed. Assuming the sediment in the flow is transport-limited (*i.e.* sediment is available at all grainsizes that the flow is capable of moving), there is then a threshold grainsize deposited in the bed for which $w_s/u_{*_{sf}} \approx 1$. Provided with a means for identifying this critical grainsize, it would then be possible to estimate $u_{*_{sf}}$ from w_s, $\langle u \rangle$ from Equation 5.5 and H from Equation 5.7.

Grading, and specifically coarse-tail grading, is the key to identifying the critical grainsize that reflects $u_{*_{sf}}$. In contrast to distribution grading which reflects a collapsing flow, in coarse-tail grading the fact that sediment is being removed dominantly from the coarse end of the suspended load indicates that a significant fraction of the sediment load is being 'scrubbed' from the flow as $u_{*_{sf}}$ becomes insufficient to suspend the complete range of grainsizes. Because there is a constant exchange of sediment between flow and bed across a broad range of grainsizes, the critical grainsize is not readily apparent in a single sample but becomes obvious when comparing temporally discreet grainsize distributions. To determine $u_{*_{sf}}$ from beds at San Clemente, I select a threshold grain abundance that defines the presence of a significant amount of a grainsize in a sample (Figure 5-19). In coarse-tail grading, the grainsize corresponding to the threshold abundance decreases between samples. Considering this threshold abundance from a slightly different perspective, if the threshold abundance corresponds to some grainsize, $g.s._1$, in an initial sediment sample and a smaller $g.s._2$ in a latter sample, then $g.s._1$ has effectively disappeared from the bed in the second sample (Figure 5-19). Since I assume transport-limited deposition in the San Clemente beds, the fact that a particular grainsize becomes scarce in a bed over time can only be due to the inability of the flow to suspend and transport that grainsize at

the sample location. Therefore, with respect to the threshold grainsize, the flow has evolved from a state where $w_s/u_{*_{sf}} < 1$ to one in which $w_s/u_{*_{sf}} > 1$. That threshold grainsize is a reasonable approximation of the case in which $u_{*_{sf}}$ is equal to the easily calculated settling velocity, w_s, for the threshold grain.

5.7 CGS transport conditions

5.7.1 Flow velocity and depth

Fining in vertical transects of the tangential beds studied here is dominantly accommodated by the D_{95} fraction and is rarely accommodated in the fine D_5 fraction. This does not strictly fit the definition of Middleton (1967) of coarse-tail grading (*i.e.* grading accommodated solely at or above D_{95}) but it does show that the fining trends in these beds are accommodated more in the coarse fraction than in any other. I therefore treat vertical grading in the tangential beds as being of the coarse-tail variety.

To estimate $u_{*_{sf}}$, I employ the original Bagnold (1990) suspension criterion of $u_{*_{sf}} = w_s$. While a range of values for $w_s/u_{*_{sf}}$ have been found in experimental (Nino et al., 2003) and natural (Mohrig and Smith, 1996; Topping et al., 1999; Kleinhans) systems, these values cluster around 1. For w_s, I set a threshold abundance of D_{95} and apply the method of Dietrich (1982) to the grainsize in the reference sample that corresponds to that abundance. I calculate $\langle u \rangle$ by plugging $u_{*_{sf}}$ into Equation 5.5 and take the lower-bound value of C_D (0.002) shown by Parker et al. (1987) to be appropriate for natural systems. Flow depth, H, is calculated from Equation 5.7. Since the San Clemente sediments are dominantly quartz, I assume a sediment density of 2.65g/cm^3. I use two values for concentration by volume, $\langle C \rangle$: 1% and 10%. The experimental results of van Kessel and Kranenburg (1996) show that 10% concentration is the upper limit at which a flow can remain turbulent. Pirmez and Imran (2003) and Mohrig (pers. comm.) have shown the Froude number, Fr, of turbidity currents to be less than 1 and often less than 0.5. For my flow depth

163

calculations, I use the relatively large value of $Fr = 1$. A Froude number of '1', in conjunction with the relatively high concentration of 10% provides a measure of the lower-bound of potential flow depth. Changes to either constant will only result in larger estimates of H.

Estimated flow velocities for the tangential beds range between 2.5 m/s and 7.5 m/s (Figure 5-20). From these velocities, I find that the total flow depth can vary by an order of magnitude depending upon flow concentration. Flow depth for these beds is measured in tens of meters at a concentration of 10% and on the order of 100 m if I apply a 1% concentration. While these are estimates, the importance of these values is seen when compared to channel and bed relief. At the lower-bound, flows were comparable in thickness to channel scour depth (Walker, 1975) and potentially an order of magnitude or more thicker depending upon concentration and Froude number. More importantly, flows were at least an order of magnitude thicker than bed relief — my proxy for effective depositional thickness. This contrast in vertical dimensions between flows and beds strongly supports the premise that effective depositional thickness for these beds was a fraction of true flow thickness and resulted in deposits that poorly represent the true flow composition.

5.7.2 Suspended sediment

My method of calculating grading ratios reveals another interesting facet of these distributions: there is a surprisingly constant fine tail in all distributions regardless of vertical or lateral position in the bed. This ubiquitous portion of the sediment load can be seen qualitatively by comparing cumulative distributions for vertical and lateral transects of the tangential beds (Figures 5-11 through 5-14). These distribution curves are virtually indistinguishable for a significant portion of the fine end of the grainsize spectrum. This similarity is confirmed in the fact that the D_5 grading ratios for the majority of sample pairs hover around a value of '1' — there is little variability in grainsize at the finer end of the distributions (Table 5.2; Figures 5-16 through 5-18). The universal nature of the fine tail requires an explanation. My first goal is to quantitatively identify the grainsize range of this common fraction. My second is to

explain the fine tail in terms of depositional mechanics — we would like to know if this fraction is a function of sediment settling or of some other mechanism.

Identifying the fine-tail

The presence of the fine tail is best illustrated by plotting the grainsize D_n as a function of the grainsize $D_{n,ref}$ where n is a closely spaced series of 'finer-than' values and $D_{n,ref}$ is the reference or basal sample for a given transect (Figures 5-21 through 5-24). We calculate the correlative grainsize for each sample distribution where n is equal to 5, 7.5, 10, 12.5, 15, 17.5 20, 22,5, and 25. We then plot the grainsize for each D_n value of both the reference sample and the comparative samples as functions of $D_{n,ref}$ grainsize (Figures 5-21 through 5-24). The result is a reference line defined by $D_{n,ref} = f(D_{n,ref})$ and comparative lines of $D_n = f(D_{n,ref})$ for each sample. The reference and comparative functions will be sub-parallel for those grainsizes in the fine tail and then the slope of $D_n = f(D_{n,ref})$ will decrease relative to $D_{n,ref} = f(D_{n,ref})$ and the curves will depart where sample distributions differ. The range of grainsizes where reference and comparative functions are sub-parallel defines the ubiquitous fine tail.

The graphical presentations in Figures 5-21 through 5-24 are a qualitative approach useful for illustrating the fine fraction that relies on a subjective determination of where each comparative sample departs significantly from the reference sample. To better quantify this behavior, I chose a departure criterion between the reference and comparative curves and applied that criterion to all cases to identify the fine tail threshold. To define that criterion, I calculate the difference, $\Delta g.s.$, between $D_{n,ref} = f(D_{n,ref})$ and $D_n = f(D_{n,ref})$ at 100 μm and then define the fine tail as that range of grainsizes for which $\Delta g.s. < 2 \times \Delta g.s._{100\mu m}$. This criterion corresponds reasonably well with the break in slope of $D_n = f(D_{n,ref})$ in Figures 5-21 through 5-24.

The results of this method of identifying the fine tail threshold are presented in Table 5.3. I find that the fine-tail threshold ranges in size from between 106 and 240 μm with an average of 165 μm. In terms of D_n, this corresponds to D_{25} or, in other

words, the fine tail composes about 25% of each sample.

Transport conditions for the fine-tail

Above (Section 5.6), I described how we can estimate u_* values based upon a Rouse analyses of the scrubbed sediment fractions. Using that same u_*, we can again employ the Rouse parameter to estimate the transport conditions for the ubiquitous fine tail. Rather than assume an Ro value as above, in this case I calculate Ro for the fine-tail sediments using the relevant w_s at the fine-tail threshold (again from Dietrich (1982)). The settling velocities at the fine tail threshold are reported in Table 5.3 as are the Rouse parameters and the u_* values taken from D_{95} of the basal or reference samples for each the vertical profile. Average Rouse parameter for these tangential beds is 0.228 indicating that these fine tails are very well suspended within the flow (Table 5.3).

Trapping

If the fine tail is well-suspended, then entrainment, E, in Equation 5.8 is much larger than sedimentation indicating that the contribution of fine sediments to the bed from simple settling dynamics should be very small. With Rouse parameters on the order of 0.2, fine sediments should be very poorly represented in the deposits yet my data confirms that these finer sediments make up a significant fraction, about 25%, of the sediment in the tangential beds.

I suggest that the fine tail of the cumulative grainsize distributions is present due to trapping of these grains during the rapid sedimentation of the coarser material. Middleton (1967) observed that, in highly depositional flows, it was difficult to identify a well-defined bed/flow interface. If the near-bed portion of the flow is well-mixed and deposition rates of the coarse sediments are high (as suggested by the structureless nature of the deposits), then it is reasonable to expect that some fraction of the fine material will be trapped in the bed. This is significant because trapping is an inefficient process and suggests that the fine sediments are under-represented in the bed relative to their true concentration in the flow.

166

This trapping model is testable. We can reasonably estimate the amount of fine material that might be trapped in a coarse bed by determining porosities for the fine and coarse sediment fractions and then 'filling' the void space in the coarse fraction with a fine fraction of appropriate porosity. Porosity behavior is dominated by sorting, mean grain size, water content, and packing (Beard and Weyl, 1973). To properly estimate a trapped fraction, I must calculate porosities for both coarse and fine fractions and to do this I must constrain sorting, S_0, and D_{50} for fine and coarse fractions of a given sediment distribution. Rather than perform these calculations for every sample, I constructed an average representative sediment sample (Figure 5-25). From the fine tail thresholds reported in Table 5.3, I partitioned each comparative sample into coarse and fine sub-distributions, calculated 'average' coarse and fine fractions, and determined fraction-specific D_{50} and S_0 of the fine and coarse average distributions. The fine tail threshold for this average representative sample is at 144 μm. The fine tail has a D_{50} of 93 μm and an S_0 of 1.49. The coarse fraction has a D_{50} of 316 μm and an S_0 of 1.39.

Beard and Weyl (1973) report porosities for dry, loose mixtures and wet, packed mixtures. The characteristic values for S_0 and D_{50} for each fraction result in a coarse fraction with a dry/loose porosity of 44% and a wet/packed porosity of 39%. Fine fraction porosities are estimated at 48% dry/loose and 36% wet/packed (Table 1 of Beard and Weyl (1973)). While neither dry/loose nor wet/packed conditions apply to the marine setting, deepwater sediments are not compacted until subsequent burial that occurs well after the trapping mechanism of interest here. At the time of deposition when trapping would occur, sediments are not packed and so I use dry/loose values to estimate a trapped sediment fraction. Using the dry/loose values of 44% coarse fraction porosity and 48% fine fraction porosity results in a fine tail that makes up 23% of the overall sediment sample ($0.44 \times (1 - 0.48) = 0.23$) — a value strikingly close to the true fine-tail fraction of 25% reported above.

5.8 Conclusions

Coarse-grained structureless (CGS) beds are one of the most prevalent of deepwater facies and yet the dynamics of the flows responsible for their deposition are not well constrained. There are two features of these deposits that make them particularly difficult to decipher. First, by definition, there are no sedimentary structures in the bed from which to extract flow information. Second, relative to other deepwater deposits, CGS beds are strikingly depleted in fine-grained sediments. These two facts have led others to appeal to unique depositional mechanisms such as high-concentration turbidity currents (Lowe, 1982) and sandy debris flows (Shanmugan, 1996; Marr et al., 2001) to account for the presence of CGS beds. Here, I view CGS deposits in the context of traditional, low-concentration turbidity currents and assess whether or not these flows could be reasonably associated with non-unique depositional mechanics.

One of the main reasons for misinterpretation of CGS beds is the fact that two of the most fundamental aspects of these sediments, those of detailed grainsize range and grainsize distribution, have been ignored. Based upon such detailed analyes, I conclude the transport conditions associated with CGS deposition are consistent with low-concentration turbidity currents. There is no reason to appeal to unique transport or depositional mechanisms.

Using vertical sample transects across beds to constrain temporal changes and lateral transects to constrain vertical spatial changes in the flow, it is possible to estimate the transport conditions of the associated flows. I find that, over time as indicated in vertical sample transects, these beds fine through the mechanism of coarse-tail grading. This indicates that a definable fraction of the sediment load is being scrubbed from the flow. Assuming no changes in sediment availability between the base and the top of the bed, the scrubbed fraction acts as an indicator of the critical transport condition and hence can be used to estimate shear velocity, layer-averaged flow velocity and flow depth. Low-concentration turbidity currents associated with the CGS beds studied here have layer-averaged velocities of between 2.5 and 7.5 m/s.

168

Flow depths would be on the order of 10 m for a flow consisting of 10% sediment by volume and 100 m for a flow of 1%. These velocities and flow depths are reasonable for low-concentration currents.

Lateral transects provide a measure of the vertical characteristics of the flow. Specifically, these transects indicate the effective depositional height and the extent of mixing of the flow. In turbidity currents, sediment in the bed is not necessarily derived from the entire flow but can be deposited from some fraction of the total flow depth. The total vertical range over which sediment is deposited reflects the effective depositional thickness. In the case where a bed completely drapes channel scour topography, effective depositional flow depth is at least comparable to the relief on that topography (Figure 5-6). If the bed is limited to deposition within a channel scour, tangentially pinching out onto the channel margin, then the vertical position of the pinchout defines effective depositional flow depth. Both cases are present in the San Clemente deposits and indicate effective depositional flow depths measured in meters.

In cases where lateral transects follow coeval horizons and mimic topography, those transects effectively sample the vertical state of the flow at a particular time (Figure 5-4). Therefore, the mode of grading found when comparing a vertically positioned lower sample to an upper sample reflects the stratification of the flow. I find that some lateral transects fine as sample position above the bed base increases suggesting a stratified flow while others have no discernable grading trend indicative of well-mixed, highly turbulent flows.

Flow depths on the order of 10 to 100 meters and velocities in the range of meters per second are consistent with low-density turbidity currents. Direct measurements of turbidity current flow depth and velocity are limited primarily to studies in reservoirs (*e.g.* Fan (1986); Chikita (1989, 1990); Fan and Morris (1992)), lakes (Lambert et al., 1976; Gilbert and Shaw, 1981; Smith et al., 1982; Weirich, 1986; Lambert and Giovanoli, 1988; Normark, 1989) and fjords (Hay et al., 1982; Hay, 1987a,b; Prior et al., 1987; Zeng et al., 1991; Phillips and Smith, 1992). Flow concentrations in these environments were less than 10% while flow depths were on the order of meters

to the low tens of meters. Flow velocities were on the order of meters per second. The observations are consistent with the flow reconstructions from San Clemente based upon grainsize analyese.

The fact that CGS beds are particularly coarse is simply a function of depositional mechanics and does not fully reflect the total composition of the flow. Fine-grained sediments are generally absent from the deposit for two reasons. First, the effective depositional thickness of the flows depositing CGS beds at San Clemente are one to two orders of magnitude smaller than true flow depth; the majority of the vertical extent of the flow is simply not represented in the bed. This effect would be particularly dramatic in the case of vertically stratified flows as suggested by some of the lateral transects presented above. Second, Rouse parameters for fine sediments found in the deposits are on the order of 0.2 indicating that these grainsizes are very well suspended and so are not generally deposited by settling dynamics even when carried close to the bed. Further, the fact that fine sediments are present and make up approximately 25% of the sediment deposited is not a function of simple settling dynamics. This fraction corresponds quite well with the volume of fine material that would be present if it were simply trapped in the pore space of the coarser material during rapid deposition.

I conclude that it is unnecessary to appeal to special depositional mechanisms to explain the presence of CGS beds. The fact that the beds are surprisingly coarse should not be interpreted to represent coarse transport mechanisms. The depositional process is biased in favor of the coarser material in the flow. The absence of fine sediment in the deposit does not indicate that the flow composition was limited to a coarse grainsize range but rather reflects an inherent bias in the mechanism of sediment deposition. There does not appear to be any reason that the CGS beds in the Capistrano Formation at San Clemente can not be explained by traditional low-concentration turbidity currents.

170

5.9 Tables

Table 5.1: Selected grainsize characteristics of samples presented in this study.

Column 1 indicates the type of bed from which a set of samples was collected. Column 2 is an identifier for each sample while Column 3 describes the position of the sample relative to the top and bottom of the bed. Column 4 records the vertical position of each sample relative to the lower-most sample for the bed (Figure 5-2). Column 5 provides the position of each sample above the local bed base (*i.e.* the base of the bed immediately below the transect; Figure 5-2). The draping bed was on the order of 10 to 20 cm thick and samples were positioned at the vertical midpoint so a nominal value of 10 cm has been assigned. The lower-most sample in every bed is assigned a dz value of 0. Columns 5 through 7 list sample characteristics: grainsize, in microns, of the D_5, D_{50} and D_{95} fractions of the sample respectively. All fractions are 'finer than' indicators so D_5 is the cut-off value of the grainsize distribution for which 5% of the sample is finer than. Column 8 is a sorting parameter defined by Trask (1931) as $S_0 = \sqrt{D_{75}/D_{25}}$. The values for D_{75} and D_{25} are not reported here. All z values are in centimeters and all grainsize values are in microns.

Bed Type	ID	Position	dz	Dz	D_5 μm	D_{50} μm	D_{95} μm	S_0
Drape	A102	Middle	0	0.10	4	24	94	1.89
	A104	Middle	0.21	0.10	4	24	91	1.98
	A105	Middle	0.65	0.10	3	20	73	1.86
	A106	Middle	1.20	0.10	2	16	41	1.59
	A107	Middle		0.10	6	44	354	2.45
	A108	Middle	1.88	0.10	4	25	74	1.76
Tangential	203A	Base	0	0.03	45	245	748	1.63
	203B	Middle	0.39	0.42	44	362	991	1.82

Continued on Next Page

Bed Type	ID	Position	dz	Dz	D_5 μm	D_{50} μm	D_{95} μm	S_0
	203C	Top	0.76	0.79	32	182	485	1.40
	203D	Base	0.09	0.03	36	240	727	1.64
	203E	Middle	0.62	0.56	46	372	967	1.78
	203F	Top	0.98	0.92	48	206	536	1.42
	203G	Base	0.39	0.03	49	271	852	1.68
	203H	Middle	0.80	0.45	61	424	1090	1.72
	203I	Top	1.08	0.72	60	241	645	1.50
	203J	Base	0.42	0.03	62	335	1351	1.75
	203K	Middle	0.73	0.34	57	350	1001	1.78
	203L	Top	1.10	0.71	51	274	831	1.63
	203M	Base	0.68	0.03	53	290	867	1.66
	203N	Top	1.22	0.57	50	193	528	1.42
Tangential	303A	Base	0	0.50	52	419	1237	1.93
	303B	Middle	0.17	0.67	49	282	712	1.55
	303C	Top	0.35	0.85	49	224	555	1.45
	303D	Base	0.05	0.13	66	413	1021	1.75
	303E	Middle	0.21	0.29	49	241	597	1.48
	303F	Top	0.34	0.32	42	205	644	1.48
	303G	Base	0.14	0.07	61	480	1401	1.91
	303H	Middle	0.26	0.19	49	279	695	1.52
	303I	Top	0.38	0.31	49	224	480	1.44
	303J	Base	0.36	0.07	60	463	1253	1.92
	303K	Top	0.58	0.29	45	185	481	1.45
	303L	Base	0.57	0.02	45	409	1311	2.03
	303M	Top	0.78	0.23	73	270	663	1.49
	303N	Base	0.75	0.07	44	365	1057	1.97

Bed Type	ID	Position	dz	Dz	D_5 μm	D_{50} μm	D_{95} μm	S_0
	303O	Top	0.96	0.28	49	182	1015	1.51
	303P	Base	0.96	0.00	58	364	944	1.82
	303Q	Top	1.08	0.12	56	201	778	1.53
	303R	Base	1.19	0.00	46	313	886	1.82
	303S	Top	1.34	0.15	48	184	711	1.48
	303T	Base	1.46	0.05	60	429	1062	1.66
	303U	Top	1.53	0.12	65	299	917	1.67
Tangential	304A	Base	0	0.02	75	496	2339	1.98
	304B	Top	0.18	0.20	69	455	1699	1.88
	304C	Base	0.00	0.07	60	461	2524	2.06
	304D	Top	0.14	0.21	73	456	1623	1.87
	304E	Base	0.32	0.03	66	485	2251	2.08
	304F	Top	0.48	0.19	73	471	1714	1.89
	304G	Base	0.46	0.03	78	480	1616	1.84
	304H	Top	0.68	0.25	65	384	1010	1.65
	304I	Base	0.74	0.03	65	438	1490	1.83
	304J	Top	0.95	0.24	56	337	854	1.58
	304K	Base	1.07	0.03	72	385	1201	1.71
	304L	Top	1.31	0.27	68	320	805	1.56
	304M	Base	1.28	0.03	66	390	1210	1.74
	304N	Top	1.38	0.13	71	309	753	1.54

Table 5.2: Grading Ratios.

Middleton (1967) defined coarse tail grading as fining between sediment samples that takes place dominantly in the coarsest 5% of the grainsize distributions when compared between samples. As a method to characterize this behavior, I calculate discreet ratios between a reference sediment sample and a comparison sample for D_{95}, D_{50} and D_5. In all cases, I take the lower-most sample in a bed as the reference. In the ratio, the reference sample is the numerator and the comparison sample the denominator so that a ratio greater than one indicates that the comparison sample is finer than the reference and a ratio less than one indicates that the comparison sample is coarse. If the D_{95} ratio is greater than the D_{50} and D_5 ratios, then I consider the trend to be coarse-tail fining. If the ratios of D_{95}, D_{50} and D_5 are comparable, then the fining, if it exists, is considered to be distribution fining.

A. Grading ratios for the draping Bed 100 (Figure 5-7). Samples are arranged in a lateral transect and positioned at the vertical midpoint of the bed. With the exception of the A102-A106 comparison, there is fining along the transect but not dramatic fining. These grading ratios are shown graphically in Figure 5-15.

Sample Pair	A102-A104	A102-A105	A102-A106	A102-A107	A102-A108
D_{95}	1.03	1.28	2.27	0.26	1.27
D_{50}	1.03	1.19	1.55	0.56	0.99
D_5	1.02	1.45	1.64	0.67	1.13

Continued on Next Page

B. Grading ratios for the tangential Bed 203 (Figure 5-8). The first nine sample pairs (203A-203B through 203M-203N) are vertical transects. In each case, the reference sample is the lower-most sample of the transect. See Figure 5-8 for the map of sample locations. Sample pairs A-D, A-G, A-J and A-M comprise a lateral transect following the bed base, sample pairs B-E, B-H and B-K are a lateral transect along the middle of the bed, and the final four pairs are a lateral transect along the bed top. These grading ratios are shown graphically in Figure 5-16.

Sample Pair	203A-203B	203A-203C		203D-203E	203D-203F
D_{95}	0.76	1.54		0.75	1.36
D_{50}	0.67	1.35		0.64	1.16
D_5	1.02	1.40		0.78	0.76
Sample Pair	203G-203H	203G-203I		203J-203K	203J-203L
D_{95}	0.78	1.32		1.35	1.63
D_{50}	0.64	1.13		0.96	1.22
D_5	0.80	0.81		1.09	1.21
Sample Pair	203M-203N				
D_{95}	1.64				
D_{50}	1.50				
D_5	1.05				
Sample Pair	203A-203D	203A-203G	203A-203J	203A-203M	
D_{95}	1.03	0.88	0.55	0.86	
D_{50}	1.02	0.90	0.73	0.84	
D_5	1.25	0.93	0.73	0.85	

Continued on Next Page

Sample Pair	203B-203E	203B-203H	203B-203K		
D_{95}	1.02	0.91	0.99		
D_{50}	0.97	0.86	1.82		
D_5	0.95	0.73	0.78		
Sample Pair	203C-203F	203C-203I	203C-203L	203C-203N	
D_{95}	0.90	0.75	0.58	0.92	
D_{50}	0.88	0.75	0.66	0.94	
D_5	0.68	0.54	0.63	0.64	

C. Recalculation of grading ratios for vertical transects of Bed 203 (Table 5.2B above) using the middle sample as reference to the upper sample (as opposed to using the lower-most samples as shown). These grading ratios are presented graphically in Figure 5-16.

Sample Pair	203B-203C	203E-203F	203H-203I	203K-203L	
D_{95}	2.04	1.80	1.69	1.21	
D_{50}	1.20	1.80	1.76	1.28	
D_5	1.36	0.97	1.01	1.11	

D. Grading ratios for the tangential Bed 303 (Figure 5-9). The first 12 sample pairs (303A-303B through 303T-303U) are vertical transects. In each case, the reference sample is the lower-most sample of the transect. See Figure 5-9 for a map of sample locations. Sample pairs A-D, A-G, A-J, A-L, A-N, A-P, A-R and A-T comprise a lateral transect following the bed base, sample pairs B-E and B-H are a lateral transect along the middle of the bed, and the final eight pairs are a lateral transect along the bed top. These grading ratios are shown graphically in Figure 5-17.

Sample Pair	303A-303B	303A-303C		303D-303E	303D-303F

Continued on Next Page

176

D_{95}	2.21	2.23		1.71	1.59
D_{50}	1.49	1.87		1.71	2.02
D_5	1.07	1.06		1.34	1.56
Sample Pair	303G-303H	303G-303I		303J-303K	
D_{95}	2.01	2.92		2.60	
D_{50}	1.72	2.14		2.50	
D_5	1.24	1.24		1.35	
Sample Pair	303L-303M		303N-303O		303P-303Q
D_{95}	1.98		1.04		1.21
D_{50}	1.52		2.01		1.81
D_5	0.62		0.89		1.05
Sample Pair	303R-303S		303T-303U		
D_{95}	1.25		1.16		
D_{50}	1.70		1.44		
D_5	0.96		0.92		
Sample Pair	303A 303D	303A 303G	303A 303J	303A 303L	303A 303N
D_{95}	1.21	0.88	0.99	0.94	1.17
D_{50}	1.01	0.87	0.90	1.02	1.15
D_5	0.79	0.86	0.87	1.17	1.19
Sample Pair	303A-303P	303A-303R	303A-303T	303B-303E	303B-303H
D_{95}	1.31	1.74	1.16	1.19	1.02
D_{50}	1.15	1.34	0.98	1.17	1.01
D_5	0.90	1.13	0.87	1.00	1.00

Sample Pair	303C-303F	303C-303I	303C-303K	303C-303M	303C-303O
D_{95}	0.86	1.16	1.15	0.84	0.55
D_{50}	1.10	1.00	1.21	0.83	1.23
D_5	1.16	1.00	1.11	0.68	1.00
Sample Pairs	303C 303Q	303C 303S	303C 303U		
D_{95}	0.71	0.78	0.60		
D_{50}	1.23	1.22	0.75		
D_5	0.88	1.02	0.76		

E. Grading ratios for the tangential Bed 304 (Figure 5-9). The first seven sample pairs (304A-304B through 304M-304N) are vertical transects. In each case, the reference sample is the lower-most sample of the transect. See Figure 5-9 for a map of sample locations. Sample pairs A-C, A-E, A-G, A-I, A-K and A-M comprise a lateral transect following the bed base and the final six pairs are a lateral transect along the bed top. These grading ratios are shown graphically in Figure 5-18.

Sample Pair	304A-303B	303C-303D	304E-304F	304G-303H	304I-304J
D_{95}	1.38	1.56	1.31	1.60	1.74
D_{50}	1.09	1.01	1.03	1.25	1.30
D_5	1.09	0.82	0.89	1.19	1.16
Sample Pair	304K-303L	303M-303N			
D_{95}	1.49	1.61			
D_{50}	1.20	1.26			
D_5	1.07	0.94			

Sample Pair	304A-304C	304A-304E	304A-304G		
D_{95}	0.93	1.04	1.45		
D_{50}	1.08	1.02	1.03		
D_5	1.25	1.14	0.96		
Sample Pair	304A 303I	304A 304K	304A 304M		
D_{95}	1.57	1.95	1.93		
D_{50}	1.13	1.29	1.27		
D_5	1.16	1.03	1.13		
Sample Pair	304B-304D	304B-304F	304B-304H		
D_{95}	1.05	0.99	1.68		
D_{50}	1.00	0.97	1.18		
D_5	0.95	0.94	1.05		
Sample Pair	304B-304J	304B-304L	304B-304N		
D_{95}	1.99	2.11	2.26		
D_{50}	1.35	1.42	1.47		
D_5	1.24	1.02	0.97		

Table 5.3: Fine-tail designation and related Rouse Number for vertical sample transects.

The fine-tail threshold is determined as described in Section 5.7.2 above. Shear velocity, u_*, is calculated based upon D_{95} for the basal sediment sample of each basal sample (Table 5.1). The Rouse Number, Ro, for the fine-tail threshold value is reported here. The critical Rouse Number of 2.5 is reached when $w_s \sim u_*$ ($w_s/u_* = 1$). Rouse numbers for the fine fractions are an order of magnitude smaller than the critical Ro suggesting that the fine-tail of the grainsize distributions at San Clemente are extremely well suspended and do not occur in the bed due to simple settling.

† indicates cases where the Upper Sample was coarser than the Reference Sample in the fine fraction and therefore I did not apply the our method of fine-tail identification.

Reference Sample	Upper Sample	Fine-tail Threshold Grain-size, μm	n of D_n	w_s, fine-tail threshold, m/s	u_* (also w_s for D_{95} of reference sample)	Ro
203B	203C	170	45	0.0174	0.154	0.283
203E	203F	127	18	0.0111	0.112	0.246
203H	203I	130	15	0.0115	0.168	0.171
203K	203L	170	25	0.0174	0.155	0.280
203M	203N	150	30	0.0144	0.135	0.267
	Bed Mean	**149**	**27**			**0.249**
303A	303B	†				
303A	303C	130	18	0.0115	0.189	0.152

Continued on Next Page

Reference Sample	Upper Sample	Fine-tail Threshold Grain-size, μm	n of D_n	w_s, fine-tail threshold, m/s	u_* (also w_s for D_{95} of reference sample)	Ro
303D	303E	182	33	0.0193	0.158	0.305
303D	303F	195	47	0.0213	0.158	0.337
303G	303H	130	14	0.0115	0.211	0.136
303G	303I	150	25	0.0144	0.211	0.170
303J	303K	160	40	0.0158	0.191	0.207
303L	303M	†				
303N	303O	114	18	0.0093	0.163	0.142
303P	303Q	114	15	0.0093	0.146	0.158
303R	303S	112	17	0.0090	0.134	0.168
303T	303U	106	10	0.0082	0.164	0.125
	Bed Mean	**139**	**24**			**0.190**
304A	304B	240	26	0.0287	0.318	0.226
304C	304D	†				
304E	304F	†				
304G	304H	220	25	0.0254	0.238	0.267
304I	304J	185	22	0.0197	0.223	0.222
304K	304L	185	23	0.0197	0.184	0.270
304M	304N	†				
	Bed Mean	**208**	**24**			**0.246**

Continued on Next Page

Reference Sample	Upper Sample	Fine-tail Threshold Grain-size, μm	n of D_n	w_s, fine-tail threshold, m/s	u_* (also w_s for D_{95} of reference sample)	Ro
	Combined Mean	165	25			0.228

5.10 Figures
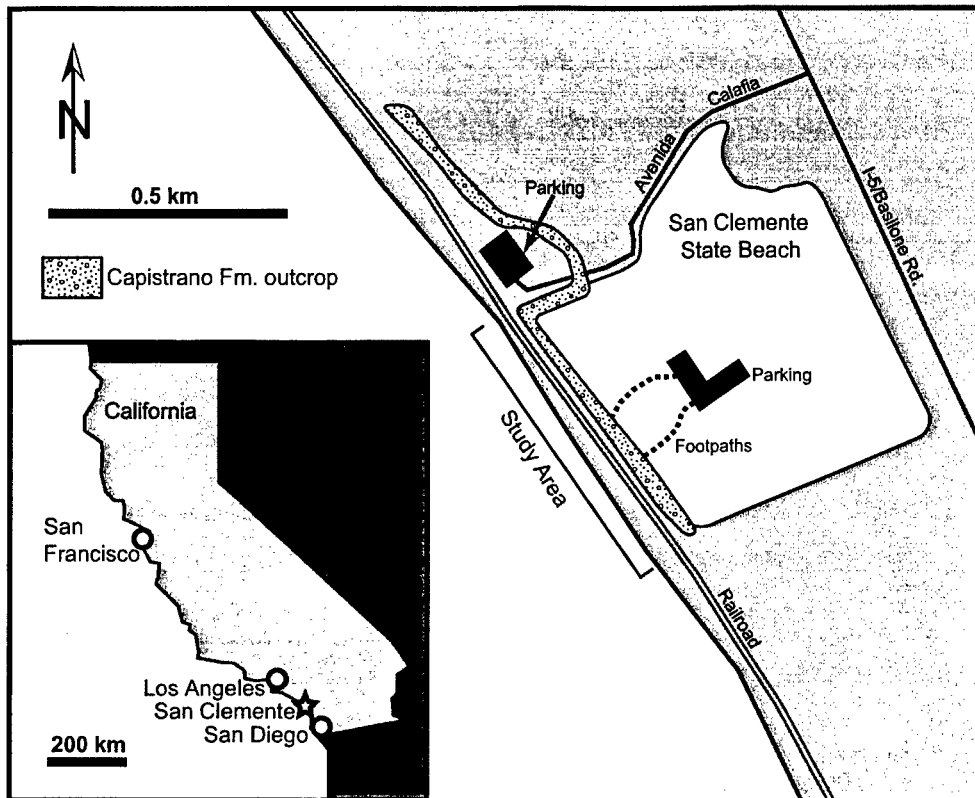
Figure 5-1: San Clemente study area. Sea cliff exposures of the Capistrano Formation are located at the San Clemente State Beach in southern California (inset). Data presented in this study were collected from the region of outcrop described by Walker (1975). After Campion et al. (2000).
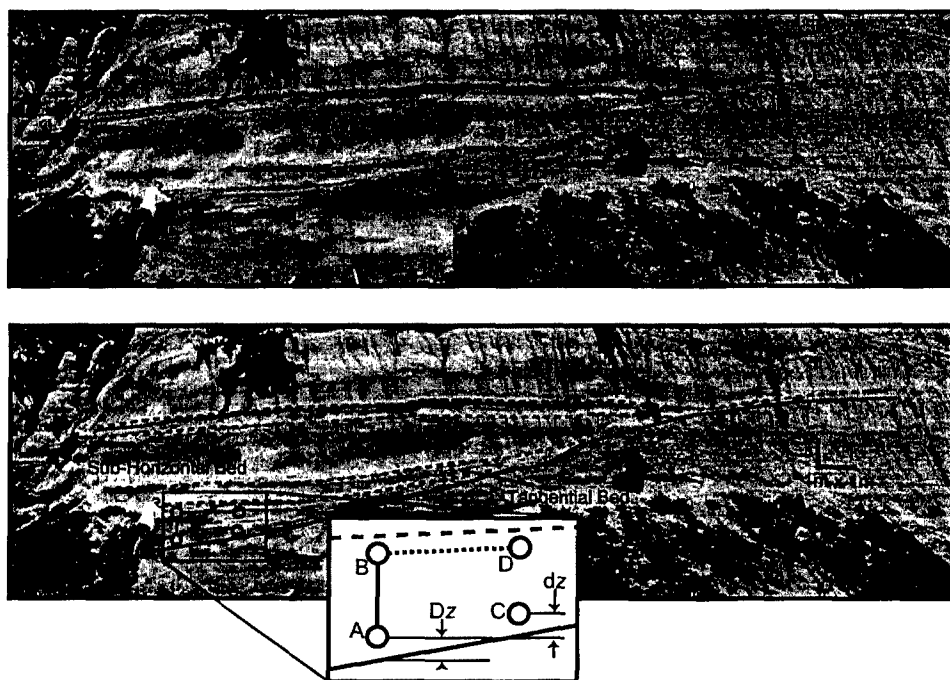
Figure 5-2: Examples of San Clemente bed types, transect orientations and pertinent dimensions. Uninterpreted (top) and interpreted (bottom) images of typical San Clemente outcrop. Two of the three bed types are indicated above. Hypothetical sample locations are indicated by circles in the lower-most bed. Inset illustrates a vertical transect (*e.g.* solid line tying Samples A and B), a lateral transect (*e.g.* dotted line tying Samples B and D), sample position relative to bed boundary, Dz, and elevation difference between successive samples, dz. The dimensions Dz and dz are not limited to basal samples or lateral comparisons and are reported for every sample. In this illustration, Sample A would serve as the reference location for vertical transect sample pair A-B as well as for a lateral transect A-C. Sample B would be the reference sample for lateral transect B-D.

184
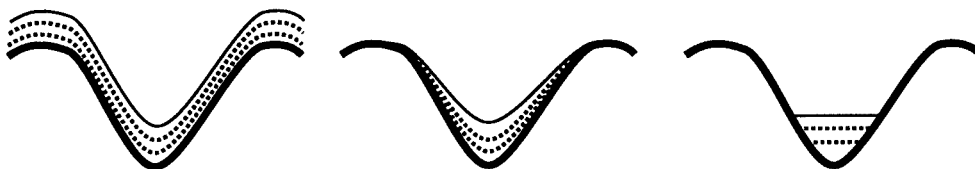
Figure 5-3: Coarse-grained massive beds are deposited in one of three geometries: draping (left), tagential (middle) andn sub-horizontal (right). In each schematic above, the preexisting erosional or depositional surface is represented by the lower, heavy line, the top of each bed is represented by the thin, upper-most line, and theoretical horizons of equal time are represented by dotted lines. In each bed architecture, sampling along interpreted timelines may provide coeval information about flow conditions. This is particularly useful for the draping and tangential deposits where timelines 'climb' relative to the lower-most portion of the flow and may record information regarding the vertical distribution of particle sizes within a depositing flow.
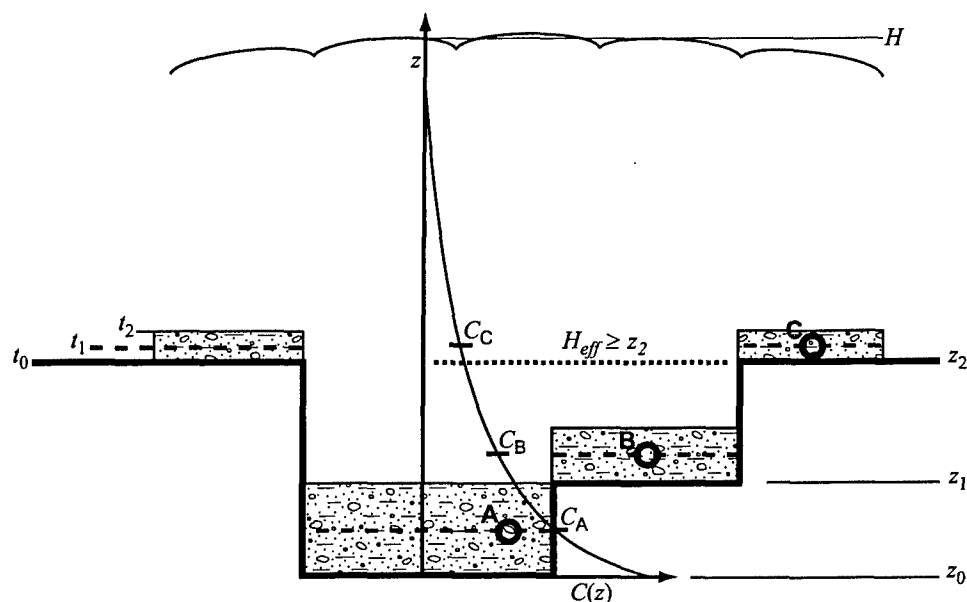
Figure 5-4: Example of how data from a single turbidite can be used to estimate the vertical structure of the depositing current through time. Beginning at t_0 and ending at time t_2, a turbidite is deposited on existing topography (heavy line). Total flow depth of the current is H. Deposition occurs initially at a bed elevations z_0, z_1 and z_2. Deposition rates and grainsize distributions on the three 'tiers' (z_0, z_1 and z_2) reflect the relative vertical decrease of flow concentration in both total sediment load as well as on a per grainsize basis. At time t_1, samples A, B and C reflect flow compositions C_A, C_B and C_C. If H is significantly larger than z_2, then the preexisting topography will have little effect on flow conditions and deposition is locally constant. This allows us to reasonably correlate samples A, B and C and use the sediment characteristics from those three samples as indicators of coeval flow conditions.
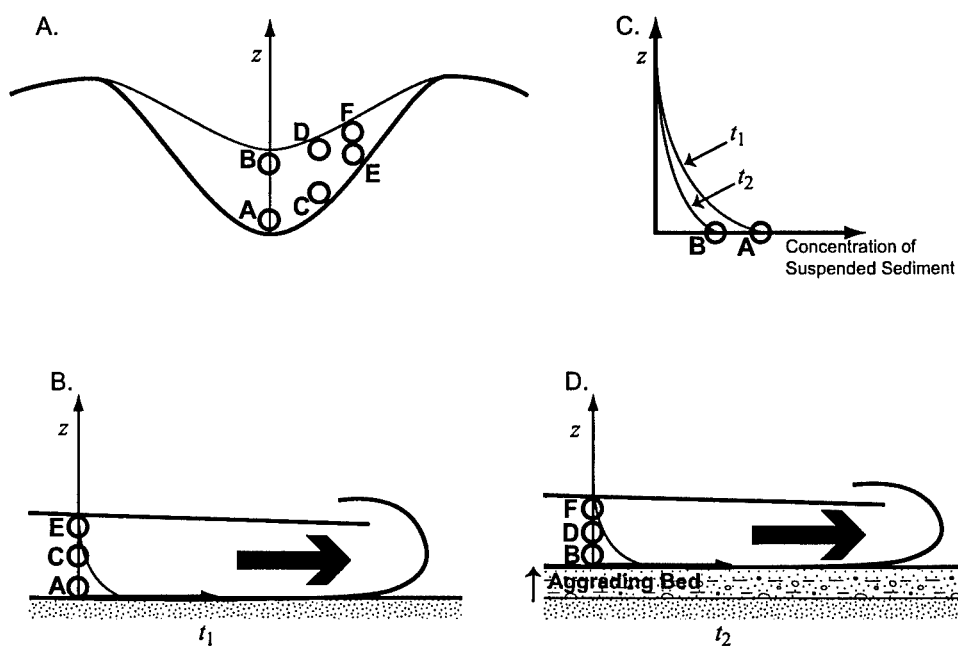
Figure 5-5: Proposed utility of beds that drap topography for reconstructing spatial and temporal character of depositing currents. In Figure A, bed cross-section with two lateral transects (ACE & BDF) representing deposition at two discrete times, t_1 and t_2. As illustrated in schematic turbidite in Figure B (flow from left to right), each data point in a lateral transect reflects flow condition at a different vertical position. Combining two or more lateral transects (Figures C and D) then reflects the temporal evolution of the turbidity current.
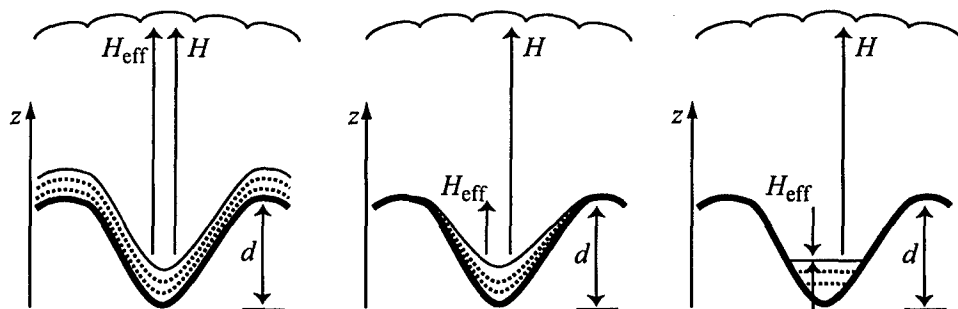
Figure 5-6: Effective depositional thickness versus true flow thickness. The effective depositional thickness of a turbidity current, H_{eff}, is the upper-most point in the flow from which sediment is deposited. The true thickness of the flow, H, is the total thickness of suspended material and may be much greater then or comporable to H_{eff}. The relative values of H_{eff} and channel relief, d, set the bed architecture. In the case of draping beds (left), H_{eff} is much greater than d and so depositional thickness of the bed is independent of vertical position. The relative magnitudes of H and H_{eff} may be comparable or H may be greater than H_{eff}. Draping beds may prove to be a reasonable representation of flow composition. In tangential beds (center), H_{eff} and d are of comparable scale and so deposition rate decreases with distance above the base of the flow. In this case, H is larger than H_{eff} and a percentage of the flow is not represented in the bed — the remainder of the flow is advected down stream without deposition. Sub-horizontal beds (right) result when H_{eff} is very small relative to d. The sediment source for the bed is limited to the very base of the flow. Total flow depth, H, is much larger than H_{eff} and it is quite likely that the majority of the flow is advected down stream without deposition. In this case, H_{eff} is a very poor representation of flow composition as a whole.

Figure 5-7: Photograph of Bed 100 — draping bed. This fine-grained deposit drapes preexisting channel topography. Sample locations are indicated by circles and labeled with alpha-numeric identifiers. See Table 5.1 for sample characteristics.
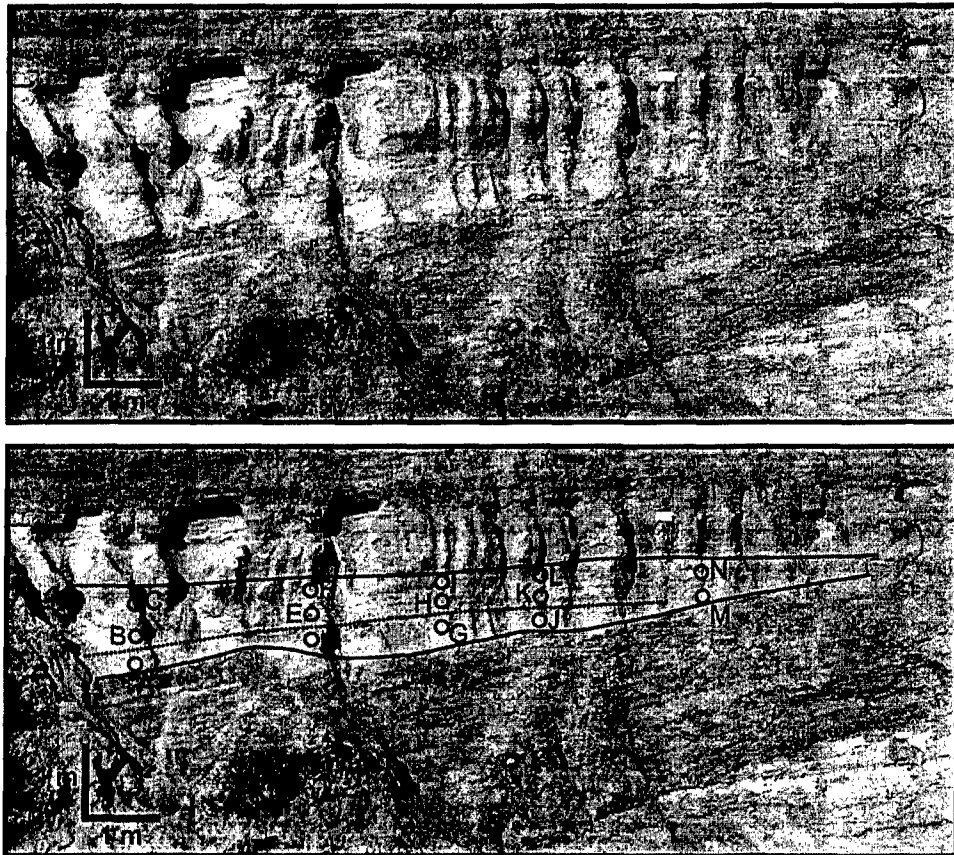
Figure 5-8: Interpreted and uninterpreted photographs of Bed 203 — tangential bed. Circles indicate sample locations and are labeled with alphabetic identifiers. Surfaces defining the base and top of the bed as mapped are marked by solid lines. Grainsize analyses suggest the presence of an internal discontinuity as indicated by dotted line. See Table 5.1 for sample characteristics.
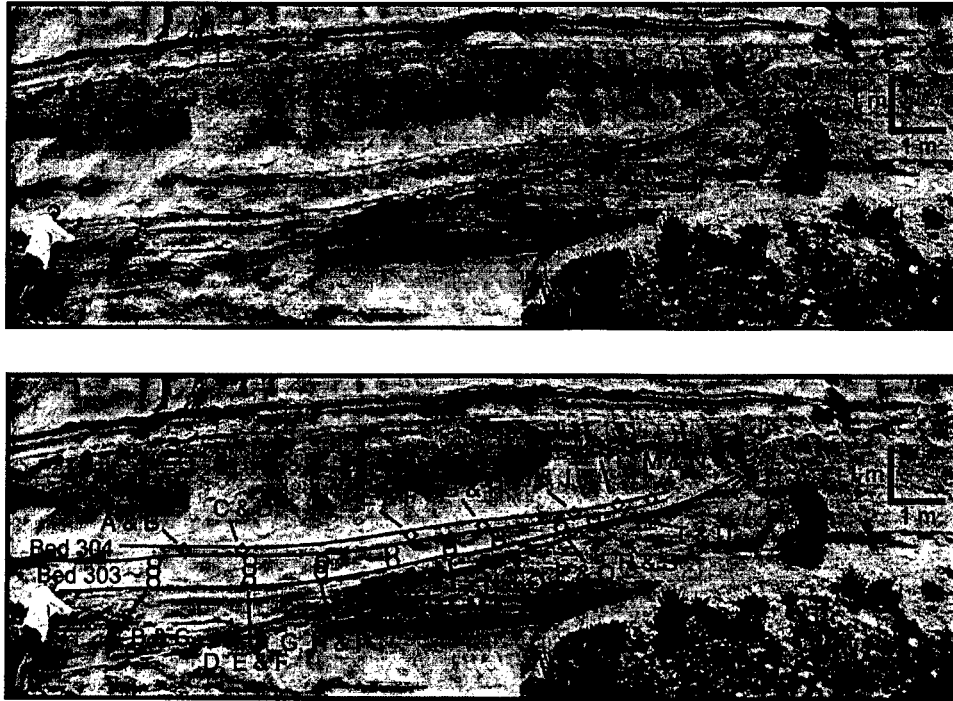
Figure 5-9: Interpreted and uninterpreted photographs of Beds 303 and 304 — tangential beds. Bed boundaries are shown with solid lines and the larger-scale scour into which these beds are deposited is indicated by the dashed line. Sample locations in Bed 303 are indicated with circles and labeled with appropriate alphabetic identifiers. Where bed thins, verticle samples are indicated with a single circle (*e.g.* P & Q) and lower sample is listed first. Bed 304 sample locations are indicated with diamonds and labeled similarly. See Table 5.1 for sample characteristics.
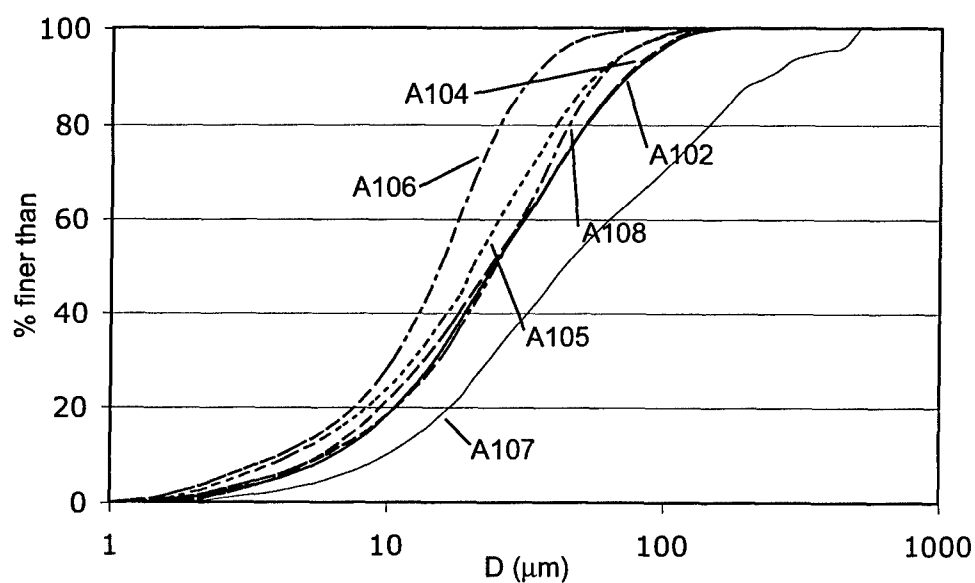
Figure 5-10: Cumulative grainsize distributions from samples collected in Bed 100 (Figure 7). Samples are labeled. There is a fining upward trend between samples A102, A104 and A106. Sample A107 is substantially coarser than the basal Sample A102. See Table 5.1 for sample characteristics.
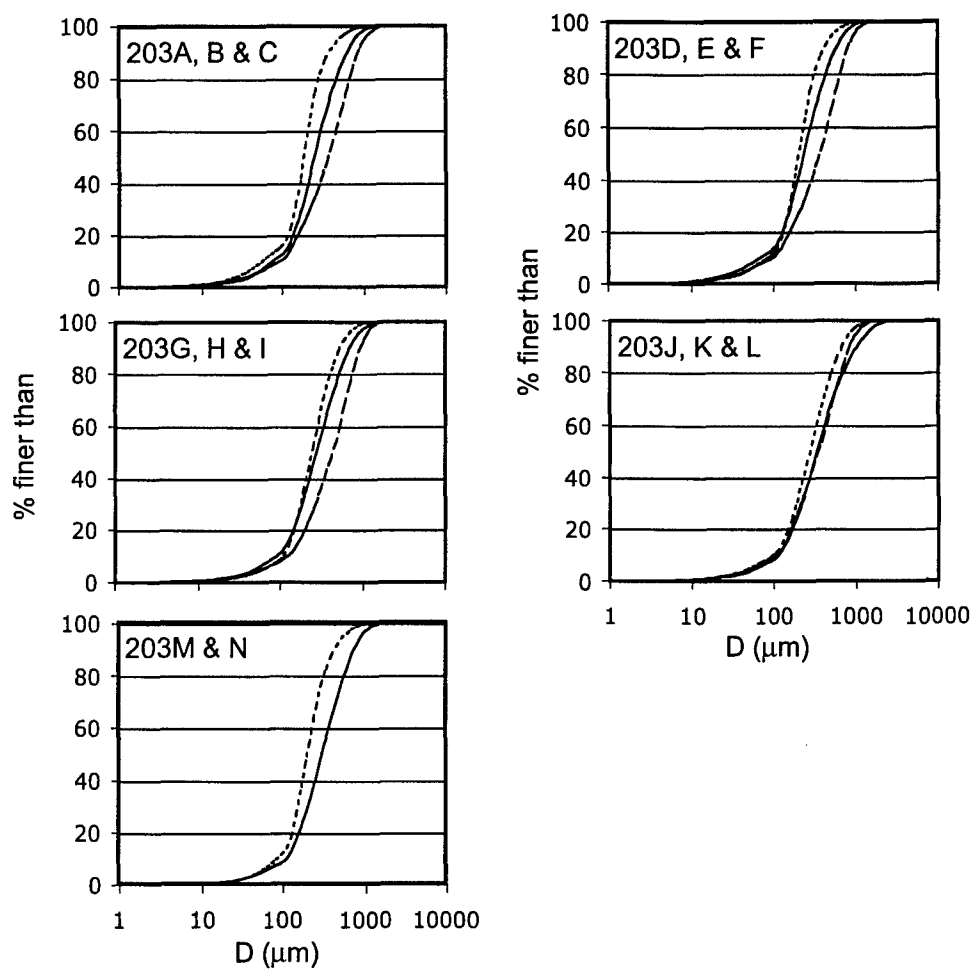
Figure 5-11: Cumulative grainsize distributions for Bed 203 (Figure 8). Samples are grouped by vertical transect. Plots are labeled with appropriate sample names. In all transects, the basal sample is indicated with a solid line and the upper sample is indicated with a dotted line. Middle samples, if present, are indicated with a dashed line. See Table 5.1 for sample characteristics.
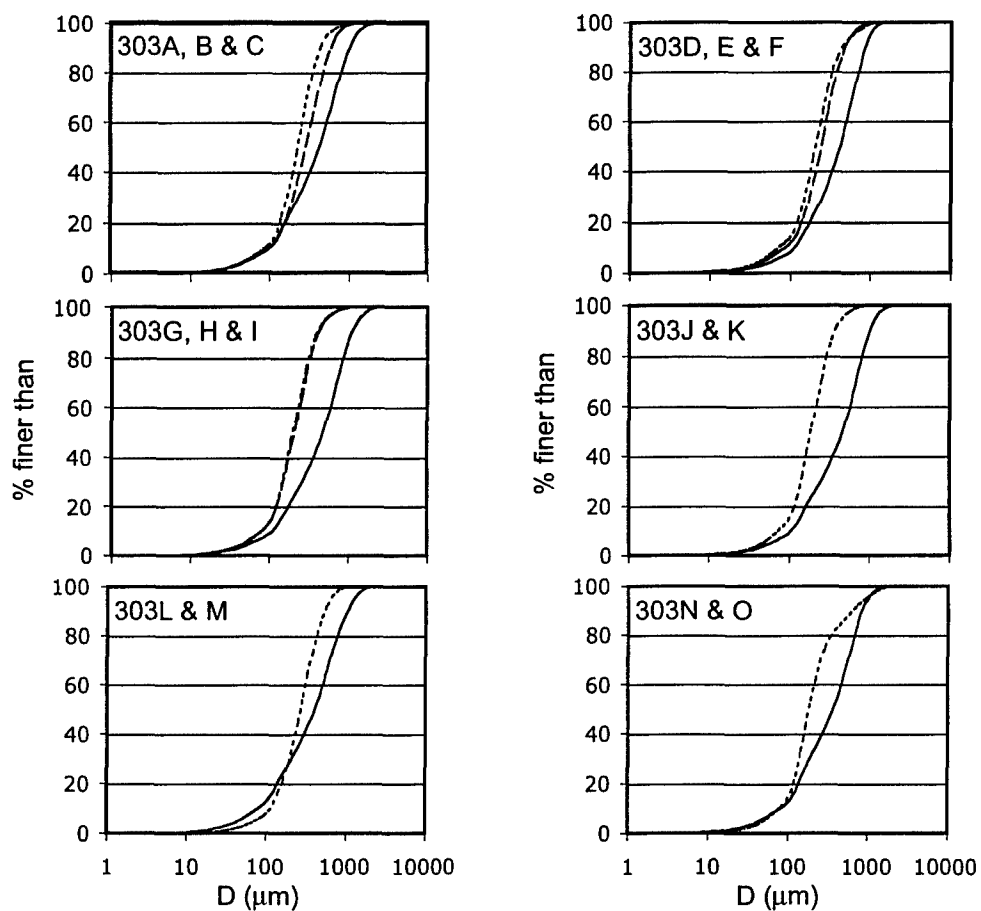
Figure 5-12: Cumulative grainsize distributions for Bed 303 (Figure 9). Samples are grouped by vertical transect. Plots are labeled with appropriate sample names. In all transects, the basal sample is indicated with a solid line and the upper sample is indicated with a dotted line. Middle samples, if present, are indicated with a dashed line. See Table 5.1 for sample characteristics.
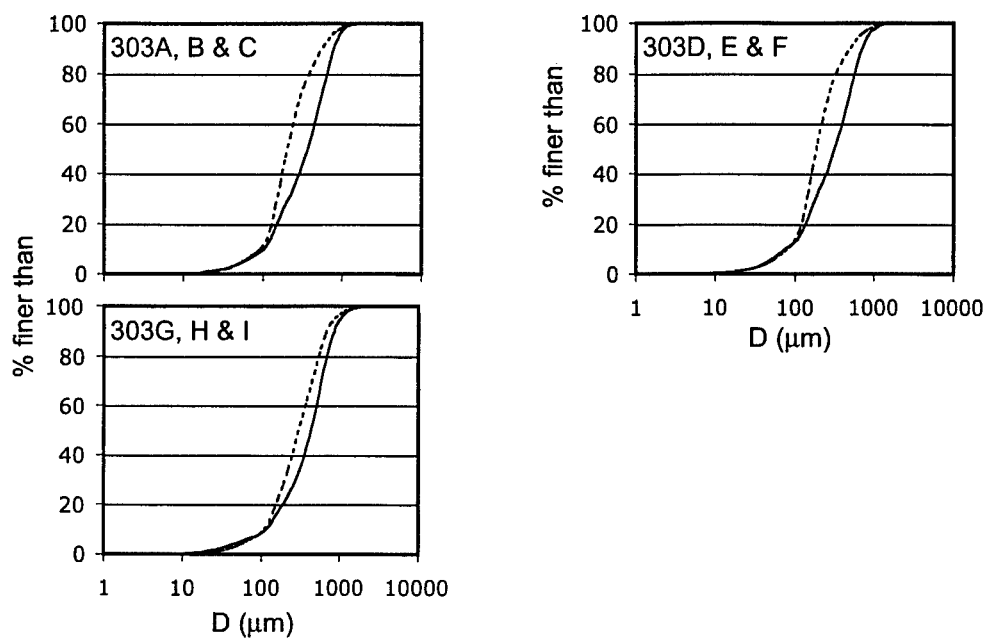
Figure 5-13: Cumulative grainsize distributions for Bed 303 continued (Figure 9). Samples are grouped by vertical transect. Plots are labeled with appropriate sample names. In all transects, the basal sample is indicated with a solid line and the upper sample is indicated with a dotted line. See Table 5.1 for sample characteristics.
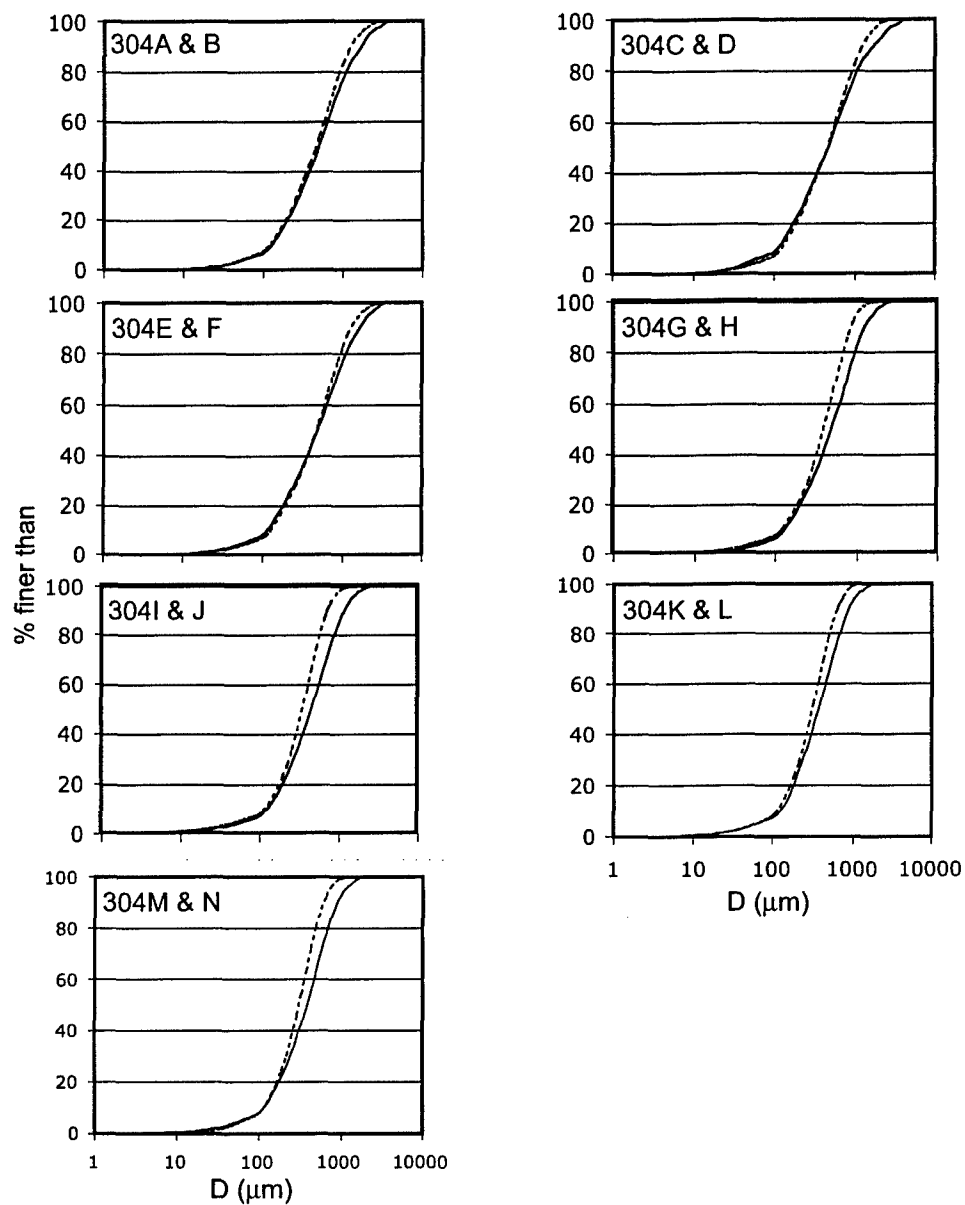
Figure 5-14: Cumulative grainsize distributions for Bed 304 (Figure 9). Samples are grouped by vertical transect. Plots are labeled with appropriate sample names. In all transects, the basal sample is indicated with a solid line and the upper sample is indicated with a dotted line. See Table 5.1 for sample characteristics.
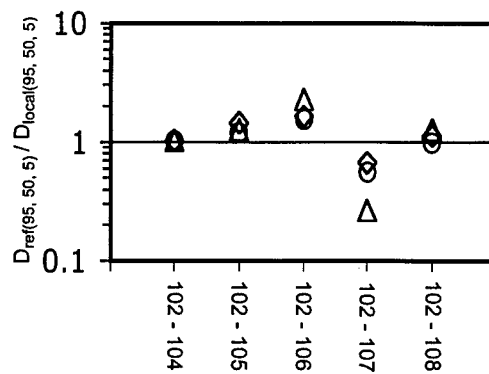
Figure 5-15: Values of the grading ratio (D_{ref}/D_{local}) for samples from Bed 100 (Figures 5-7 and 5-10; Table 5.2). This thin bed was only sampled laterally. Grading ratios for D_{95} are indicated with triangles, D_{50} with circles and D_5 with diamonds. With the exception of the 102-107 sample pair, this bed shows fining with increased elevation above the channel base consistent with suspended grainsize distributions in turbidity currents. Coarser grained partings occur in this bed and it is likely that one such sandy interval is responsible for the relative coarsening of the 102-107 sample pair. See Table 5.2 for grading ratios.
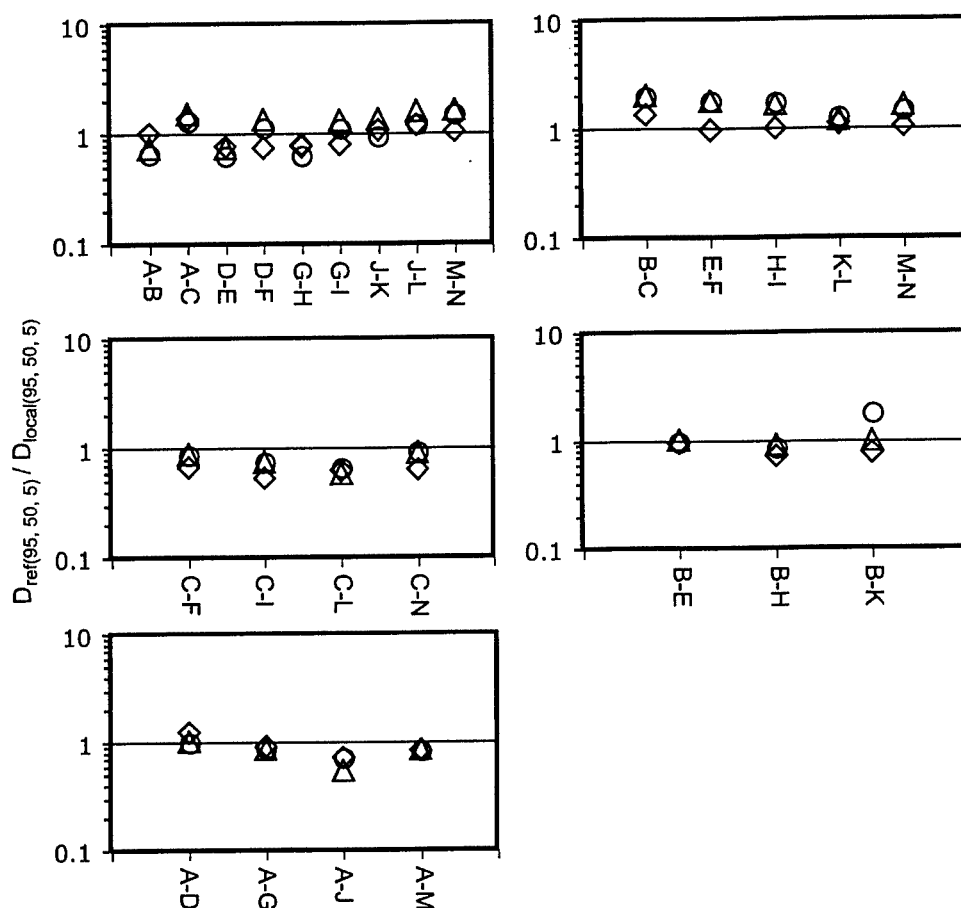
Figure 5-16: Values of the grading ratio (D_{ref}/D_{local}) for samples from Bed 203 (Figures 5-8 and 5-11; Table 5.2). Grading ratios for D_{95} are indicated with triangles, D_{50} with circles and D_5 with diamonds. Vertical transects exhibit a 'saw tooth' grading behavior when middle and upper samples are compared to basal samples (upper left plot). Base-Middle pairs (e.g. A-B) coarsen while Base-Upper pairs fine (e.g. A-C) suggesting a bed boundary between basal and middle samples. Recasting vertical transects using the middle sample as reference produces fining-upwards behavior consistent with samples confined to a single bed (upper right plot). Lateral transects (middle and lower plots) do not show consistent grading behavior. For a given plot, sample pairs reflect increasing vertical offset from left to right (e.g. $dz_{C-F} < dz_{C-N}$; see Table 5.2). This lack of trend suggests that the flow depositing the bed was vertically well-mixed.
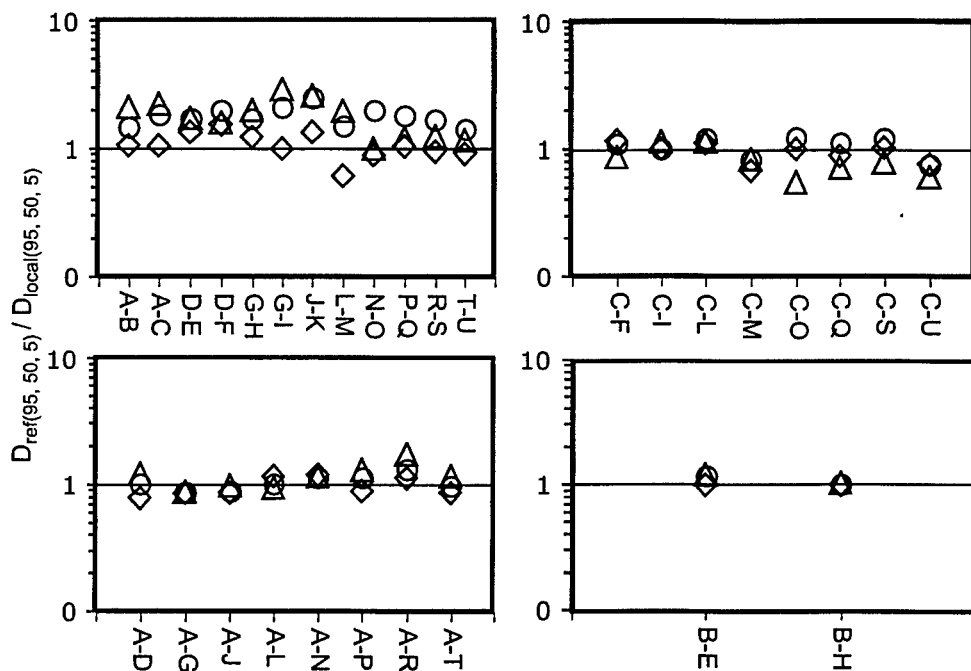
Figure 5-17: Values of the grading ratio (D_{ref}/D_{local}) for samples from Bed 303 (Figures 5-9, 5-12 and 5-13; Table 5.2). Grading ratios for D_{95} are indicated with triangles, D_{50} with circles and D_5 with diamonds. Vertical transects (upper left plot) show coarse-tail grading for the transects in the lower portion of the channel fill and distribution grading in the final four examples (N-O through T-U). Lateral transects (upper right and lower plots) show fining trends and, on average, grading ratios are comparable for all grainsize fractions indicating of distribution grading.

199
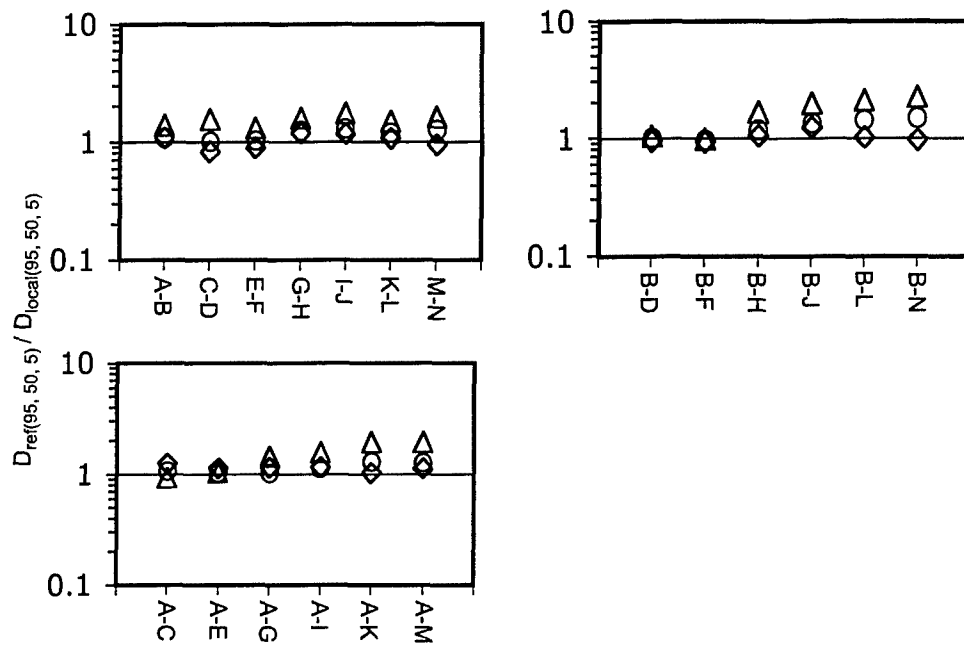
Figure 5-18: Values of the grading ratio (D_{ref}/D_{local}) for samples from Bed 304 (Figures 5-9, 5-14 ; Table 5.2). Grading ratios for D_{95} are indicated with triangles, D_{50} with circles and D_5 with diamonds. Vertical transects (upper left plot) show coarse-tail grading. Similarly, lateral transects (upper right and lower plots) show fining trends accomodated primarily in the coarsest (D_{95}) fraction of the grainsize distribution.
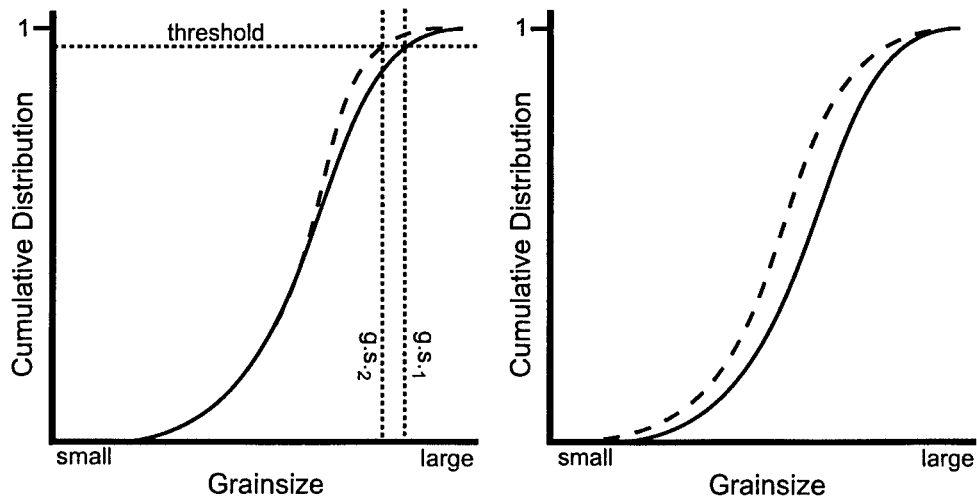
Figure 5-19: Examples of normal grading (fining) defined by two hypothetical grainsize distributions taken from a single bed. Left: Coarse-tail grading where reduction in grainsize abundance is dominantly in the coarser fraction of the available sediment. Coarse-tail fining suggests there exists a coarse grainsize range that is completely scrubbed from the flow between the earlier (solid line) and later (dashed line) samples. The scrubbed fraction can be determined by selecting a threshold cumulative fraction above which grainsizes are effectively absent from the sample. With the threshold above, the scrubbed fraction would consist of grains between $g.s._1$ and $g.s._2$. Sediment within this range define the critical grainsizes at which ϵ_{susp} equals E in Equation 5.8 and at which the critical Rouse parameter, $Ro = 2.5$ ($w_s = u^*$), is reached. Right, Distribution grading in which there is a reduction in occurrence across the entire grainsize range.
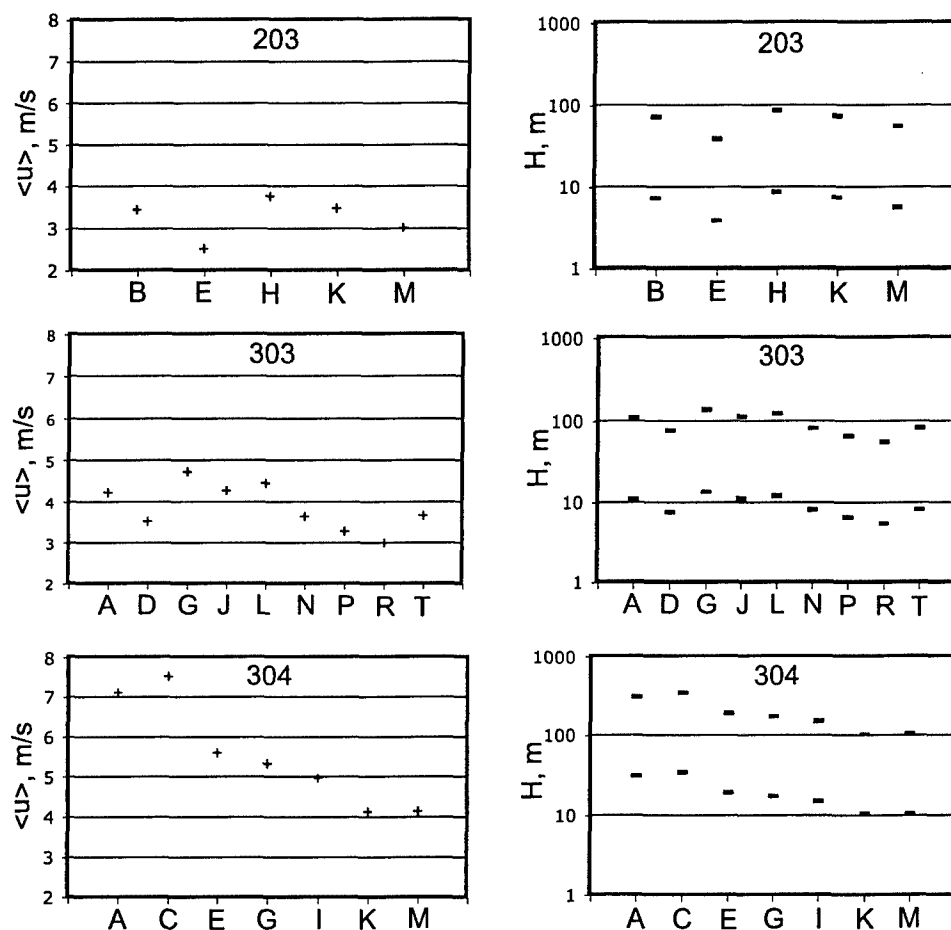
Figure 5-20: Flow reconstructions for the three tangential beds described in this paper (Beds 203, 303 and 304; Figures 5-8 and 5-9) based upon grainsize analyses. Plots are labeled to indicate bed and sample. Plots of estimated layer-averaged flow velocity (left) and projected flow depth (right). Velocities were calculated based upon D_{95}. Flow depths (right) were calculated using the velocities from the plots at left. Depths are reported for flows of both 1% concentration by volume and 10%. Flow velocities are on the order of meters per second. Depths for low concentration flows are on the order of 100 meters. The order of magnitude increase in concentration from 1% to 10% results in an order of magnitude decrease in flow depth to about 10 m.
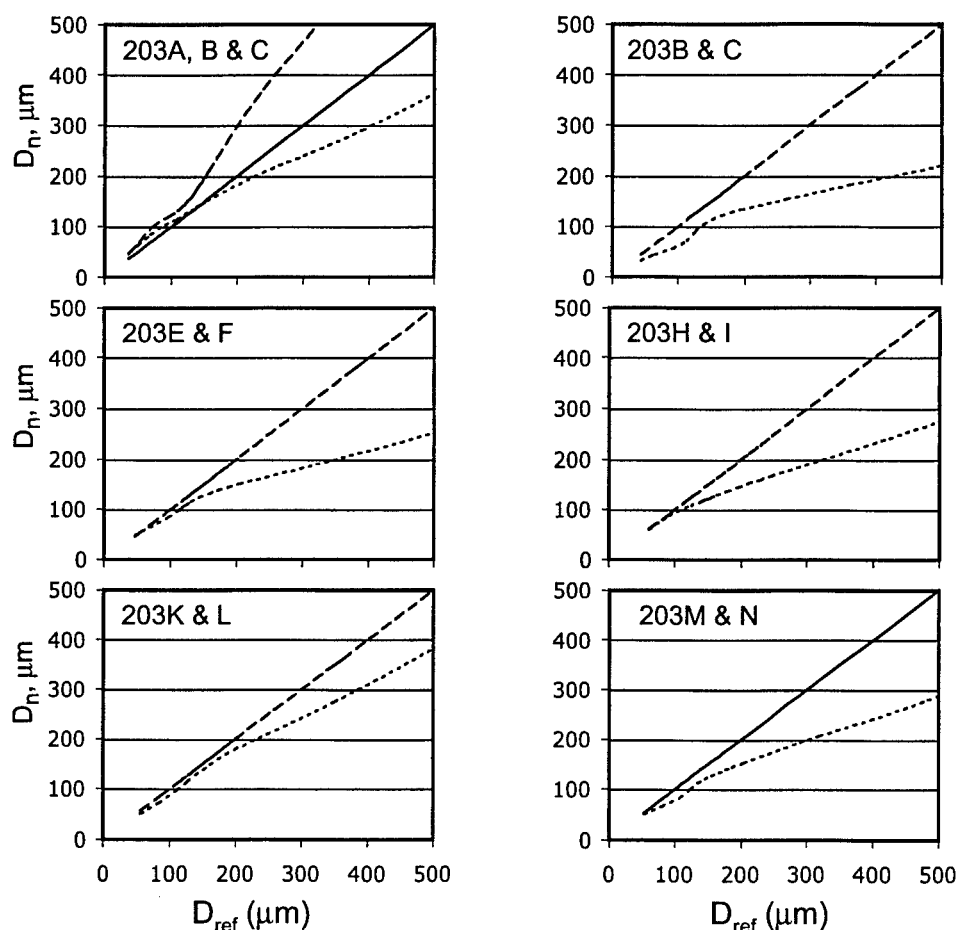
Figure 5-21: Fine-tail grainsize comparisons for Bed 203 (Figures 8 and 11). The similarity in fine-tails for each sample can be illustrated by plotting sample grainsize as a function of the reference sample grainsize. The one-to-one correlation in each plot is the reference sample plotted against itself and the other lines are a comparative sample plotted against the reference sample. For example, in the plot labeled 203A, B & C, when a comparative sample (*e.g.* 203B) is plotted as a function of the reference sample 203A, the dashed 203B=f(203A) line parallels the solid 203A=f(203A) line for the grainsize range of the common fine tail. The basal sample of a transect is always plotted as a solid line, the middle sample as a dashed line, and the upper sample as a dotted line. Middle samples of Bed 203 are coarser than the basal samples (*e.g.* the 203A/203B example above; see text for explanation). This is illustrated well in the upper left plot. We therefore treat Bed 203 as a aggragate bed and consider only the middle and upper samples for the bed in the remaining plots in this figure. The reference sample is always listed first in the plot label.

203
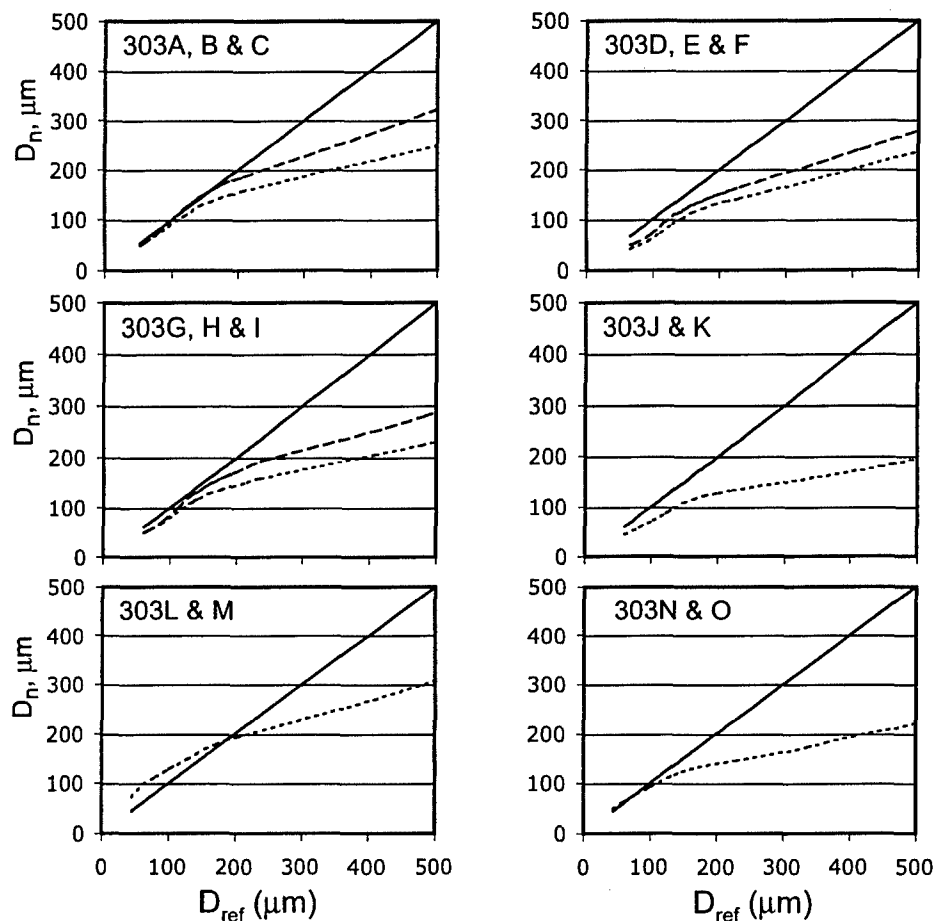
Figure 5-22: Fine-tail grainsize comparisons for Bed 303 (Figures 9 and 12). The similarity in fine-tails for each sample can be illustrated by plotting sample grainsize as a function of the reference sample grainsize. The one-to-one correlation in each plot is the reference sample plotted against itself and the other lines are a comparative sample plotted against the reference sample. For example, in the plot labeled 303A, B & C, when a comparative sample (e.g. 303B) is plotted as a function of the reference sample 303A, the dashed 303B=f(303A) line parallels the solid 303A=f(303A) line for the grainsize range of the common fine tail. The basal sample of a transect is always plotted as a solid line, the middle sample as a dashed line, and the upper sample as a dotted line. The reference sample is always listed first in the plot label.

204
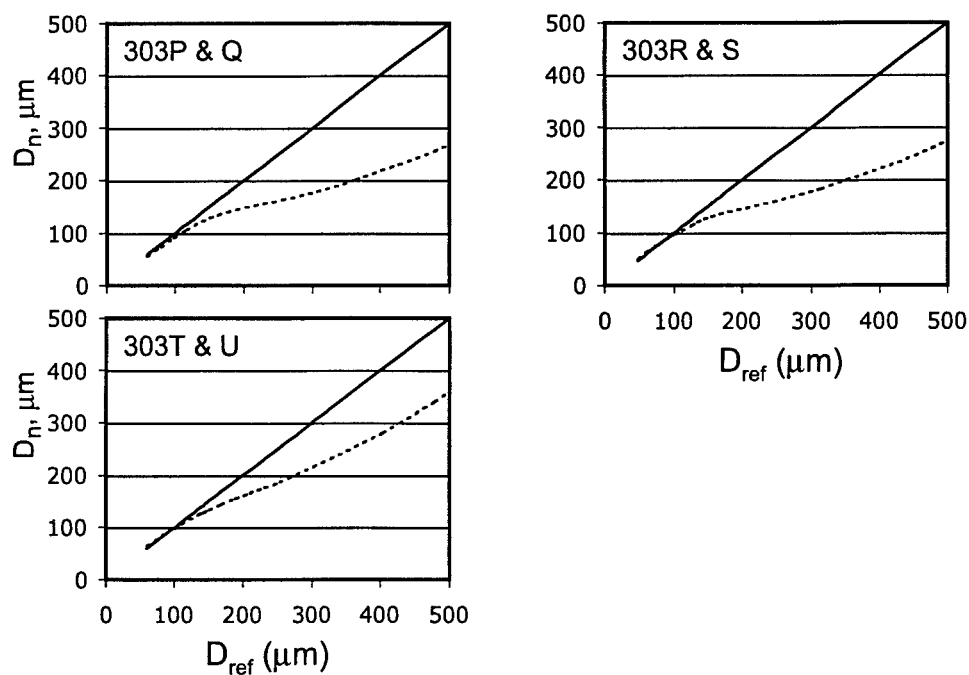
Figure 5-23: Fine-tail grainsize comparisons for Bed 303 (Figures 9 and 12). The similarity in fine-tails for each sample can be illustrated by plotting sample grainsize as a function of the reference sample grainsize. The one-to-one correlation in each plot is the reference sample plotted against itself and the other line is the comparative sample plotted against the reference sample. For example, in the plot labeled 303P & Q, when the comparative sample, 303Q, is plotted as a function of the reference sample, 303P, the dotted $303Q=f(303P)$ line parallels the solid $303P=f(303P)$ line for the grainsize range of the common fine tail. The basal sample of a transect is always plotted as a solid line and the upper sample as a dotted line. The reference sample is always listed first in the plot label.
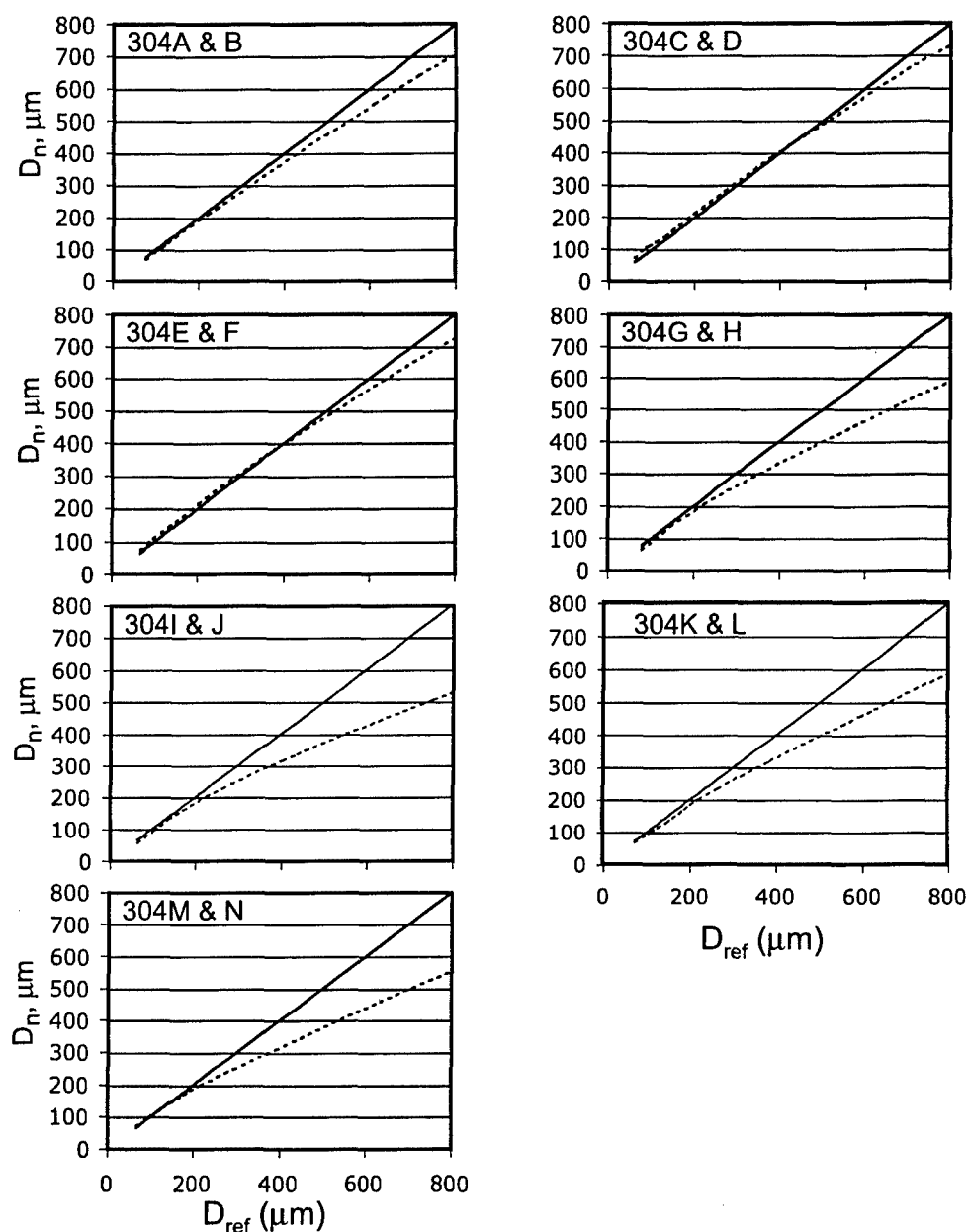
Figure 5-24: Fine-tail grainsize comparisons for Bed 304 (Figures 9 and 13). The similarity in fine-tails for each sample can be illustrated by plotting sample grainsize as a function of the reference sample grainsize. The one-to-one correlation in each plot is the reference sample plotted against itself and the other line is the comparative sample plotted against the reference sample. For example, in the plot labeled 304A & B, when the comparative sample, 304B, is plotted as a function of the reference sample, 304A, the dotted 304B=f(304A) line parallels the solid 304A=f(304A) line for the grainsize range of the common fine tail. The basal sample of a transect is always plotted as a solid line and the upper sample as a dotted line. The reference sample is always listed first in the plot label.
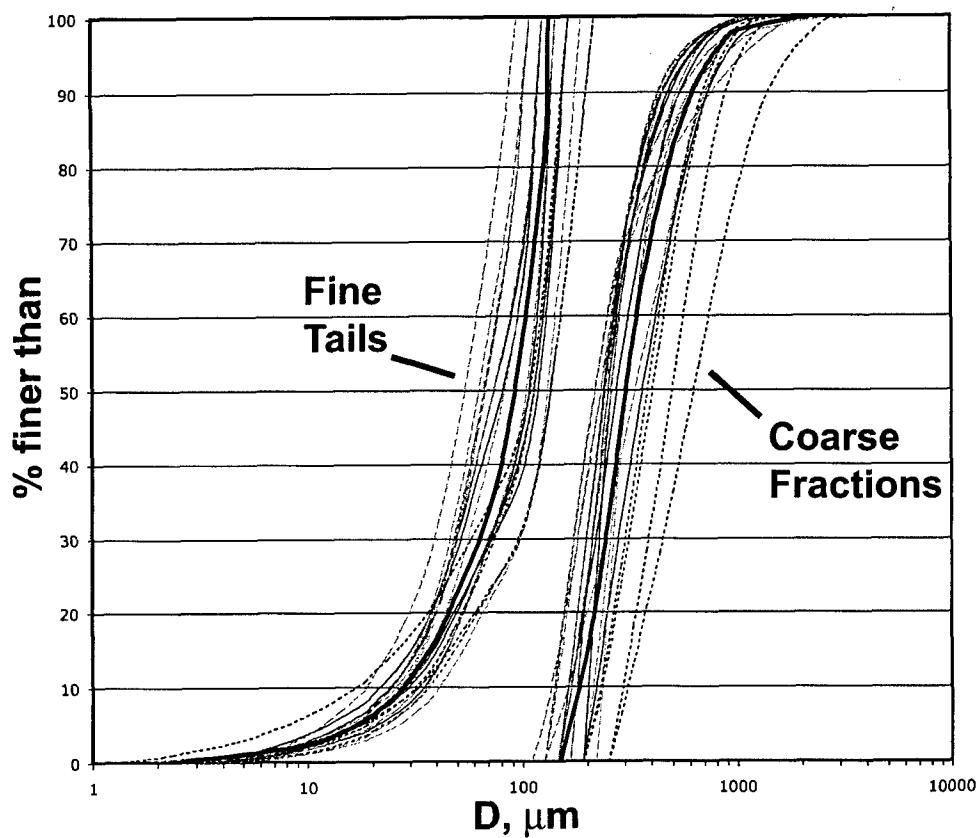
Figure 5-25: Fine and coarse fractions of cumulative distributions from tangential beds (thin lines) and average or representative fine and coarse distributions (heavy lines). Original distributions are shown in Figures 5-11 through 5-14. Cumulative distributions were taken only from comparative samples (*i.e.* not from reference samples). Samples included are 203C, F, I, L and N, 303C, E, F, H, I, K, O, Q, S and U, and 304B, H, J and L.

Chapter 6

The spatial continuity of sandy unconfined turbidites from the exceptionally well-exposed Zerrissene Turbidite System, Namibia

6.1 Introduction

Hydrocarbon production depends upon reservoir characteristics at a broad range of scales from the regional distribution of sediments at the large scale to grainsize variations within those sediments at the small scale. Geologic models must then incorporate data across this entire range to more accurately predict reservoir behavior. Regional information and vertical stratigraphy at the scale of 100's of meters and greater can be obtained through seismic surveys. That framework can then be augmented with finer-scale reservoir characteristics such as grainsize distributions, rock porosity and permeability, and centimeter to meter scale bed structure by data collected from wells. There is, however, a gap in scales between these two data sources

which is manifest when we attempt to extrapolate the local data obtained at the well up to the seismic/regional scale. Wells, particularly in deepwater environments, are spaced kilometers apart and provide little constraint on the intra-well lateral variability that is so critical to reservoir models.

In order to project data from the well scale to the basin or reservoir scale, we must have rules describing how local, borehole-derived characteristics vary laterally across lengths ranging from meters to many kilometers. Outcrops have proven useful in the attempt to develop such rules for reservoir models (*e.g.* Pickering et al. (1995)) but such analogues break down at approximately the same scales at which there exists the disconnect between well and seismic data. Unambiguous, continuous outcrop exposures rarely exceed a kilometer in length (*e.g.* Rehy Cliffs, Ross Formation, western Ireland in Martinsen et al. (2003); Grès d'Annot, southeast France or Tanqua, Karoo Basin, South Africa in Pickering et al. (1995)) falling well short of the desirable continuous regional exposure. As a result of these limited outcrop exposure lengths, constraining basin or reservoir-scale sedimentologic characteristics from outcrop requires correlation between exposures separated by 100's of meters to kilometers (Hilton, 1995; Hiscott and DeVries, 1995; Zelt and Rossen, 1995) or across comparably sized regions of obscured stratigraphy (Smith, 1995) Such correlation introduces considerable uncertainty at exactly the scale we would like to augment.

One solution for providing better constraints on lateral reservoir variability is to seek outcrops of exceptional exposure and the Neoproterozoic Zerrisene Turbidite System of western Namibia is just such an example (Figure 6-1). The Zerrissene turbidites are often exposed over distances approaching an order of magnitude greater than systems presented previously (Hilton, 1995; Hiscott and DeVries, 1995; Zelt and Rossen, 1995). In the work presented here, a photo mosaic composed of six kilometers of completely and continuously exposed outcrop was analyzed through photomosaic interpretation and extensive field checking to determine the lateral continuity of turbidite bundles, the thickness of those bundles, and the apparent sand fraction and net-to-gross of the sandy units constructed of those bundles. The continuous exposure of the Zerrissene Turbidites provides unparalleled lateral continuity. With this

data, it is possible to explore such questions as how continuous are turbidite bundles in unconfined systems; do the fine-grained sediments between bundles represent a local lobe switching or a more regionally extensive halt to sedimentation; and, what are the correlation length scales of those sediment characteristics measurable in core or outcrop but difficult to project throughout a reservoir? This study contains data that can help to answer such questions.

6.2 Field area

6.2.1 The Zerrissene Turbidites

The Neoproterozoic Zerrissene Turbidite system is named for the Zerrissene Mountains found to the southwest of the field area (Swart, 1992). The turbidite outcrops extend about 90 km in the east-west direction and 30 km in the north-south direction. The region is dominated by north-south trending, westward vergent, overturned folds. A shortening factor for the system of at least 50% (Swart, 1992) suggests that the exposed turbidites represent a depositional system more than 180 km long in the east-west direction. The full extent of the deposits is unknown; to the north and south, the Zerrissene is covered by Mesozoic Karoo sediments and lavas while to the west it is terminated by a belt of strongly deformed rocks. In the east, the system is truncated by a prominant north-south striking shear zone (Freyer and Hälbich, 1983; Miller, 1988; Swart, 1992). The turbidites have not been dated directly but the presence of glacial dropstones in the Brak River Formation suggests a correlation to the glacial Chuos Formation (750 m.a.) in the Northern Zone of the Damara Orogen (Evans et al., 1994).

The earliest geologic studies in the Zerrisene region focused on defining the igneous, structural, metamorphic and stratigraphic features of the Neoproterozoic Damara Orogen (Willemse et al., 1944; Jeppe, 1952). A more focused study of the turbidites was not undertaken until Miller et al. (1983). Prior to the work of Swart (1992), there was disagreement as to the depositional setting of the Zerrissene. While Miller et al.

(1983) argued that the Zerrisene sediments were deepwater deposits, Porada (1983) interpreted the Zerrissene as representing shallow marine deposits and proposed the existence of a structural high in the basin to account for his interpretation of the observed facies. Swart (1992) focused on the sedimentological attributes and showed that the Zerrissene was indeed a deep water system.

6.2.2   Structural history of the Zerrissene

The Zerrissene turbidites were deformed during development of the late Proterozoic Damara Orogen (Kennedy, 1964). Subsequent uplift in Permian and Cretaceous times exhumed these rocks (Miller et al., 1983; Porada, 1983). The Damara Orogen is a component of the Pan-African system of mobile belts (Kennedy, 1964) and is composed of two distinct arms: the north-south trending coastal Kaoko Belt and a northeast-southwest trending intercratonic arm (Figure 6-1). The Zerrissene Basin lies at the junction of these two arms. The turbidites have undergone at least three distinct phases of deformation. The initial and primary deformation is evidenced by north-south trending, westward vergent, tight to isoclinal folds (Miller et al., 1983; Porada, 1983). Two lesser and subsequent deformations resulted in the refolding of the westward vergent folds into kink folds followed by the development of Ramsay type 2c interference folds. Both secondary folding events reflect north-south shortening (Ramsay, 1967; Coward, 1981; Swart, 1992). Modern erosion has resulted in horizontally-oriented exposures of the folded limbs and, as such, provides multiple laterally extensive cross sections through the Zerrissene system (Figure 6-2).

The primary stage of folding produced highly attenuated upright limbs which are not conducive to sedimentological study. Usefulness of these limbs is further limited by a fold-related penetrative cleavage oriented sub-parallel to bedding obscures stratification.

In contrast to the upright limbs, the overturned limbs are much more conducive to sedimentologic work. Detailed structural analysis of the Zerrissene has yet to be published but the attenuation of the overturned limbs is limited and these sections preserve relatively undeformed depositional features such as cross-bedding and

climbing ripples (Swart, 1992). In addition, the structurally induced foliation fabric intersects bedding in the overturned limbs at high angles such that stratification is relatively unaffected. For these reasons, this work focuses exclusively on strata in the overturned portion of a fold.

6.2.3   Stratigraphy of the Zerrissene Turbidites

The Zerrissene system is divided into five distinct formations (Miller et al., 1983): three siliciclastic turbidite units separated by two intervening carbonate-rich turbidite units. From oldest to youngest these units are: 1) the clastic Zebrapüts Formation; 2) the calcareous Brandberg West Formation; 3) the clastic Brak River Formation; 4) the calcareous Gemsbok River Formation; and 5) the clastic Amis River Formation. Total thickness of the sedimentary package is about 1.7 kilometers (Swart, 1992) composed primarily of turbidites with minor intervening pelagic deposits. The rocks have been subjected to low grade metamorphism (Miller et al., 1983; Swart, 1992). The work presented here focuses on the middle siliciclastic unit, the Brak River Formation. The maximum measured thickness of this unit is 500 m (Swart, 1992).

The clastic formations of the Zerrissene are composed of distinct, but not regionally correlatable, sandy packages or "bundles" separated by intervening, finer grained sediments. The bundles are, in turn, made up of individual turbidity current event beds. Grossly, the event beds are on the order of 10 centimeters in thickness while the bundles are on the order of one to several meters in thickness. In the section of the Brak River Formation studied here, the turbidite bundles are grouped into two sandy units separated by an intervening package in which coarse-grained bundles are rarely found. Individual turbidite beds are usually visible only in cleanly weathered drainages and cannot be easily traced laterally for long distances. Sedimentary features (*e.g.* cross-bedding and flute casts) are not common. Whether the absence of such features is due to the fact that the depositional setting was not conducive to their generation or whether those features existed but were subsequently obscured during deformation, metamorphism or weathering is not clear.

The absence of sedimentary features and the metamorphism which, while low-

213

grade, still obscures original grainsize, make it difficult to place the Zerrissene deposits exactly (proximal vs. distal) within a regional depositional context. However, the lower siliciclastic and the lower carbonate units are composed of laterally extensive sands with interbedded fine pelagic muds and are devoid of significant syndepositional topographic or structural features. Likewise, the Brak River Formation is composed of extensive, tabular packages of sediment. These observations of the underlying formations, combined with the characteristics of the Brak River Formation itself, suggest that the Brak River consists of unconfined deposits similar to the Type 1 deposits of Pickering (Pickering, 1981, 1985; Swart, 1992).

6.3   Methods

This study combines remote sensing in the form of quantitative photo interpretation with extensive field calibration. To provide a comprehensive view of the kilometers-long field area and to adequately characterize the Brak River Formation, low-level aerial photographs were compiled into a photomosaic of the region (Figure 6-4). To avoid the misinterpretation of features in the photopanel, the entire area was walked out and features on the photographs were verified.

As described above (Section 6.2.3), there are two distinct sandy units in the field area. These are considered separately and will be referred to as the lower and upper units (Figure 6-4). The analyses presented will ignore the intervening, 75 m thick, fine-grained deposit.

6.3.1   Unit thickness

Variations in sand unit thickness could not be determined over the entire region because the aerial photographs do not always capture the complete unit. A portion of the outcrop was also eliminated from analysis due to the presence of a reverse/right-lateral fault which cuts the upper unit (Figure 6-4). It was necessary, therefore, to examine the lower unit in discrete zones rather than in its entirety and to consider only a portion of the upper unit (Figure 6-4). The lower unit was broken into three

regions (surrounding transects AA', BB' and CC') with areas of 0.26, 0.14, and 0.27 km², respectively. In zone AA', the unit thickness is 140 meters at the southern end and 145 meters at the northern end with the two measurements separated by a distance of 1.8 kilometers. Similarly, zone BB' has thicknesses of 140 and 135 meters over 1 kilometer and CC' is a constant 135 meters thoughout its 2 kilometer length. The upper unit (DD') has an area of 0.19 km² with a thickness at the southern end of 120 meters and of 135 meters to the north. The section DD' is 1.4 kilometers long.

6.3.2 Aerial photos

The work presented here was conducted using a photo-mosaic constructed from low altitude aerial photographs (Figure 6-4). The location of this mosaic is indicated in Figure 6-2. The exposure will be referred to as the "koppie" area because of the prominant hill, composed of Cretaceous dolerite, that outcrops in the section. The aerial photos were taken from an elevation of 2100 meters above the outcrop using a 35 mm camera equipped with a 50mm lens. From this altitude, meter-scale features are easily identifiable.

Sand fraction

Quantitative measure of sand fraction, as well as net-to-gross, could be obtained through photo-interpretation because the coarser-grained turbidite bundles weather as prominent, dark-colored ridges while the shales weather as light-colored recessive intervals. Sand fraction estimates were made for each image based on the distribution of grayscale intensity values. These intensity maps were generated using the public domain imaging-processing software *NIH Image* (http://rsb.info.nih.gov/nih-image/). A simple linear mixing model was applied to each image in order to constrain the fraction of sand versus shale in each section. Care was taken to avoid areas of excessive shadowing and distortion when selecting the portions of the photographs used in this analysis (Figure 6-5). Sand fraction was taken simply as a measure of the overall "sandyness" of a given section and is used primarily for identifying spatial change in

the bulk sand content.

Grayscale analysis was a multi-step process. Selected regions of the color photographs were converted to 8-bit black and white images (Figure 6-5). These black and white images were then corrected for brightness and contrast to normalize the distribution of grayscale values. Through these adjustments, it was possible to generate images with comparable minimum and maximum grayscale values and with roughly similar shapes to the overall grayscale distribution. Once normalized, the mean grayscale value for the selected interval was taken as a measure of its coarseness. In this scheme, a value of 0 (black) corresponded to 100% coarse sediment and 255 (white) corresponded to 100% fine sediment. The lower the mean grayscale value for a normalized image, the higher the sand fraction composing the beds in the selected region.

The simple mixing model must be modified slightly to produce more accurate results. The intervening fine sediments in the Brak River Formation are not 100% mud but rather some mix of mud, silt and sand. In the Brak River, the recessive intervals are composed of very fine grained turbidites with some pelagic deposits (Swart, 1992). Hence, sand fraction values must be adjusted to reflect the mixed composition of the fine-grained lithology. This adjustment is accomplished by multiplying the average mean grayscale value by the reciprocal of the sandstone/shale ratio for the fine sediments (*Average of Means* × *1/Sandstone : Shale Ratio*). The effect of this adjustment is to raise result of the sand fraction calculation (*i.e.* make the outcrop sandier).

Net-to-Gross calculations

Net-to-gross estimates were also calculated based upon grayscale values. In this paper, 'net' refers to net sand *sensu* Shanley et al. (2000). Since the work presented here is two dimensional, net and gross are areas, not volumes.

To calculate net-to-gross, *NIH Image* was again used to generate histograms of grayscale value for the 8-bit black and white images. These histograms were then partitioned such that all pixels containing a grayscale value below some threshold

were assigned a new value of 0 and the remaining pixels were reassigned to 255. This threshold is comparable to a Vshale cutoff (Shanley et al., 2000). In essence, the threshold value differentiates net sand (grayscale value of 0) from gross (255). The ratio of black pixels (net sand) to total pixels (gross) is taken as a measure of net-to-gross.

6.3.3   Field calibration

To verify the interpretations of features in the photographs, the field area was walked so that bed boundaries and terminations could be distinguished from unrelated features such as game trails, overburden, drainage routes, and faults. Cleavage behavior was used to confirm that a recessive area was finer grained. If both fine and coarse-grained lithologies are subjected to the same deformation, the spacing between cleavage planes in the fine-grained rock will be less than the cleavage spacing in the coarse-grained bed (van der Pluijm and Marshak, 1997). In addition, if fine and coarse-grained beds are adjacent, the cleavage angle will refract across at the boundaries between lithologies – conversely, if lithologies are comparable across the bedding, refraction will not occur (van der Pluijm and Marshak, 1997). In the field, if the cleavage spacing in a recessive unit was seen to decrease relative to the spacing in the adjacent bundle, and if the cleavage planes had different strikes in the recessive and prominent areas, then the cleavage behavior was taken as an indicator that the recessive unit was finer-grained than the prominent.

In addition to distinguishing between coarse and fine sediments, field work was necessary to scale the aerial photographs. In each image, distances between distinct features were measured so that dimensions could be obtained directly from the images.

217

6.4 Results

6.4.1 Turbidite bundle dimensions

Average bundle thickness for the two units can be estimated based upon bundle count over the measured thicknesses and factoring in the average net-to-gross ($ave.\ thickness =$ $unit\ thickness \times net-to-gross \div no.\ of\ bundles$) (see Section 6.4.3 below for description of net-to-gross calculations). Note that, even with the low-altitude photographs, individual bundles are quite thin and measuring thicknesses directly from the images would introduce substantial error. In addition, simply dividing unit thickness by number of bundles will not produce the correct bundle thickness because substantial portions of the units are composed of fine-grained sediments. The average bundle thickness for the lower unit is 2.0 m while the average thickness for the upper unit is 2.3 m. Conversely, the average thicknesses of the intervening fine-grained layers between bundles is 2.5 m and 2.6 m for the lower and upper units, respectively.

The lateral dimensions of the turbidite bundles are set by the presence of bed terminations (*e.g.* Figure 6-6). In this portion of the Brak River Formation, such terminations are extremely rare (Figure 6-7). Only four terminations were confidently identified within the two units. With the lower and upper sandy units covering a combined area of 200,000 m^2, this frequency of terminations translates into one termination per 50,000 m^2 of outcrop. It is also important to note that when bundle terminations do occur, rather than step up in the stratigraphy, the subsequent bundle is deposited along the same horizon as its predecessor (Figure 6-6).

Major erosional features (*e.g.* channels, mega-flutes, slump scars, etc.) with the potential of providing direct vertical communication between bundles are non-existent in this field area. There are two locations where the bundles appear to be amalgamated (Figures 6-7) however no clear erosional surfaces were found at either of these sites and little importance is given to these features in this work.

6.4.2 Sand fraction

Mean grayscale values for each of the images in the mosaic are shown in Figures 6-8 and 6-9. The most striking feature of this data is the lack of any spatial trends in sand fraction; the mean grayscale value is constant across the entire length of each unit (Figure 6-8). The average of the grayscale means was found to be 146.96. Adjusted for the fact that the fine intervals are not 100% mud (see Section 6.3.2), and assuming a sandstone/shale ratio for the recessive units of 2:1, the average of the means becomes 73.48 or a sand fracton of 0.86. Similarly, the average of the mean grayscale values across the upper unit (Figure 6-9) is 151.02. Adjusted, this becomes 75.51 which corresponds to a sand fraction of 0.85.

6.4.3 Net-to-Gross

The results of the net-to-gross calculations are shown in Figures 6-10 and 6-11. While there is scatter (primarily due to variations in shading in the photographs), as with the sand fraction there are no clear trends in net-to-gross for either the lower or upper units. The average net-to-gross is a relatively constant 0.45 along the length of the lower unit and 0.48 along the upper.

6.4.4 Variograms of stratigraphic continuity

In order to make an estimate of the appropriate length scales over which sand fraction and net-to-gross data may be applied, variograms were constructed for the two data sets for the lower unit. The sand fraction and net-to-gross data sets for the upper unit are too small to be considered statistically robust (Olea, 1999). The data for the lower unit generates 19 pairs and is therefore analyzed here.

Variograms for both the sand fraction and net-to-gross data are presented in Figures 6-12 and 6-13. The average spacing between individual photographs was taken as the lag spacing for the construction of the variograms (Olea, 1999). The calculations used to construct these plots define the length scales of correlation for sand fraction and net-to-gross. At some distance (*i.e.* some multiple of the lag spacing), the

value of the variogram approaches the calculated variance of the data set (γ). This distance corresponds to the correlation length scale for the characteristic of interest (Olea, 1999). In the case of the sand fraction data, γ is 5.32 and is reached at four times the lag spacing or 1.0 km (Figure 6-12). For the net-to-gross data, γ of 58.81 is reached at six times the lag or 1.5 km (Figure 6-13).

6.5 Interpreted basin context

The Zerrissene Turbidites are exceptionally well exposed but the conditions of deposition are not well constrained. The profile and subsidence history of the basin, as well as the position and orientation of the outcrops relative to sediment source, are not known definitively. However, the constancy observed within the deposits is striking. Unit-averaged sand fraction is essentially constant throughout the study area. The thicknesses of the two sandy units that make up the Brak River Formation change by no more than a few meters (roughly 3-4% of total thickness) over distances of six km for the lower unit and 2.5 km for the upper. Net-to-Gross values, while scattered, show no definable trend. Finally, variograms of both sand fraction and net-to-gross data for the lower unit indicate long correlation lengths of 1.0 km and 1.5 km, respectively. The lack of variability in bed thickness, average grainsize and net-to-gross help constrain the depositional context for the Zerrissene turbidites.

Parsons et al. (2002) conducted laboratory experiments on unconfined, well-suspended turbidity currents and found the ratio of down-stream velocity to cross-stream velocity to be 1.5. The deposits resulting from such flows are expected to have length to width ratios comparable to the velocity ratio. The Brak River Formation is dominated by "medium- to thick-bedded, fine- to coarse-grained sandstones" and "very-thinly to medium-bedded, fine-grained sandstone-shale couplets" (Swart, 1992); both of these facies could reasonably be the result of well-suspended flows. The koppie section displays six kilometers of exposure and, if that exposure is perpendicular to flow, the associated fan system can be expected to extend for at least 10 km in the streamwise direction. However, the rarity of bed terminations in outcrop suggests two things.

First, the outcrop in the koppie area does not extend anywhere near the total width of the system. If the outcrop were of a size comparable to system width, bed terminations would be prevalent. Second, it is unlikely that this outcrop represents an exposure near the distal fringes of the lobe deposits. If the outcrop were at the distal extent of the system, bed terminations and variations in lithology should be common.

If, rather than being oriented perpendicular to flow as assumed above, the outcrop is oriented parallel to flow, reasoning similar to that above may be applied regarding outcrop position within the overall system. Mutti and Davoli (1992) presented a conceptual model of the streamwise depositional behavior of turbidity current systems which is useful in assessing the outcrop studied here (Figure 6-14). The model considers facies associations as a function of the parent flow and the depositional position within the turbidity current system. While there is no information on the parent flows associated with the Zerrissene deposits, Muttti's model may be applied qualitatively to constrain outcrop position based upon facies associations.

The facies described by Swart (1992) in the Brak River Formation are most similar to Mutti's F7 through F9a: medium to fine sand at one extreme (F7) and very fine sand to mud at the other (F9a). The Mutti model allows for the coexistence of F7 through F9a facies from the medial to the distal portions of the system, however, the model also reflects the fact that bed terminations and changes in lithology become more prevalent at the distal extent of the deposits. It is in the medial portions of the system where laterally extensive beds reside and terminations are rare and where average grainsize and net-to-gross can be expected to remain constant over large portions of the outcrop (Figure 6-14). The characteristics of the Zerrissene system described above coincide well with this medial lobe location.

Regardless of outcrop orientation, there are two points of interest worth noting. First, all of the bundle terminations occur at the southern end of the exposure (Figure 6-7). This suggests that end of the outcrop is closer to the margin – either lateral or distal – of the fan system. Second, when bundle terminations are identified, subsequent bundles do not occur higher in the stratigraphy relative to the predecessor but rather at the same stratigraphic horizon (Figure 6-6). This has implications for

the depositional history of the bundles. If bundle deposition was affected by local lobe switching, then compensational sedimentation would be expected wherein a bed that is seen to be locally fine-grained is coarse-grained at some other lateral position (Figure 6-15). However, at the scale of the outcrop analyzed here, fine-grained intervals remain as such across the entire 6 km of exposure. This argues that there were distinct periods during which coarse-grained sediments were not supplied to the area. At least, if lobe switching did lead to times of fine-grained deposition, the depocenter for the coarse-grained sediments experienced dramatic shifts away from the region of this outcrop.

6.6   Conclusion

The late Proterozoic Zerrissene Turbidite System is an exceptionally well exposed example of an unconfined deep-water turbidity current system. Lack of vegetation and other cover results in continuous outcrops on the order of five to ten km in length. Through the use of aerial photographic mosaics and field work, this study focuses on a single, six kilometer long outcroping of the Brak River Formation and explores the sub-seismic scale lateral and vertical architecture of sandy, deep-water deposits.

The Brak River Formation is composed of sandy bundles of turbidites separated by finer-grained sediments. The stacked bundles are interpreted to be lobe deposits and are grouped into two units (lower and upper), each roughly 140 m in thickness. The two units are separated by a 75 m thick fine-grained interval. Bundles have an average thickness of 2.0 m for the lower unit and 2.3 m for the upper unit and are laterally continuous. Only four lateral bundle terminations were identified in 200,000 m^2 of outcrop. Major erosional features (channels) were entirely absent. The apparent sand fraction of the outcrop, estimated by a grayscale analysis of the aerial photographs, was virtually unchanged across the exposure and equaled 0.86 and 0.85 for upper and lower units, respectively. Net-to-gross calculations indicate a relatively constant value of 0.45 for the lower unit and 0.48 for the upper unit. Variograms indicate a correlation length of 1 km for the sand fraction value and 1.5 km for the

net-to-gross calculation.

The absence of bundle terminations, in conjunction with the extensive lateral lithologic continuity indicated by variograms of the sand fraction and net-to-gross data, suggest that the Brak River Formation outcrop considered here is located in the medial portion of the depositional system. Mutti's model of turbidite facies associations (Mutti and Davoli, 1992) suggests that both the distal and lateral extents of turbidite lobe systems should exhibit terminations in sandy beds and distinct changes in lithologic character. Neither of these behaviors are seen in this study area and this absence argues for a medial position for the Brak River deposits. Furthermore, where terminations do occur in this system, the subsequent bundle is deposited at the same stratigraphic level as the precursor and the intervening fine-grained beds are seen to extend across the entire outcrop area. This is in contrast to compensational sedimentation expected with local lobe switching and suggests that fine-grained intervals in the outcrop represent regional cesation of coarse-grained sediment supply.

6.7 Figures
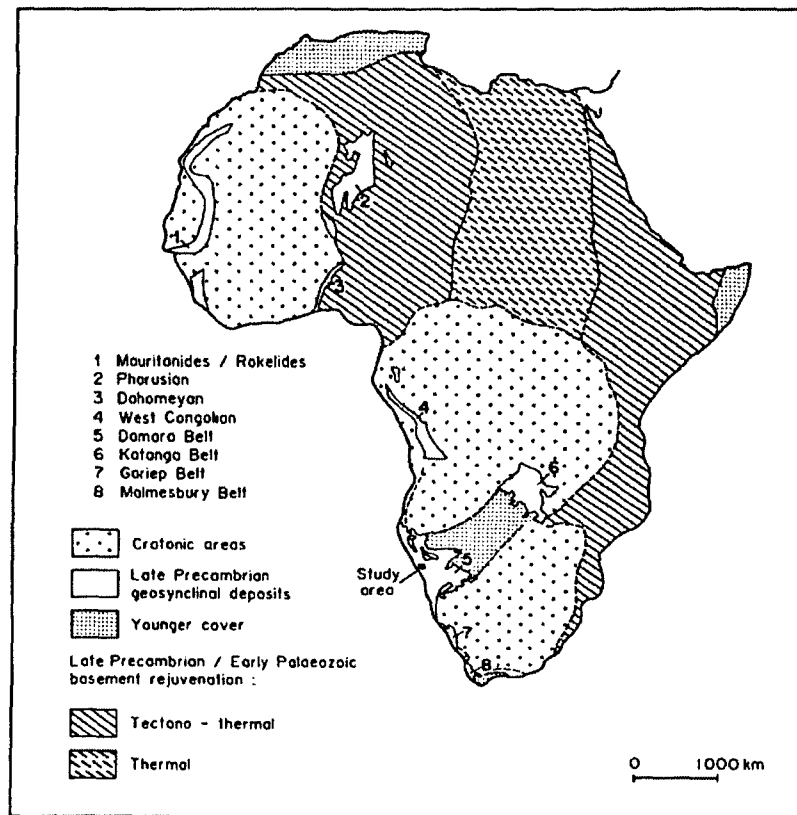
Figure 6-1: Geologic map of Africa indicating location of the Zerrissene Turbidite System relative to the general geology of the continent. From Swart (1992).
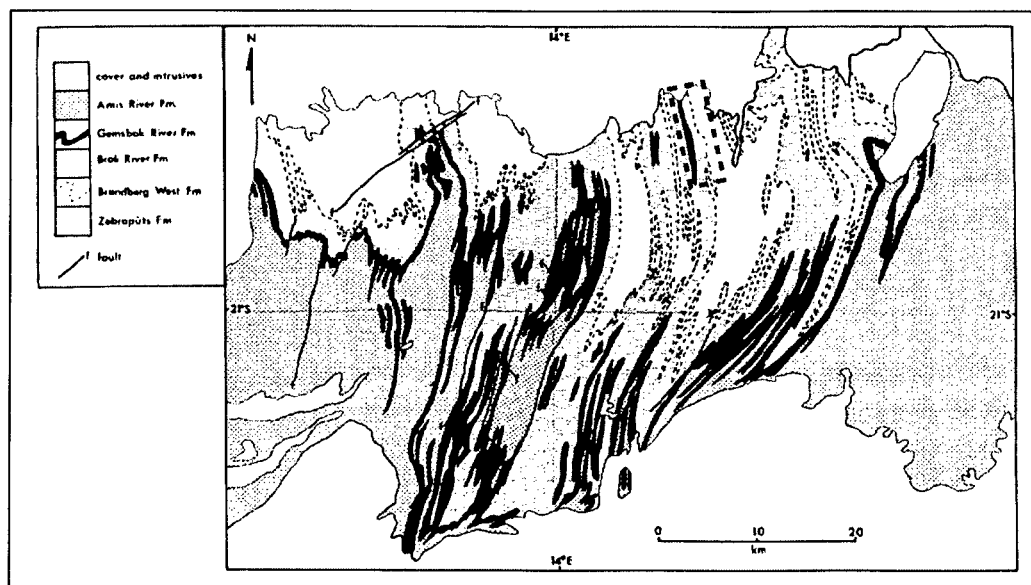
Figure 6-2: Geologic map of the field area of this study illustrating the five formations of the Zerrissene Turbidite System. The Brak River Formation is indicated in gray and the field area for this study is outlined with a dashed box. Modified from Swart (1992).
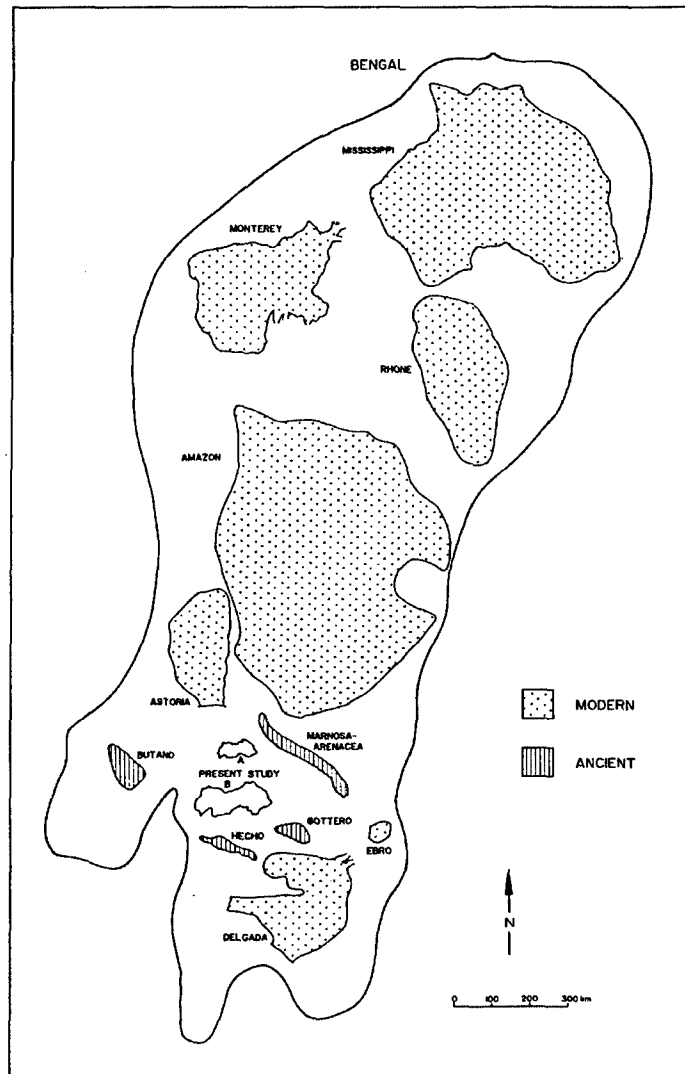
Figure 6-3: Diagram illustrating the size of the Zerrissene Turbidite System relative to both modern, active systems and ancient, preserved systems. The Zerrissene is shown in its current, folded state (A) and unfolded (B). From Swart (1992).
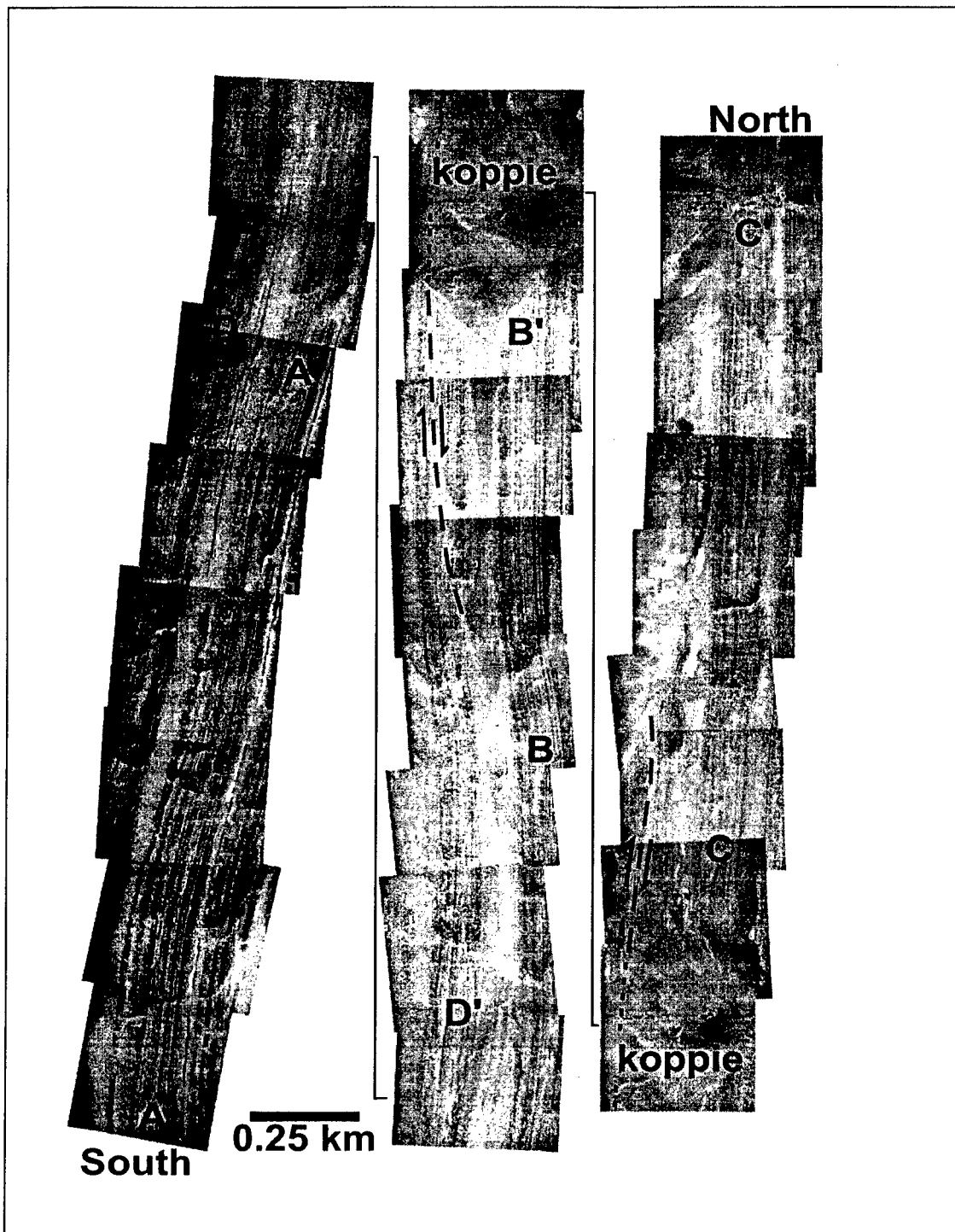
Figure 6-4: Annotated photomosaic showing the two sandy units (the lower which includes AA', BB' and CC' and the upper which includes DD'). For bed thickness calculations, only the lettered sub-sections were used.
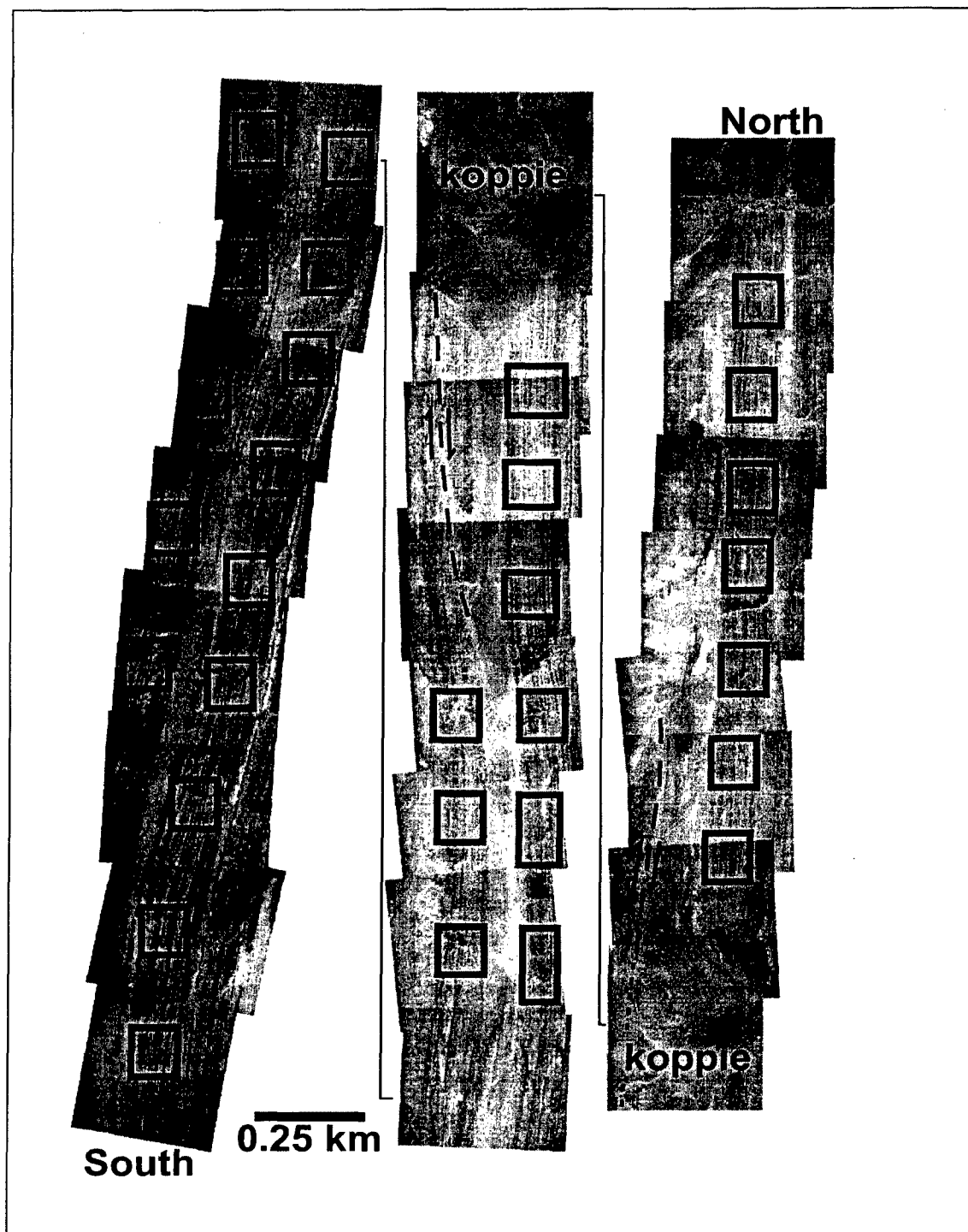
Figure 6-5: Photomosaic of study area. Boxes indicate locations of regions sampled for grayscale analysis. Sample regions are of equal area.
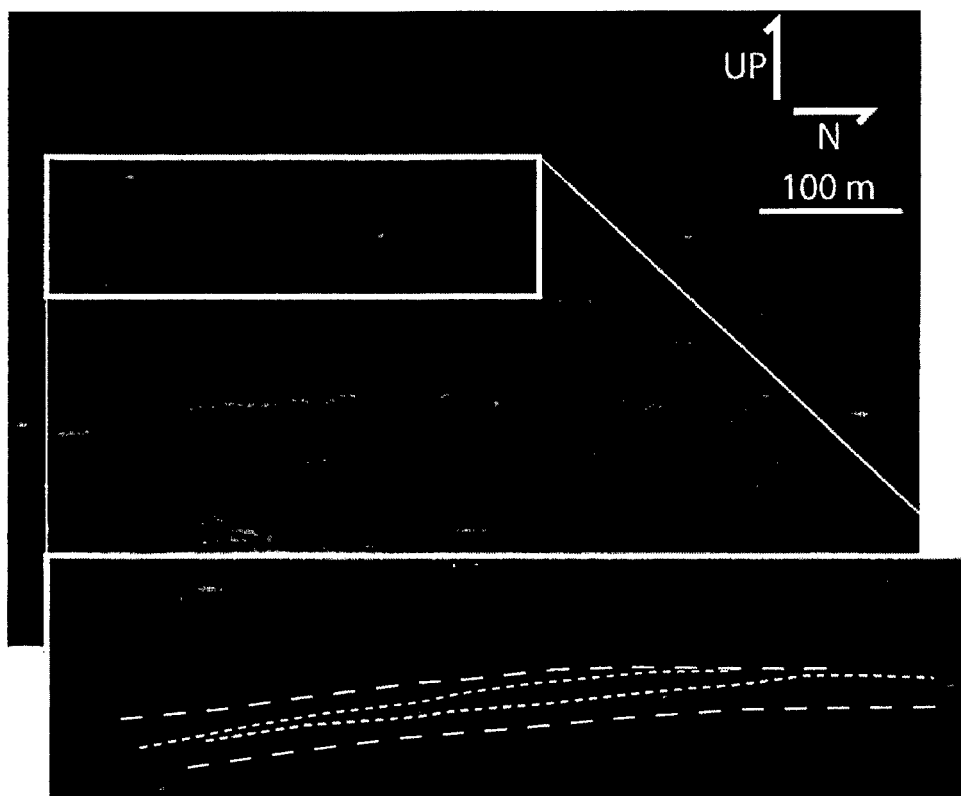
Figure 6-6: Example of a bundle termination. Such terminations are rare in this exposure of the Brak River Formation. The termination shown here is the southern-most termination identified in Figure 6-7.
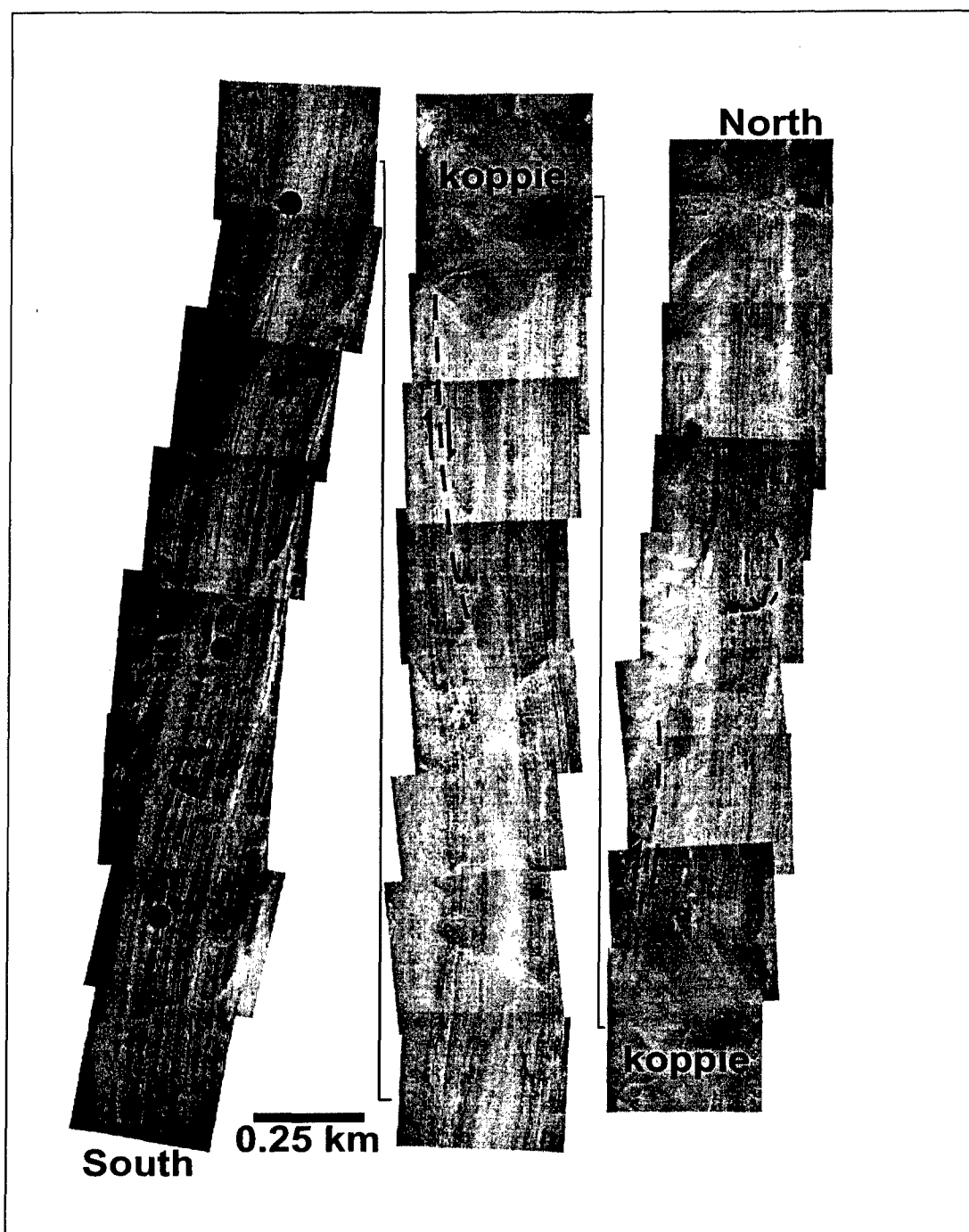
Figure 6-7: Photomosaic indicating locations of bundle terminations (red dots). See Figure 6-6 for a detailed view of a bundle termination. Note that the terminations are concentrated in the southern portion of the photomosaic suggesting that this end of the outcrop is closer to a margin – lateral or distal extent – of the depositional system. Major erosional features (e.g. channels) are absent in this field area however there are two locations where bundles appear amalgamated and lack intervening fine-grained deposits. These two areas are circled with dashed ovals.
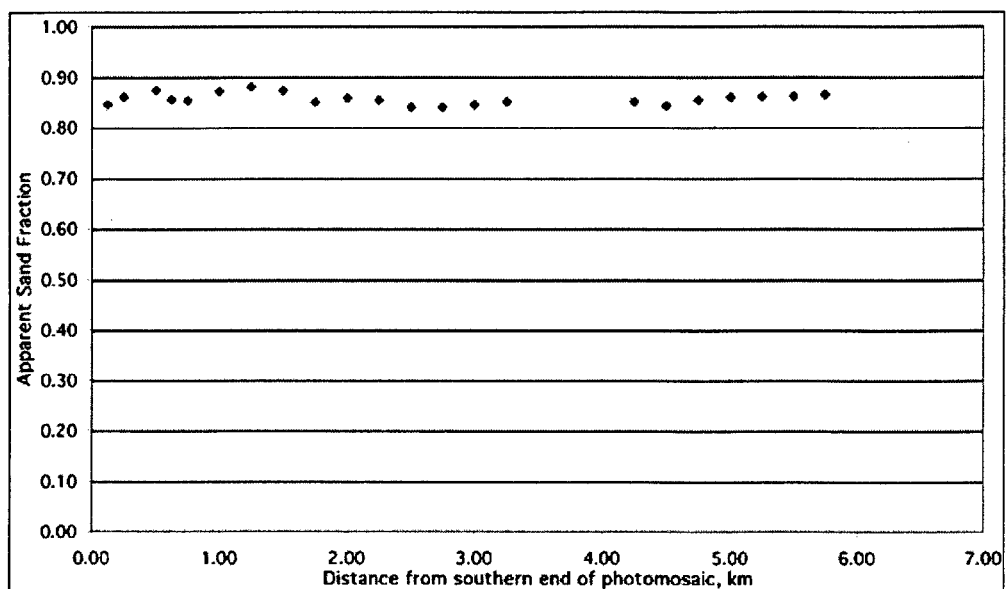
Figure 6-8: Apparent sand fractions for lower unit calculated from the mean grayscale values of the regions indicated in Figure 6-5. Distance from south end of photo mosaic, in kilometers, is indicated on the x-axis. The average value of these means is 0.86.
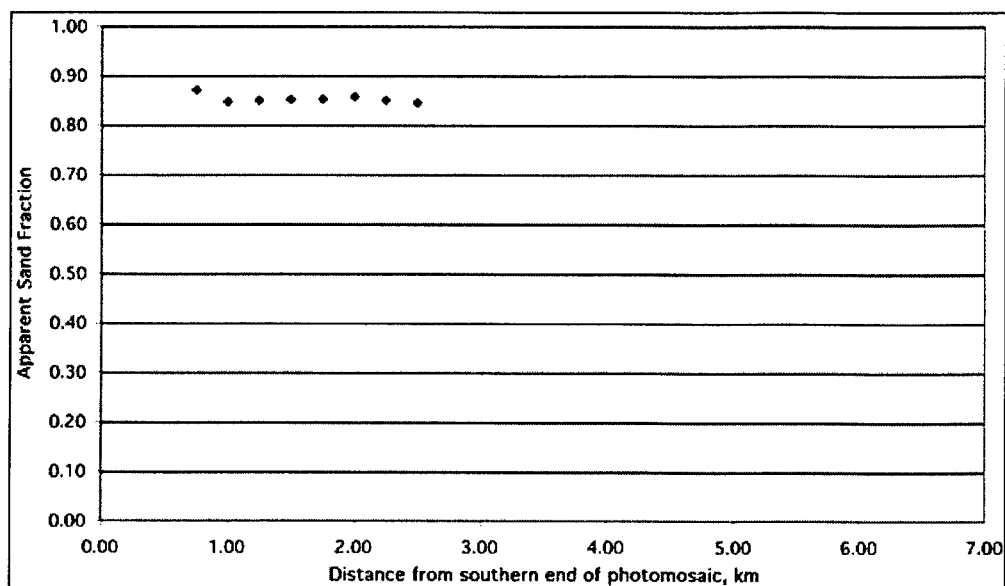
Figure 6-9: Apparent sand fraction for upper unit calculated from the mean grayscale values of the regions indcated in Figure 6-5. Distance from south end of photo mosaic, in kilomters, is indicated on the x-axis. The average value of these means is 0.85.

231
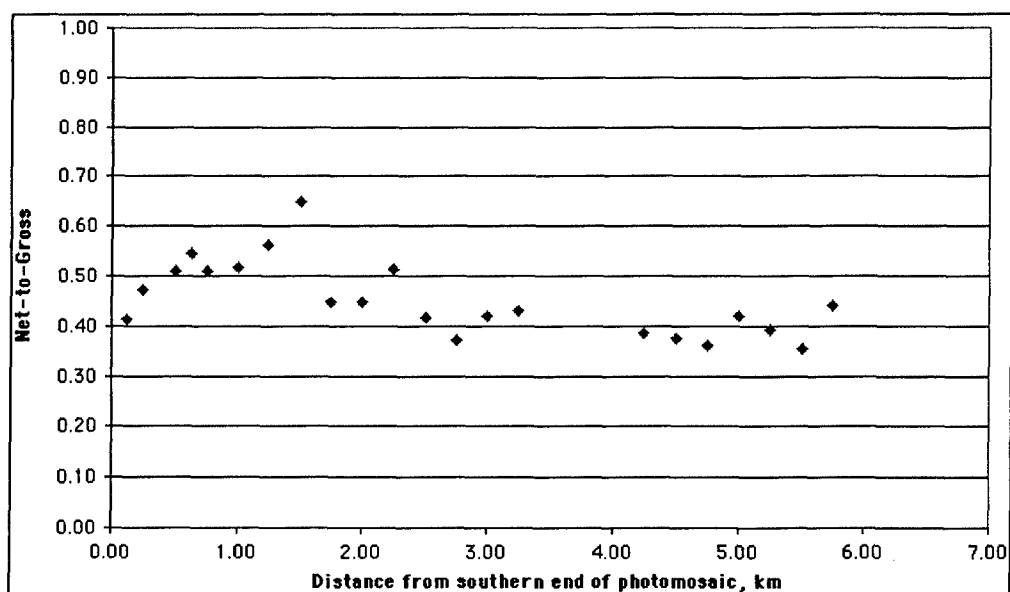
Figure 6-10: Net-to-gross values for lower unit calculated through thresholding of grayscale histograms from the regions indicated in Figure 6-5. Distance from the south end of the photo mosaic is, in kilometers, is indicated on the x-axis. The average of these net-to-gross values is 0.45.
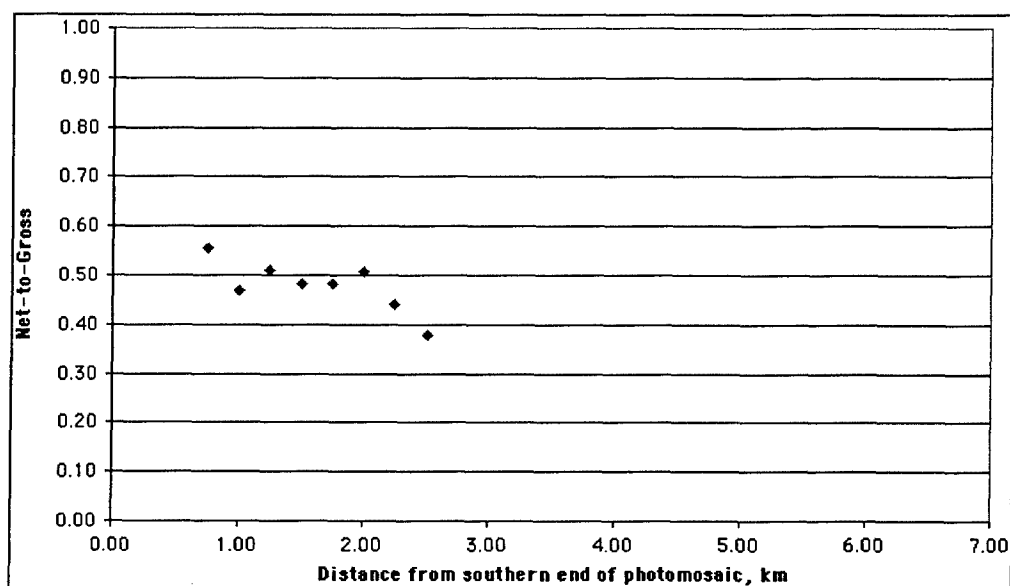
Figure 6-11: Net-to-gross values for upper unit calculated through thresholding of grayscale histograms from the regions indicated in Figure 6-5. Distance from the south end of the photo mosaic, in kilometers, is indicated the on x-axis. The average of these net-to-gross values is 0.48.
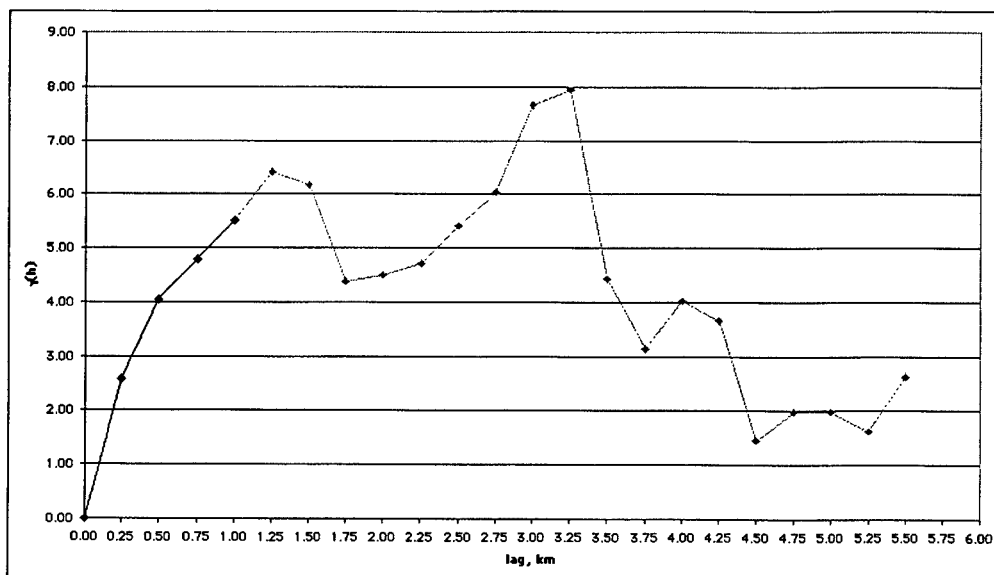
Figure 6-12: Variogram of sand fraction data for lower unit (see Figure 6-8). A lag of 0.25 km, the spacing between analyzed subregions, was employed. In those cases where two subregions were analyzed in a single image, the sand fraction values for those two subregions were averaged and treated as a single data point. Data outside of the correlation lengthscale is indicated in grey. The correlation length scale is 1.00 km.
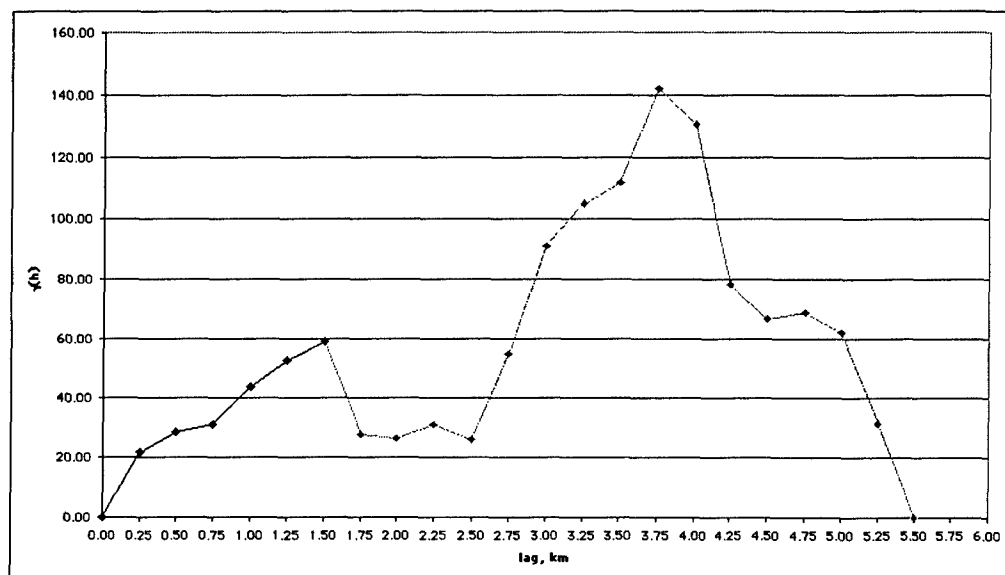
Figure 6-13: Variogram of net-to-gross data for lower unit (see Figure 6-10 for data). A lag of 0.25 km, the distance between analyzed subregions, was employed. In those cases where two subregions were analyzed in a single image, the net-to-gross values for those two subregions were averaged and treated as a single data point. Data outside of the correlation lengthscale is indicated in grey. The correlation lengthscale is 1.50 km.

TURBIDITE FACIES TRACTS AS RELATED TO THE TEXTURAL COMPOSITION OF PARENT FLOW
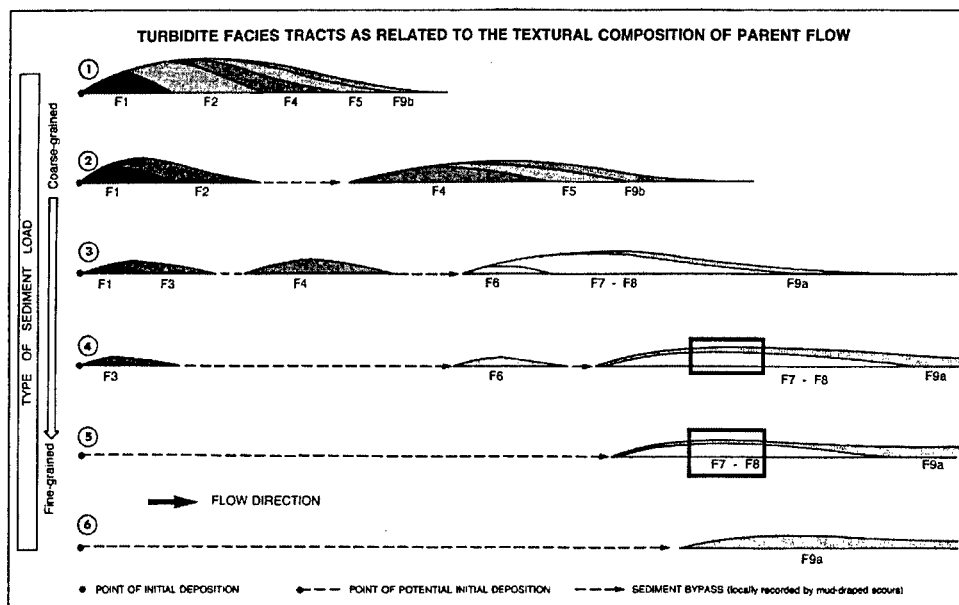
Figure 6-14: Model of turbidite depositional facies modified to illustrate potential postion of Brak River Formation outcrop used in this study. Areas with facies comparable to the Brak River Formation bundles and intervening fines, and that have relatively constant lithology as observed in this study area, are indicated with boxes. Modified from Mutti and Davoli (1992).

A. Compensation-style lobe deposition

B. Koppie region deposition
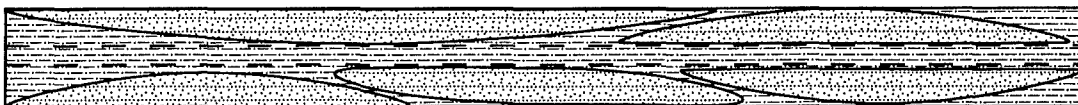
Coarse-grained turbidite bundles

Intervening fine-grained sediments

Fine-grained sediments representing a local hiatus in sand deposition

Figure 6-15: Examples of two styles of lobe deposition. A) Compensation stacking whereby lobes adjust to fill local accommodation space. The supply of coarse-grained material to the area is relatively constant. B) Stacking style observed in this study. There are distinct interruptions in the local supply of coarse-grained sediment. In B, the fine-grained sediments between the dashed lines represent a hiatus in coarse-grained deposition. This fine-grained zone is comparable to the intervening fines between turbidite bundles described in this work.

Chapter 7

Conclusion

This thesis has addressed a series of questions at a range of scales. At the largest scale, I have developed a method for quantifying the response time of natural basins and the interplay between sedimentation and subsidence and used it to answer the fundamental question of the scale at which sedimentation and subsidence are in balance. At the mesoscale, I have taken advantage of one of the most extensive deepwater outcrops in the world to evaluate the lateral extent of deposition for unconfined deepwater deposits. And at the bed scale, I have shown that simple but detailed evaluations of grainsize distributions and, more importantly, vertical and lateral grainsize trends within a bed can be used to constrain the depositional conditions of one of the more enigmatic deepwater facies.

Equilibrium analyses of sheet-like deepwater deposits from Fisk Basin, Gulf of Mexico reveal surprisingly long equilibrium times. I find this interval of time to be 4.6×10^5 years, corresponding to an interval thickness of about 600 m. This characteristic time is well above known allocyclic forcings and suggests that such signals can not be confidently interpreted in this particular instance. Many of the more detailed analyses of basin fill patterns and related dynamics are below this temporal and spatial scale and the results of this thesis supports the fact that only stratigraphic trends on the order of half a million years or longer should be given significance beyond simple autocyclic system behavior. Extending this analyses to a channelized system in Chapter 3, I obtained the surprising result that the confined flow, topography gener-

237

ating channel/levee complexes with reduced basin averaged sedimentation rates have an equilibrium time less than half that of the broadly distributed sheets in Chapter 2. This suggests that mobility of the depositional system sets the equilibrium time and that the sheet systems are not nearly as sensitive to subsidence rate and local slope as previously believed.

Data for Chapter 5 was composed of closely spaced, digitally mapped stratigraphic horizons and sediment sample locations that enable me first to relate geometries of individual beds to the larger scale channel forms and then to define vertical and lateral changes in grain size and sorting within the individual beds. Working with this data I show how: 1) bed geometry can be used to constrain vertical and temporal flow characteristics; 2) coarse-tail grading can be used to set bounds on current velocities and depths information that has been particularly elusive for deepwater environments; and 3) estimates for the finest-grained component within depositing currents can be derived through analysis of sorting trends in CGS beds. I calculated that the depositing flows at the San Clemente site were moving with vertically averaged velocities of several meters per second and were on the order of a few tens of meters in thickness. Furthermore, the relating grainsize data in the bed to what I know to be in the flows, I show that coarse-grained massive beds are a poor representation of the flows from which they were deposited.

Finally, in Chapter 6 I show the true extend, albeit potentially an end member, of the lateral continuity of unconfined deepwater systems. I find that the Zerrissene Turbidites of Namibia have lateral continuities measured on the scale of kilometers while vertical dimensions are a few tens of meters. I also determined that lithologic characteristics such as sand fraction can be correlated over exceptionally long distances of a kilometer or more.

Bibliography

J.R.L. Allen. *Current ripples their relation to patterns of water and sediment motion.* North-Holland Publishing Co., Amsterdam, 1968.

J.R.L. Allen. The Bouma division A and the possible duration of turbidity currents. *Journal of Sedimentary Petrology*, 61:291–295, 1973.

C.L. Angevine, P.L. Heller, and C. Paola. *Quantitative Sediment Basin Modeling.* American Association of Petroleum Geologists, Tulsa, OK, 1990.

R.A. Bagnold. *An approach to the sediment transport problem from general physics.* USGS Professional Paper. U.S. Geological Survey, Tulsa, OK, 1990.

D.C. Beard and P.K. Weyl. Influence of texture on porosity and permeability of unconsolidated sand. *American Association of Petroleum Geologists Bulletin*, 57: 349–369, 1973.

J.R. Benjamin and C.A. Cornell. *Probability, Statistics and Decision for Civil Engineers.* McGraw-Hill Book Company, New York, 1970.

G.C. Bond, M.A. Kominz, and W.J. Devlin. Thermal subsidence and eustacy in the Lower Paleozoic miogeocline of western North America. *Nature*, 306:775–779, 1983.

J.R. Booth, M.C. Dean, A.E. DuVernay III, and M.J. Styzen. Paleao-bathymetric controls on the stratigraphic architecture and reservoir development of confined fans in the Auger Basin: central Gulf of Mexico. *Marine and Petroleum Geology*, 20: 563–586, 2003.

J.R. Booth, A.E. DuVernay III, D.S. Pfeiffer, and M.J. Styzen. Sequence stratigraphic framework, depositional models, and stacking patterns of ponded and slope fan systems in Auger Basin: Central Gulf of Mexico slope. In *Deep-Water Reservoirs of the World; GCSSEPM Foundation 20th Annual Research Conference*, pages 82–103. Gulf Coast Section, Society of Economic Petrologists and Mineralogists, 2000.

A.H. Bouma. *Sedimentology of some Flysch Deposits*. Elsevier, Amsterdam, 1962.

A.H. Bouma and W.R. Bryant. Physiographic features on the northern Gulf of Mexico continental slope. *Geo-Marine Letters*, 14:252–263, 1994.

S.Q. Breard, A.D. Callender, D. Arden, and M.J. Nault. Biostratigraphic application and ecology of agglutinated foraminifera in Gulf of Mexico Basin Cenozoic exploration. *GCAGS Transactions*, 52:65–76, 2002.

S.Q. Breard, A.D. Callender, and M.J. Nault. Paleoecologic and biostratigraphic models for Pleistocene through Miocene foraminiferal assemblages of the Gulf Coast Basin. *GCAGS Transactions*, 43:493–502, 1993.

S.Q. Breard, A.D. Callender, and M.J. Nault. Local foraminiferal faunas: the key to enhanced stratigraphic resolution of expanded Cenozoic sections in the Gulf Coast Basin. *GCAGS Transactions*, 46:55–62, 1996.

S.Q. Breard, A.D. Callender, and M.J. Nault. Application of bathyal foraminiferal events to the Neogene through Pliestocene biostratigraphic framework of the Gulf of Mexico Basin. *GCAGS Transactions*, 47:65–73, 1997.

H. Camacho, C.J. Busby, and B Kneller. A new depositional model for the classical

turbidite locality at San Clemente State Beach, California. *AAPG Bulletin*, 89(9): 1543–1560, 2002.

K.M. Campion, A.R. Sprague, D. Mohrig, R.W. Lovell, P.A. Drzewiecki, M.D. Sullivan, J.A. Ardill, G.N. Jensen, and D.K. Sickafoose. Outcrop expression of confined channel complexes. In *Deep-Water Reservoirs of the World; GCSSEPM Foundation 20th Annual Research Conference*, pages 127–150. Gulf Coast Section, Society of Economic Petrologists and Mineralogists, 2000.

C. Chakrabarti and D.R. Lowe. Diffusion of sediment on the lee of dune-like bedforms: theoretical and numerical analysis. *Sedimentology*, 28:531–545, 1981.

K. Chikita. A field study on turbidity currents initiated from spring runoffs. *Water Resources Research*, 25:257–271, 1989.

K. Chikita. Sedimentation by river-induced turbidity currents: field measurements and interpretation. *Sedimentology*, 37:891–905, 1990.

J.D. Clark and K.T. Pickering. *Submarine channels: Processes and architecture.* Vallis Press, London, 1996a.

J.D. Clark and K.T. Pickering. Architectural elements and growth patterns of submarine channels: Application to hydrocarbon exploration. *AAPG Bulletin*, 80:194–221, 1996b.

M.P. Coward. The junction between the Pan-African mobile belts in Namibia: its structural history. *Tectonophysics*, 76:59–73, 1981.

J.C. Davis. *Statistics and data analysis in Geology.* John Wiley & Sons, New York, 1986.

M.C. Dean, J.R. Booth, and K.M. King. Sequence stratigraphic framework, depositional models, and stacking patterns of ponded and slope fan systems in the Greater Auger Basin: Central Gulf of Mexico slope. In *Deep-Water Reservoirs of*

the World; GCSSEPM Foundation 20th Annual Research Conference, pages 193–303. Gulf Coast Section, Society of Economic Petrologists and Mineralogists, 2000.

M.C. Dean, J.R. Booth, and B.T. Mitchell. Multiple fields withing the sequence stratigraphic framework of the Greater Auger Basin, Gulf of Mexico. In *22nd Annual Gulf Coast Section SEPM Bob F. Perkins Research Conference*, pages 661–680. Gulf Coast Section, Society of Economic Petrologists and Mineralogists, 2002.

F.A. Diegel, J.F. Karlo, D.C. Schuster, R.C. Shoup, and P.R. Tauvers. Cenozoic structural evolution and tectono-stratigraphic framework of the northern Gulf coast continental margin. In M.P.A. Jackson, D.G. Roberts, and S. Snelson, editors, *Salt tectonics: a global perspective*, volume 65 of *AAPG Memoir*, pages 109–151. American Association of Petroleum Geologists, 1983.

W.E. Dietrich. Settling velocity of natural particles. *Water Resources Research*, 18: 1615–1626, 1982.

W.E. Dietrich, D.G. Bellugi, L.S. Sklar, J.D. Stock, A.M. Heimsath, and J.J. Roering. Geomorphic transport laws for predicting landscape form and dynamics. In P.R. Wilcock, editor, *Prediction in geomorphology*, number 135 in Geophysical Monograph, pages 103–132. American Geophysical Union, 2003.

H.A. Einstein. *The bed load function for sediment transportation in open channels*. Technical Bulletin 1026. Soil Conservation Service, U.S. Dept. of Agriculture, Washington, DC, 1950.

D.A. Evans, J.L. Kirshvink, and J.W. Holt. Paleomagnetism of the Chuos Formation, Otavi Mountains, Namibia. In *Windhoek Conference on Proterozoic Tectonics and Metallogeny, abstracts*, page 17, Windhoek, Namibia, Aug. 29–Sept. 1 1994.

J. Fan. Turbid density currents in reservoirs. *Water International*, 11:107–116, 1986.

J. Fan and G.L. Morris. Reservoir sedimentation. i: delta and density current deposits. *Journal of Hydraulic Engineering*, 118(3):354–369, 1992.

P.B. Flemings and T.E. Jordan. A synthetic statigraphic model of foreland basin development. *Journal of Geophysical Research B*, 94:3851–3866, 1989.

J. Fredsöe and R. Deigaard. *Mechanics of Coastal Sediment Transport*. World Scientific, Singapore, 1994.

E.E. Freyer and I.W. Hälbich. A note on the Ogden Rocks Formation: a proto-mylonite belt in the Damara Orogen. In R.McG. Miller, editor, *Evolution of the Damara Orogen of South West Africa/Namibia*, volume 11 of *Special Publication of the Geologic Society of South Africa*, pages 173–174. 1983.

M. Garcia, Y. Nino, and F. Lopez. Laboratory observations of particle entrainment into suspension by turbulent bursting. In P.J. Ashworth, S.J. Bennett, J.L. Best, and S.J. McLelland, editors, *Coherent flow structures in open channels*, pages 63–86. John Wiley and Sons, 1996.

M. Garcia and G. Parker. Entrainment of bed sediment into suspension. *Journal of Hydraulic Engineering*, 117:414–435, 1991.

M. Garcia and G. Parker. Experiments on the entrainment of sediment into suspension by a dense bottom current. *Journal of Geophysical Research*, 98:4793–4807, 1993.

R. Gilbert and J. Shaw. Sedimentation in proglacial Sunwapta lake, Alberta. *Canadian Journal of Earth Sciences*, 18:81–93, 1981.

B.M. Hand and C.E. Bartberger. Leeside sediment fallout patterns and the stability of angular bedforms. *Journal of Sedimentary Petrology*, 58:33–43, 1988.

B.U. Haq, J. Hardenbol, and P.R. Vail. The chronology of fluctuating sea level since the Triassic. *Science*, 235:1156–1167, 1987.

L.E. Hasbargen and C. Paola. Landscape instability in an experimental drainage basin. *Geology*, 28:1067–1070, 2000.

A.E.. Hay. Turbidity currents and submarine channel formation in Rupert Inlet, British Columbia, 1. Surge observations. *Journal of Geophysical Research*, 92(C3): 2875–2881, 1987a.

A.E.. Hay. Turbidity currents and submarine channel formation in Rupert Inlet, British Columbia, 1. The roles of continuous and surge-type flow. *Journal of Geophysical Research*, 92(C3):2883–2900, 1987b.

A.E.. Hay, R.W. Burling, and J.W. Murray. Remote acoustic detection of a turbidity current surge. *Science*, 217:833–835, 1982.

P.L. Heller and C. Paola. The large-scale dynamics of grain-size variation in alluvial basins, 2: Application to syntectonic conglomerate. *Basin Research*, 4:91–102, 1992.

G.R. Hess. Miocene and pliocene inner suprafan channel complex, San Clemente, California. In C.J. Stuart, editor, *A guidebook to Miocene lithofacies and depositional environments, coastal southern California and northwestern Baja California*, pages 99–105. 1979.

V.C. Hilton. Sandstone architecture and facies from the Annot Basin of the Tertiary SW Alpine Foreland Basin, SE France. In K.T. Pickering, R.N. Hiscott, N.H. Kenyon, F. Ricci Lucchi, and R.D.A. Smith, editors, *Atlas of Deepwater Environments: Architectural style in turbidite systems*, pages 227–235. 1995.

R.N. Hiscott and M. DeVries. Internal characteristics of sandbodies of the Ordovician Tourelle Formation, Quebec, Canada. In K.T. Pickering, R.N. Hiscott, N.H. Kenyon, F. Ricci Lucchi, and R.D.A. Smith, editors, *Atlas of Deepwater Environments: Architectural style in turbidite systems*, pages 207–211. 1995.

J. Imran, G. Parker, and N. Katopodes. A numerical model of channel inception on submarine fans. *Journal of the Geophysical Research, C, Oceans*, 103(1):1219–1238, 1998.

D.C. Jennette, T.R. Garfield, D.C. Mohrig, and G.T. Cayley. The interaction of shelf accommodation, sediment supply and sea level in controlling the facies, architecture

and sequence stracking patterns of the Tay and Forties/Seles basin-floor fans, central North Sea. In *Deep-Water Reservoirs of the World; GCSSEPM Foundation 20th Annual Research Conference*, pages 402–421. Gulf Coast Section, Society of Economic Petrologists and Mineralogists, 2000.

J.F.B. Jeppe. *The geology of the area along the Ugab River, west of the Brandberg.* PhD thesis, University of the Witwatersrand, Johannesburg, South Africa, 1952.

T.E. Jordan, P.B. Flemings, and J.A. Beer. Dating thrust-fault activity by use of foreland-basin strata. In K.L. Kleinspehn and C. Paola, editors, *New Perspectives in Basin Analysis*, pages 307–330. Springer-Verlag, New York, 1988.

W.Q. Kennedy. The structural differentiation of Africa in the Pan-African (+500 m.y.) tectonic episode. *8th Annual Report of the Research Institute of African Geology*, pages 48–99, 1964.

M.G. Kleinhans. *Sorting out sand and gravel: sediment transport and deposition in sand-gravel bed rivers.* The Royal Dutch Geographical Society, Utrecht.

P.D. Komar. The hydraulic interpretation of turbidites from their grain sizes and sedimentary structures. *Sedimentology*, 32:395–408, 1985.

G.H. Kuelegan. Laws of turbulent flow in open channels. In *Research Paper No. 1151*, number 21 in Journal of Research, pages 701–741. National Bureau of Standards, 1950.

P.H. Kuenen. Turbidity currents of high density. In *Report of the 18th International Geological Congress*, pages 44–52. London, 1950.

P.H. Kuenen. Properties of turbidity currents of high density. Number 2 in SEPM Special Publication, pages 14–33. Society of Economic Paleontologists and Mineralogists, 1951.

A.M. Lambert and F. Giovanoli. Records of riverborne turbidity currents and indications of slope failures in the Rhone delta of Lake Geneva. *Limnology and Oceanography*, 33:458–468, 1988.

A.M. Lambert, K.R. Kelts, and N.F. Marshall. Measurements of density underflows from Walensee, Switzerland. *Sedimentology*, 23:87–105, 1976.

P.N. Lawless, R.H. Fillon, and R.G. Lytton. Gulf of Mexico Cenozoic biostratigraphic lithostratigraphic and sequence stratigraphic even chronology. In B. Kohl, editor, *1997 GCAGS; geology cross the Gulf, new offshore technologies, keys to onshore revitalization*, number 47 in Transactions, pages 271–283. Gulf Coast Association of Geological Societies, 1951.

E.H. Lindsay, G.A. Smith, C.V. Haynes, and N.D. Opdyke. Sediments, geomorphology, magnetostratigraphy, and vertebrate paleontology in the San Pedro Valley, Arizona. *Journal of Geology*, 98:605–619, 1990.

D.R. Lowe. Sediment gravity flows: II. Depositional models with specific reference to the deposits of high-density turbidity currents. *Journal of Sedimentary Petrology*, 52:279–297, 1982.

J.H. Mackin. Concept of the graded river. *Bulletin of the Geologic Society of America*, 59:463–512, 1948.

J.G. Marr, P.A. Harff, G. Shanmugan, and G. Parker. Experiments on subaqueous sandy gravity flows: The role of clay and water content in flow dynamics and depositional structures. *Geological Society of America Bulletin*, 113:1377–1386, 2001.

O.J. Martinsen, T. Lien, R.G. Walker, and J.D. Collinson. Facies and sequential organisation of mudstone-dominated slope and basin floor succession; the Gull Island Formation, Shannon Basin, western Ireland. In E. Mutti, G.S. Steffens, C. Primez, M. Orlando, and D. Roberts, editors, *Turbidites; models and problems*, volume 20 of *Marine and Petroleum Geology*, pages 789–807. Parma, Italy, 2003.

G.V. Middleton. Experiments on density and turbidity currents III: Deposition of sediment. *Canadian Journal of Earth Sciences*, 4:475–505, 1967.

G.V. Middleton. Sediment deposition from turbidity currents. *Annual Review of Earth and Planetary Sciences*, 21:89–115, 1993.

R.McG. Miller. *Geological Map 2013 Cape Cross; 1:250 000.* Geologic Survey of Namibia, Windhoek, 1988.

R.McG. Miller, E.E. Freyer, and I.W. Hälbich. A turbidite succession equivalent to the entire Swakop Group. In R.McG. Miller, editor, *Evolution of the Damara Orogen of South West Africa/Namibia,* volume 11 of *Special Publication of the Geologic Society of South Africa,* pages 65–71. 1983.

B.T. Mitchell and M.C. Dean. A "healed slope" model for the deposition of turbidite reservoirs applied to Shell's Zia and Oregano discoveries in the deep water Gulf of Mexico. In *Deep-Water Reservoirs of the World; GCSSEPM Foundation 20th Annual Research Conference,* pages 653–616. Gulf Coast Section, Society of Economic Petrologists and Mineralogists, 2000.

D. Mohrig, P.L. Heller, C. Paola, and W.J. Lyons. Interpreting avulsion process from ancient alluvial sequences: Guadalope-Matarranya system (northern Spain) and Wasatch Formation (western Colorado). *Geological Society of America Bulletin,* 112(12):1787–1803, 2000.

D. Mohrig and J.D. Smith. Predicting the migration rates of subaqueous dunes. *Water Resources Research,* 32:3207–3217, 1996.

E. Mutti and G. Davoli. *Turbidite Sandstones.* AGIP & Instituto di Geologia, Università, Milan, 1992.

J.M. Nelson and J.D. Smith. Flow in meandering channels with natural topography. In S. Ikeda and G. Parker, editors, *River meandering,* pages 69–102. American Geophysical Union, Washington, DC, 1989.

T.H. Nelson. Salt tectonics and listric-normal faulting. In A. Salvador, editor, *The Gulf of Mexico Basin,* volume J of *The Geology of North America,* pages 73–98. Geologic Society of America, 1991.

Y. Nino, F. Lopez, and M. Garcia. Threshold for particle entrainment into suspension. *Sedimentology,* 50:247–263, 2003.

W.R. Normark. Growth patterns of deep-sea fans. *American Association of Petroleum Geologists Bulletin*, 54:2170–2195, 1970.

W.R. Normark. Submarine canyons and fan valleys. In R.H. Dott Jr. and R.H. Shaver, editors, *Modern and ancient geosynclinal sedimentation*, volume 19 of *SEPM Special Publication*, pages 56–68. Society of Economic Paleontologists and Mineralogists, 1974.

W.R. Normark. Observed parameters for turbidity-current flow in channels, Reserve Fan, Lake Superior. *Journal of Sedimentary Petrology*, 59:423–431, 1989.

R.A. Olea. *Geostatistics for engineers and earth scientists*. Kluwer Academic, Boston, 1999.

C. Paola, P.L. Heller, and C.L. Angevine. The large-scale dynamics of grain-size variation in alluvial basins, 1: Theory. *Basin Research*, 4:73–90, 1992.

G. Parker, M. Garcia, Y. Fukushima, and W. Yu. Experiments on turbidity currents over an erodible bed. *Journal of Hydraulic Research*, 25:123–147, 1987.

J.D. Parsons, W.J. Schweller, C.W. Stelting, J.B. Southard, W.J. Lyons, and J.P. Grotzinger. A preliminary experimental study of turbidite fan deposits. *Journal of Sedimentary Research*, 72:619–628, 2002.

A.C. Phillips and N.D. Smith. Delta slope processes and turbidity currents in prodeltaic submarine channels, Queen Inlet, Glacier Bay, Alaska. *Canadian Journal of Earth Science*, 29:93–101, 1992.

K.T. Pickering. Two types of outer fan lobe sequence, from the late Precambrian Kongsfjord Formation submarine fan, Finnmark, north Norway. *Journal of Sedimentary Petrology*, 51:1277–1286, 1981.

K.T. Pickering. Kongsfjord turbidite system. In A.H. Bouma, N.E. Barnes, and W.R. Normark, editors, *Submarine fans and related turbidite systems*, pages 237–244. Springer-Verlag, Berlin, 1985.

K.T. Pickering, R.N. Hiscott, and F.J. Hein. *Deep marine environments: Clastic sedimentation and tectonics*. Unwin Hyman, London, 1989.

K.T. Pickering, R.N. Hiscott, N.H. Kenyon, F. Ricci Lucchi, and R.D.A. Smith. *Atlas of Deepwater Environments: Architectural style in turbidite systems*. Conoco and Chapman & Hall, Aberdeen and London, 1995.

C. Pirmez and J. Imran. Reconstruction of turbidity currents in Amazon Channel. *Marine and Petroleum Geology*, 20:823–849, 2003.

H. Porada. Geodynamic model for the geosynclinal development of the Damara Orogen, Namibia/South West Africa. In H. Martin and F.W. Eder, editors, *Intracontinental fold belts*, pages 901–912. Springer-Verlag, Berlin, 1983.

B.E. Prather, J.R. Booth, G.S. Steffens, and P.A. Craig. Classification, lithologic calibration and stratigraphic succession of seismic facies from intraslope basins, deep water Gulf of Mexico, USA. *American Association of Petroleum Geologists Bulletin*, 82:701–728, 1998.

D.B. Prior, B.D. Bornhold, W. Wiseman Jr., and D.R. Lowe. Turbidity current activity in a British Columbia fjord. *Science*, 237:1330–1333, 1987.

J.G. Ramsay. *The folding and fracturing of rocks*. McGraw-Hill, London, 1967.

J.H. Reynolds, T.E. Jordan, N.M. Johnson, J.F. Damanti, and K.D. Tabbutt. Neogene deformation of the flat-subduction segment of the Argentine-Chilean Andes: Magnetostratigraphic constraints from Las Juntas, La Rioja province Argentina. *Bulletin of the Geologic Society of America*, 102:1607–1622, 1990.

R.N. Rosen et al. *Gulf of Mexico Basin biostratigraphic index microfossils: A geoscientists guide, foraminifers and nannofossils, Parts I and II — Oligocene through Pliostocene foraminifers*. Gulf Coast Section, Society of Economic Petrologists and Mineralogists, 1999.

A. Salvador. Origin and development of the Gulf of Mexico basin. In A. Salvador, editor, *The Gulf of Mexico Basin*, volume J of *The Geology of North America*, pages 131–180. Geologic Society of America, 1991.

J.G. Sclater and P.A.F. Christie. Continental stretching: an explanation of the post-Mid-Cretaceous subsidence of the central North Sea. *Journal of Geophysical Research*, 85(B7):3711–3739, 1980.

K.W. Shanley, C.J. O'Byrne, R.R. Fisher, and T.M. Smith. Preliminary discussion of net/gross distribution in Gulf of Mexico deep water reservoirs. In *Deep-Water Reservoirs of the World*, GCSSEPM Foundation 20th Annual Research Conference, pages 911–927. GCSSEPM, 2000.

G. Shanmugan. High-density turbidity currents: Are they sandy debris flows? *Journal of Sedimentary Research*, 66:2–10, 1996.

B.A. Sheets, T.A. Hickson, and C. Paola. Assembling the stratigraphic record: depositional patterns and time-scales in an experimental alluvial basin. *Basin Research*, 14:287–301, 2002.

N.D. Smith, M.A. Vendl, and S.K. Kennedy. Comparison of sedimentation regimes in four glacier-fed lakes of western Alberta. In R. Davidson-Arnott, W. Nickling, and B.D. Fahey, editors, *Research in Glacial, Glaciofluvial, and Glaciolacustrine Systems*, pages 203–238. Geobooks, Norwich, UK, 1982.

R.D.A. Smith. Sheet-like and channelized sediment bodies in a Silurian turbidite system, Welsh Basin, UK. In K.T. Pickering, R.N. Hiscott, N.H. Kenyon, F. Ricci Lucchi, and R.D.A. Smith, editors, *Atlas of Deepwater Environments: Architectural style in turbidite systems*, pages 250–254. 1995.

M.S. Steckler and A.B. Watts. The Gulf of Lion: Subsidence of a young continental margin. *Nature*, 287:425–429, 1980.

M.J. Styzen. *Late Cenozoic chronostratigraphy of the Gulf of Mexico.* chart in

2 sheets. Gulf Coast Section, Society of Economic Petrologists and Mineralogists, 1996.

B.M. Sumer and B. Oguz. Particle motions near the bottom in turbulent flow in an open channel. *Journal of Fluid Mechanics*, 86:109–127, 1978.

R. Swart. *The sedimentology of the Zerrissene Turbidite System, Damara Orogen, Namibia*. Memoir 13. Geological Survey of Namibia, Ministry of Mines and Energy, 1992.

D.J. Topping, D.M. Rubin, J.M. Nelson, P.J. Kinzel, and J.P. Bennett. Linkage between grain-size evolution and sediment depletion during Colorado River floods. In R.H. Webb, J.C. Schmidt, G.R. Marzolf, and R.A. Valdez, editors, *The controlled flood in Grand Canyon*, volume 110 of *AGU Monograph*. American Geophysical Union, 1999.

P.D. Trask. Compaction of sediments. *AAPG Bulletin*, 15(3):271–276, 1931.

B.A. van der Pluijm and S. Marshak. *Earth Structure: an introduction to structural geology and tectonics*. WCB/McGraw-Hill, 1997.

T. van Kessel and C. Kranenburg. Gravity currents of fluid mud on sloping bed. *Journal of Hydraulic Engineering*, 122:710–717, 1996.

R.G. Walker. Nested submarine-fan channels in the Capistrano Formation, San Clemente, California. *Geological Society of America Bulletin*, 86:915–924, 1975.

R.G. Walker and E. Mutti. Turbidite facies and facies associations. In G.V. Middleton and A.H. Bouma, editors, *Turbidites and deep water sedimentation*, Short course lecture notes, pages 119–157. Society of Economic Paleontologists and Mineralogists, Pacific Section, 1971.

F.H. Weirich. The record of density-induced underflows in a glacial lake. *Sedimentology*, 33:261–277, 1986.

O.E. Weser. Proximal turbidite environment, San Clemente Formation, Dana Point-Capistrano Beach area, California. In F.W. Bergen et al., editor, *Geologic guidebook, Newport Lagoon to San Clemente, California*, pages 50–54. Society of Economic Paleontologists and Mineralogists, Pacific Section, 1971.

K.X. Whipple. Fluvial landscape response time: How plausible is the steady-state denudation? *American Journal of Science*, 301:313–325, 2001.

J. Willemse, C.M. Schwellnus, J.W. Brandt, H.D. Russell, and D.P. van Rooyen. Lead deposits in the Union of South Africa and South West Africa. *Memoirs of the Geological Survey of South Africa*, 39:177, 1944.

C.D. Winker and J.R. Booth. Sedimentary dynamics of the salt-dominated continental slope, Gulf of Mexico: Integration of observations from the seafloor, near-surface, and deep subsurface. In *Deep-Water Reservoirs of the World; GCSSEPM Foundation 20th Annual Research Conference*, pages 1059–1086. Gulf Coast Section, Society of Economic Petrologists and Mineralogists, 2000.

B.P.K. Yung, H. Merry, and T.R. Bott. The role of turbulent bursts in particle re-entrainment in aqueous systems. *Chemical Engineering Science*, 44:873–882, 1988.

F. Zelt and C. Rossen. Geometry and continuity of deep-water sandstone and silt-stones of the Brushy Canyon formation (Permian) Delaware Mountains, Texas. In K.T. Pickering, R.N. Hiscott, N.H. Kenyon, F. Ricci Lucchi, and R.D.A. Smith, editors, *Atlas of Deepwater Environments: Architectural style in turbidite systems*, pages 167–183. 1995.

J. Zeng, D.R. Lowe, D.B. Prior, W.J. Wiseman Jr., and B.D. Bornhold. Flow properties of turbidity currents in Bute Inlet, British Columbia. *Sedimentology*, 38: 975–996, 1991.

50272-101

REPORT DOCUMENTATION PAGE	1. REPORT NO. MIT/WHOI 2004-15	2.	3. Recipient's Accession No.

4. Title and Subtitle

Quantifying Channelized Submarine Depositional Systems From Bed to Basin Scale

5. Report Date September 2004	
6.	

7. Author(s) William J. Lyons, III

8. Performing Organization Rept. No.

9. Performing Organization Name and Address

MIT/WHOI Joint Program in Oceanography/Applied Ocean Science & Engineering

10. Project/Task/Work Unit No. MIT/WHOI 2004-15

11. Contract(C) or Grant(G) No.

(C)

(G)

12. Sponsoring Organization Name and Address
Massachusetts Institute of Technology

13. Type of Report & Period Covered Ph.D. Thesis

14.

15. Supplementary Notes

This thesis should be cited as: William J. Lyons, III, 2004. Quantifying Channelized Submarine Depositional Systems From Bed to Basin Scale. Ph.D. Thesis. MIT/WHOI, 2004-15.

16. Abstract (Limit: 200 words)

In this thesis, I employ 3-D seismic data and outcrops to study turbidites from bed to basin scales. Using seismic data from the Fisk Basin, Gulf of Mexico, I develop a method to estimate the timeframe over which sedimentation and subsidence come into equilibrium within a basin. Basin-specific equilibrium times are found to range from 4.6×10^5 years to 2.0×10^5 years, depending upon depositional architecture. Such equilibrium times are critical; they define the threshold at which we can differentiate autogenic and allogenic stratigraphic signals. At the scale of turbidite beds, grainsize analyses of sediment samples from the Capistrano Formation, San Clemente, California, reveal the potential for misinterpretation that arises when deposits are studied without consideration of sedimentation dynamics. Simple bed shear calculations and Froude scaling indicate that, in contrast to earlier work, the coarse Capistrano Formation sediments are consistent with classical muddy, low-density turbidity currents. Finally, at the scale of amalgamated turbidite beds, outcrop mapping and aerial photography of the Zerrissene Turbidite System, Namibia, provide a measure of the lateral and vertical continuity of a deepwater turbidite system. The extensive continuous exposure of the Zerrissene reveal that correlation lengths of these systems can exceed 1.5 km.

17. Document Analysis   a. Descriptors
Turbidite
Equilibrium
Scale

b. Identifiers/Open-Ended Terms

c. COSATI Field/Group

18. Availability Statement Approved for publication; distribution unlimited.	**19. Security Class (This Report)** UNCLASSIFIED	**21. No. of Pages** 252
	20. Security Class (This Page)	**22. Price**

(See ANSI-Z39.18)   *See Instructions on Reverse*   OPTIONAL FORM 272 (4-77)
(Formerly NTIS-35)
Department of Commerce